



Calhoun: The NPS Institutional Archive
DSpace Repository

Theses and Dissertations

1. Thesis and Dissertation Collection, all items

2013-09

Increasing slew performance of reaction wheel attitude control systems

Crews, Steven R.,II

Monterey, California: Naval Postgraduate School

<http://hdl.handle.net/10945/37606>

This publication is a work of the U.S. Government as defined in Title 17, United States Code, Section 101. Copyright protection is not available for this work in the United States.

Downloaded from NPS Archive: Calhoun



Calhoun is the Naval Postgraduate School's public access digital repository for research materials and institutional publications created by the NPS community. Calhoun is named for Professor of Mathematics Guy K. Calhoun, NPS's first appointed -- and published -- scholarly author.

Dudley Knox Library / Naval Postgraduate School
411 Dyer Road / 1 University Circle
Monterey, California USA 93943

<http://www.nps.edu/library>



NAVAL POSTGRADUATE SCHOOL

MONTEREY, CALIFORNIA

THESIS

INCREASING SLEW PERFORMANCE OF REACTION WHEEL ATTITUDE CONTROL SYSTEMS

by

Steven R. Crews II

September 2013

Co-Advisors:

Mark Karpenko
Isaac M. Ross

Approved for public release; distribution is unlimited

THIS PAGE INTENTIONALLY LEFT BLANK

REPORT DOCUMENTATION PAGE			<i>Form Approved OMB No. 0704-0188</i>	
Public reporting burden for this collection of information is estimated to average 1 hour per response, including the time for reviewing instruction, searching existing data sources, gathering and maintaining the data needed, and completing and reviewing the collection of information. Send comments regarding this burden estimate or any other aspect of this collection of information, including suggestions for reducing this burden, to Washington headquarters Services, Directorate for Information Operations and Reports, 1215 Jefferson Davis Highway, Suite 1204, Arlington, VA 22202-4302, and to the Office of Management and Budget, Paperwork Reduction Project (0704-0188) Washington DC 20503.				
1. AGENCY USE ONLY (Leave blank)		2. REPORT DATE September 2013	3. REPORT TYPE AND DATES COVERED Master's Thesis	
4. TITLE AND SUBTITLE INCREASING SLEW PERFORMANCE OF REACTION WHEEL ATTITUDE CONTROL SYSTEMS			5. FUNDING NUMBERS	
6. AUTHOR(S) Steven R. Crews II				
7. PERFORMING ORGANIZATION NAME(S) AND ADDRESS(ES) Naval Postgraduate School Monterey, CA 93943-5000			8. PERFORMING ORGANIZATION REPORT NUMBER	
9. SPONSORING /MONITORING AGENCY NAME(S) AND ADDRESS(ES) N/A			10. SPONSORING/MONITORING AGENCY REPORT NUMBER	
11. SUPPLEMENTARY NOTES The views expressed in this thesis are those of the author and do not reflect the official policy or position of the Department of Defense or the U.S. Government. IRB Protocol number ____ N/A ____.				
12a. DISTRIBUTION / AVAILABILITY STATEMENT Approved for public release; distribution is unlimited			12b. DISTRIBUTION CODE	
13. ABSTRACT (maximum 200 words) This thesis explores the physical and mathematical limitations of two common attitude control systems: one based on reaction wheels and another based on control moment gyroscopes (CMGs). The dynamics are derived from first principles and control algorithms for achieving maximum reaction wheel potential are discussed. The shaped eigenaxis input is utilized to establish baseline maneuver performance. A time-optimal shaped input is introduced and implemented in a feedback setting, subject to the limitations of the Moore-Penrose pseudo-inverse control allocation. Finally, a feed-forward plus feedback controller is introduced to implement the time-optimal torque inputs directly to the reaction wheels. This obviates the need for the pseudo-inverse control allocation, and therefore exploits the total capacities of both the reaction wheel momentum envelope and torque envelope. These reaction wheel control approaches are compared with CMG performance to establish spacecraft size and slew parameters that make the use of reaction wheels a reasonable choice				
14. SUBJECT TERMS reaction wheel, control moment gyroscope, CMG, momentum envelope, torque envelope, optimization, optimal control, pseudo-inverse, DIDO, scaling, effective eigenaxis, reaction wheel advantage angle			15. NUMBER OF PAGES 197	
			16. PRICE CODE	
17. SECURITY CLASSIFICATION OF REPORT Unclassified	18. SECURITY CLASSIFICATION OF THIS PAGE Unclassified	19. SECURITY CLASSIFICATION OF ABSTRACT Unclassified	20. LIMITATION OF ABSTRACT UU	

THIS PAGE INTENTIONALLY LEFT BLANK

Approved for public release; distribution is unlimited

**INCREASING SLEW PERFORMANCE OF REACTION WHEEL ATTITUDE
CONTROL SYSTEMS**

Steven R. Crews II
Major, United States Army
B.S., United States Military Academy, 2003

Submitted in partial fulfillment of the
requirements for the degrees of

**MASTER OF SCIENCE IN ASTRONAUTICAL ENGINEERING
AND
MASTER OF SCIENCE IN MECHANICAL ENGINEERING
AND
ASTRONAUTICAL ENGINEER**

from the

**NAVAL POSTGRADUATE SCHOOL
September 2013**

Author: Steven R. Crews II

Approved by: Dr. Mark Karpenko
Co-Advisor

Dr. Isaac M. Ross
Co-Advisor

Dr. Knox T. Millsaps
Chair, Department of Mechanical and Aerospace Engineering

THIS PAGE INTENTIONALLY LEFT BLANK

ABSTRACT

This thesis explores the physical and mathematical limitations of two common attitude control systems: one based on reaction wheels and another based on control moment gyroscopes (CMGs). The dynamics are derived from first principles and control algorithms for achieving maximum reaction wheel potential are discussed. The shaped eigenaxis input is utilized to establish baseline maneuver performance. A time-optimal shaped input is introduced and implemented in a feedback setting, subject to the limitations of the Moore-Penrose pseudo-inverse control allocation. Finally, a feed-forward plus feedback controller is introduced to implement the time-optimal torque inputs directly to the reaction wheels. This obviates the need for the pseudo-inverse control allocation, and therefore exploits the total capacities of both the reaction wheel momentum envelope and torque envelope. These reaction wheel control approaches are compared with CMG performance to establish spacecraft size and slew parameters that make the use of reaction wheels a reasonable choice.

THIS PAGE INTENTIONALLY LEFT BLANK

TABLE OF CONTENTS

I.	INTRODUCTION.....	1
A.	MOTIVATION	1
B.	BACKGROUND	2
C.	LIMITATIONS ON AGILITY.....	4
D.	OBJECTIVES AND SCOPE OF THIS THESIS.....	6
II.	SPACECRAFT KINEMATICS AND DYNAMICS.....	9
A.	MODELING A SPACECRAFT	9
B.	QUATERNION KINEMATICS.....	10
C.	MODELING SPACECRAFT KINEMATICS.....	11
D.	SPACECRAFT DYNAMICS.....	11
E.	MODELING SPACECRAFT DYNAMICS	15
III.	EIGENAXIS REORIENTATION.....	17
A.	SHORTEST ANGLE MANEUVER	17
B.	QUATERNION FEEDBACK.....	19
C.	GAIN DESIGN FOR QUATERNION ERROR FEEDBACK	22
D.	TRAJECTORY SHAPING.....	26
IV.	REACTION WHEELS.....	29
A.	ORIENTATION.....	30
B.	DIFFERENTIAL EQUATIONS OF MOTION.....	36
C.	MODELING REACTION WHEELS	40
D.	REACTION WHEEL MOMENTUM SPACE	41
E.	LARGEST INSCRIBED SPHERE	44
F.	REACTION WHEEL PSEUDO-INVERSE STEERING LOGIC.....	46
1.	Pseudo-Inverse Control Allocation	46
2.	Performance Loss.....	49
G.	PSEUDO-INVERSE LARGEST INSCRIBED SPHERE.....	52
V.	OPTIMAL REACTION WHEEL ATTITUDE CONTROL.....	55
A.	TIME-OPTIMAL EIGENAXIS REORIENTATION.....	55
1.	Problem Formulation	55
2.	The Hamiltonian	58
3.	The Hamiltonian Minimization Condition	58
4.	The Costate Dynamics and the Adjoint Equation	59
5.	Transversality.....	60
6.	Bang-Bang Control	61
B.	OPTIMAL CONTROL EQUATIONS OF MOTION.....	63
1.	Spacecraft Kinematics	63
2.	Reaction Wheel Dynamics.....	64
3.	Spacecraft Dynamics	64
4.	State and Control Variables.....	64
5.	Actuator Constraints	65

6.	Initial and Final Conditions	65
7.	Cost Function	66
8.	Optimal Control Problem	66
C.	SCALING THE PROBLEM.....	66
1.	Designer Units	67
2.	Scaled Optimal Control Problem	68
D.	DIDO IMPLEMENTATION.....	69
1.	Cost Function	69
2.	Endpoint Function	70
3.	Path Function	70
4.	Dynamics Function	70
5.	Main Function	72
E.	OPTIMAL MANEUVER IMPLEMENTATION.....	74
F.	EXAMPLE TIME-OPTIMAL MANEUVER.....	77
1.	Optimal Solution	78
2.	Feasibility	79
3.	Optimality	83
G.	EIGENAXIS SLEW COMPARISON.....	85
H.	EFFECTIVE EIGENAXIS OF TIME-OPTIMAL MANEUVER – ANALYTICAL APPROACH.....	88
I.	EFFECTIVE EIGENAXIS OF TIME-OPTIMAL MANEUVER – NUMERICAL VERIFICATION OF ANALYTICAL APPROACH	93
J.	EFFECTIVE EIGENAXIS OF PSEUDO-INVERSE LIMITED TIME-OPTIMAL MANEUVER.....	96
K.	SUMMARY	98
VI.	CONTROL MOMENT GYROSCOPES.....	101
A.	ORIENTATION.....	103
B.	MODELING CMG ORIENTATION MATRICES.....	109
C.	DIFFERENTIAL EQUATIONS OF MOTION.....	111
1.	Gimbal Momentum and Torque.....	112
a.	CMG Gimbal Momentum – Single Gimbal	112
b.	CMG Gimbal Momentum – Gimbal Array	113
c.	CMG Gimbal Torque	114
2.	Wheel Momentum and Torque.....	115
a.	CMG Wheel Momentum – Single Wheel.....	115
b.	CMG Wheel Momentum – Wheel Array.....	116
c.	CMG Wheel Torque – Wheel Array.....	117
3.	Total Momentum and Torque	120
D.	MODELING CMGS.....	121
E.	CMG MOMENTUM SPACE	122
F.	CMG SINGULARITIES.....	124
1.	Solving Singularity Conditions	125
2.	Hyperbolic Singularities	126
3.	Elliptic Singularities.....	128
G.	CMG LARGEST INSCRIBED SPHERE	131

H.	SUMMARY	132
VII.	REACTION WHEEL AND CMG COMPARISON.....	135
A.	MOMENTUM SPACE AS A VISUALIZATION TOOL	135
B.	MOMENTUM AND TORQUE RELATIONSHIP	141
1.	Simplified Dynamics	141
2.	Market Research and Simplified Momentum and Torque Equations	141
C.	COMPARISON DEVELOPMENT	143
D.	MOMENTUM EXCHANGE DEVICE PERFORMANCE AS A FUNCTION OF MASS.....	154
E.	SUMMARY	157
VIII.	CONCLUSIONS AND FUTURE WORK.....	159
A.	CONCLUSIONS	159
B.	FUTURE WORK.....	160
	APPENDIX A. OPTIMAL CONTROL PROBLEM IN DESIGNER UNITS.....	163
	APPENDIX B. MARKET RESEARCH	165
A.	REACTION WHEELS.....	165
B.	CMGS.....	167
	LIST OF REFERENCES	169
	INITIAL DISTRIBUTION LIST	175

THIS PAGE INTENTIONALLY LEFT BLANK

LIST OF FIGURES

Figure 1.	Sphere Inscribed within a Cube	6
Figure 2.	Spacecraft Simulation Model.....	9
Figure 3.	Spacecraft Kinematics Model	11
Figure 4.	Spacecraft Dynamics Model	15
Figure 5.	Eigenaxis Slew.....	18
Figure 6.	PD Control of a Double Integrator Model	21
Figure 7.	Underdamped Reorientation (solid 10°, dashed 20° slews)	23
Figure 8.	Underdamped Reorientation (solid 10°, dashed 60° slews)	24
Figure 9.	Underdamped Reorientation (solid 10°, dashed 20° slews) α , ω Limited	25
Figure 10.	Critically Damped Reorientation (solid 10°, dashed 20° slews)	25
Figure 11.	Torque Input Shaping Model.....	27
Figure 12.	Angle Input Shaping Model.....	27
Figure 13.	Rate Limited Eigenaxis Slew	28
Figure 14.	Reaction Wheel Schematic	29
Figure 15.	Reaction Wheel Transformation	31
Figure 16.	Body Frame to MED Rotations	33
Figure 17.	Reaction Wheel Model	40
Figure 18.	Momentum Space for 4 Wheel Reaction Wheel ($\alpha = 0, 90, 180, 270^\circ$)	42
Figure 19.	Momentum Space of a 4 Reaction Wheel System.....	43
Figure 20.	Reaction Wheel Momentum Space with Largest Inscribed Sphere.....	45
Figure 21.	Reaction Wheel Momentum/Torque Space Showing Pseudo-Inverse Limit .	50
Figure 22.	Reaction Wheel Pseudo-Inverse Limited Space	51
Figure 23.	Reaction Wheel Pseudo-Inverse Limited Space – Orthogonal	52
Figure 24.	Pseudo-Inverse Momentum Space with Largest Sphere	53
Figure 25.	Momentum Space Comparison.....	54
Figure 26.	Acceleration Limited Eigenaxis Slew	62
Figure 27.	Rate Limited Eigenaxis Slew.....	63
Figure 28.	Cost Function Implemented as a DIDO Function.....	70
Figure 29.	Endpoint Function Implemented as a DIDO Function	70
Figure 30.	Dynamics Function Implemented as a DIDO Function.....	72
Figure 31.	DIDO Bounds Implemented within a DIDO script	73
Figure 32.	DIDO No Guess (20 nodes) Implemented within a DIDO script.....	73
Figure 33.	DIDO Seeded Guess (120 nodes) Implemented within a DIDO script	74
Figure 34.	Architecture for Optimal Maneuver Implementation: Spacecraft Model.....	74
Figure 35.	Architecture for Optimal Maneuver Implementation: Reaction Wheel Subsystem	75
Figure 36.	Architecture for Optimal Maneuver Implementation: Eigenaxis Quaternion Feedback Controller.....	75
Figure 37.	DIDO Control Solution (120 Nodes).....	78
Figure 38.	Optimal Quaternion Trajectory (120 Nodes).....	79
Figure 39.	State Quaternion Propagation (120 Nodes)	80
Figure 40.	State Spacecraft Body Rate Propagation (120 Nodes)	81

Figure 41.	State Reaction Wheel Rate Propagation (120 Nodes)	81
Figure 42.	DIDO Scaled States	82
Figure 43.	Scaled Costates	83
Figure 44.	Hamiltonian.....	84
Figure 45.	Torque and the Switching Functions	85
Figure 46.	Optimal and Eigenaxis Comparison: Quaternions.....	86
Figure 47.	Optimal and Eigenaxis Comparison: Euler Angles and Rates.....	87
Figure 48.	Optimal and Eigenaxis Comparison: Body Rates.....	88
Figure 49.	Time-Optimal Accessible Regions	89
Figure 50.	Reaction Wheel Effective Eigenaxis Sphere for Time-Optimal Maneuvers ..	91
Figure 51.	Reaction Wheel Effective Eigenaxis for Time-Optimal Maneuver – Analytical ($j_s=25.4 \text{ kg-m}^2$)	92
Figure 52.	Reaction Wheel Effective Eigenaxis for Time-Optimal Maneuver – Numerical Approach with $1.807 \tau_{\max}$ ($j_s=25.4 \text{ kg-m}^2$).....	94
Figure 53.	Reaction Wheel Effective Eigenaxis for Time-Optimal Maneuver – Numerical Approach with $[1.333, 1.569, 1.807] \tau_{\max}$ ($j_s=25.4 \text{ kg-m}^2$)	95
Figure 54.	Pseudo-Inverse Limited Time-Optimal Spacecraft Model	96
Figure 55.	Pseudo-Inverse Limited Time-Optimal Accessible Regions	97
Figure 56.	Pseudo-Inverse Limited Time-Optimal Momentum Sphere.....	98
Figure 57.	CMG Schematic.....	102
Figure 58.	CMG Transformation.....	104
Figure 59.	Body Frame to CMG Schematic.....	106
Figure 60.	CMG ith Orientation Matrix Column Model.....	109
Figure 61.	Rotation Matrix Model	110
Figure 62.	CMG Orientation Matrix Model.....	111
Figure 63.	CMG Model.....	122
Figure 64.	Momentum Space of a 4 CMG System Given $\beta=54.73^\circ$	123
Figure 65.	Hyperbolic Singularity Surface for $\epsilon_i=\pm[1 \ -1 \ 1 \ -1]^T$	127
Figure 66.	Hyperbolic Singularities	128
Figure 67.	Elliptic Singularity Surface (case 1)	129
Figure 68.	Elliptic Singularities.....	130
Figure 69.	Elliptic and Surface Singularities.....	131
Figure 70.	CMG Largest Sphere	132
Figure 71.	Normalized Momentum and Torque for a Trapezoidal Response.....	136
Figure 72.	Momentum/Torque Space During Eigenaxis Slew.....	137
Figure 73.	Normalized Momentum and Torque for an Optimal Maneuver.....	138
Figure 74.	Momentum/Torque Space During Optimal Maneuver	139
Figure 75.	Optimal Slew Example 2, $q_0=[0.36 \ 0 \ 0.79 \ 0.5]$, $q_f=[0 \ 0 \ 0 \ 1]$	140
Figure 76.	Optimal Slew Example 3, $q_0=[0.23 \ 0.17 \ 0.82 \ 0.5]$, $q_f=[0 \ 0 \ 0 \ 1]$	140
Figure 77.	Market Research Torque vs. Angular Momentum for Reaction Wheel and CMG Systems.....	142
Figure 78.	Slew Angle vs. Time Comparison for a 25.5 kg-m^2 Class Spacecraft	146
Figure 79.	Slew Angle vs. Time Comparison for a 2.55 kg-m^2 Class Spacecraft	148
Figure 80.	Maneuver Angles where Reaction Wheel Systems Outperform CMGs for a 2.55 kg-m^2 Class Spacecraft	149

Figure 81.	Slew Angle vs. Time Comparison for a 0.255 kg-m ² Class Spacecraft	150
Figure 82.	Maneuver Angles where Reaction Wheel Systems Outperform CMGs for a 0.255 kg-m ² Class Spacecraft	150
Figure 83.	Reaction Wheel Advantage Angle vs. Wheel/Rotor Momentum: Where RWs Overcome CMGs ($\omega=3^\circ/\text{s}$)	151
Figure 84.	Reaction Wheel Advantage Angle vs. Spacecraft Inertia: Where RWs Overcome CMGs ($\omega=3^\circ/\text{s}$)	152
Figure 85.	Zoom in: Reaction Wheel Advantage Angle vs. Spacecraft Inertia: Where RWs Overcome CMGs ($\omega=3^\circ/\text{s}$)	153
Figure 86.	Optimal Improvement over normal Reaction Wheel Systems	154
Figure 87.	Market Research Angular Momentum vs. Mass.....	155
Figure 88.	Array Momentum vs. Mass.....	156
Figure 89.	Array Torque vs. Mass.....	157

THIS PAGE INTENTIONALLY LEFT BLANK

LIST OF TABLES

Table 1.	Reaction Wheel Significant Axes	44
Table 2.	Optimal vs. Eigenaxis Comparison (120° slews)	88
Table 3.	Body Momentum/Torque Comparison Table – 1 Nms Momentum.....	144
Table 4.	Body Rate/Acceleration Comparison for a 25.5 kg-m ² Class Spacecraft.....	145
Table 5.	Body Rate/Acceleration Comparison for a 2.55 kg-m ² Class Spacecraft.....	147
Table 6.	Body Rate/Acceleration Comparison for a 0.255 kg-m ² Class Spacecraft...	149
Table 7.	Market Research Reaction Wheels	165
Table 8.	Market Research Reaction Wheels (cont.).....	166
Table 9.	Market Research Control Moment Gyroscopes.....	167

THIS PAGE INTENTIONALLY LEFT BLANK

LIST OF ACRONYMS AND NOMENCLATURE

Acronyms

ACS	Attitude Control System
CMG	Control Moment Gyroscope
DCM	Direction Cosine Matrix
EE	Effective Eigenaxis
EQF	Eigenaxis Quaternion Feedback
MED	Momentum Exchange Device
RW	Reaction Wheel

Nomenclature

h	Angular momentum
τ, \dot{h}	Torque
\mathbf{J}	Moment of Inertia Tensor
j	Element of Moment of Inertia Tensor
ω	Angular Velocity
Ω	Angular Velocity of the Wheel
δ	Gimbal angle
n	Number of MEDs in a Generic Array. The n th MED.
q	Quaternion
\mathbf{q}_{123}	Vector of First Three Quaternions

Superscripts

N	Inertial (i.e., h^N)
B	Body of Spacecraft
G	Gimbal
W	Wheel
${}^N\omega^B$	Angular Rate of Spacecraft Body Frame with Respect to Inertial Frame

Subscripts

s/c	Spacecraft
medA	Momentum Exchange Device Array
rw	Reaction Wheel
rwA	Reaction Wheel Array
cmg	Control Moment Gyroscope (CMG)
cmgA	Control Moment Gyroscope Array

tot	Total Momentum or Total Torque of the Spacecraft and MED Array Combined
req	Momentum or Torque Required of the MED Array
min	Minimum (i.e., minimum magnitude of the momentum in the body frame h_{\min}^B)
max	Maximum (i.e., maximum magnitude of the momentum for a single wheel: h_{\max})
i	The generic i th number out of a set
x,y,z	Body Coordinate Rates (i.e., ω_x, ω_y)
1,2,3	Column Components of the Respective Reorientation Matrices (i.e., ${}^B\mathbf{Z}_3^W$)
Opt	Time-Optimal
PseOpt	Time-Optimal subject to the Mathematical Limitations of the Pseudo-Inverse Limited Momentum and Torque Envelopes
Other	
•	Dot refers to rate of change with respect to time (i.e., $\dot{\delta}, \dot{h}$)
^	Carrot refers to unit dyadic (i.e., \hat{b}_1, \hat{w}_1)
+	Plus indicates Moore-Penrose pseudo-inverse (right)

Bold (i.e., $\mathbf{h}, \boldsymbol{\omega}$) indicates vector, while unbolded (i.e., h, ω) indicates scalar.
The International System of Units (SI) is used for all variables.

ACKNOWLEDGMENTS

I would like to express my sincere gratitude to my advisors, Prof. Mark Karpenko and Prof. Mike Ross. I am indebted to their continuous support and patience during my study and research. I could not have done this without their insight, brilliance and experience in spacecraft attitude control.

To the NPS faculty, research assistants, Ph.D. candidates, and fellow master's students. Thank you for pushing the envelope of discovery in every class. The stimulating discussions invigorated me far beyond the classroom.

I am grateful to my wife, Tara, for the encouragement, moral support and sacrifices. To my children, Abby, Carlie, and Gavin. May you be able to read and understand this thesis someday.

THIS PAGE INTENTIONALLY LEFT BLANK

I. INTRODUCTION

A. MOTIVATION

Spacecraft in low earth orbit (LEO) traverse around the earth at very high rates. For instance, a spacecraft in a circular orbit at 200 nautical miles altitude travels at speeds in excess of 17,000 mph. This equates to approximately 4 degrees of the orbit traveled every minute, completing a full orbit in 90 minutes. From the point of view of an imaging satellite, the spacecraft may only be able to see a ground target for 3–4 minutes, but this amount of time requires the orbit to pass directly over the target. Because much resolution is lost when taking low angle photographs, only the 20 degrees off-nadir is conventionally used [1, Table I-1], [2]. The off-nadir constraint significantly reduces the amount of time the target is within the line of sight. Depending on how far left or right of the orbit track the target is, the satellite may only have seconds to obtain an image. The problem is further complicated when multiple targets lie along that small target zone.

This space-based problem is even passed forward to the military ground commander. The battlefield owner requires timely battlespace situational awareness for his mission but may not have the state-sponsored weight in order to gain access to national assets within a timely manner. The Army's new imaging satellite concept, Kestrel Eye, is a new approach to fill this void. The intent is to put many small, inexpensive satellites into orbit to obtain images and transmit them to the battlespace owner more quickly. These satellites must be agile to get multiple images per target zone and responsive to last-minute request changes. Therefore, conventional slew rate limitation of about $2^\circ/\text{sec}$ must be overcome [2]. The mechanisms that induce rotation (momentum exchange devices) must therefore be used to their highest potential. In this way, the spacecraft can move from target to target as quickly as possible to minimize otherwise unproductive slew time. This thesis explores techniques to maximize actuator performance and minimize slew time without any hardware changes.

B. BACKGROUND

Control engineers typically employ two different types of electro-mechanical momentum exchange devices (MEDs) to perform spacecraft attitude control. The first is reaction wheels, which cause a reactionary body torque and momentum by counter-rotating a small rotor. Reaction wheels are simple to control and have a high momentum capacity, which translates to high angular velocity rates for the spacecraft. The second MED is a control moment gyroscope (CMG), which houses a spinning wheel within an intermediate gimbal frame. The gimbal frame is allowed to rotate, changing the orientation of the wheel's momentum vector. The gimbal torque input is in turn amplified (as the product of the gimbal rate and the magnitude of the momentum vector). The high torque output of CMGs is complicated by mechanical complexity of multiple rotating frames and the presence of zero-output singularities that must be avoided [3]. The elevated torque, and therefore higher acceleration of the spacecraft body, has led CMGs to become the de facto solution to generate agile spacecraft. Although reaction wheels are more prevalent [4] (Appendix B), cost less, are mechanically simpler, weigh less (Appendix B), and are easier to control, the torque output of CMGs simply cannot be matched by reaction wheels.

A spacecraft slew is the reorientation from one orientation in three dimensional space to another. For a basic slew, the initial and final spacecraft orientations are given in terms of their quaternion reference points. To reconcile the difference, the most basic approach is to treat the difference in quaternion vectors as a single arc. The arc of minimum distance rotates about a single axis, known as the Euler axis [5, p. 155] or eigenaxis [6, pp. 329–338]. A basic approach of control therefore is to treat the three-dimensional reorientation problem as a one-dimensional single angle slew along this arc, about the eigenaxis. The eigenaxis attitude control maneuver requires a single quaternion to be called for and error is regulated to zero as the spacecraft gets closer to the desired quaternion. This maneuver can be done as a step input, where the error is constantly corrected for by the controller [7]–[9]. The step input approach is simple to implement and stability is dependent upon only a few gains. Thus, the approach is popular in

spacecraft attitude control [10, pp. 212–267] [5, pp. 152–194] [6, pp. 403–452] [11, pp. 351–430].

One of the challenges of the step input approach is gain selection. The gains designed for large maneuvers may act slowly for small maneuvers, causing poor performance. Another approach is to use a shaped trajectory. Instead of passing a single final quaternion to the controller, a quaternion path for the maneuver is calculated and a set of discrete intermediate quaternions is passed as a target trajectory. Here, the gains are tuned to give acceptable performance and their values are agnostic to the slew size. Creamer *et al.* [12] developed a shaped bang-coast-bang maneuver about the eigenaxis, used on board the Clementine spacecraft. Time-optimal quaternion shaping was used on the TRACE spacecraft [13]. Additionally, [14] suggests shaping both trajectory and body rates and using these as inputs to the spacecraft attitude control (ACS) system.

A typical ACS uses four or more wheels for redundancy. However, the use of four or more wheels presents a control allocation problem. This is caused when torque or momentum required in the body frame must be produced by the redundant set of MEDs. A common method of torque and momentum allocation is to use the Moore-Penrose pseudo-inverse, which provides a least squares (L2) solution [5, p. 169] [6, p. 440] [11, p. 416] [15]. According to this approach, the full magnitude of the requested body torque may not be available in every direction. The minimum norm solution is devised, providing a unique allocation of wheel torques [16, pp. 49–57]. The pseudo-inverse does not take physical wheel limitations into account and may request more torque than is available. Once any wheel is saturated, then the remaining allocated torque is simply lost. This is because to remain on eigenaxis, the integrity of the least squares solution must be maintained. Thereby, proportional saturation across all wheels is necessary. Because of the nature of the Moore Penrose pseudo-inverse, maximum momentum and torque will be unavailable about certain axes. The pseudo-inverse is described within [15] in great detail, providing detailed illustrations of the L2 solution in three-dimensional space given various reaction wheel array configurations.

A way to bypass the L2 limitation is to operate the ACS in the open-loop (feedforward). One approach is to calculate the optimal torque solution and command the

wheels directly. This is far from conventional thinking, because the individual wheel torque solution is not generally available. The shape of the torque signal can be derived over the course of the maneuver. This feedforward concept has been around for decades [17]–[19], but the approach is susceptible to instability due to external disturbances and uncertainties of the spacecraft inertia or initial states [9]. For the solution to work properly, all states and parameters must be established exactly prior to reorientation, with no uncertainties throughout the maneuver. This ideal scenario is unlikely, so a merger of open-loop and closed-loop (feedback) must be used to improve stability and performance. Closed-loop implementation of open-loop maneuvers was flown on TRACE [20] with great success, but the performance gains were somewhat limited by the spacecraft preexisting software. Based on the literature available, it appears that industry may not be utilizing reaction wheels to their full potential, fostering a greater disparity between the capabilities of reaction wheels and CMGs.

C. LIMITATIONS ON AGILITY

In practice, a spacecraft slew rate is restricted for a variety of reasons. The most obvious limitations are due to the physical limitations of the MED array. For a reaction wheel system, an individual wheel is limited on how fast it can spin, thus the momentum it can produce. Positive rotation at maximum angular velocity results in a maximum momentum vector, while counter-rotating results in a momentum vector of equal magnitude and opposite direction. Given a skewed array of several reaction wheels, the vector sum of the maximum momentum vectors in any arbitrary direction creates the momentum envelope (Chapter IV). The shape of the reaction wheel momentum envelope is a polyhedron [15], involving sharp edges and vertices. This signifies that more momentum is available in certain directions than others. This momentum envelope produces the physical rate limit of the system about any given axis.

Many attitude control systems involve restricting the axis of rotation to the eigenaxis, thereby minimizing the angle of rotation. Since the momentum space is not spherically uniform, some axes allow faster rotation rates. This causes additional problems with slew planning. Not only are two quaternions in space given, but there is

also an eigenaxis-specific slew rate. Not to mention the increase in eigenaxis-specific slew acceleration (derived from the torque envelope, Chapter IV) to be concerned about.

When operators want an imaging satellite to obtain an image, the rate and acceleration variations over 4π steradians require them to focus on the temporal aspect of the maneuver. Typical questions are: Given the slew angle and specific eigenaxis, will the spacecraft arrive at the desired quaternion at the correct time? Is there another axis the spacecraft can slew about more quickly to image something else? Even with automation, trajectory planning becomes a time-consuming task. It may be far easier from an operational point of view to operate within a single capability, even if it means a loss of performance. This procedural limitation further reduces the operable reaction wheel momentum space polyhedron to the largest inscribed sphere, which provides guaranteed capability achievable in every direction. A simple example is a sphere inscribed inside of a cube (Figure 1). The envelope (cube) restricts the magnitude of the vector to 1.0 in some directions, while the maximum magnitude is 1.73 at the vertices. This amounts to a non-uniform momentum space, offering values of momentum about some axes that are considerably less than others. If operating at the envelope, the motion is difficult to predict without correlating the specific eigenaxis with the available momentum. Therefore, the engineer might design to the lowest magnitude (sphere) and provide this momentum limit to the planners as their planning constraint for travel about any axis. The same logic can be applied for torque limitations, but the main point here is that some performance is lost due to the need to simplify other aspects of spacecraft operations.

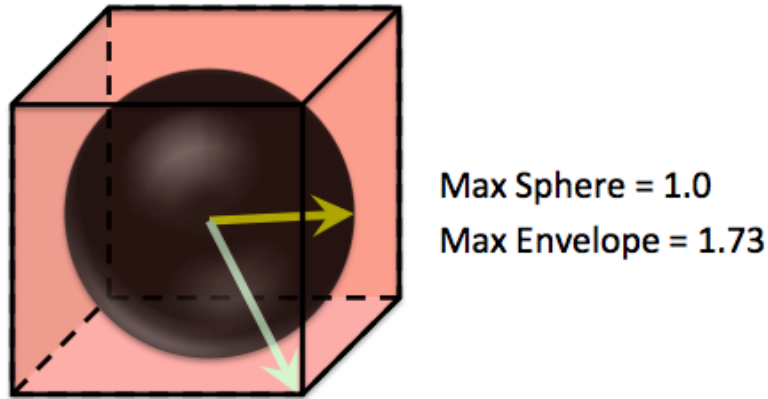


Figure 1. Sphere Inscribed within a Cube

D. OBJECTIVES AND SCOPE OF THIS THESIS

This thesis is an attempt to close some of the performance gaps between reaction wheels and CMGs, with the hope of identifying some key regions where reaction wheels may actually outperform CMGs. The true capabilities of reaction wheels are therefore explored to determine whether or not such an improvement is even feasible. The shaped trajectory used on the Clementine spacecraft [12] is developed (Chapter III) and analyzed (Chapter V). This maneuver becomes the basis for comparison of two different reaction wheel control algorithms that were developed as part of this thesis.

The main development is the time-optimal maneuver, which merges shaped torque feedforward with shaped quaternion and spacecraft body rate feedback (Chapter V). This approach avoids the mathematical limitations of pseudo-inverse control allocation by applying torque signals directly to the reaction wheels. The caveat of using feedforward plus feedback is that a margin must be built in to account for uncertainties. This adds to the body of knowledge because the use of optimal quaternion and body rate trajectories has the ability to correct for spacecraft parameter uncertainties and disturbances. An approach for adding system margin based on a level of uncertainty is discussed. Optimal solutions are solved using DIDO [21] and then propagated through a computer simulation of the spacecraft dynamics to verify their feasibility.

The second reaction wheel enhancement is an extension of the time-optimal trajectory, but limited to the pseudo-inverse space. This method again breaks away from the eigenaxis, but operates entirely within the confines of the L2 volume. This allows the control engineer to upload the time-optimal quaternion trajectory instead of simply the eigenaxis quaternion trajectory [12]. Since the only change is the shape of the trajectory, it is not very intrusive on the current employment of a standard shaped quaternion trajectory implementation. This method will be introduced at the end of Chapter V.

To aid in the setup of the problem, the spacecraft, reaction wheel, and CMG dynamics will be derived from first principles. This is done in Chapters II, IV, and VI, respectively. The equations of motion are then implemented within Simulink, which will act as a computer simulation of the actual nonlinear spacecraft dynamics. Various control algorithms will be applied to the same simulation to retain the structure of the model. Either the reaction wheel or CMG simulations can be selected as the current MED device within the model. Simulink also offers a graphical depiction of mathematical changes to the full dynamic setup, whereas changes can be hidden within loops if utilizing MATLAB alone.

The sphere concept is applied to the time-optimal case. For a series of time-optimal maneuvers between any two quaternions, it is shown how the minimum guaranteed momentum and torque can be derived for any direction of travel about any *effective eigenaxis*. This adds the ability for the planner to devise a single slew rate over any rotation angle, because the sphere remains independent of rotation axis and angle size. The effective sphere increases in size twice from the smallest inscribed sphere, once for each of the two optimal control techniques mentioned above. Therefore, two levels of ACS improvement are given as part of this work. Chapter V presents the concept of effective eigenaxis for an optimal maneuver and the details of the derivation.

A new technique for visualizing slews is introduced in Chapter VII. This method utilizes the normalized momentum and torque envelopes as the surface to display momentum and torque vectors throughout the maneuver. In the literature review, eigenaxis and quaternion traces were found, which only accounts for the path traveled. This new visualization tool allows the behavior of the rate and acceleration to be

observed with respect to the available momentum and torque capacity. The tool demonstrates fundamental features of the optimal control maneuvers.

Finally, the performance of all three reaction wheel control approaches are compared against that of a like-sized CMG in Chapter VII. Data from the market research from over 75 reaction wheels and CMGs is used to generate trends and differences between these different systems. A simple method of comparing reaction wheels and CMGs is developed. Momentum and torque capacities are compared with slew angle sizes to determine regions where reaction wheels outperform CMGs under the various control algorithms tested. Concluding remarks and suggestions for future work are given in Chapter VIII.

II. SPACECRAFT KINEMATICS AND DYNAMICS

The purpose of this chapter is to develop the spacecraft kinematics and dynamics. Spacecraft attitude kinematics will be modeled using quaternions. Spacecraft dynamics will be derived from first principles, showing the dynamic relationship between the momentum exchange device (MED) action and the spacecraft body reaction. The MED assembly (subscript *medA* in this chapter) is any generic arrangement of momentum exchange devices. It can be 3, 4, or n reaction wheels, n CMGs, or any combination of thereof.

A. MODELING A SPACECRAFT

The spacecraft, MED assembly, and feedback can be modeled within Simulink, shown in Figure 2.

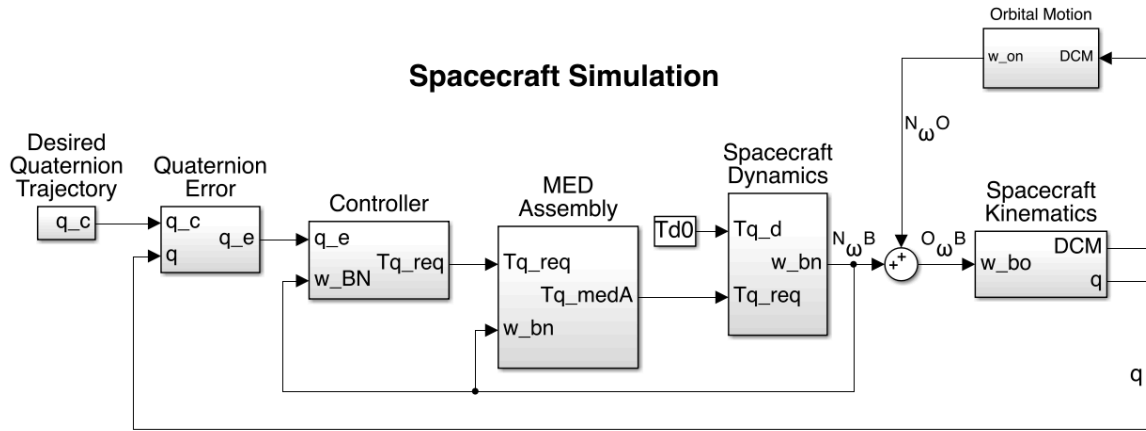


Figure 2. Spacecraft Simulation Model

Given a desired (commanded) quaternion and a current quaternion state, a quaternion error vector is produced. The controller attempts to drive that error to zero by producing an appropriate torque on the spacecraft. The MED Assembly attempts to produce that torque. The Spacecraft Dynamics model the spacecraft response, with torque disturbances (Td) possible, but these are not considered in this thesis. The spacecraft kinematics determines the current quaternion state. In this thesis, orbital motion is not

considered, so ${}^N\boldsymbol{\omega}^O = 0$, but it is shown to clarify the relationship between ${}^N\boldsymbol{\omega}^B$ and ${}^O\boldsymbol{\omega}^B$. The rate of the body with respect to the orbit is utilized within the spacecraft kinematics. This is determined by subtracting the orbital motion ${}^N\boldsymbol{\omega}^O$ from ${}^N\boldsymbol{\omega}^B$.

$$\begin{aligned} {}^N\boldsymbol{\omega}^B &= {}^N\boldsymbol{\omega}^O + {}^O\boldsymbol{\omega}^B \\ {}^O\boldsymbol{\omega}^B &= {}^N\boldsymbol{\omega}^B - {}^N\boldsymbol{\omega}^O \end{aligned} \quad (1)$$

Since orbital motion is not considered, ${}^N\boldsymbol{\omega}^B = {}^O\boldsymbol{\omega}^B$. The angular rate of the body with respect to inertial space is thus defined in Equation (2).

$${}^N\boldsymbol{\omega}^B = \begin{bmatrix} \omega_x \\ \omega_y \\ \omega_z \end{bmatrix}^B \quad (2)$$

B. QUATERNION KINEMATICS

Quaternion kinematics can be written as a set of four differential equations. The first three quaternions can be written as \mathbf{q}_{123} , while q_4 is kept as a separate dynamic equation for simplicity, shown in Equation (3) [6, Algorithm 5.76].

$$\begin{aligned} \dot{\mathbf{q}}_{123} &= \frac{1}{2} \left(q_4 {}^O\boldsymbol{\omega}^B - {}^O\boldsymbol{\omega}^B \times \mathbf{q}_{123} \right) \\ \dot{q}_4 &= -\frac{1}{2} \left({}^O\boldsymbol{\omega}^B \right)^T \mathbf{q}_{123} \end{aligned} \quad (3)$$

where $\mathbf{q}_{123} = \begin{bmatrix} q_1 & q_2 & q_3 \end{bmatrix}^T$. The entire quaternion vector can be written as $\mathbf{q} = \begin{bmatrix} \mathbf{q}_{123}^T & q_4 \end{bmatrix}^T$. Another thing to note about quaternions is that the two-norm is always equal to one. This allows one to solve for q_4 , given \mathbf{q}_{123} . The origin for this thesis will be defined as $\mathbf{q} = \begin{bmatrix} 0 & 0 & 0 & 1 \end{bmatrix}^T$.

$$\begin{aligned} \|\mathbf{q}\|_2 &= \sqrt{q_1^2 + q_2^2 + q_3^2 + q_4^2} = 1 \\ q_4 &= \sqrt{1 - q_1^2 - q_2^2 - q_3^2} \end{aligned} \quad (4)$$

C. MODELING SPACECRAFT KINEMATICS

Equation (3) is modeled into the Spacecraft Kinematics Simulink block, shown in Figure 3. The direction cosine matrix (DCM) mentioned is only used to determine the disturbance torques and is not used here as the disturbances are taken to be zero.

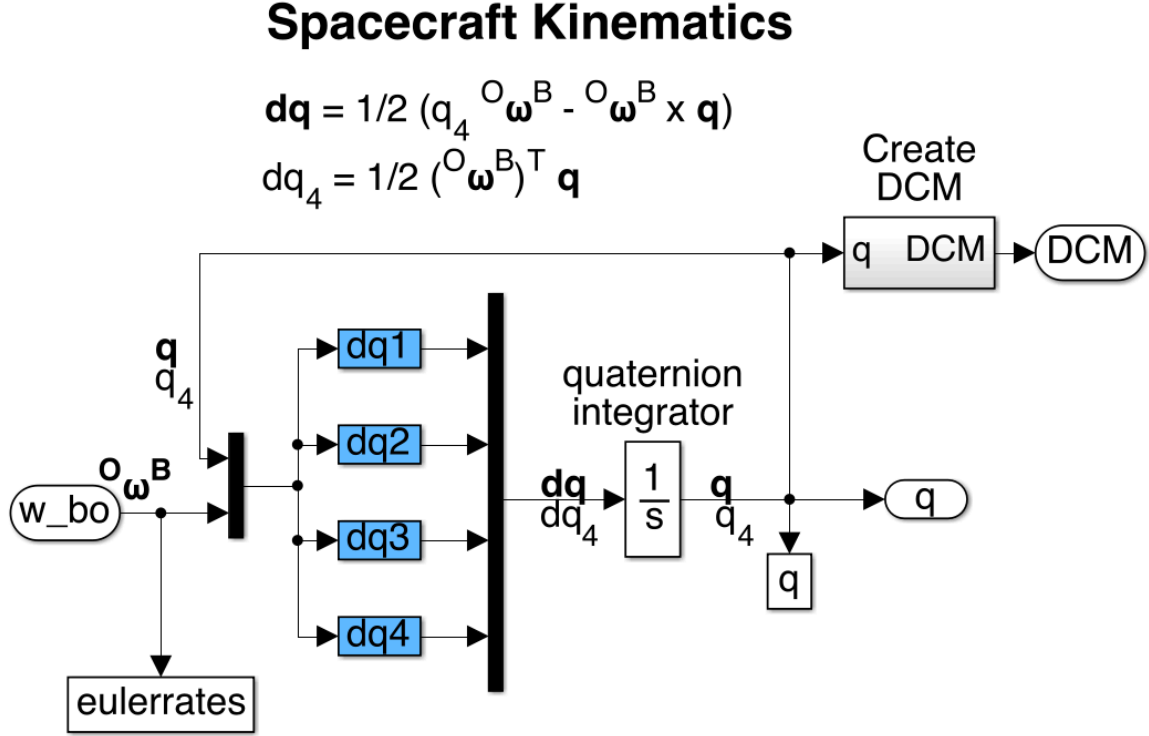


Figure 3. Spacecraft Kinematics Model

D. SPACECRAFT DYNAMICS

For a rigid body spacecraft with no external torques applied, the total angular momentum must be conserved. Since the total angular momentum \mathbf{h}_{tot}^N must be constant, then a positive variation in the MED assembly angular momentum \mathbf{h}_{medA}^N will have an opposite impact on spacecraft angular momentum $\mathbf{h}_{s/c}^N$ and vice versa. All momenta are written with respect to the inertial frame.

$$\mathbf{h}_{tot}^N = \mathbf{h}_{s/c}^N + \mathbf{h}_{medA}^N$$

$$\text{where } \|\mathbf{h}_{tot}^N\| = \text{constant} \quad (5)$$

Angular momentum is equivalent to the product of inertia and angular rate ($h = J\omega$). Applied specifically to the spacecraft, $\mathbf{J}_{s/c}$ represents the total structural inertia of the spacecraft. The inertia of the MED assembly is included within the spacecraft inertia. All configuration changes of the MED assembly with respect to the relatively small spacecraft body angular velocity will be considered negligible ($\dot{\mathbf{J}}_{medA}^N \boldsymbol{\omega}^B \approx 0$). The angular rate of the spacecraft is expressed in the body frame relative to the inertial frame $\boldsymbol{\omega}_{s/c} = {}^N \boldsymbol{\omega}^B$.

$$\mathbf{h}_{s/c}^B = \mathbf{J}_{s/c} \boldsymbol{\omega}_{s/c} = (\mathbf{J}_{s/cbody} + \mathbf{J}_{medA})^N \boldsymbol{\omega}^B \quad (6)$$

In this thesis, equations often are written in dyadic form to ensure that notation of the bases is clearly understood. Some derivations involving multiple frames can be easier manipulated (and understood) when utilizing dyadic form. Following this notation and assuming a diagonal inertia tensor, Equation (6) can be rewritten as

$$\begin{aligned} \mathbf{h}_{s/c}^B &= (j_{s/c11} \hat{b}_1 \hat{b}_1 + j_{s/c22} \hat{b}_2 \hat{b}_2 + j_{s/c33} \hat{b}_3 \hat{b}_3) \bullet (\omega_x \hat{b}_1 + \omega_y \hat{b}_2 + \omega_z \hat{b}_3) \\ &= j_{s/c11} \omega_x \hat{b}_1 (\hat{b}_1 \bullet \hat{b}_1) + j_{s/c11} \omega_y \hat{b}_1 (\hat{b}_1 \bullet \hat{b}_2) + j_{s/c11} \omega_z \hat{b}_1 (\hat{b}_1 \bullet \hat{b}_3) \\ &\quad + j_{s/c22} \omega_x \hat{b}_2 (\hat{b}_2 \bullet \hat{b}_1) + j_{s/c22} \omega_y \hat{b}_2 (\hat{b}_2 \bullet \hat{b}_2) + j_{s/c22} \omega_z \hat{b}_2 (\hat{b}_2 \bullet \hat{b}_3) \\ &\quad + j_{s/c33} \omega_x \hat{b}_3 (\hat{b}_3 \bullet \hat{b}_1) + j_{s/c33} \omega_y \hat{b}_3 (\hat{b}_3 \bullet \hat{b}_2) + j_{s/c33} \omega_z \hat{b}_3 (\hat{b}_3 \bullet \hat{b}_3) \end{aligned} \quad (7)$$

Since $\hat{b}_1, \hat{b}_2, \hat{b}_3$ are orthogonal, $\hat{b}_i \bullet \hat{b}_i = 1$ and $\hat{b}_i \bullet \hat{b}_j = 0$. This leads to

$$\mathbf{h}_{s/c}^B = j_{s/c11} \omega_x \hat{b}_1 + j_{s/c22} \omega_y \hat{b}_2 + j_{s/c33} \omega_z \hat{b}_3. \quad (8)$$

Sometimes it will be more convenient to show an equation in matrix form, Equation (9), but either form can be used universally.

$$\mathbf{h}_{s/c}^B = \begin{bmatrix} j_{s/c11} & 0 & 0 \\ 0 & j_{s/c22} & 0 \\ 0 & 0 & j_{s/c33} \end{bmatrix}^B \begin{bmatrix} \omega_x \\ \omega_y \\ \omega_z \end{bmatrix}^B = \begin{bmatrix} j_{s/c11} \omega_x \\ j_{s/c22} \omega_y \\ j_{s/c33} \omega_z \end{bmatrix}^B \quad (9)$$

Since angular momentum must be constant, the derivative with respect to time must be zero.

$$\dot{\mathbf{h}}_{tot}^N = \dot{\mathbf{h}}_{s/c}^N + \dot{\mathbf{h}}_{medA}^N = 0 \quad (10)$$

External torques can be added as disturbance torques per Equation (11).

$$\dot{\mathbf{h}}_{tot}^N = \dot{\mathbf{h}}_{s/c}^N + \dot{\mathbf{h}}_{medA}^N = \boldsymbol{\tau}_{ext}^N \quad (11)$$

Disturbance examples in LEO are gravity gradient, aerodynamic loads, and solar radiation. These and other external torques will be considered negligible in this thesis and will be set to zero ($\boldsymbol{\tau}_{ext}^N = 0$).

Equation (10) reveals that the spacecraft and MED assembly angular momentum rates must be equivalent in magnitude, opposite in direction. Also, the torque required to manipulate the spacecraft corresponds to the spacecraft angular momentum derivative in the inertial frame $\dot{\mathbf{h}}_{s/c}^N = \boldsymbol{\tau}_{req}^N$. Thus, the two terms can be used interchangeably to express the torque applied to the spacecraft by the MED assembly. Accordingly, the torque required of the MED assembly is equivalent to the negative torque in the body frame, shown in Equation (12).

$$\dot{\mathbf{h}}_{medA}^N = -\dot{\mathbf{h}}_{s/c}^N = -\boldsymbol{\tau}_{req}^N \quad (12)$$

To obtain the angular momentum rate with respect to the reference frame, the angular rate between the frames is necessary. Therefore, the angular momentum rate (torque) with respect to the inertial frame is equal to the sum of the torque in the body frame and the cross product between angular rate and angular momentum.

$$\dot{\mathbf{h}}_{s/c}^N = \dot{\mathbf{h}}_{s/c}^B + {}^N\boldsymbol{\omega}^B \times \mathbf{h}_{s/c}^B \quad (13)$$

The time derivative of Equation (6) is shown in Equation (14). The $\dot{\mathbf{J}}_{s/c}$ component is only applicable if fuel is being expended during the maneuver or if flexible elements are causing change. It is assumed that any changes would be very small; therefore the spacecraft can be modeled as a rigid body. Moreover, it is assumed that the

inertia of the spacecraft is not changing over the course of a maneuver and the term is zero, shown in Equation (15).

$$\dot{\mathbf{h}}_{s/c}^B = \mathbf{J}_{s/c}^N \boldsymbol{\omega}^B + \mathbf{J}_{s/c}^N \dot{\boldsymbol{\omega}}^B \quad (14)$$

$$\dot{\mathbf{h}}_{s/c}^B = \mathbf{J}_{s/c}^N \dot{\boldsymbol{\omega}}^B \quad (15)$$

Substituting Equation (6) and Equation (15) into Equation (13) yields

$$\dot{\mathbf{h}}_{s/c}^N = \mathbf{J}_{s/c}^N \dot{\boldsymbol{\omega}}^B + {}^N \boldsymbol{\omega}^B \times \mathbf{J}_{s/c}^N \boldsymbol{\omega}^B \quad (16)$$

Equation (17) shows the derivation in matrix form.

$$\dot{\mathbf{h}}_{s/c}^B = \begin{bmatrix} j_{s/c_{11}} \dot{\omega}_x + (j_{s/c_{33}} - j_{s/c_{22}}) \omega_z \omega_y \\ j_{s/c_{22}} \dot{\omega}_y + (j_{s/c_{11}} - j_{s/c_{33}}) \omega_x \omega_z \\ j_{s/c_{33}} \dot{\omega}_z + (j_{s/c_{22}} - j_{s/c_{11}}) \omega_y \omega_x \end{bmatrix}^B \quad (17)$$

The derivation may also be carried out in dyadic form:

$$\begin{aligned} \mathbf{h}_{s/c}^B &= j_{s/c_{11}} \dot{\omega}_x \hat{b}_1 + j_{s/c_{22}} \dot{\omega}_y \hat{b}_2 + j_{s/c_{33}} \dot{\omega}_z \hat{b}_3 \\ &\quad + (\omega_x \hat{b}_1 + \omega_y \hat{b}_2 + \omega_z \hat{b}_3) \times (j_{s/c_{11}} \omega_x \hat{b}_1 + j_{s/c_{22}} \omega_y \hat{b}_2 + j_{s/c_{33}} \omega_z \hat{b}_3) \end{aligned} \quad (18)$$

$$\begin{aligned} \dot{\mathbf{h}}_{s/c}^B &= j_{s/c_{11}} \dot{\omega}_x \hat{b}_1 + j_{s/c_{22}} \dot{\omega}_y \hat{b}_2 + j_{s/c_{33}} \dot{\omega}_z \hat{b}_3 \\ &\quad + (j_{s/c_{33}} - j_{s/c_{22}}) \omega_z \omega_y \hat{b}_1 + (j_{s/c_{11}} - j_{s/c_{33}}) \omega_x \omega_z \hat{b}_2 + (j_{s/c_{22}} - j_{s/c_{11}}) \omega_y \omega_x \hat{b}_3 \\ &= (j_{s/c_{11}} \dot{\omega}_x + (j_{s/c_{33}} - j_{s/c_{22}}) \omega_z \omega_y) \hat{b}_1 \\ &\quad + (j_{s/c_{22}} \dot{\omega}_y + (j_{s/c_{11}} - j_{s/c_{33}}) \omega_x \omega_z) \hat{b}_2 \\ &\quad + (j_{s/c_{33}} \dot{\omega}_z + (j_{s/c_{22}} - j_{s/c_{11}}) \omega_y \omega_x) \hat{b}_3 \end{aligned} \quad (19)$$

Correspondingly, by referring back to Equation (12), the torque of the MED assembly is related to the spacecraft torque per Equation (20). The MED portion is written in the inertial frame and includes the stored momentum in the body frame, to be later derived in Chapters IV and VI for reaction wheels and CMGs, respectively.

$$\dot{\mathbf{h}}_{medA}^N = -\mathbf{J}_{s/c}^N \dot{\boldsymbol{\omega}}^B - {}^N \boldsymbol{\omega}^B \times \mathbf{J}_{s/c}^N \boldsymbol{\omega}^B \quad (20)$$

Rewriting the angular momentum rate in Equation (20) as its corresponding torque yields

$$\tau_{medA}^N = -\tau_{s/c}^B - {}^N\dot{\omega}^B \times J_{s/c} {}^N\omega^B \quad (21)$$

E. MODELING SPACECRAFT DYNAMICS

As a slight variation of Equation (21), Equation (22) is modeled within the Spacecraft Dynamics Simulink block, shown in Figure 4.

$$\begin{aligned} \tau_{s/c}^B &= -\tau_{medA}^N - {}^N\dot{\omega}^B \times J_{s/c} {}^N\omega^B \\ {}^N\omega^B &= \int J_{s/c}^{-1} \tau_{s/c}^B dt \end{aligned} \quad (22)$$

Note that the disturbance torques $\tau_d = 0$. Thus, this term is not included in (22).

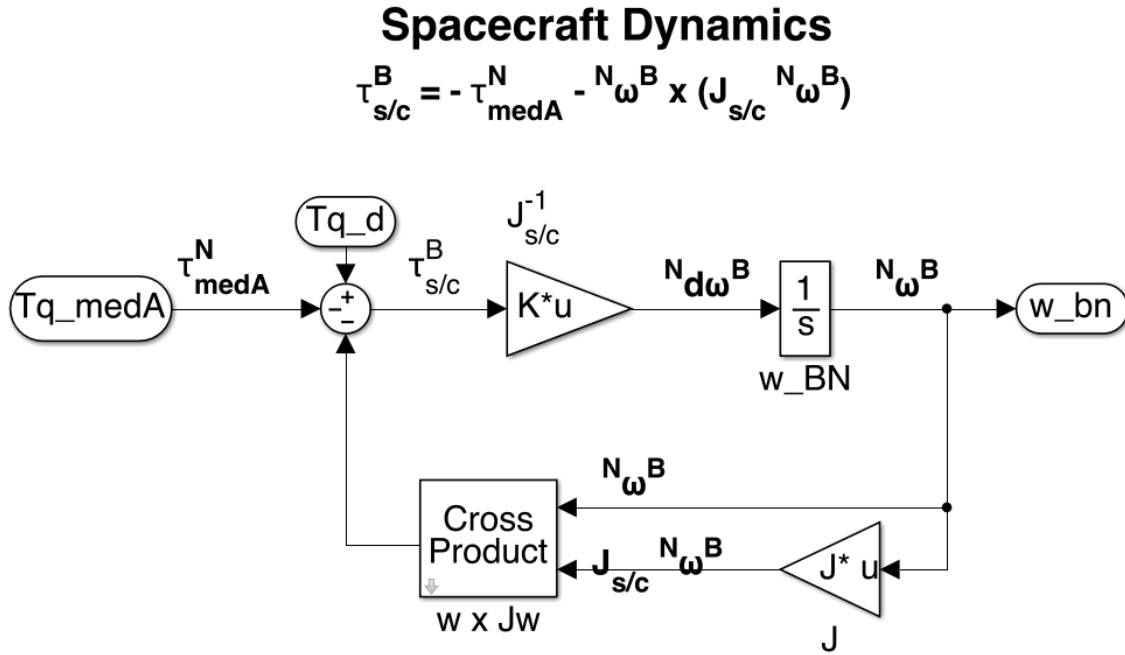


Figure 4. Spacecraft Dynamics Model

THIS PAGE INTENTIONALLY LEFT BLANK

III. EIGENAXIS REORIENTATION

While traveling at several thousand kilometers per second, a spacecraft is commanded to move from one quaternion state to another. This reorientation time may take a second or two for small maneuvers or tens of seconds to minutes for large maneuvers. For LEO Earth-imaging spacecraft, this reorientation must occur swiftly and precisely. Reorientation (slew) time is time lost as it is time not conducting mission-essential targeting. Since spacecraft can traverse key areas in minutes (or possibly seconds), slew time ultimately limits the number of targets per pass. Since these multi-million or billion dollar spacecraft are only productive when they are not slewing, slew time is productivity lost.

A. SHORTEST ANGLE MANEUVER

A simple, effective slew maneuver is the eigenaxis reorientation or eigenaxis slew. The eigenaxis slew is a rotation along the shortest arc between two attitudes. This maneuver is used due to its simplicity, predictability, and reasonably rapid speed, as opposed to performing successive rotations about the individual body axes. Given three-axis control, there are infinite paths that may be taken to transition between two attitudes. The eigenaxis slew utilizes the shortest of these paths. The axis of rotation is known as the eigenaxis, whose direction remains constant and orthogonal to the direction of angular travel throughout the maneuver. Assuming that the spacecraft can be reoriented while maintaining rotation about the eigenaxis, the problem can be simplified into a single angle slew, shown in Figure 5.

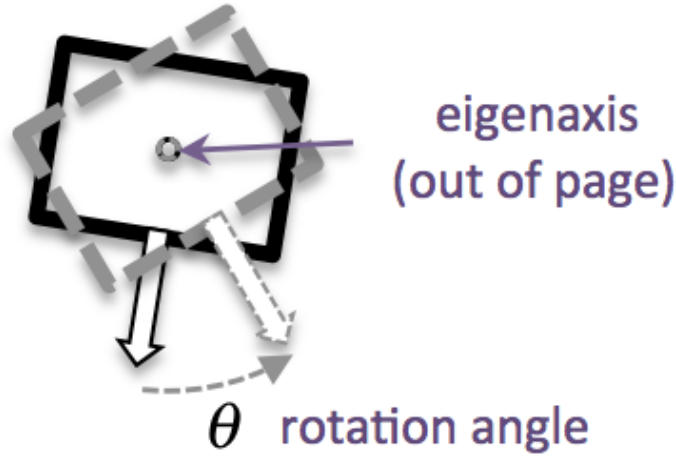


Figure 5. Eigenaxis Slew

For a reorientation from one angle to another, a direction cosine matrix (DCM) ${}^B\mathbf{R}^A$ (discussed in greater detail in Chapter IV) can be used to show the necessary relative reorientation from reference A to reference B. There is at least one eigenvector associated with the DCM that produces a unity eigenvalue shown by Sidi [5, Algorithm 4.1].

$${}^B\mathbf{R}^A\mathbf{e} = 1\mathbf{e} \quad (23)$$

Equation (23) represents the fact that instead of breaking a DCM into a series of three consecutive rotations, the reorientation can be created by using a single rotation about a specific axis or eigenvector. Unity eigenvalue occurs when rotating about the principle eigenvector or eigenaxis. Because of this, the eigenaxis slew is the shortest angle maneuver.

Assume the spacecraft's orientation is originally described by quaternions such that $\mathbf{q}_0 = [q_{0_1} \ q_{0_2} \ q_{0_3} \ q_{0_4}]^T$ with a requirement to slew to some final quaternion state $\mathbf{q}_f = [q_{f_1} \ q_{f_2} \ q_{f_3} \ q_{f_4}]^T$. Note, q_4 is the scalar. The quaternion difference \mathbf{q}_d can be described by Equation (24) [6, Algorithm 7.69].

$$\begin{bmatrix} q_{d_1} \\ q_{d_2} \\ q_{d_3} \\ q_{d_4} \end{bmatrix} = \begin{bmatrix} q_{f_4} & q_{f_3} & -q_{f_2} & -q_{f_1} \\ -q_{f_3} & q_{f_4} & q_{f_1} & -q_{f_2} \\ q_{f_2} & -q_{f_1} & q_{f_4} & -q_{f_3} \\ q_{f_1} & q_{f_2} & q_{f_3} & q_{f_4} \end{bmatrix} \begin{bmatrix} q_{0_1} \\ q_{0_2} \\ q_{0_3} \\ q_{0_4} \end{bmatrix} \quad (24)$$

Equation (25) shows the relationship between the quaternion difference, the eigenaxis, and the slew angle [5, Algorithm 4.11].

$$\begin{aligned} \mathbf{q}_{d_{123}} &= \mathbf{e} \sin\left(\frac{\theta_d}{2}\right) \\ q_{d_4} &= \cos\left(\frac{\theta_d}{2}\right) \end{aligned} \quad (25)$$

Rearranging Equation (25), the desired slew angle can now be solved for.

$$\theta_d = 2 \cos^{-1}(q_{d_4}) \quad (26)$$

The eigenaxis can now be solved as

$$\mathbf{e} = \frac{1}{\sin(\theta_d / 2)} \mathbf{q}_{d_{123}} \quad (27)$$

B. QUATERNION FEEDBACK

Using an eigenaxis slew, the reorientation problem can be simplified into a single angle slew, like the tracing of an arc of a circle on a 2D plane. This section will explain how the complicated spacecraft dynamics derived in Chapter II can be modeled as a linear double integrator, providing the spacecraft travels precisely along this eigenaxis arc. The double integrator model will be obtained from the eigenaxis quaternion feedback (EQF) control logic often used in spacecraft ACS [6, Algorithm 7.74].

$$\mathbf{u}'' = -k \mathbf{J}_{s/c} \mathbf{q}_{e_{123}} - c \mathbf{J}_{s/c}^N \boldsymbol{\omega}^B + \boldsymbol{\omega}^B \times \mathbf{J}_{s/c}^N \boldsymbol{\omega}^B, \quad (28)$$

Recall the nonlinear spacecraft torque from Equation (16). This inertial torque is what the EQF controller is attempting to control ($\mathbf{u}'' = \boldsymbol{\tau}_{s/c}^N$).

$$\mathbf{u}'' = \boldsymbol{\tau}_{s/c}^N = \mathbf{J}_{s/c}^N \dot{\boldsymbol{\omega}}^B + {}^N\boldsymbol{\omega}^B \times \mathbf{J}_{s/c}^N \boldsymbol{\omega}^B. \quad (29)$$

Equations (28) and (29) both contain the same gyroscopic coupling term, a term not conducive to solving a linear trajectory along an arc. The nonlinearity can be eliminated and a new control \mathbf{u}' is determined in Equation (30). This shows that the gyroscopic coupling term was simply added to the EQF to eliminate this nonlinearity in the control.

$$\begin{aligned} \mathbf{u}' &= \mathbf{u}'' - {}^N\boldsymbol{\omega}^B \times \mathbf{J}_{s/c}^N \boldsymbol{\omega}^B \\ &= -k \mathbf{J}_{s/c} \mathbf{q}_{e_{123}} - c \mathbf{J}_{s/c}^N \boldsymbol{\omega}^B \\ &= \mathbf{J}_{s/c}^N \dot{\boldsymbol{\omega}}^B \end{aligned} \quad (30)$$

Since $\boldsymbol{\tau}_{s/c}^B = \mathbf{J}_{s/c}^N \dot{\boldsymbol{\omega}}^B$ from Equation (15), the control \mathbf{u}' is effectively a torque control in the body frame. Equation (30) can be rearranged as follows.

$$\begin{aligned} \mathbf{u}' + k \mathbf{J}_{s/c} \mathbf{q}_{e_{123}} + c \mathbf{J}_{s/c}^N \boldsymbol{\omega}^B &= 0 \\ \mathbf{J}_{s/c}^N \dot{\boldsymbol{\omega}}^B + k \mathbf{J}_{s/c} \mathbf{q}_{e_{123}} + c \mathbf{J}_{s/c}^N \boldsymbol{\omega}^B &= 0 \end{aligned} \quad (31)$$

The constant inertia can then be divided out to assume acceleration as the control variable.

$$\mathbf{u} = \mathbf{u}' / \mathbf{J}_{s/c} \quad (32)$$

$$\begin{aligned} \mathbf{u} + k \mathbf{q}_{e_{123}} + c {}^N\boldsymbol{\omega}^B &= 0 \\ {}^N\dot{\boldsymbol{\omega}}^B + k \mathbf{q}_{e_{123}} + c {}^N\boldsymbol{\omega}^B &= 0 \end{aligned} \quad (33)$$

The problem thus far is measured in three-dimensional space. But the purpose of an EQF is to maintain the trajectory along the eigenaxis. Since the arc is measured along a plane, the quaternion trajectory can be measured approximately as a single angle, while the body rate can be measured as a single angular rate, both measured as an error. The simplification is explained in [6, Example 7.15].

$$\theta_E = \theta - \theta_d \quad (34)$$

$$\begin{aligned} u + k(\theta - \theta_d) + c(\dot{\theta} - \dot{\theta}_d) &= 0 \\ \ddot{\theta}_E + k(\theta - \theta_d) + c(\dot{\theta} - \dot{\theta}_d) &= 0 \end{aligned} \quad (35)$$

In Equation (33), ${}^N\boldsymbol{\omega}^B$ was not considered an error term because the control assumes no shaped angular velocity. Instead, it regulates it to zero. Therefore, the rate error is equal to body rate $\dot{\theta}_E = \dot{\theta} = {}^N\boldsymbol{\omega}^B$. The fundamental formula for a proportional plus derivative controller (PD) is shown as

$$\ddot{\theta}_E + k\theta_E + c\dot{\theta}_E = 0 \quad (36)$$

Equation (36) is now written in terms of a double integrator, where the control is equal to the second derivative of the signal $u = \ddot{\theta}_E = \alpha$.

$$\begin{aligned} u &= \alpha \\ &= -k\theta_E - c\dot{\theta}_E \end{aligned} \quad (37)$$

Assume a desired angle and rate are given. The controller can now regulate the acceleration signal to drive the error to zero. As stated previously, the desired rate is zero, therefore it is eliminated from the equation. This means that Equation (28) was treated as a rest-to-rest maneuver. The double integrator in Equation (38) is implemented in Figure 6.

$$u = \alpha = -k(\theta - \theta_d) - c\omega \quad (38)$$

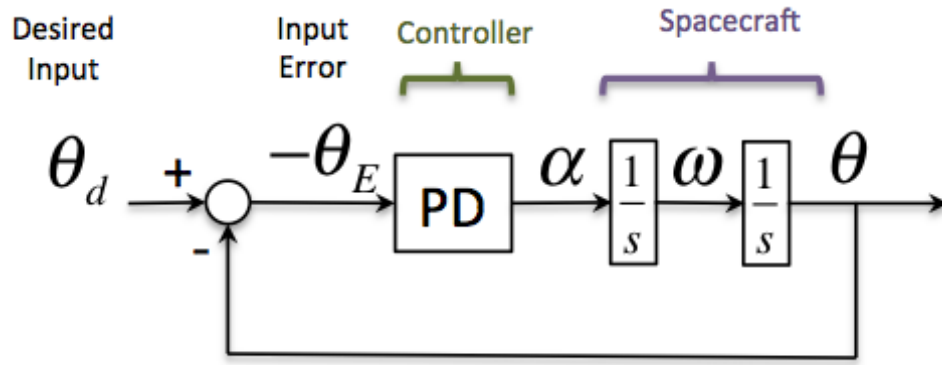


Figure 6. PD Control of a Double Integrator Model

Therefore, the EQF controller is essentially just a PD control system in disguise. The gyroscopic coupling term can be added back in to the PD controller, just to be

subtracted back out by the spacecraft physics. Therefore, the spacecraft can be slewed as a double integrator, as shown in the simplistic spacecraft simulation in Figure 6.

C. GAIN DESIGN FOR QUATERNION ERROR FEEDBACK

If the goal is to perform a rest-to-rest reorientation, θ_d may be fixed and act as a step input, which moves from zero to the desired angle. As with any step input, the error is very large at first and decreases significantly over time. Proportional and Differential Gains (k, c) must therefore be chosen carefully.

Underdamped systems are the quickest to respond, but must be carefully designed so the torque (acceleration) and overshoot do not become too large. The percent overshoot (Mp) is a measure of the overshoot compared to the starting/ending condition difference. For the following example, 10% overshoot is used. Settling time t_s is the time it takes the system to fall and remain within a certain band, commonly determined by imaging and targeting requirements (e.g., 2% of the final or steady-state value). An example of gain selection is shown in (39) such that the percent overshoot and settling time is the selection criteria for damping ratio and natural frequency [22, Algorithms 4.39, 4.42].

$$\begin{aligned}\zeta &= \frac{-\ln(Mp/100)}{\sqrt{\pi^2 + \ln(Mp/100)^2}} \\ \omega_n &= \frac{4}{\zeta t_s}\end{aligned}\tag{39}$$

The previously mentioned k and c are the feedback gains for the second order, homogeneous system shown in Equation (40). The same canonical expression is shown in Equation (41) in terms of the damping ratio and natural frequency.

$$\ddot{e} + c\dot{e} + ke = 0\tag{40}$$

$$\ddot{e} + 2\zeta\omega_n\dot{e} + \omega_n^2 e = 0\tag{41}$$

Now, it can be seen that

$$\begin{aligned} c &= 2\zeta\omega_n \\ k &= \omega_n^2 \end{aligned} \quad (42)$$

Using the feedback control system mentioned in Section C, the ideal gains for a quick 10° slew will be much different than those for a 60° slew due to the fact that the control system operates proportional to the angle error, given the same hardware. As an example, Figure 7 shows the time history of the system variables for the underdamped case. Both 10° (solid lines) and 20° (dashed lines) reorientations occurred using the same set of gains. Notice that they both settle at the same time. The 20° slew, however, shows significantly higher acceleration and rate commands. The phase space indicates that both slews follow essentially the same trajectory, and the magnitudes are scaled since the system is linear.

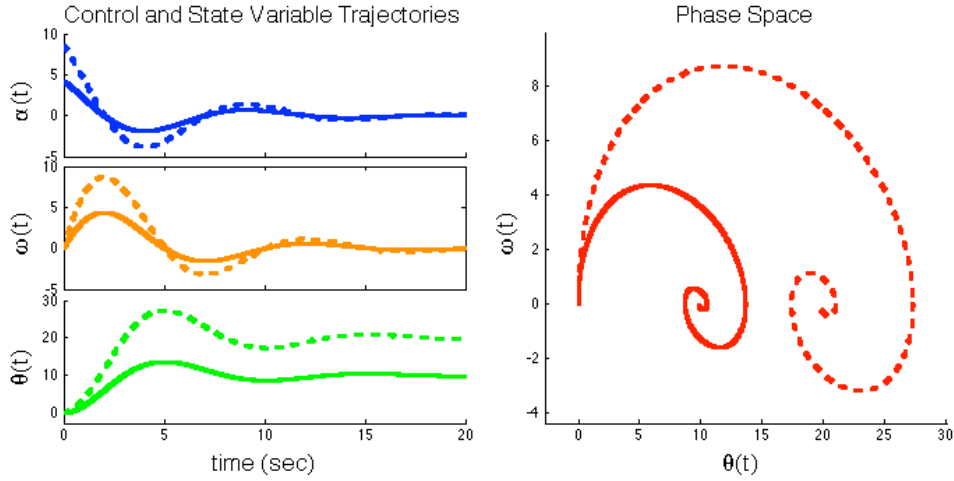


Figure 7. Underdamped Reorientation (solid 10° , dashed 20° slews)

It would be expected that a 10° slew could occur about twice as fast as a 20° slew for a given value of peak acceleration, but naturally, the linear control system prevents this. As a further example, the same 10° slew is compared with a 60° slew to show further exaggeration of this restriction. Figure 8 demonstrates that the required acceleration and rates increase significantly with the slew size.

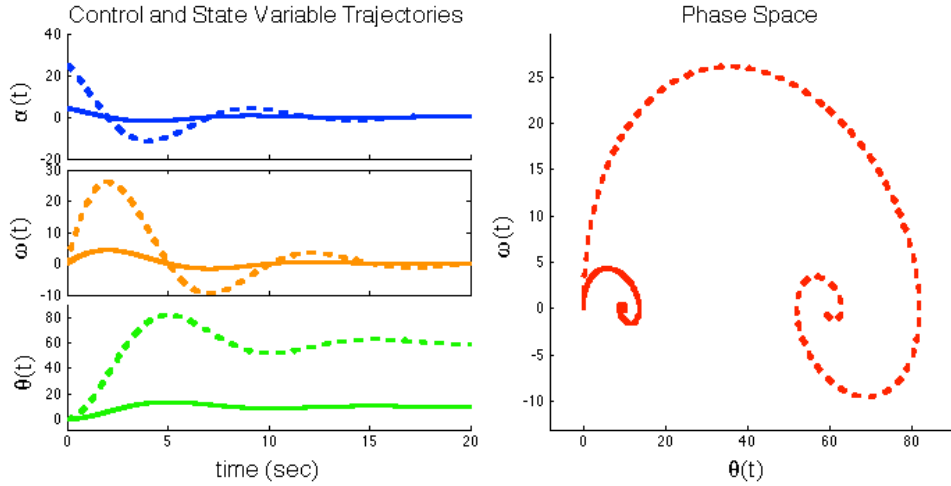


Figure 8. Underdamped Reorientation (solid 10° , dashed 60° slews)

At some point, the actuators will not be able to produce the required torque (acceleration) and/or angular momentum (rate). Suppose the $10/20^\circ$ slews from Figure 7 are now subject to torque and momentum saturation limits that are equivalent to $5^\circ/s^2$ and $4^\circ/s$, respectively (values representing a very agile spacecraft). This means the MED array cannot produce more than these limitations around the desired eigenaxis. Figure 9 demonstrates the saturations by flat regions, where maximum torque and acceleration are held for extended periods of time. The phase space indicates both trajectories were saturated, but the 20° slew was saturated twice. Within the same 20 seconds, the 20° slew was not complete due to the torque and momentum limits.

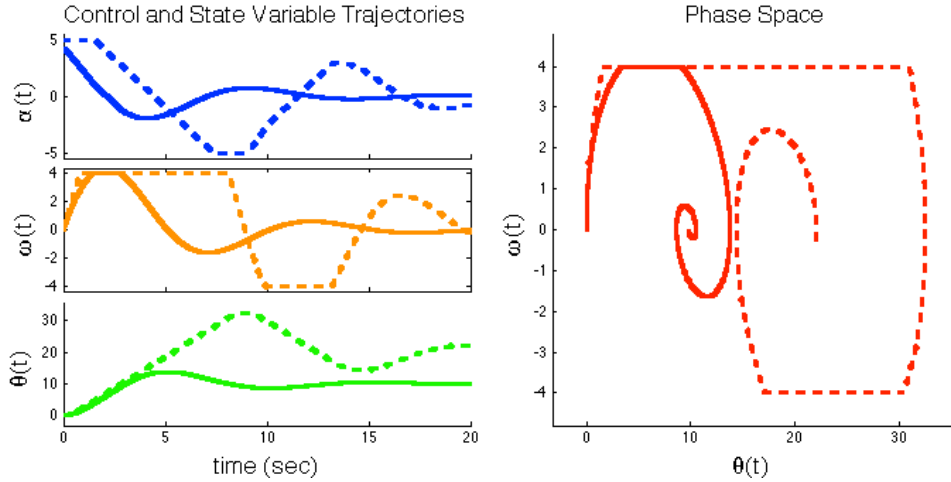


Figure 9. Underdamped Reorientation (solid 10°, dashed 20° slews) α , ω Limited

Notice that the spacecraft began at maximum torque and held it until the momentum limit was reached. At that point, maximum momentum was held until crossing the target angle, after which the spacecraft decelerated at maximum torque.

Engineers typically want to optimize trajectories, minimizing overshoot and settling time to reduce wasted transient distance and time. To perform a slew quickly with no overshoot, the critically damped case may be tried (Figure 10).

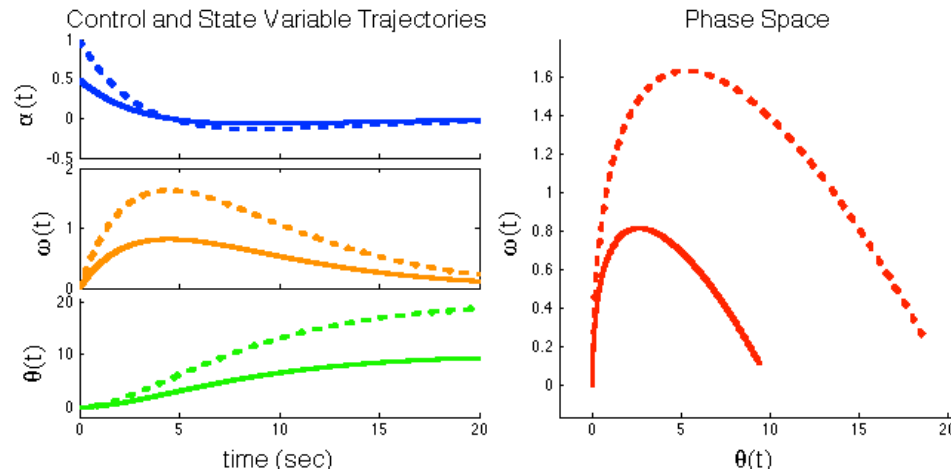


Figure 10. Critically Damped Reorientation (solid 10°, dashed 20° slews)

Notice that in Figure 10, both slews do not require anywhere near maximum torque or momentum. In this simulation, using the critically damped gains seems like a good approach. In a real spacecraft, the mass (inertia) will decrease over time as fuel is expended. Thus, space system engineers must plan in a buffer factor in order to account for the change in mass. As a “rule of thumb,” an engineer may select an initial damping ratio around $\zeta = 0.7$. As mass decreases, the damping ratio increases since the two values are inversely proportional ($\zeta \propto 1/m$). The damping ratio will eventually approach critical damping and move into overdamped towards the end of the life of the spacecraft. Thus, one could argue that the critical damping or near-critical damping scenarios would not be useful in spacecraft design.

A simple approach to control system design is to devise a set of gains that work across a large range of slew angles. To satisfy all angles, the control engineer must design the gains for the largest slew angle the spacecraft is regularly expected to perform. If this is done using a linear model, the system may perform very poorly for small angle reorientations. Therefore, the engineer can be forced to overdesign the hardware to satisfy the torque and momentum requirements for smaller angle maneuvers.

D. TRAJECTORY SHAPING

Gain design is very delicate because the engineer must tune the gains special for the spacecraft, regardless of slew size. Instead, input shaping allows a fixed set of gains that must correct for only a discrete minimal error to be utilized for multiple slew sizes. Optimal trajectories can be pursued without major hardware upgrades.

Input shaping is an alternative to using a step command as the input to the attitude control system. Input shaping can be introduced in the form of a set of shaped torque commands, represented as an acceleration input in Figure 13 [17]–[18]. This is ideal, because it completely avoids the need for a controller. Torque/acceleration input shaping is, however, unrealistic because the system would be operated in the open loop. This means that it does not have a feedback mechanism to account for uncertainties in the spacecraft inertia and external disturbances on the spacecraft, which is undesirable.

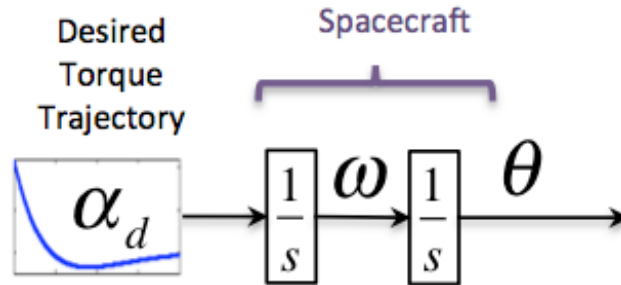


Figure 11. Torque Input Shaping Model

A better approach is to shape the trajectory of the input to a closed-loop system: the input angle itself. Rather than simply inserting a desired angle θ_d and letting the onboard controller calculate how to respond. The desired spacecraft response can be decided ahead of time and then implemented as a series of small steps. For example, a 10° slew can be divided into 100 or 1,000 incremental steps. Now, the gains can be optimized for the step size (fixed or extremely small) rather than the entire maneuver size (variable).

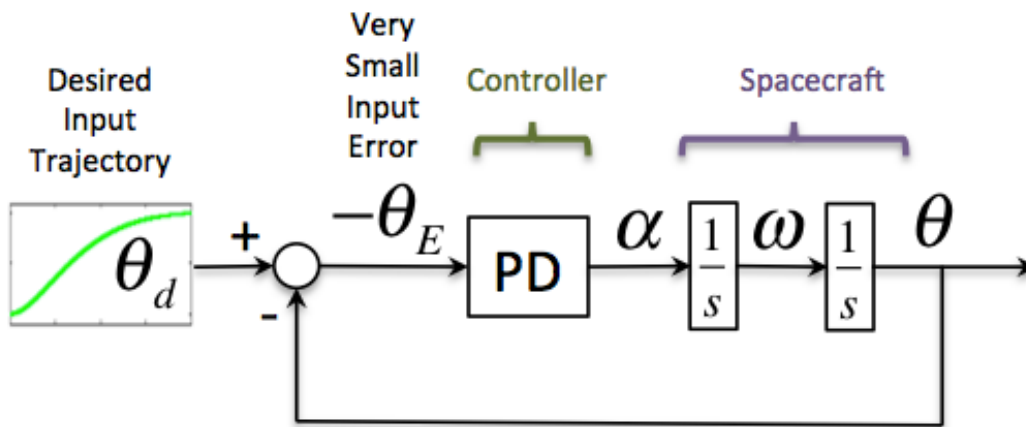


Figure 12. Angle Input Shaping Model

As long as the spacecraft model is reasonably accurate, the path can be predetermined accurately. The feedback loop then adjusts the path to accommodate spacecraft uncertainties and external disturbances. Similar methods have been used in at

least a few cases in the industry [12]–[14]. The input shaped trajectory θ_d is fed to the system much like that in Figure 12.

The ideal input is the trapezoidal input (referring to shape of ω) shown in Figure 13. This input accounts for both the torque and momentum limits a priori to control the error θ_d so that the control system does not saturate.

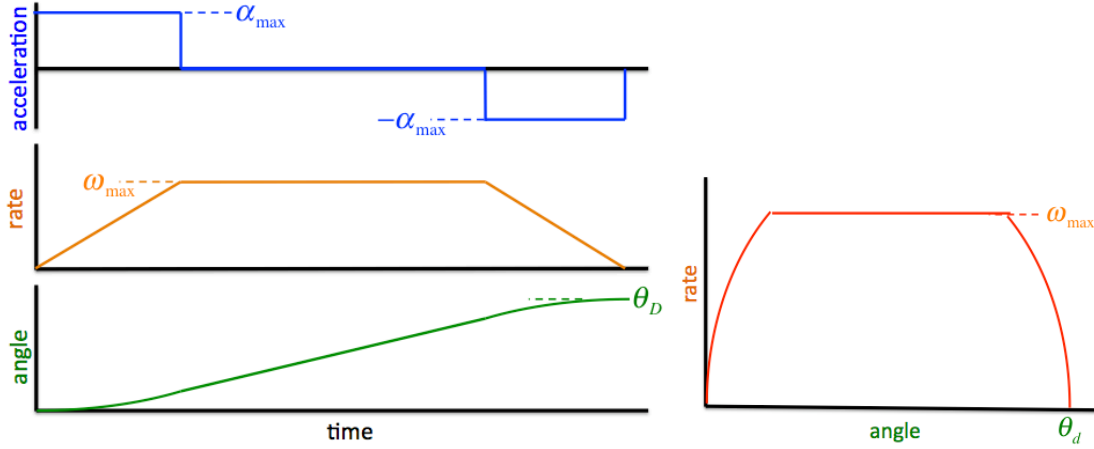


Figure 13. Rate Limited Eigenaxis Slew

Due to the shape of the angular rate trajectory, the torque/momentum limited input is also referred to as a bang-coast-bang maneuver. This is exactly the command-generated trajectory used for the Clementine spacecraft that was used for lunar mapping in 1994 [12, Figure 2]. The eigenaxis and trajectory angle were first calculated by the onboard computer to transit from the current quaternion to the desired quaternion. In Chapter V, it will be confirmed that this trapezoidal input is in fact the time-optimal solution for eigenaxis slews.

IV. REACTION WHEELS

Reaction wheels have their physical limitations. They have maximum angular rates and accelerations that must be modeled. This will ensure that even if a large torque is demanded, only the maximum MED assembly torque will be applied. In order to apply the saturations, a model of the reaction wheels must be created.

A basic model of a reaction wheel is shown in Figure 14. The reaction wheel is shown in its own local frame, referenced as the wheel frame with its spin axis aligned with the \hat{w}_3 axis. A motor, attached to the body frame, drives rotation of the wheel. The principle of operation is for the motor to apply a torque to the wheel. This causes the wheel to rotate quickly. The resultant equal and opposite torque is applied back through the motor to the body frame. This causes a rotation of the much larger spacecraft body. The momentum and torque vectors align with the \hat{w}_3 axis.

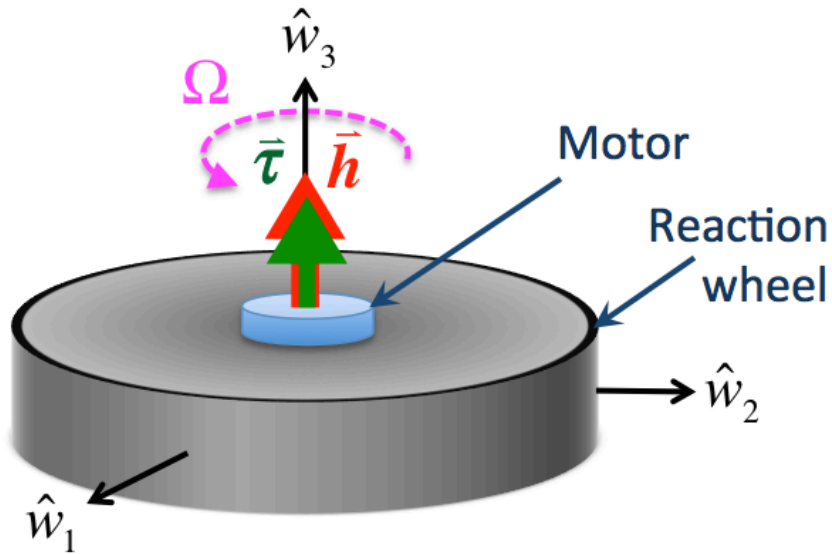


Figure 14. Reaction Wheel Schematic

A. ORIENTATION

The angular momentum of a single reaction wheel (RW) within its (ith) wheel frame \hat{W} with respect to body can be shown in the spacecraft body frame \hat{B} through a simple rotation. The fundamental formula for this change of basis is given as

$$\mathbf{h}_i^B = \left[{}^B \mathbf{R}^{W_i} \right] \mathbf{h}_i^{W_i} \quad (43)$$

In dyadic form, (43) can be looked at as the projection of the wheel frame onto the body frame (component-wise dot product).

$$\mathbf{h}_i^B = \left[\hat{\mathbf{b}} \hat{\mathbf{w}}_i^T \right] \mathbf{h}_i^{W_i} = \begin{bmatrix} \hat{b}_1 \bullet \hat{w}_{i1} & \hat{b}_1 \bullet \hat{w}_{i2} & \hat{b}_1 \bullet \hat{w}_{i3} \\ \hat{b}_2 \bullet \hat{w}_{i1} & \hat{b}_2 \bullet \hat{w}_{i2} & \hat{b}_2 \bullet \hat{w}_{i3} \\ \hat{b}_3 \bullet \hat{w}_{i1} & \hat{b}_3 \bullet \hat{w}_{i2} & \hat{b}_3 \bullet \hat{w}_{i3} \end{bmatrix}^{W_i} \mathbf{h}_i^{W_i} \quad (44)$$

This transformation can be completed as a matter of three fundamental rotations, and represented as a direction cosine matrix (DCM). A DCM is an invertible square matrix where the transpose is the inverse such that

$${}^B \mathbf{R}^{W_i} = \left[{}^{W_i} \mathbf{R}^B \right]^T \quad \text{or} \quad {}^B \mathbf{R}^{W_i} \left[{}^B \mathbf{R}^{W_i} \right]^T = I \quad (45)$$

This property allows a much more straightforward approach of first placing the RW in the \hat{B} frame, converting to the \hat{W}_i frame via ${}^{W_i} \mathbf{R}^B$, and then using the transpose ${}^B \mathbf{R}^{W_i}$ to convert back. In the example shown in Figure 15a, the MED is placed directly on the \hat{B} xyz origin, rotating about the \hat{b}_3 axis per Figure 14. This produces an angular momentum \mathbf{h}_{rw}^B directly in the \hat{b}_3 direction for a reaction wheel.

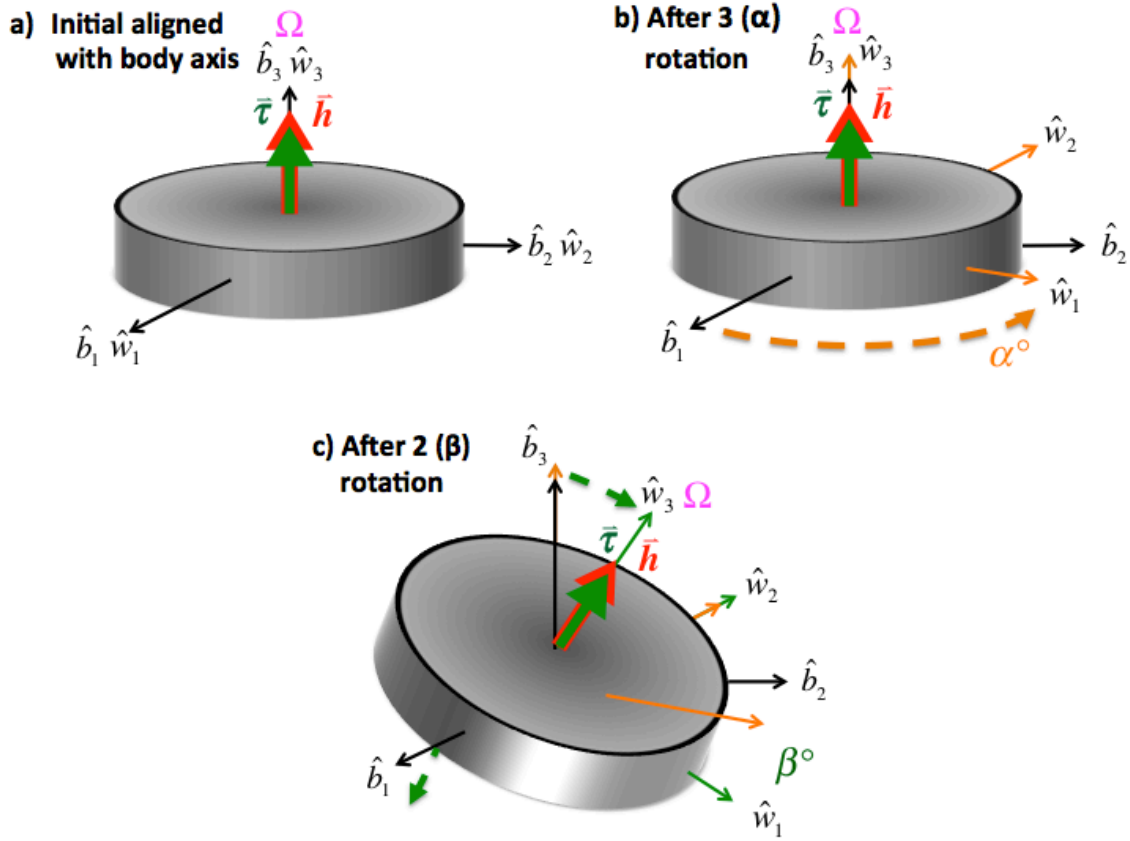


Figure 15. Reaction Wheel Transformation

First, a fundamental 3 rotation about the shared \hat{b}_3 / \hat{w}_3 axis must be completed to orient the \hat{w}_1 and \hat{w}_2 axes for subsequent rotations (Figure 15b). This will allow for multiple reaction wheels placed along the same skew angle (β), forming a pyramid. This first rotation can be represented in (46).

$$\mathbf{R}_3(\alpha_i) = \begin{pmatrix} \cos \alpha_i & \sin \alpha_i & 0 \\ -\sin \alpha_i & \cos \alpha_i & 0 \\ 0 & 0 & 1 \end{pmatrix} \quad (46)$$

Assuming $\alpha = \text{constant}$ for the initial 3 rotation of the representative wheel, a 2 rotation is now completed about the \hat{w}_2 axis (Figure 15c). This rotation is used for both reaction wheels and CMGs, and is referred to as the skew angle. The skew angle is

normally assumed the same across all devices, so the subscript “ i ” will not be used to distinguish which MED it refers to. This rotation can be represented in Equation (47).

$$\mathbf{R}_2(\beta) = \begin{pmatrix} \cos \beta & 0 & -\sin \beta \\ 0 & 1 & 0 \\ \sin \beta & 0 & \cos \beta \end{pmatrix} \quad (47)$$

The previous series of rotations can now be combined into a single transformation converting a vector from the body frame to the wheel frame.

$$\begin{aligned} {}^{w_i} \mathbf{R}^B &= \mathbf{R}_2(\beta) \mathbf{R}_3(\alpha_i) \\ &= \begin{bmatrix} c\beta & 0 & -s\beta \\ 0 & 1 & 0 \\ s\beta & 0 & c\beta \end{bmatrix}_2 \begin{bmatrix} c\alpha_i & s\alpha_i & 0 \\ -s\alpha_i & c\alpha_i & 0 \\ 0 & 0 & 1 \end{bmatrix}_3 \\ &= \begin{bmatrix} c\alpha_i c\beta & s\alpha_i c\beta & -s\beta \\ -s\alpha_i & c\alpha_i & 0 \\ c\alpha_i s\beta & s\alpha_i s\beta & c\beta \end{bmatrix}^B \end{aligned} \quad (48)$$

It follows from Equation (45) that ${}^B \mathbf{R}^{w_i}$ is now the transpose, which is equivalent to the reverse sequence via the negative angle of each rotation. Equation (49) is the physical representation of the dot product matrix shown in Equation (44).

$$\begin{aligned} {}^B \mathbf{R}^{w_i} &= \mathbf{R}_3(-\alpha_i) \mathbf{R}_2(-\beta) = \left[{}^{w_i} \mathbf{R}^B \right]^T \\ &= \begin{bmatrix} c\alpha_i c\beta & -s\alpha_i & c\alpha_i s\beta \\ s\alpha_i c\beta & c\alpha_i & s\alpha_i s\beta \\ -s\beta & 0 & c\beta \end{bmatrix}^{w_i} \end{aligned} \quad (49)$$

Note also that

$$\begin{bmatrix} \hat{b}_1 \bullet \hat{w}_{i1} & \hat{b}_1 \bullet \hat{w}_{i2} & \hat{b}_1 \bullet \hat{w}_{i3} \\ \hat{b}_2 \bullet \hat{w}_{i1} & \hat{b}_2 \bullet \hat{w}_{i2} & \hat{b}_2 \bullet \hat{w}_{i3} \\ \hat{b}_3 \bullet \hat{w}_{i1} & \hat{b}_3 \bullet \hat{w}_{i2} & \hat{b}_3 \bullet \hat{w}_{i3} \end{bmatrix}^B = \begin{bmatrix} c\alpha_i c\beta & -s\alpha_i & c\alpha_i s\beta \\ s\alpha_i c\beta & c\alpha_i & s\alpha_i s\beta \\ -s\beta & 0 & c\beta \end{bmatrix}^{w_i} \quad (50)$$

As an example, place the initial MED at angle $\alpha=0^\circ$. The resultant transformation from the \hat{W} frame to the \hat{B} frame is shown in Equation (51) for a reaction wheel.

$${}^B\mathbf{R}_{rw}^W = \mathbf{R}_3(-0^\circ)\mathbf{R}_2(-\beta) = \begin{bmatrix} c\beta & 0 & s\beta \\ 0 & 1 & 0 \\ -s\beta & 0 & c\beta \end{bmatrix}^W \quad (51)$$

Recall that the RWs in Equation (51) were stationed at $\alpha=0^\circ$. A classic configuration is using four MEDs in a square pyramid configuration in which each of the MEDs are placed 90° apart [15]. Arranged at the proper skew angle, this tricetrix arrangement maximizes torques in all directions, minimizing torque cancellations. This also provides redundancy in case of a single wheel failure. The arrangement used will be: $\alpha_1=0^\circ, \alpha_2=90^\circ, \alpha_3=180^\circ, \alpha_4=270^\circ$. Figure 16 demonstrates this common placement.

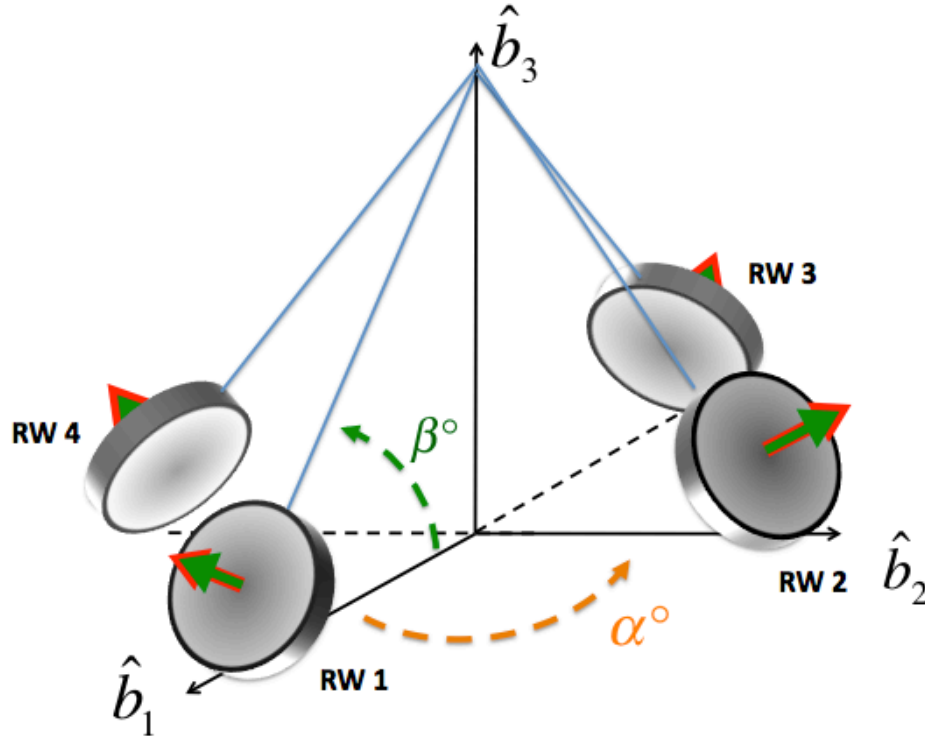


Figure 16. Body Frame to MED Rotations

Based on the wheel axis description mentioned above, the angular momentum in the wheel frames can be written as

$$\mathbf{h}_{rw_i}^{W_i} = \begin{bmatrix} 0 \\ 0 \\ 1 \end{bmatrix}^{W_i} h_i . \quad (52)$$

Transforming angular momentum from the \hat{W} frame to the \hat{B} frame using Equation (43) and $\alpha = 0^\circ$ yields (53).

$$\mathbf{h}_{rw_i}^B = \begin{bmatrix} s\beta \\ 0 \\ c\beta \end{bmatrix}^B h_i \quad (53)$$

or in general form

$$\mathbf{h}_{rw_i}^B = \begin{bmatrix} \hat{b}_1 \cdot \hat{w}_{i_3} \\ \hat{b}_2 \cdot \hat{w}_{i_3} \\ \hat{b}_3 \cdot \hat{w}_{i_3} \end{bmatrix}^B h_i . \quad (54)$$

The total angular momentum of the system is simply the sum of each of the MEDs in the body frame.

$$\mathbf{h}_{medA}^B = \sum_i^n \mathbf{h}_{med_i}^B \quad (55)$$

For the reaction wheel case in Equation (54), the individual rotation matrix and angular momentum components can be combined into the product of two matrices, equivalent to Equation (55). The first matrix represents the orientation of each wheel with respect to the body frame, separated as individual columns. For n MEDs, this $3 \times n$ orientation matrix is multiplied by an $n \times 1$ vector containing the momentum in the wheel frame as shown in Equation (56).

$$\sum_{i=1}^n \mathbf{h}_{rw_i}^B = \begin{bmatrix} \hat{b}_1 \cdot \hat{w}_{1_3} & \hat{b}_1 \cdot \hat{w}_{2_3} & \dots & \hat{b}_1 \cdot \hat{w}_{n_3} \\ \hat{b}_2 \cdot \hat{w}_{1_3} & \hat{b}_2 \cdot \hat{w}_{2_3} & \dots & \hat{b}_2 \cdot \hat{w}_{n_3} \\ \hat{b}_3 \cdot \hat{w}_{1_3} & \hat{b}_3 \cdot \hat{w}_{2_3} & \dots & \hat{b}_3 \cdot \hat{w}_{n_3} \end{bmatrix}^B \begin{bmatrix} h_1 \\ h_2 \\ \vdots \\ h_n \end{bmatrix}^W \quad (56)$$

The $3 \times n$ matrix that relates n MEDs to the principle body axes will be labeled this point forward as the orientation matrix ${}^B\mathbf{Z}^W$. Since it contains only elements from the 3rd column of the original rotation matrix, it will be further described with a subscript 3: ${}^B\mathbf{Z}_3^W$.

$${}^B\mathbf{Z}_3^W = \begin{bmatrix} \hat{b}_1 \cdot \hat{w}_{1_3} & \hat{b}_1 \cdot \hat{w}_{2_3} & \dots & \hat{b}_1 \cdot \hat{w}_{n_3} \\ \hat{b}_2 \cdot \hat{w}_{1_3} & \hat{b}_2 \cdot \hat{w}_{2_3} & \dots & \hat{b}_2 \cdot \hat{w}_{n_3} \\ \hat{b}_3 \cdot \hat{w}_{1_3} & \hat{b}_3 \cdot \hat{w}_{2_3} & \dots & \hat{b}_3 \cdot \hat{w}_{n_3} \end{bmatrix}^B \quad (57)$$

Now, Equation (56) can be rewritten as

$$\mathbf{h}_{rw}^B = \sum_{i=1}^n \mathbf{h}_{w_i}^B = {}^B\mathbf{Z}_3^W \mathbf{h}^W \quad (58)$$

$$\text{where } \mathbf{h}^W = \begin{bmatrix} h_1 \\ h_2 \\ \vdots \\ h_n \end{bmatrix}^W. \quad (59)$$

For the square pyramid mentioned, the orientation matrix is shown in Equation (60) for reaction wheels.

$${}^B\mathbf{Z}_3^W = \begin{bmatrix} s\beta & 0 & -s\beta & 0 \\ 0 & s\beta & 0 & -s\beta \\ c\beta & c\beta & c\beta & c\beta \end{bmatrix}^B \quad (60)$$

Any RW orientation configuration Z can be modeled by specifying the appropriate α and β rotations. Note that Equation (60) assumes

$$\alpha = \begin{bmatrix} 0 & 90 & 180 & 270 \end{bmatrix}^T.$$

Other than the case where $n=3$, Z will always be a $3 \times n$ matrix where $n > 3$. This is caused because the system is over-actuated, i.e., more wheels exist than are necessary to control the spacecraft attitude. A common approach for performing control allocation in the over-actuated case is to use the pseudo-inverse to map three orthogonal commands in the body frame to n commands for the individual wheels.

$$Z^+ = Z^T (ZZ^T)^{-1} \quad (61)$$

B. DIFFERENTIAL EQUATIONS OF MOTION

Like the spacecraft, the momentum of the reaction wheel can be defined as the product of wheel inertia and angular velocity of the wheel, all with respect to the inertial frame.

$$H_{w_i} = J_{wi}^N \omega_i^{W_i} \quad (62)$$

Previously, the wheel inertia was combined into the spacecraft inertia in Equation (6), where $h_{s/c}^N = (J_{s/c/body} + J_{medA})^N \omega^B$. Therefore, the wheel inertia rotating with the spacecraft body must be pulled out, leaving only the configuration of the wheel with respect to the body.

$$\begin{aligned} H_{w_i} &= J_{wi}^N \omega_i^B + J_{wi}^B \omega_i^{W_i} \\ H_{w_i} - (J_{wi}^N \omega_i^B) &= h_{w_i}^{W_i} \end{aligned} \quad (63)$$

$$h_{w_i}^{W_i} = J_{w_i}^B \omega_i^{W_i} = \begin{bmatrix} j_{wi11} & 0 & 0 \\ 0 & j_{wi22} & 0 \\ 0 & 0 & j_{wi33} \end{bmatrix} \begin{bmatrix} 0 \\ 0 \\ \Omega_i \end{bmatrix}^{W_i} = \begin{bmatrix} 0 \\ 0 \\ J_{wi33} \Omega_i \end{bmatrix}^{W_i} \quad (64)$$

Shown in dyadic form:

$$\begin{aligned}
\mathbf{h}_{wi}^{W_i} &= (j_{wi11}\hat{\mathbf{w}}_{i_1}\hat{\mathbf{w}}_{i_1} + j_{wi22}\hat{\mathbf{w}}_{i_2}\hat{\mathbf{w}}_{i_2} + j_{wi33}\hat{\mathbf{w}}_{i_3}\hat{\mathbf{w}}_{i_3}) \bullet (\boldsymbol{\Omega}_i\hat{\mathbf{w}}_{i_3}) \\
&= j_{wi33}\boldsymbol{\Omega}_i\hat{\mathbf{w}}_{i_3}(\hat{\mathbf{w}}_{i_3} \bullet \hat{\mathbf{w}}_{i_3}) \\
&= j_{wi33}\boldsymbol{\Omega}_i\hat{\mathbf{w}}_{i_3}
\end{aligned} \tag{65}$$

Change of basis to the body frame:

$$\begin{aligned}
\mathbf{h}_{wi}^B &= j_{wi33}\boldsymbol{\Omega}_i\hat{\mathbf{w}}_{i_3} \bullet (\hat{\mathbf{b}}_1\hat{\mathbf{b}}_1 + \hat{\mathbf{b}}_2\hat{\mathbf{b}}_2 + \hat{\mathbf{b}}_3\hat{\mathbf{b}}_3) \\
&= j_{wi33}\boldsymbol{\Omega}_i(\hat{\mathbf{w}}_{i_3} \bullet \hat{\mathbf{b}}_1)\hat{\mathbf{b}}_1 + j_{wi33}\boldsymbol{\Omega}_i(\hat{\mathbf{w}}_{i_3} \bullet \hat{\mathbf{b}}_2)\hat{\mathbf{b}}_2 + j_{wi33}\boldsymbol{\Omega}_i(\hat{\mathbf{w}}_{i_3} \bullet \hat{\mathbf{b}}_3)\hat{\mathbf{b}}_3
\end{aligned} \tag{66}$$

The dot product of two vector components can be flipped interchangeably (i.e., $\hat{\mathbf{b}}_1 \bullet \hat{\mathbf{w}}_{i_1} = \hat{\mathbf{w}}_{i_1} \bullet \hat{\mathbf{b}}_1$). This is important to note because the transformation matrix can now be written in the more conventional notation shown in Equation (44). The resultant rotation matrix is shown in Equation (67).

$$\begin{aligned}
\mathbf{h}_{wi}^B &= \begin{bmatrix} \hat{\mathbf{b}}_1 \bullet \hat{\mathbf{w}}_{i_1} & \hat{\mathbf{b}}_1 \bullet \hat{\mathbf{w}}_{i_2} & \hat{\mathbf{b}}_1 \bullet \hat{\mathbf{w}}_{i_3} \\ \hat{\mathbf{b}}_2 \bullet \hat{\mathbf{w}}_{i_1} & \hat{\mathbf{b}}_2 \bullet \hat{\mathbf{w}}_{i_2} & \hat{\mathbf{b}}_2 \bullet \hat{\mathbf{w}}_{i_3} \\ \hat{\mathbf{b}}_3 \bullet \hat{\mathbf{w}}_{i_1} & \hat{\mathbf{b}}_3 \bullet \hat{\mathbf{w}}_{i_2} & \hat{\mathbf{b}}_3 \bullet \hat{\mathbf{w}}_{i_3} \end{bmatrix}^{W_i} \begin{bmatrix} 0 \\ 0 \\ j_{wi33}\boldsymbol{\Omega}_i \end{bmatrix}^{W_i} \\
&= \begin{bmatrix} (\hat{\mathbf{b}}_1 \bullet \hat{\mathbf{w}}_{i_3})j_{wi33}\boldsymbol{\Omega}_i \\ (\hat{\mathbf{b}}_2 \bullet \hat{\mathbf{w}}_{i_3})j_{wi33}\boldsymbol{\Omega}_i \\ (\hat{\mathbf{b}}_3 \bullet \hat{\mathbf{w}}_{i_3})j_{wi33}\boldsymbol{\Omega}_i \end{bmatrix}^B
\end{aligned} \tag{67}$$

Equation (67) can be simplified into a version containing only the rotation matrix portion multiplied by its momentum, expressed in the body frame.

$$\mathbf{h}_{wi}^B = \begin{bmatrix} \hat{\mathbf{b}}_1 \bullet \hat{\mathbf{w}}_{i_3} \\ \hat{\mathbf{b}}_2 \bullet \hat{\mathbf{w}}_{i_3} \\ \hat{\mathbf{b}}_3 \bullet \hat{\mathbf{w}}_{i_3} \end{bmatrix}^B j_{wi33}\boldsymbol{\Omega}_i \tag{68}$$

From Equation (56), the total angular momentum for n wheels in the body frame can be rewritten as

$$\mathbf{h}_w^B = \begin{bmatrix} \hat{b}_1 \cdot \hat{w}_{1_3} & \hat{b}_1 \cdot \hat{w}_{2_3} & \dots & \hat{b}_1 \cdot \hat{w}_{n_3} \\ \hat{b}_2 \cdot \hat{w}_{1_3} & \hat{b}_2 \cdot \hat{w}_{2_3} & \dots & \hat{b}_2 \cdot \hat{w}_{n_3} \\ \hat{b}_3 \cdot \hat{w}_{1_3} & \hat{b}_3 \cdot \hat{w}_{2_3} & \dots & \hat{b}_3 \cdot \hat{w}_{n_3} \end{bmatrix}^B \begin{bmatrix} j_{w_1 33} \Omega_1 \\ j_{w_2 33} \Omega_2 \\ \vdots \\ j_{w_n 33} \Omega_n \end{bmatrix}^W \quad (69)$$

Equation (69) is equivalent to Equation (58), where $\mathbf{h}_w^B = {}^B \mathbf{Z}_3^W \mathbf{h}_w^W$. Within the model, the inertia and rates are expanded out in the following manner to keep track of them separately.

$$\mathbf{h}_w^W = \mathbf{J}_w \boldsymbol{\Omega}^W = \begin{bmatrix} j_{w_1 33} & 0 & 0 & 0 \\ 0 & j_{w_2 33} & 0 & 0 \\ 0 & 0 & \ddots & 0 \\ 0 & 0 & 0 & j_{w_n 33} \end{bmatrix}^W \begin{bmatrix} \Omega_1 \\ \Omega_2 \\ \vdots \\ \Omega_n \end{bmatrix}^W \quad (70)$$

The torque with respect to the wheel frame is the time derivative of Equation (70).

$$\boldsymbol{\tau}_w^W = \frac{d}{dt}(\mathbf{h}_w^W) = \mathbf{J}_w \dot{\boldsymbol{\Omega}}^W \quad (71)$$

The torque with respect to the body will be defined as the change in angular momentum with between the wheel and body frames.

$$\boldsymbol{\tau}_w^B = \frac{d}{dt}(\mathbf{h}_w^B) = \dot{\mathbf{h}}_w^B \quad \text{where } \mathbf{h}_w^B = {}^B \mathbf{Z}_3^W \mathbf{h}_w^W \quad (72)$$

Expanding out these terms following the chain rule yields Equation (73). Since this is a reaction wheel, the orientation is fixed and therefore ${}^B \dot{\mathbf{Z}}_3^W = 0$. The inertia is assumed to not change with time, $\dot{J}_{rw} = 0$.

$$\boldsymbol{\tau}_w^B = \cancel{{}^B \dot{\mathbf{Z}}_3^W \mathbf{J}_w^W} + {}^B \mathbf{Z}_3^W \cancel{\dot{\mathbf{J}}_w^W} + {}^B \mathbf{Z}_3^W \mathbf{J}_w^W \dot{\boldsymbol{\Omega}}^W \quad (73)$$

$$\boldsymbol{\tau}_w^B = {}^B \mathbf{Z}_3^W \mathbf{J}_w^W \dot{\boldsymbol{\Omega}}^W \quad (74)$$

In dyadic form, a single reaction wheel torque can be found using the derivative of Equation (66).

$$\begin{aligned}
\frac{{}^B d}{dt}(\mathbf{h}_{wi}^B) = & \dot{j}_{wi33} \Omega_i (\hat{\mathbf{w}}_{i_3} \cdot \hat{\mathbf{b}}_1) \hat{\mathbf{b}}_1 + \dot{j}_{wi33} \Omega_i (\hat{\mathbf{w}}_{i_3} \cdot \hat{\mathbf{b}}_2) \hat{\mathbf{b}}_2 + \dot{j}_{wi33} \Omega_i (\hat{\mathbf{w}}_{i_3} \cdot \hat{\mathbf{b}}_3) \hat{\mathbf{b}}_3 \\
& + j_{wi33} \dot{\Omega}_i (\hat{\mathbf{w}}_{i_3} \cdot \hat{\mathbf{b}}_1) \hat{\mathbf{b}}_1 + j_{wi33} \dot{\Omega}_i (\hat{\mathbf{w}}_{i_3} \cdot \hat{\mathbf{b}}_2) \hat{\mathbf{b}}_2 + j_{wi33} \dot{\Omega}_i (\hat{\mathbf{w}}_{i_3} \cdot \hat{\mathbf{b}}_3) \hat{\mathbf{b}}_3 \\
& + j_{wi33} \Omega_i (\dot{\hat{\mathbf{w}}}_{i_3} \cdot \hat{\mathbf{b}}_1) \hat{\mathbf{b}}_1 + j_{wi33} \Omega_i (\dot{\hat{\mathbf{w}}}_{i_3} \cdot \hat{\mathbf{b}}_2) \hat{\mathbf{b}}_2 + j_{wi33} \Omega_i (\dot{\hat{\mathbf{w}}}_{i_3} \cdot \hat{\mathbf{b}}_3) \hat{\mathbf{b}}_3
\end{aligned} \tag{75}$$

The inertia of the wheel is not changing with respect to the wheel frame. Also, the orientation of the 3 axis of wheel frame is not moving with respect to the body frame.

$$\dot{j}_{wi33} = 0 \quad \text{and} \quad \dot{\hat{\mathbf{w}}}_{i_3} = 0 \tag{76}$$

Equation (75) now becomes

$$\frac{{}^B d}{dt}(\mathbf{h}_{wi}^B) = j_{wi33} \dot{\Omega}_i (\hat{\mathbf{w}}_{i_3} \cdot \hat{\mathbf{b}}_1) \hat{\mathbf{b}}_1 + j_{wi33} \dot{\Omega}_i (\hat{\mathbf{w}}_{i_3} \cdot \hat{\mathbf{b}}_2) \hat{\mathbf{b}}_2 + j_{wi33} \dot{\Omega}_i (\hat{\mathbf{w}}_{i_3} \cdot \hat{\mathbf{b}}_3) \hat{\mathbf{b}}_3 \tag{77}$$

$$\frac{{}^B d}{dt}(\mathbf{h}_{wi}^B) = \begin{bmatrix} j_{wi33} \dot{\Omega}_i (\hat{\mathbf{b}}_1 \cdot \hat{\mathbf{w}}_{i_3}) \\ j_{wi33} \dot{\Omega}_i (\hat{\mathbf{b}}_2 \cdot \hat{\mathbf{w}}_{i_3}) \\ j_{wi33} \dot{\Omega}_i (\hat{\mathbf{b}}_3 \cdot \hat{\mathbf{w}}_{i_3}) \end{bmatrix}^B = \begin{bmatrix} \hat{\mathbf{b}}_1 \cdot \hat{\mathbf{w}}_{i_3} \\ \hat{\mathbf{b}}_2 \cdot \hat{\mathbf{w}}_{i_3} \\ \hat{\mathbf{b}}_3 \cdot \hat{\mathbf{w}}_{i_3} \end{bmatrix}^B j_{wi33} \dot{\Omega}_i \tag{78}$$

By Euler's transport theorem adopted from [23, Algorithm 8.18a], the inertial derivative of Equation (74) is

$$\begin{aligned}
\frac{{}^N d(\mathbf{h}_w^N)}{dt} &= \frac{{}^B d(\mathbf{h}_w^B)}{dt} + {}^N \boldsymbol{\omega}^B \times \mathbf{h}_w^B \\
\dot{\mathbf{h}}_w^N &= \dot{\mathbf{h}}_w^B + {}^N \boldsymbol{\omega}^B \times \mathbf{h}_w^B
\end{aligned} \tag{79}$$

Equation (79) can be rewritten by substituting the body torque from Equation (74) and body angular momentum terms as

$$\boldsymbol{\tau}_w^N = {}^B \mathbf{Z}_3^W \mathbf{J}_w \dot{\boldsymbol{\Omega}}^W + {}^N \boldsymbol{\omega}^B \times {}^B \mathbf{Z}_3^W \mathbf{J}_w \boldsymbol{\Omega}^W \tag{80}$$

By substituting Equation (80) into Equation (12), knowledge that torque is in the wheel frame as defined in $\boldsymbol{\tau}_w^W = \mathbf{J}_w \dot{\boldsymbol{\Omega}}^W$ from Equation (71), and a rearrangement of terms, the result is an equation in terms of the torque of the reaction wheel. This equation now

involves the pseudo-inverse to translate torque commands given in the body frame to n wheels, shown in Equation (82).

$$-\tau_{req}^N = {}^B Z_3^W \tau_w^W + {}^N \omega^B \times {}^B Z_3^W J_w \Omega^W \quad (81)$$

$$\tau_w^W = [{}^B Z_3^W]^+ \left(-\tau_{req}^N - {}^N \omega^B \times {}^B Z_3^W J_w \Omega^W \right) \quad (82)$$

Further, Equation (82) can be reduced to Equation (83), solving for the reaction wheel dynamics in terms of the spacecraft.

$$\dot{\Omega}^W = J_w^{-1} [{}^B Z_3^W]^+ \left(-\tau_{req}^N - {}^N \omega^B \times {}^B Z_3^W J_w \Omega^W \right) \quad (83)$$

C. MODELING REACTION WHEELS

In order to apply the physical limits of the reaction wheel actuator, the torque required of the assembly must be broken down, torque and wheel speed limit saturations applied, and then the torque of the reaction wheel assembly rebuilt in Figure 17. Equation (82) is used to break down the torque required and (80) is used to rebuild it.

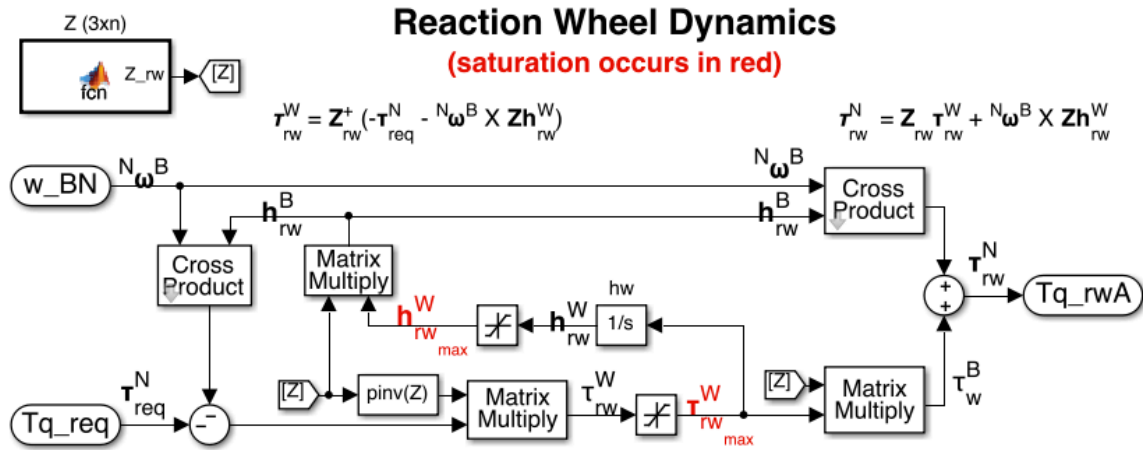


Figure 17. Reaction Wheel Model

This model is contingent that momentum in the wheel frame is derived directly from wheel torque from Equation (71) such that

$$\mathbf{h}_w^w = \int \boldsymbol{\tau}_w^w dt . \quad (84)$$

The wheel torque limitations occur in the individual wheel frames. The rate limitations are modeled as wheel momentum saturations. Note, this model does not shut off the wheel torque when $\|\mathbf{h}_i\| = h_{\max}$. It is not necessary for the comparisons in this thesis because only torque and momentum limited signals are used.

D. REACTION WHEEL MOMENTUM SPACE

By measuring the maximum momentum in any given direction over a 2π steradian for a particular reaction wheel configuration, a boundary can be defined that describes the maximum momentum capacity of the array. This is the physical limitation of the system defined by the vector sum of the maximum capacities of the individual momentum wheels. If this boundary is created for every possible direction around a unit circle in the body frame, the surface of boundaries is typically known as the momentum envelope [15, p. 1607]. To determine the best possible mechanical configuration of systems, the volume must be maximized, ideally forming the most spherical shape possible. Since each of four wheels is maximized individually, the resultant shape has radii larger than h_{\max} . If all four wheels were aligned, a maximum radius of 4 could be achieved, leaving zero momentum in other directions. The maximum momentum space for an evenly-spaced ($\Delta\alpha = 90^\circ$) four wheel system is achieved when

$$\beta = \cos^{-1}\left(\frac{1}{\sqrt{3}}\right) rad = 54.74^\circ . \quad (85)$$

The maximum angle in Equation (85) is shown in [15, p. 1610] as the conjugate 35.26° . The resulting envelope is shown in Figure 18. The figure was created using a mesh of triangles between all surface points.

Assuming all four wheels have equal momentum storage, Figure 17 is calculated as a function of the maximum momentum available to any given wheel h_{\max} . The envelope scales symmetrically with the size of the wheel (h_{\max}). Therefore, larger wheels would push the surface outward, allowing more momentum capacity, but the shape would

be retained. This is why the dodecahedron is generic for any four-wheel system, but unique to only four-wheel systems. A five-wheel system would have a much different shape with a maximum at a different angle β and a larger volume (see [15]).

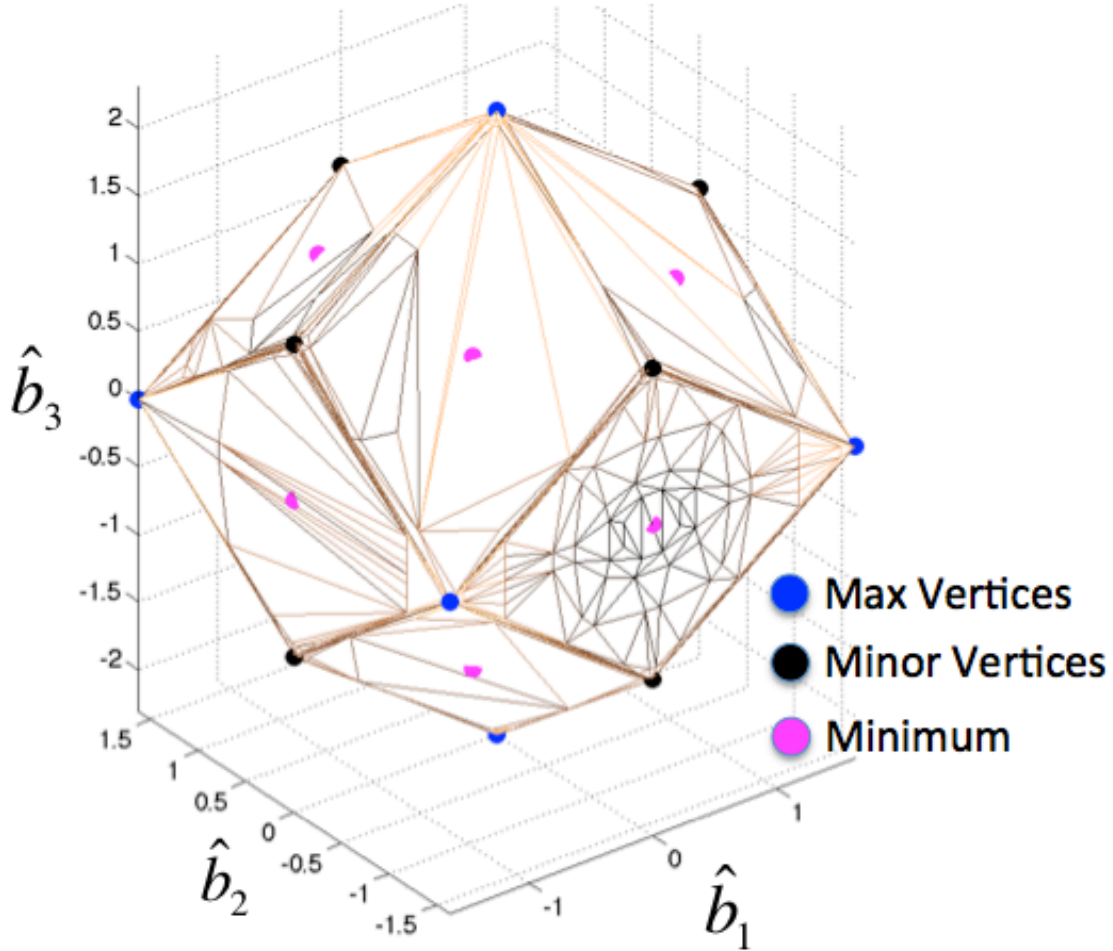


Figure 18. Momentum Space for 4 Wheel Reaction Wheel ($\alpha=0,90,180,270^\circ$)

The momentum envelope shown represents the angular momentum available about any given rotation axis. During times of maximum momentum use, the momentum vector would touch the outside surface of the envelope until the system begins to decelerate and momentum decreases back to the center of the shape where momentum is zero. The vertices of the momentum envelope indicate optimal axes that allow locally-rapid rotation rates. Although fourteen vertices exist, only six are global maxima (marked

with blue). The centers of each facet indicate the minima for each respective plane. These minima are also the global minima, each marked in magenta.

The four-wheel polyhedron is again shown in three orthogonal views in Figure 19 to clarify its shape. The blue maximum vertices (global maxima) occur at magnitudes equal to $h_{\max}^B = 2.309h_{\max}$. The black minor vertices (local maxima) occur at $h_{\max}^B = 2.0h_{\max}$. The minimum h^B is actually zero, but h_{\min}^B represents the minimum across the momentum envelope. The minimum radius occurs at the middle of the flat facets where $h_{\min}^B = 1.633h_{\max}$, interestingly equal for every axis.

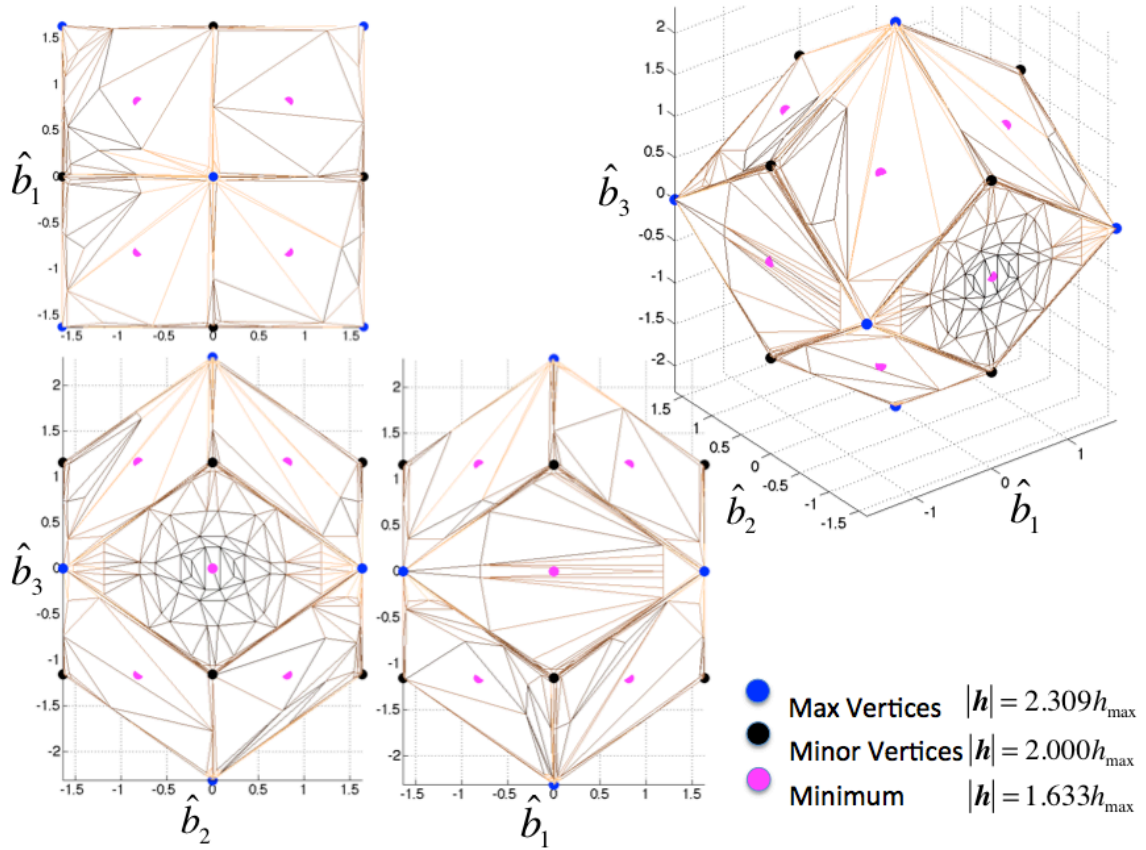


Figure 19. Momentum Space of a 4 Reaction Wheel System

Table 1 lists all of the possible configurations of momentum vertices and facet minimums. Once normalized, these represent the respective axes with the momentum magnitudes listed above.

Max Vertices	Minor Vertices	Minimum Facets
[1 1 0]	[sin(β) 0 cos(β)]	[1 0 0]
[1 -1 0]	[sin(β) 0 -cos(β)]	[-1 0 0]
[-1 1 0]	[-sin(β) 0 cos(β)]	[0 1 0]
[-1 -1 0]	[-sin(β) 0 -cos(β)]	[0 -1 0]
[0 0 1]	[0 sin(β) cos(β)]	[sin(β) sin(β) 2cos(β)]
[0 0 -1]	[0 sin(β) -cos(β)]	[sin(β) sin(β) -2cos(β)]
	[0 -sin(β) cos(β)]	[sin(β) -sin(β) 2cos(β)]
	[0 -sin(β) -cos(β)]	[sin(β) -sin(β) -2cos(β)]
		[-sin(β) sin(β) 2cos(β)]
		[-sin(β) sin(β) -2cos(β)]
		[-sin(β) -sin(β) 2cos(β)]
		[-sin(β) -sin(β) -2cos(β)]

Table 1. Reaction Wheel Significant Axes

From Figure 17, the wheel torque vectors directly align with the wheel momentum vectors. This causes a torque envelope equal in shape to that in Figures 18 and 19. Instead of using h_{\max} as the scaling factor, the dodecahedron would be instead scaled by the maximum individual wheel torque τ_{\max} . All maximum and minimum vertices are co-aligned with the momentum vertices, just with different units.

E. LARGEST INSCRIBED SPHERE

As mentioned in Chapter I, sometimes it is necessary to create artificial limitations on a control system. Recall from Figure 18 that the twelve facet minima occur at $h_{\min}^B = 1.633h_{\max}$. Although they are considered minima, they still lie on the momentum surface. For example, on axis $\begin{bmatrix} 1 & 0 & 0 \end{bmatrix}$, momentum up to $1.633h_{\max}$ (torque up to $1.633\tau_{\max}$) is available. This is the physical system limit that cannot be exceeded for an eigenaxis rotation about that specific axis. Since this is the global envelope minimum, a sphere can be created with radius $1.633h_{\max}$ that includes all twelve points. Such a sphere

is the largest possible sphere within the momentum space, shown in Figure 20. Restricting commanded momentum to lie within the inscribed spherical volume ensures that $1.633h_{\max}$ is available about every possible axis.

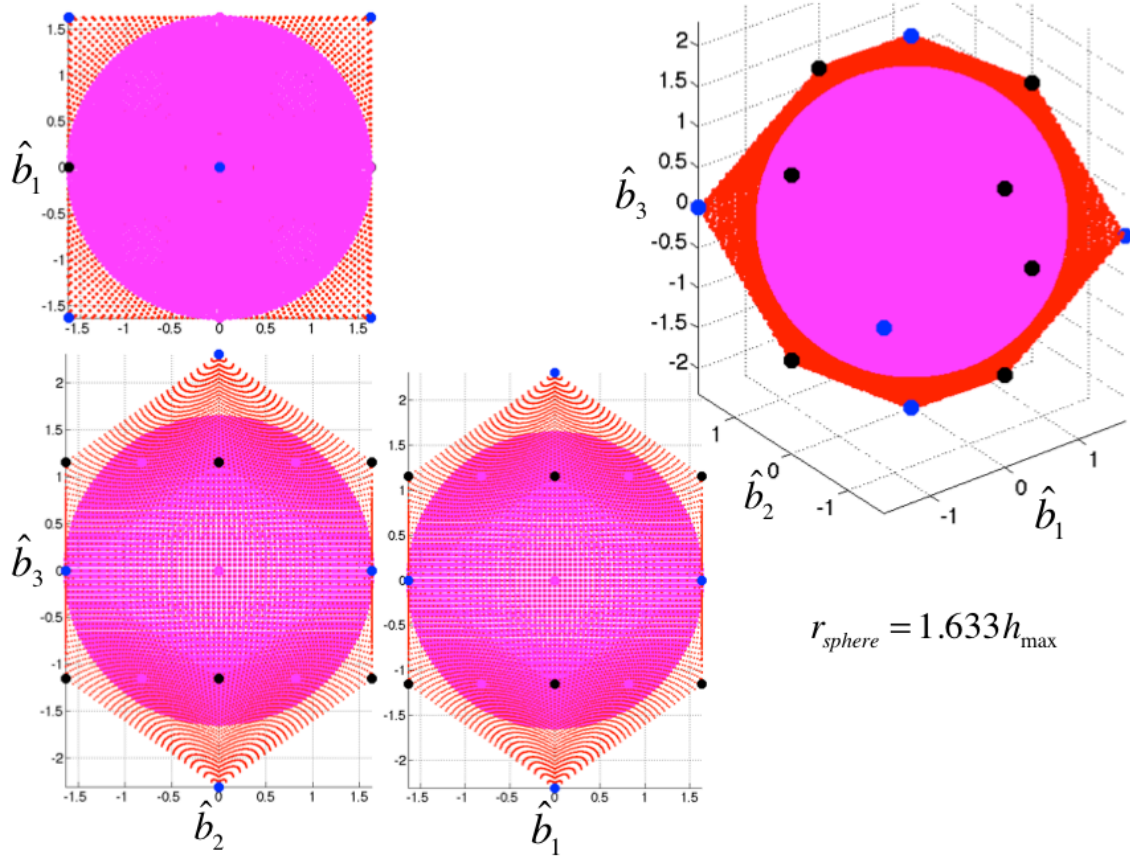


Figure 20. Reaction Wheel Momentum Space with Largest Inscribed Sphere

Of course, 40% more momentum is available about the maximum axes shown in Table 1, but in a conventional attitude control system design, this additional torque/momentum capacity is sacrificed. This sacrifice is made to ensure a designed slew rate is available for any given slew. The inertia of a spacecraft is rarely symmetric and equal about every major axis. The resultant is an inertia ellipsoid, further reducing the momentum space envelope. This occurs due to the need to ensure the momentum does not change with a non-symmetric inertia matrix. The maximum spacecraft inertia value is also used about every axis, further limiting the system to enforce consistent slew rates.

F. REACTION WHEEL PSEUDO-INVERSE STEERING LOGIC

The physical limitation of a reaction wheel system was previously discussed. Another limitation associated with reaction wheels is the mathematical limitation of the Moore-Penrose pseudo-inverse, Equation (61). When reorienting coordinates from the n wheels in the wheel frame \hat{W} to three orthogonal coordinates of the body frame \hat{B} , there is a unique solution.

$$\begin{aligned} \mathbf{h}^B &= {}^B\mathbf{Z}_3^W \mathbf{h}^W \\ \boldsymbol{\tau}^B &= {}^B\mathbf{Z}_3^W \boldsymbol{\tau}^W \end{aligned} \quad (86)$$

The pseudo-inverse offers a single solution for translating the actuation from the body coordinates (3×1 vector) uniformly across n wheels ($nx1$ vector). The pseudo-inverse is desirable because it is the minimum least squares (L2) solution, minimizing the sum of the squares of all of the wheels' individual momenta/torque [15, p. 1609].

$$\begin{aligned} \mathbf{h}^W &= [{}^B\mathbf{Z}_3^W]^+ \mathbf{h}^B \\ \boldsymbol{\tau}^W &= [{}^B\mathbf{Z}_3^W]^+ \boldsymbol{\tau}^B \end{aligned} \quad (87)$$

Since the system is underdetermined, there are infinite possible $nx1$ wheel configurations that will satisfy the body coordinate solution, but the pseudo-inverse will give only one such configuration.

1. Pseudo-Inverse Control Allocation

Using the reaction wheel orientation matrix for a 4 wheel system mentioned in (60) and $\beta = \cos^{-1}\left(\frac{1}{\sqrt{3}}\right) \text{rad} = 54.74^\circ$, the resultant orientation matrix and pseudo-inverse used in this example is

$${}^B\mathbf{Z}^W = \frac{1}{\sqrt{3}} \begin{bmatrix} \sqrt{2} & 0 & -\sqrt{2} & 0 \\ 0 & \sqrt{2} & 0 & -\sqrt{2} \\ 1 & 1 & 1 & 1 \end{bmatrix}^W \quad (88)$$

$$\left[{}^B\mathbf{Z}_3^W \right]^+ = \frac{\sqrt{3}}{4} \begin{bmatrix} \sqrt{2} & 0 & 1 \\ 0 & \sqrt{2} & 1 \\ -\sqrt{2} & 0 & 1 \\ 0 & -\sqrt{2} & 1 \end{bmatrix}^B \quad (89)$$

To illustrate the implications of $\left[{}^B\mathbf{Z}_3^W \right]^+$, consider the following possible wheel momentum configuration where $1.0 h_{\max}$ represents a scalar of the maximum possible momentum for a given wheel.

$$\mathbf{h}_{possible}^W = \begin{bmatrix} 1 \\ 1 \\ -1 \\ 1 \end{bmatrix} h_{\max} \quad (90)$$

Using Equation (90) leads to the following possible momentum in the body frame.

$$\mathbf{h}_{possible}^B = {}^B\mathbf{Z}_3^W \mathbf{h}_{possible}^W = {}^B\mathbf{Z}_3^W \begin{bmatrix} 1 \\ 1 \\ -1 \\ 1 \end{bmatrix}^W h_{\max} = \begin{bmatrix} 1.633 \\ 0 \\ 1.155 \end{bmatrix}^B h_{\max} \quad (91)$$

Assume this possible \mathbf{h}^B was commanded rather than derived. Now, the pseudo-inverse would be required to derive the individual wheel momentum commands, \mathbf{h}^W . Applying the least-squares solution $\left[{}^B\mathbf{Z}_3^W \right]^+$ leads to a different solution than $\left[\begin{array}{cccc} 1 & 1 & -1 & 1 \end{array} \right]^T$). The pseudo-inverse solution is actually physically unachievable because the largest momentum command, $1.5 h_{\max}$, is higher than the maximum h_{\max} for a given wheel:

$$\mathbf{h}_{pseudo-unacheivable}^W = [\mathbf{Z}_3^W]^+ \mathbf{h}_{possible}^B = [\mathbf{Z}_3^W]^+ \begin{bmatrix} 1.633 \\ 0 \\ 1.155 \end{bmatrix}^B h_{\max} = \begin{bmatrix} 1.5 \\ 0.5 \\ -0.5 \\ 0.5 \end{bmatrix}^W h_{\max} \quad (92)$$

In order to implement the least squares control allocation, the proportionality of the solution must remain intact [24, pp. 880–883]. The wheel momentum vector in Equation (92) is therefore normalized by the highest element (greatest in magnitude). This allows appropriate control allocation to rotate the spacecraft predictably about the desired axis.

$$\begin{aligned} \mathbf{h}_{pseudo-lim}^W &= \frac{[\mathbf{Z}_3^W]^+ \mathbf{h}_{desired}^B}{\max\left(\left|[\mathbf{Z}_3^W]^+ \mathbf{h}_{desired}^B\right|\right)} \\ &= \frac{\mathbf{h}_{pseudo-unacheivable}^W}{\max\left(\left|\mathbf{h}_{pseudo-unacheivable}^W\right|\right)} \\ &= \begin{bmatrix} 1.000 \\ 0.333 \\ -0.333 \\ 0.333 \end{bmatrix}^W h_{\max} \end{aligned} \quad (93)$$

The normalized solution Equation (93) is far different than the wheel momentum configuration at the beginning of this example, Equation (90). Translating back to the body frame reveals that the pseudo-inverse limited solution in Equation (94) can only achieve 67% of the possible momentum shown in Equation (91).

$$\mathbf{h}_{pseudo-lim}^B = \mathbf{Z}^W \mathbf{h}_{pseudo-lim}^W = \mathbf{Z}^W \begin{bmatrix} 1.000 \\ 0.333 \\ -0.333 \\ 0.333 \end{bmatrix}^W h_{\max} = \begin{bmatrix} 1.089 \\ 0 \\ 0.770 \end{bmatrix}^B h_{\max} \quad (94)$$

The previous example can be redone using

$$\mathbf{h}_{possible}^W = \begin{bmatrix} 1 \\ a \\ -a \\ a \end{bmatrix} h_{\max} \quad (95)$$

with a as anything from 0.333 to 1.0. The system returns the same limit at

$$\mathbf{h}_{pseudo-lim}^B = \begin{bmatrix} 1.089 \\ 0 \\ 0.770 \end{bmatrix}^B h_{\max} \quad (96)$$

which is only 67% of the possible body momentum in this example.

$$\mathbf{h}_{possible}^B = \begin{bmatrix} 1.633 \\ 0 \\ 1.155 \end{bmatrix}^B h_{\max} \quad (97)$$

The same performance limitation results in a loss of torque per Equation (87).

2. Performance Loss

The momentum vector in the previous example corresponds to a minor vertex (see Figure 19).

$$\mathbf{h}_{possible}^B = \begin{bmatrix} 1.633 \\ 0 \\ 1.155 \end{bmatrix}^B h_{\max} = \begin{bmatrix} c\beta \\ 0 \\ s\beta \end{bmatrix}^B 2.0 h_{\max} \quad (98)$$

The pseudo-inverse limited vector is 67% of $\mathbf{h}_{possible}^B$ giving a magnitude of $|\mathbf{h}| = 1.33 h_{\max}$.

$$\mathbf{h}_{pseudo-lim}^B = \begin{bmatrix} 1.089 \\ 0 \\ 0.770 \end{bmatrix}^B h_{\max} = \begin{bmatrix} c\beta \\ 0 \\ s\beta \end{bmatrix}^B 1.33 h_{\max} = 0.67 \mathbf{h}_{possible}^B \quad (99)$$

Graphically, $\mathbf{h}_{pseudo-lim}^B$ would be well within the reaction wheel momentum envelope. Shown in Figure 21, the red shape represents the full reaction wheel momentum space. It is the physical limitation of the reaction wheel system utilizing the maximum momentum possible to rotate about any given axis. The black dot represents the original point (minor vertex) shown in Equation (98). The red dot represents the pseudo-inverse limited system shown in Equation (99). The blue/black lines represent all possible magnitudes that share the same eigenaxis as the minor vertex. The blue line specifically represents the set of all achievable configurations by the pseudo-inverse. The black line represents the set of all unachievable, yet still possible, configurations.

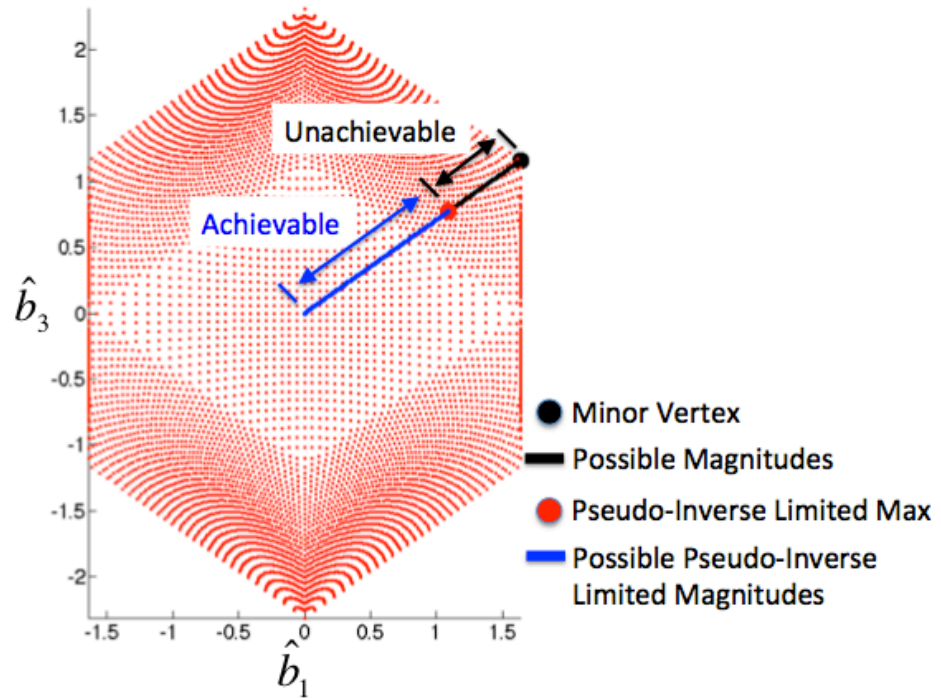


Figure 21. Reaction Wheel Momentum/Torque Space Showing Pseudo-Inverse Limit

The same is true for all other minor vertices, as they are unachievable using the pseudo-inverse. On the other hand, the minimum points and the maximum vertices are all achievable, shown in Figures 22 to 23.

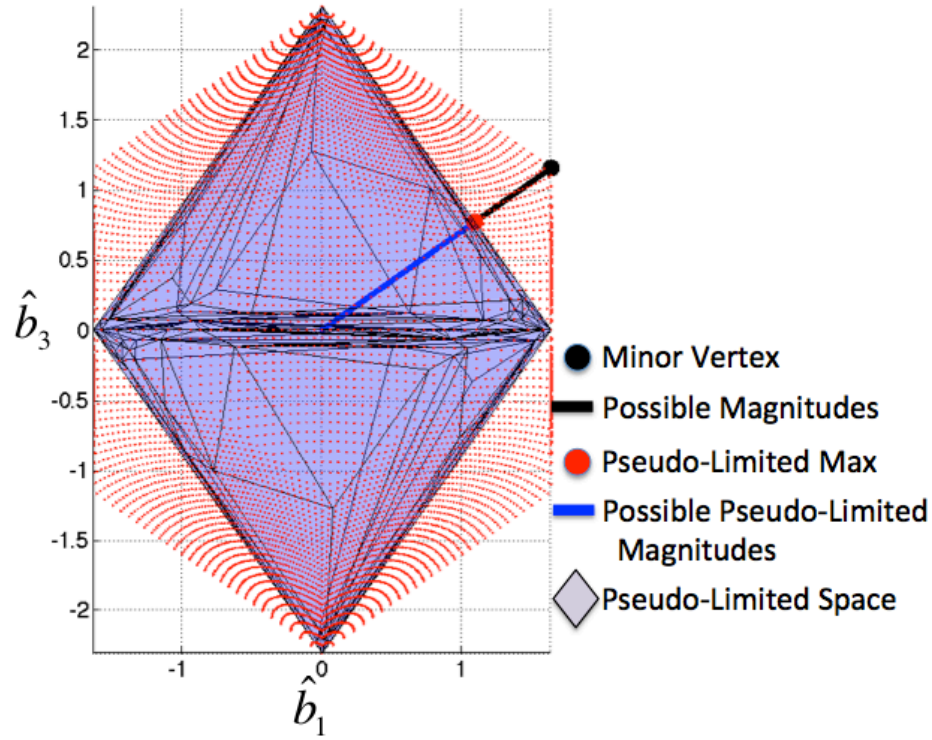


Figure 22. Reaction Wheel Pseudo-Inverse Limited Space

The representation shown in Figure 22 makes it clear that the pseudo-inverse is a mathematical limitation on the system performance and not a physical system limitation. Indeed, this is true because the pseudo-inverse minimizes the sum of the squares of the moment/torque in a given direction. The least squares solution discards some of the available moment capacity in favor of an L2 control allocation. In reality, the spacecraft has the ability to rotate faster (higher momentum) about many axes, but the pseudo-inverse does not necessarily allow this. Going from wheel space to body space, there is only one mathematical answer. Going from body space to wheel space, there are an infinite number of potential arrangements. The pseudo-inverse only provides the least-squares solution, a mathematically limited solution.

Figure 23 shows the pseudo-inverse limited momentum space from Figure 22 overlaid into the full reaction wheel space from Figure 19. This makes it clear how much volume is missing across the different orthogonal views. An interesting note is that the

pseudo-inverse solution intersects all six of the maximum vertices and all twelve of the minimum points, but none of the eight minor vertices.

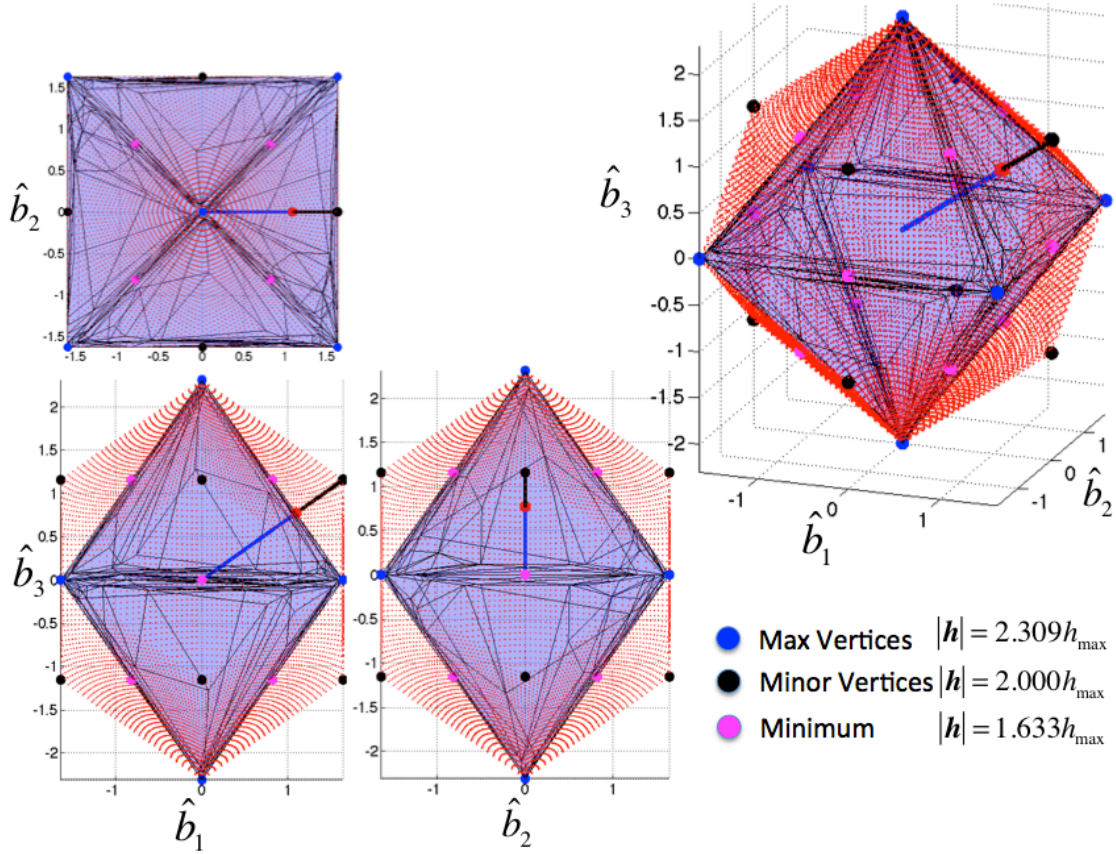


Figure 23. Reaction Wheel Pseudo-Inverse Limited Space – Orthogonal

G. PSEUDO-INVERSE LARGEST INSCRIBED SPHERE

As previously shown with the full reaction wheel space, the full momentum envelope can be further limited to an enclosed sphere (Figure 19). Similarly, the pseudo-inverse limited space can be confined to a sphere to ensure a constant value of achievable momentum in all directions. The minimum pseudo-inverse envelope surfaces occur at $1.333h_{\max}$. Therefore, the pseudo-inverse space can be confined to a sphere with a radius of $1.333h_{\max}$ (Figure 24). This will ensure that this momentum is available in all directions.

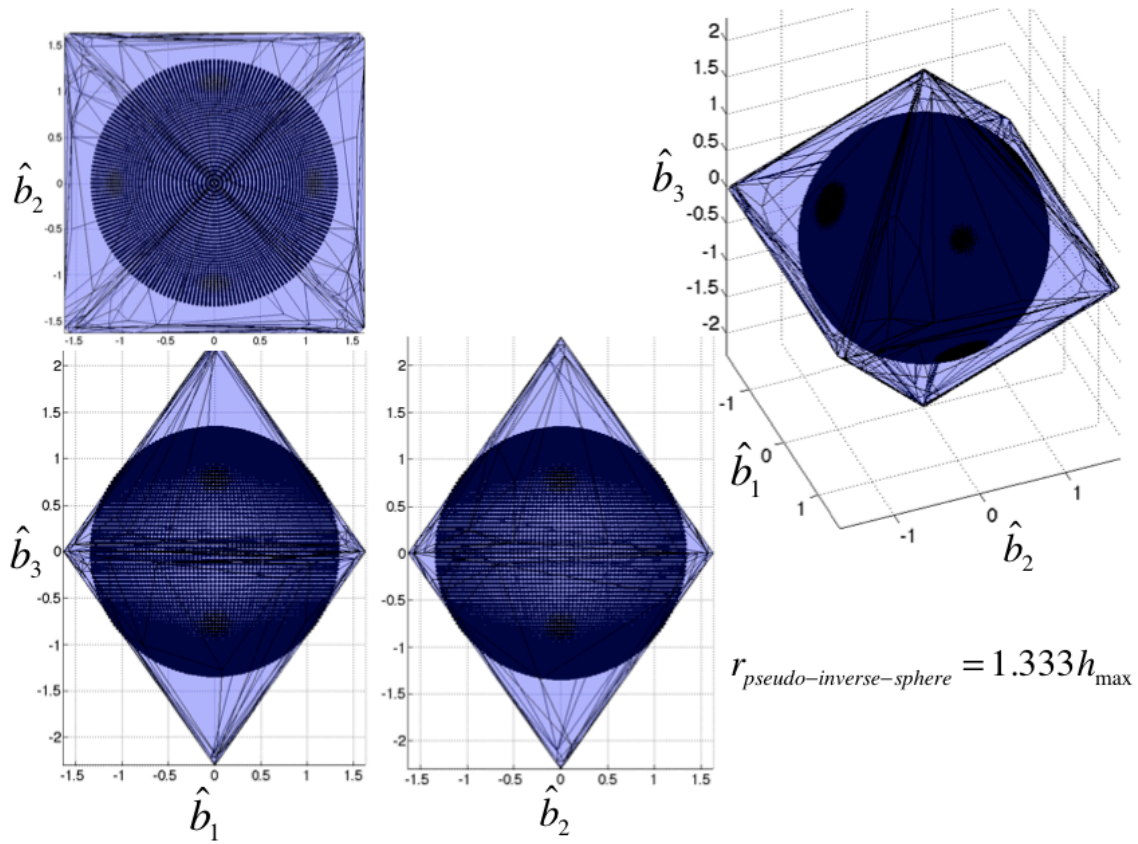


Figure 24. Pseudo-Inverse Momentum Space with Largest Sphere

Figure 25 shows a comparison of the reaction wheel momentum space under the various control limitations. Here it is obvious the huge loss of momentum space that occurs under the typical spherical simplification utilized in the design of a spacecraft attitude control system. Later chapters will be used to discuss methods, particularly the use of optimal control, to improve the usage of the available system capacity.

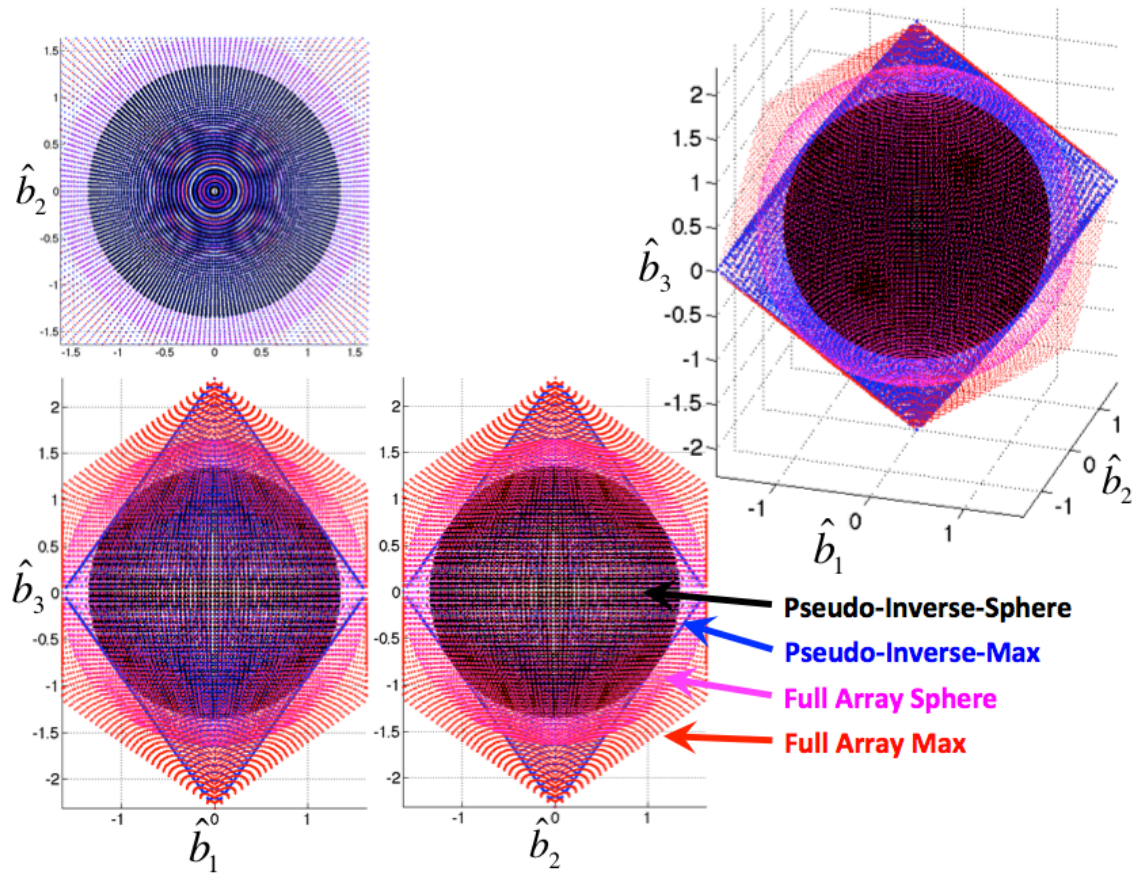


Figure 25. Momentum Space Comparison

V. OPTIMAL REACTION WHEEL ATTITUDE CONTROL

This chapter will be used to derive the time-optimal slew for a reaction wheel system. First, the time-optimal eigenaxis slew will be generated. This standard heritage maneuver is best only if the engineer wants the spacecraft to stay on the eigenaxis to minimize the overall rotation angle. The spacecraft often has more momentum and torque available to exploit, but it is necessary to deviate from an eigenaxis path in order to accomplish this. The remaining sections of the chapter will expand the linear derivation from Section A into the nonlinear reaction wheel and spacecraft dynamics developed in Chapters II and IV. DIDO, an optimal control solver [21], will be used to obtain the optimal control solution. An attitude control architecture will also be presented in order to implement the optimal solution.

A. TIME-OPTIMAL EIGENAXIS REORIENTATION

The time-optimal, rest-to-rest eigenaxis slew solution is fairly straightforward. Not all of the following steps are necessary to solve this problem, but all steps will be covered for completeness. The optimal control methodology is necessary to understand prior to Section B, where a much more complicated derivation is presented.

1. Problem Formulation

In general, figures of merit are used to determine how well the slew meets the requirements important to the engineers and/or customer. These are broken up into costs (stuff to minimize) and constraints (boundary conditions that must not be exceeded). The maneuver is defined as rest-to-rest with the initial and final angles predetermined.

Initial time is zero and the final time is free (term to be optimized), if it is desired to design a rapid slew maneuver.

$$\begin{aligned} t_0 &= t^0 = 0 \\ t_f &= t^f \end{aligned} \tag{100}$$

As shown in Chapter III, the spacecraft model can be simplified as a double integrator. In this case, the state variables and control are

$$\mathbf{x}(t) = \begin{bmatrix} \theta(t) \\ \dot{\theta}(t) \end{bmatrix} = \begin{bmatrix} \theta(t) \\ \omega(t) \end{bmatrix} \quad (101)$$

$$\mathbf{u} = [u(t)] = [\alpha(t)] \quad (102)$$

The state space representation of Equation (101) is shown as

$$\dot{\mathbf{x}} = \mathbf{f}(\mathbf{x}(t), \mathbf{u}(t)) = \begin{bmatrix} \dot{\theta}(t) \\ \dot{\omega}(t) \end{bmatrix} = \begin{bmatrix} \omega(t) \\ \alpha(t) \end{bmatrix} = \begin{bmatrix} \omega(t) \\ u(t) \end{bmatrix} \quad (103)$$

First and foremost, the solution must meet the boundary conditions. The purpose of slewing is to accurately point at a new target (end condition). If the spacecraft slews but does not get the desired end condition, then it may not be possible to perform the mission requirements. The final angle will be defined as the difference from start to finish. Therefore, the initial angle will be set as zero. Initial and final rates are zero because the maneuver is considered rest-to-rest. The boundary conditions are defined as follows.

$$\begin{aligned} \theta(t_0) &= \theta_0 = 0 \\ \omega(t_0) &= \omega_0 = 0 \\ \theta(t_f) &= \theta_f = \theta_d \\ \omega(t_f) &= \omega_f = 0 \end{aligned} \quad (104)$$

These boundary conditions can be rewritten as

$$\mathbf{x}(t_0) = \mathbf{x}^0 = \begin{bmatrix} \theta_0 \\ \omega_0 \end{bmatrix} = \begin{bmatrix} 0 \\ 0 \end{bmatrix} \quad (105)$$

$$\mathbf{x}(t_f) = \mathbf{x}^f = \begin{bmatrix} \theta_f \\ \omega_f \end{bmatrix} = \begin{bmatrix} \theta_d \\ 0 \end{bmatrix} \quad (106)$$

A convention to be used to define the endpoint conditions \mathbf{e} will be to set Equation (106) equal to zero.

$$\mathbf{e}(\mathbf{x}(t_f)) = \begin{bmatrix} \theta_f - \theta_d \\ \omega_f \end{bmatrix} = \begin{bmatrix} 0 \\ 0 \end{bmatrix} \quad (107)$$

The Mayer cost E is a form of endpoint cost. Assuming the boundary conditions “must” be met, this is the measure of optimality that quantifies the solution in terms of the final state. Since this is a time-optimal slew, the endpoint cost is the final time.

$$E(\mathbf{x}(t_f)) = t_f \quad (108)$$

The Lagrange cost F is a form of running cost. This measure quantifies the cost of the maneuver itself. A common form is the quadratic cost $F = \int_{t_0}^{t_f} u^2(t) dt$, which represents the “energy” or efficiency of the system. Since the control u is directly related to torque, this cost can be used to minimize torque-related functions like power during a maneuver. For the simplified case of individual time-optimal slews, the Lagrange cost will not be used. The superscript $(D.N.E.)$ will be used to show that the term is not only zero, but it does not exist for this problem.

$$\int_{t_0}^{t_f} F(\mathbf{x}(t), \mathbf{u}(t)) dt = 0^{(D.N.E.)} \quad (109)$$

The cost functional \mathfrak{J} can be composed of both Mayer and Lagrange costs.

$$\begin{aligned} \mathfrak{J}[\mathbf{x}(\cdot), \mathbf{u}(\cdot), t_f] &= E(\mathbf{x}(t_f)) + \int_{t_0}^{t_f} F(\mathbf{x}(t), \mathbf{u}(t)) dt \\ \mathfrak{J}[\mathbf{x}(\cdot), \mathbf{u}(\cdot), t_f] &= t_f \end{aligned} \quad (110)$$

Rewriting this problem in the format used by Ross [25, p. 43], we get

$$\begin{aligned}
\text{Given} \quad & \mathbf{x} = \begin{bmatrix} \theta \\ \omega \end{bmatrix}, \mathbf{u} = [u] \\
\text{Minimize} \quad & \mathfrak{J}[\mathbf{x}(\cdot), \mathbf{u}(\cdot), t_f] = t_f \\
\text{Subject to} \quad & \dot{\mathbf{x}} = \begin{bmatrix} \omega \\ u \end{bmatrix} \\
& (\theta_0, \omega_0, t_0) = (0, 0, 0) \\
& (\theta_f - \theta_d, \omega_f) = (0, 0)
\end{aligned} \tag{111}$$

2. The Hamiltonian

For every state, a costate will be defined with subscripts to match their respective states.

$$\boldsymbol{\lambda} = \begin{bmatrix} \lambda_1 \\ \lambda_1 \end{bmatrix} = \begin{bmatrix} \lambda_\theta \\ \lambda_\omega \end{bmatrix} \tag{112}$$

The control Hamiltonian is given by

$$H(\boldsymbol{\lambda}, \mathbf{x}, \mathbf{u}) = F(\mathbf{x}, \mathbf{u}) + \boldsymbol{\lambda}^T \mathbf{f}(\mathbf{x}, \mathbf{u}) \tag{113}$$

$$\begin{aligned}
H(\boldsymbol{\lambda}, \mathbf{x}, \mathbf{u}) &= 0^{(D.N.E.)} + \begin{bmatrix} \lambda_\theta & \lambda_\omega \end{bmatrix} \begin{bmatrix} \omega \\ u \end{bmatrix} \\
&= \lambda_\theta \omega + \lambda_\omega u
\end{aligned} \tag{114}$$

3. The Hamiltonian Minimization Condition

The Hamiltonian Minimization Condition states that the Hamiltonian \mathbf{H} must be minimized over the control \mathbf{u} [26, p. 108]. This leads to the Euler Lagrange equation.

$$\begin{aligned}
\frac{\partial \mathbf{H}}{\partial \mathbf{u}} &= 0 \\
\frac{\partial}{\partial u}(\lambda_\theta \omega + \lambda_\omega u) &= \lambda_\omega = 0
\end{aligned} \tag{115}$$

Since u does not appear, Pontryagin's Principle must be used. From [26, Algorithm 3.8.13], Pontryagin's Principle states the following.

$$\frac{\partial H}{\partial u} = \begin{cases} > 0, & u = -u_{\max} \\ = 0, & -u_{\max} < u < u_{\max} \\ < 0, & u = u_{\max} \end{cases} \quad (116)$$

Applied to this problem, the switching function in Equation (116) becomes

$$\lambda_{\omega} = \begin{cases} > 0, & u = -u_{\max} \\ = 0, & -u_{\max} < u < u_{\max} \\ < 0, & u = u_{\max} \end{cases} \quad (117)$$

By rearranging Equation (117) in terms of the costate to solve for the control, the rule in Equation (118) results. Since the value of the control does not matter when the costate $\lambda_{\omega} = 0$, the control can be set to zero. This is not necessary, but it is acceptable since the use of any control during this state will not affect the optimal control problem. This is stated simply as an energy conservation technique. Thus, the control is given as:

$$u = \begin{cases} -u_{\max} & \lambda_{\omega} > 0 \\ 0 & \text{for } \lambda_{\omega} = 0 \\ u_{\max} & \lambda_{\omega} < 0 \end{cases} \quad (118)$$

Ultimately, Equation (118) states that the control must be at its positive or negative maxima. The function sgn will be defined as the sign of its independent variable.

$$\text{sgn}(\bullet) = \begin{cases} 1 & (\bullet) > 0 \\ 0 & \text{for } (\bullet) = 0 \\ -1 & (\bullet) < 0 \end{cases} \quad (119)$$

Equation (118) can now be written compactly as

$$u = -\text{sgn}(\lambda_{\omega})u_{\max} \quad (120)$$

Equation (120) matches the formulation by [25, Algorithm 3.36].

4. The Costate Dynamics and the Adjoint Equation

From [25, Algorithm 2.2], the adjoint equation states

$$-\dot{\lambda}(t) = \frac{\partial \mathbf{H}}{\partial \mathbf{x}} \quad (121)$$

$$-\begin{bmatrix} \dot{\lambda}_\theta \\ \dot{\lambda}_\omega \end{bmatrix} = \begin{bmatrix} \frac{\partial \mathbf{H}}{\partial \theta} \\ \frac{\partial \mathbf{H}}{\partial \omega} \end{bmatrix} = \begin{bmatrix} 0 \\ \lambda_\theta \end{bmatrix} \quad (122)$$

The differential costate equations shown in Equation (122) can be integrated to create equations for the costates in terms of unknown constants.

$$\lambda(t) = \begin{bmatrix} \lambda_\theta \\ \lambda_\omega \end{bmatrix} = \begin{bmatrix} c_1 \\ -c_1 t + c_2 \end{bmatrix} \quad (123)$$

5. Transversality

The endpoint Lagrangian is given by [25, Algorithm 2.9].

$$\bar{E}(\mathbf{x}_f, t_f) = E(\mathbf{x}(t_f)) + \mathbf{v}^T \mathbf{e}(\mathbf{x}(t_f)) \quad (124)$$

$$\begin{aligned} \bar{E}(\mathbf{x}_f, t_f) &= t_f + \begin{bmatrix} v_\theta & v_\omega \end{bmatrix} \begin{bmatrix} \theta_f - \theta_d \\ \omega_f \end{bmatrix} \\ &= t_f + v_\theta (\theta_f - \theta_d) + v_\omega (\omega_f) \end{aligned} \quad (125)$$

The terminal transversality conditions are given by [25, Algorithm 2.8].

$$\lambda(t_f) = \frac{\partial \bar{E}}{\partial \mathbf{x}_f} \quad (126)$$

$$\lambda(t_f) = \begin{bmatrix} \frac{\partial \bar{E}}{\partial \theta_f} \\ \frac{\partial \bar{E}}{\partial \omega_f} \end{bmatrix} = \begin{bmatrix} v_\theta \\ v_\omega \end{bmatrix} \quad (127)$$

$$\text{or more simply } \lambda_f = \mathbf{v} \quad (128)$$

Since the final conditions of the costates simply equal new unknown variables, nothing new is learned by analyzing the transversality condition. Since the final time is free, the Hamiltonian Value Condition is necessary. This states terminal conditions for the Hamiltonian [25, Algorithm 2.10].

$$H(t_f) = -\frac{\partial \bar{E}}{\partial t_f} \quad (129)$$

$$H(t_f) = -1 \quad (130)$$

The Hamiltonian is minimized when the $\partial H / \partial u = 0$ and $\partial^2 H / \partial u^2 \geq 0$. Equation (130) provides a fixed point for the terminal point of the Hamiltonian. Since $\partial H(t) / \partial u = 0$, then $H(t) = -1$ for all time.

6. Bang-Bang Control

Ultimately, the primary lesson learned above is

$$u = -\text{sgn}(\lambda_\omega) u_{\max} \quad (131)$$

$$\lambda_\omega = -c_1 t + c_2 \quad (132)$$

Equations (131) and (132) can be combined as

$$u = -\text{sgn}(-c_1 t + c_2) u_{\max} . \quad (133)$$

Since λ_ω is linear, it can only intersect $\lambda_\omega = 0$ once. This may or may not occur within the range $[0, t^f]$, therefore it can be stated that at most, only one sign change (switch) occurs within (133). [19, pp. 193–200] additionally confirms that only one sign change occurs for initial rest-to-rest maneuvers. For arbitrary initial or final conditions, it is possible for no switches to occur (e.g., high initial velocity with constant deceleration to slow down). Therefore, for the rest-to-rest maneuver in this example, the quickest method of rotation about this single eigenaxis would be to use bang-bang control where one switch occurs between $[0, t^f]$. This means to use maximum torque available along that axis until half way there, then reverse torque in order to slow down to zero right at

the point in which the desired slew angle θ_d is achieved. The resulting trajectory is shown in Figure 26.

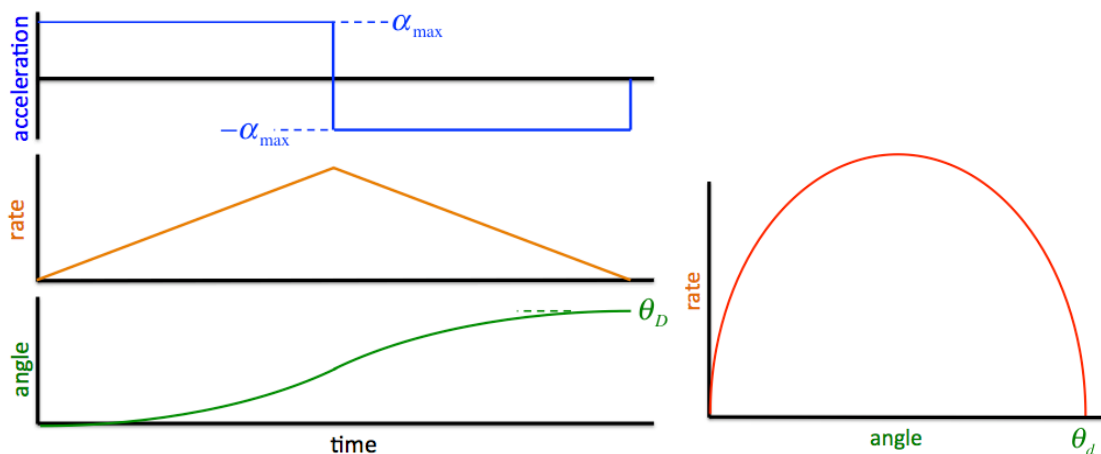


Figure 26. Acceleration Limited Eigenaxis Slew

Since spacecraft attitude reorientations may also be momentum-limited in addition to torque-limited, large angle maneuvers may look closer to that in Figure 29 (heritage maneuver from Chapter III). Momentum is proportional to angular rate, therefore the trajectory is shown as rate-limited. The maneuver is initially torque-limited $\tau_{\max}(\alpha_{\max})$ until the maximum momentum $h_{\max}(\omega_{\max})$ is reached. During this momentum-limited section, the spacecraft coasts at ω_{\max} , until it can decelerate at its maximum torque $-\tau_{\max}(-\alpha_{\max})$. Figure 27 is the solution to the optimal control problem with an additional rate limit.

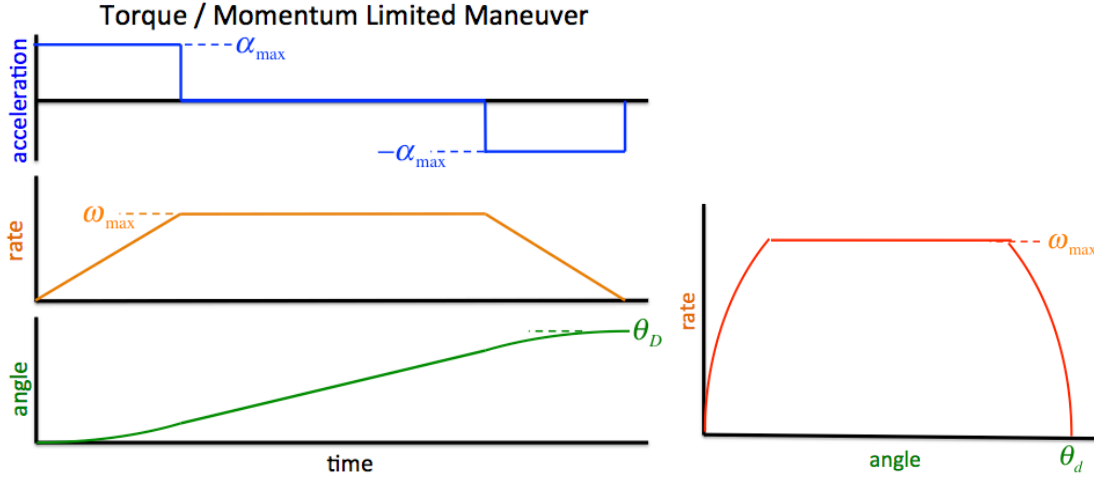


Figure 27. Rate Limited Eigenaxis Slew

B. OPTIMAL CONTROL EQUATIONS OF MOTION

Since the input is already going to be determined offline per the shaped heritage maneuver, the time-optimal solution should instead be utilized. With theoretically unlimited computing power at the ground station, the optimal solution can be computed for every individual slew. The equations of motion for the spacecraft and reaction wheel system from Chapters II and IV will now be consolidated. Although the equations are listed in matrix form for simplicity, the number of dynamic equations reflects the number of independent equations that can be extracted from the equation set.

1. Spacecraft Kinematics

The spacecraft kinematics are repeated from Chapter II. Since the orbital motion is set to zero (${}^N\boldsymbol{\omega}^O = 0$, see Chapter III), then ${}^N\boldsymbol{\omega}^B = {}^O\boldsymbol{\omega}^B$. This simplifies the dynamics slightly allowing the removal of three states. This change is reflected immediately in Equation (134).

$$\begin{aligned}\dot{\mathbf{q}}_{123} &= \frac{1}{2} \left(q_4 {}^N\boldsymbol{\omega}^B - {}^N\boldsymbol{\omega}^B \times \mathbf{q}_{123} \right) \\ \dot{q}_4 &= -\frac{1}{2} \left({}^N\boldsymbol{\omega}^B \right)^T \mathbf{q}_{123}\end{aligned}\tag{134}$$

where $\mathbf{q}_{123} = \begin{bmatrix} q_1 & q_2 & q_3 \end{bmatrix}^T$.

2. Reaction Wheel Dynamics

The torques of the individual reaction wheels follow from Equation (71).

$$\boldsymbol{\tau}_w^W = J_w \dot{\boldsymbol{\Omega}}^W \quad (135)$$

Equation (135) can be solved in terms of the reaction wheel acceleration.

$$\dot{\boldsymbol{\Omega}}^W = J_w^{-1} \boldsymbol{\tau}_w^W \quad (136)$$

3. Spacecraft Dynamics

The spacecraft dynamics were developed in Chapters II and IV.

$$\boldsymbol{\tau}_{req}^N = J_{s/c}^N \dot{\boldsymbol{\omega}}^B + {}^N \boldsymbol{\omega}^B \times J_{s/c}^N \boldsymbol{\omega}^B \quad (137)$$

$$-\boldsymbol{\tau}_{req}^N = {}^b Z_3^w \boldsymbol{\tau}_w^W + {}^N \boldsymbol{\omega}^B \times {}^b Z_3^w J_w \boldsymbol{\Omega}^W \quad (138)$$

Combining Equations (137) and (138) yields the following.

$$J_{s/c}^N \dot{\boldsymbol{\omega}}^B + {}^N \boldsymbol{\omega}^B \times J_{s/c}^N \boldsymbol{\omega}^B = -{}^b Z_3^w \boldsymbol{\tau}_w^W - {}^N \boldsymbol{\omega}^B \times {}^b Z_3^w J_w \boldsymbol{\Omega}^W \quad (139)$$

$$J_{s/c}^N \dot{\boldsymbol{\omega}}^B = -{}^b Z_3^w \boldsymbol{\tau}_w^W - {}^N \boldsymbol{\omega}^B \times (J_{s/c}^N \boldsymbol{\omega}^B + {}^b Z_3^w J_w \boldsymbol{\Omega}^W) \quad (140)$$

Solving Equation (140) in terms of the spacecraft angular velocity rate yields

$${}^N \dot{\boldsymbol{\omega}}^B = J_{s/c}^{-1} \left(-{}^b Z_3^w \boldsymbol{\tau}_w^W - {}^N \boldsymbol{\omega}^B \times (J_{s/c}^N \boldsymbol{\omega}^B + {}^b Z_3^w J_w \boldsymbol{\Omega}^W) \right) \quad (141)$$

4. State and Control Variables

The state vector now has $7+n$ states and the control vector has n states, where n refers to the number of reaction wheels in the array.

$$\mathbf{x} = \begin{bmatrix} q_1 \\ q_2 \\ q_3 \\ q_4 \\ {}^N\omega_x^B \\ {}^N\omega_y^B \\ {}^N\omega_z^B \\ \Omega_1^W \\ \vdots \\ \Omega_n^W \end{bmatrix} \quad \text{and} \quad \mathbf{u} = \begin{bmatrix} \tau_1^W \\ \vdots \\ \tau_n^W \end{bmatrix} \quad (142)$$

5. Actuator Constraints

Torque and momentum limitations will be included in the optimal control problem, as these constraints represent the physical limitations of the attitude control system.

$$-\tau_{\max}^W \leq \tau_i^W \leq \tau_{\max}^W, \quad i = 1, 2, \dots, n \quad (143)$$

$$-\Omega_{\max}^W \leq \Omega_i^W \leq \Omega_{\max}^W, \quad i = 1, 2, \dots, n \quad (144)$$

6. Initial and Final Conditions

The spacecraft will be conducting rest-to-rest slews. This means initial and final quaternions are known. Initial and final spacecraft rotation rates are zero. For this analysis, initial and final reaction wheel rates will be considered zero. In reality, engineers operate the reaction wheel at some nominally non-zero value. This is because $\Omega_{i_0}^W = 0$ can cause jitter in the presence of “stiction” (friction from static positions) [13, p. 5]. The initial and final states can be represented as follows.

$$(q_{1_0}, q_{2_0}, q_{3_0}, q_{4_0}, {}^N\omega_{x_0}^B, {}^N\omega_{y_0}^B, {}^N\omega_{z_0}^B, \Omega_{1_0}^W, \dots, \Omega_{n_0}^W) = (q_1^0, q_2^0, q_3^0, q_4^0, 0, 0, 0, 0, \dots, 0) \quad (145)$$

$$(q_{1_f}, q_{2_f}, q_{3_f}, q_{4_f}, {}^N\omega_{x_f}^B, {}^N\omega_{y_f}^B, {}^N\omega_{z_f}^B, \Omega_{1_f}^W, \dots, \Omega_{n_f}^W) = (q_1^f, q_2^f, q_3^f, q_4^f, 0, 0, 0, 0, \dots, 0) \quad (146)$$

7. Cost Function

The objective is to minimize the overall maneuver time. Therefore, the cost function is

$$\mathcal{J}[\mathbf{x}(\cdot), \mathbf{u}(\cdot), t_f] = t_f \quad (147)$$

8. Optimal Control Problem

By gathering Equations (134) to (147), the optimal control problem can now be defined:

$$\begin{aligned} \text{Given} \quad \mathbf{x} &= \begin{bmatrix} q_1 & q_2 & q_3 & q_4 & {}^N\boldsymbol{\omega}_x^B & {}^N\boldsymbol{\omega}_x^B & {}^N\boldsymbol{\omega}_x^B & \boldsymbol{\Omega}_1^W & \cdots & \boldsymbol{\Omega}_n^W \end{bmatrix}^T \\ \mathbf{u} &= \begin{bmatrix} \boldsymbol{\tau}_1^W & \cdots & \boldsymbol{\tau}_n^W \end{bmatrix}^T \\ \text{Minimize} \quad \mathcal{J}[\mathbf{x}(\cdot), \mathbf{u}(\cdot), t_f] &= t_f \\ \text{Subject to} \quad \dot{q}_{123} &= \frac{1}{2} (q_4 {}^N\boldsymbol{\omega}^B - {}^N\boldsymbol{\omega}^B \times q_{123}) \\ \dot{q}_4 &= -\frac{1}{2} ({}^N\boldsymbol{\omega}^B)^T q_{123} \\ {}^N\dot{\boldsymbol{\omega}}^B &= \mathbf{J}_{s/c}^{-1} (-{}^b\mathbf{Z}_3^w \boldsymbol{\tau}_w^W - {}^N\boldsymbol{\omega}^B \times (\mathbf{J}_{s/c} {}^N\boldsymbol{\omega}^B + {}^b\mathbf{Z}_3^w \mathbf{J}_w \boldsymbol{\Omega}^W)) \\ \dot{\boldsymbol{\Omega}}^W &= \mathbf{J}_w^{-1} \boldsymbol{\tau}_w^W \\ (q_{1_0}, q_{2_0}, q_{3_0}, q_{4_0}, {}^N\boldsymbol{\omega}_{x_0}^B, {}^N\boldsymbol{\omega}_{y_0}^B, {}^N\boldsymbol{\omega}_{z_0}^B, \boldsymbol{\Omega}_{1_0}^W, \cdots, \boldsymbol{\Omega}_{n_0}^W) &= (q_1^0, q_2^0, q_3^0, q_4^0, 0, 0, 0, 0, \cdots, 0) \\ (q_{1_f}, q_{2_f}, q_{3_f}, q_{4_f}, {}^N\boldsymbol{\omega}_{x_f}^B, {}^N\boldsymbol{\omega}_{y_f}^B, {}^N\boldsymbol{\omega}_{z_f}^B, \boldsymbol{\Omega}_{1_f}^W, \cdots, \boldsymbol{\Omega}_{n_f}^W) &= (q_1^f, q_2^f, q_3^f, q_4^f, 0, 0, 0, 0, \cdots, 0) \\ -\boldsymbol{\tau}_{\max}^W &\leq \boldsymbol{\tau}_i^W \leq \boldsymbol{\tau}_{\max}^W \\ -\boldsymbol{\Omega}_{\max}^W &\leq \boldsymbol{\Omega}_i^W \leq \boldsymbol{\Omega}_{\max}^W \end{aligned} \quad (148)$$

C. SCALING THE PROBLEM

The purpose of scaling is to generalize all states to within similar orders of magnitude. Without scaling, one state may take on large values (10^6) while others are comparatively small (10^{-6}). The relative difference would be is (10^{-12}), which causes numerical problems due to operating near machine epsilon. By simply multiplying each

state by the appropriate “scaling factor” their values can be made the same order of magnitude, and numerical issues successfully sidestepped.

The common formulation for scaling units is done through “canonical units.” Canonical refers to a specific definition where, for example, a velocity unit (VU) is equal to the quotient of a distance unit (DU) and a time unit (TU).

$$VU = \frac{DU}{TU} \quad (149)$$

Within [21], “designer units” are chosen instead to keep the states and costates in relative orders of magnitude. Instead of looking at the costates, nor at the coupling between position and velocity, this thesis outlines a different kind of designer unit. They will be denoted by a superscript * (or state followed by “z” within any listed code).

1. Designer Units

As scaling factors, the following designer units are used to bring all variables close to the first order of magnitude.

Wheel torque: $\tau^* = \tau_{max}$ (maximum wheel torque for chosen RW)

Time: $T^* = 1s$ (use real time)

Quaternion: No further scaling. Assumes $-1 \leq q \leq 1$ is sufficiently scaled

S/C Spin Rate: $\omega^* = 3^\circ / s = 0.0524 rad / s$ (slightly faster than conventional rate)

Wheel Rate: $\Omega^* = \Omega_{max}$ (maximum wheel spin rate for chosen RW)

For example, the relationship between the torque τ and the scaled torque $\bar{\tau}$ will be the proportionality constant τ^* .

$$\tau = \bar{\tau} \tau^* \quad (150)$$

Therefore, the scaled torque would always operate in the range $[-1,1]$.

$$\bar{\tau} = \frac{\tau}{\tau^*} = \frac{\tau}{\tau_{max}} \quad (151)$$

Scaling of constants within a canonical unit representation can be useful because many terms will cancel out leaving simpler equations to manipulate and code. If all scaling terms are directly coded into the software, scaling of constants does nothing. This is because the constant must be scaled down first, then scaled back up to its original value within the dynamic equation. In the case of designer units where many mismatched units are being manipulated, it is unlikely that convenient units will cancel leaving an elegant equation. Therefore, scaling is not required and not completed for constants. An example of designer unit scaling is as follows for the spacecraft dynamics. The full set of scaled equations is shown in Appendix A.

$$\begin{aligned}
{}^N\dot{\boldsymbol{\omega}}^B &= \mathbf{J}_{s/c}^{-1} \left(-{}^b\mathbf{Z}_3^w \boldsymbol{\tau}_w^W - {}^N\boldsymbol{\omega}^B \times \left(\mathbf{J}_{s/c} {}^N\boldsymbol{\omega}^B + {}^b\mathbf{Z}_3^w \mathbf{J}_w \boldsymbol{\Omega}^W \right) \right) \\
\Rightarrow {}^N\dot{\bar{\boldsymbol{\omega}}}^B \left(\frac{\boldsymbol{\omega}^*}{T^*} \right) &= \mathbf{J}_{s/c}^{-1} \left(\begin{aligned} &-{}^b\mathbf{Z}_3^w \bar{\boldsymbol{\tau}}_w^W (\boldsymbol{\tau}^*) - {}^N\bar{\boldsymbol{\omega}}^B (\boldsymbol{\omega}^*) \times \\ &\left(\mathbf{J}_{s/c} {}^N\bar{\boldsymbol{\omega}}^B (\boldsymbol{\omega}^*) + {}^b\mathbf{Z}_3^w \mathbf{J}_w \bar{\boldsymbol{\Omega}}^W (\boldsymbol{\Omega}^*) \right) \end{aligned} \right) \quad (152) \\
\Rightarrow {}^N\dot{\bar{\boldsymbol{\omega}}}^B &= \mathbf{J}_{s/c}^{-1} \left(-{}^b\mathbf{Z}_3^w \bar{\boldsymbol{\tau}}_w^W \left(\frac{\boldsymbol{\tau}^* T^*}{\boldsymbol{\omega}^*} \right) - {}^N\bar{\boldsymbol{\omega}}^B (T^*) \times \left(\mathbf{J}_{s/c} {}^N\bar{\boldsymbol{\omega}}^B (\boldsymbol{\omega}^*) + {}^b\mathbf{Z}_3^w \mathbf{J}_w \bar{\boldsymbol{\Omega}}^W (\boldsymbol{\Omega}^*) \right) \right)
\end{aligned}$$

2. Scaled Optimal Control Problem

The scaled optimal control problem is

$$\begin{aligned}
\text{Given } \quad \bar{\mathbf{x}} &= \begin{bmatrix} \bar{q}_1 & \bar{q}_2 & \bar{q}_3 & \bar{q}_4 & {}^N\bar{\omega}_x^B & {}^N\bar{\omega}_x^B & {}^N\bar{\omega}_x^B & \bar{\Omega}_1^W & \dots & \bar{\Omega}_n^W \end{bmatrix}^T \\
\bar{\mathbf{u}} &= \begin{bmatrix} \bar{\tau}_1^W & \dots & \bar{\tau}_n^W \end{bmatrix}^T \\
\text{Minimize } \quad \bar{\mathcal{J}}[\bar{\mathbf{x}}(\cdot), \bar{\mathbf{u}}(\cdot), \bar{t}_f] &= \bar{t}_f \\
\text{Subject to } \quad \dot{\bar{q}}_{123} &= \frac{1}{2}(\bar{q}_4 {}^N\bar{\omega}^B - {}^N\bar{\omega}^B \times \bar{q}_{123})(T^* \omega^*) \\
\dot{\bar{q}}_4 &= -\frac{1}{2}({}^N\bar{\omega}^B)^T \bar{q}_{123}(T^* \omega^*) \\
{}^N\dot{\bar{\omega}}^B &= J_{s/c}^{-1} \left(-{}^bZ_3^w \bar{\tau}_w^W \left(\frac{\tau^* T^*}{\omega^*} \right) - {}^N\bar{\omega}^B(T^*) \times (J_{s/c} {}^N\bar{\omega}^B(\omega^*) + {}^bZ_3^w J_w \bar{\Omega}^W(\Omega^*)) \right) \\
\dot{\bar{\Omega}}^W &= J_w^{-1} \bar{\tau}_w^W \left(\frac{\tau^* T^*}{\Omega^*} \right) \\
(\bar{q}_{1_0}, \bar{q}_{2_0}, \bar{q}_{3_0}, \bar{q}_{4_0}, {}^N\bar{\omega}_{x_0}^B, {}^N\bar{\omega}_{y_0}^B, {}^N\bar{\omega}_{z_0}^B, \bar{\Omega}_{1_0}^W, \dots, \bar{\Omega}_{n_0}^W) &= \left(\frac{q_1^0}{q^*}, \frac{q_2^0}{q^*}, \frac{q_3^0}{q^*}, \frac{q_4^0}{q^*}, 0, 0, 0, 0, \dots, 0 \right) \\
(\bar{q}_{1_f}, \bar{q}_{2_f}, \bar{q}_{3_f}, \bar{q}_{4_f}, {}^N\bar{\omega}_{x_f}^B, {}^N\bar{\omega}_{y_f}^B, {}^N\bar{\omega}_{z_f}^B, \bar{\Omega}_{1_f}^W, \dots, \bar{\Omega}_{n_f}^W) &= \left(\frac{q_1^f}{q^*}, \frac{q_2^f}{q^*}, \frac{q_3^f}{q^*}, \frac{q_4^f}{q^*}, 0, 0, 0, 0, \dots, 0 \right) \\
-1 &\leq \bar{\tau}_i^W \leq 1 \\
-1 &\leq \bar{\Omega}_i^W \leq 1
\end{aligned} \tag{153}$$

D. DIDO IMPLEMENTATION

DIDO is a MATLAB-based software package for solving optimal control problems [21]. A huge advantage of DIDO is that the optimal control problem from Equation (153) is the only necessary derivation. Since Pontryagin's Principle, discussed in Section A, is automatically integrated by the DIDO software, further analysis is not required. But, Pontryagin's Principle can be checked to verify the numerical solution. The code simply requires the optimal control problem to be inputted into a series of four functions run from a single m-file.

1. Cost Function

The cost function comes from Appendix A, Equation (275), implemented in Figure 28.

$$\bar{\mathcal{J}}[\bar{\mathbf{x}}(\cdot), \bar{\mathbf{u}}(\cdot), \bar{t}_f] = \bar{t}_f \tag{154}$$


```

% Cost function for the Min Time Slew using RWs
function [endpointCost, runningCost] = MinTimeSlewRWCost(primal)

tf      = primal.nodes(end);

endpointCost = tf;
runningCost  = 0;

```

Figure 28. Cost Function Implemented as a DIDO Function

2. Endpoint Function

The endpoint function contains the boundary conditions from Equations (280) and (281), implemented in Figure 29.

$$\begin{aligned}
 (\bar{q}_{1_0}, \bar{q}_{2_0}, \bar{q}_{3_0}, \bar{q}_{4_0}, {}^N\bar{\omega}_{x_0}^B, {}^N\bar{\omega}_{y_0}^B, {}^N\bar{\omega}_{z_0}^B, \bar{\Omega}_{1_0}^W, \dots, \bar{\Omega}_{n_0}^W) &= \left(\frac{q_1^0}{q_*}, \frac{q_2^0}{q_*}, \frac{q_3^0}{q_*}, \frac{q_4^0}{q_*}, 0, 0, 0, 0, \dots, 0 \right) \\
 (\bar{q}_{1_f}, \bar{q}_{2_f}, \bar{q}_{3_f}, \bar{q}_{4_f}, {}^N\bar{\omega}_{x_f}^B, {}^N\bar{\omega}_{y_f}^B, {}^N\bar{\omega}_{z_f}^B, \bar{\Omega}_{1_f}^W, \dots, \bar{\Omega}_{n_f}^W) &= \left(\frac{q_1^f}{q_*}, \frac{q_2^f}{q_*}, \frac{q_3^f}{q_*}, \frac{q_4^f}{q_*}, 0, 0, 0, 0, \dots, 0 \right)
 \end{aligned} \tag{155}$$

```

% Events function for the Minimum Time Slew using RWs
function endpointFunction = MinTimeSlewRWEndpoint(primal)

global CONSTANTS
Zn      = CONSTANTS.Zn ; % number of RWs

q0 = primal.states(1:3,1) ; qf = primal.states(1:3,end) ;
q40 = primal.states(4,1) ; q4f = primal.states(4,end) ;
w0 = primal.states(5:7,1) ; wf = primal.states(5:7,end) ;
W0 = primal.states(8:7+Zn,1); Wf = primal.states(8:7+Zn,end);

endpointFunction = [q0; q40; w0; W0; qf; q4f; wf; Wf];

```

Figure 29. Endpoint Function Implemented as a DIDO Function

3. Path Function

The path is not necessary for this problem, so no path function script is needed.

4. Dynamics Function

The dynamic equations are from Equations (276) through (279).

$$\begin{aligned}
\dot{\bar{\mathbf{q}}}_{123} &= \frac{1}{2} \left(\bar{q}_4 {}^N \bar{\boldsymbol{\omega}}^B - {}^N \bar{\boldsymbol{\omega}}^B \times \bar{\mathbf{q}}_{123} \right) (T^* \boldsymbol{\omega}^*) \\
\dot{\bar{q}}_4 &= -\frac{1}{2} \left({}^N \bar{\boldsymbol{\omega}}^B \right)^T \bar{\mathbf{q}}_{123} (T^* \boldsymbol{\omega}^*) \\
{}^N \dot{\bar{\boldsymbol{\omega}}}^B &= \mathbf{J}_{s/c}^{-1} \left(-{}^b \mathbf{Z}_3^w \bar{\boldsymbol{\tau}}_w^W \left(\frac{\boldsymbol{\tau}^* T^*}{\boldsymbol{\omega}^*} \right) - {}^N \bar{\boldsymbol{\omega}}^B (T^*) \times \left(\mathbf{J}_{s/c} {}^N \bar{\boldsymbol{\omega}}^B (\boldsymbol{\omega}^*) + {}^b \mathbf{Z}_3^w \mathbf{J}_w \bar{\boldsymbol{\Omega}}^W (\boldsymbol{\Omega}^*) \right) \right) \\
\dot{\bar{\boldsymbol{\Omega}}}^W &= \mathbf{J}_w^{-1} \bar{\boldsymbol{\tau}}_w^W \left(\frac{\boldsymbol{\tau}^* T^*}{\boldsymbol{\Omega}^*} \right)
\end{aligned} \tag{156}$$

Within the dynamics function shown in Figure 30, state scaling occurs at the point of state assignment and is then accounted for in the equations of motion.

```

% Dynamics function for the Minimum Time Slew using RWs
function xdot = MinTimeSlewRWDynamics(primal)

global CONSTANTS
Js = CONSTANTS.Js ;% spacecraft inertia matrix
Jw = CONSTANTS.Jw ;% wheel inertia matrix
Z = CONSTANTS.Z ;% RW orientation
Zn = CONSTANTS.Zn ;% number of RWs

Tauz = CONSTANTS.Tauz ;% torque unit
Wz = CONSTANTS.Wz ;% wheel rate unit
wz = CONSTANTS.wz ;% wheel rate unit
Tz = CONSTANTS.Tz ;% time unit
qz = CONSTANTS.qz ;% quaternion unit

% States and controls
q = primal.states(1:3,:)*qz ;% quaternions 1-3
q4 = primal.states(4,:)*qz ;% quaternion 4
w = primal.states(5:7,:)*wz ;% spacecraft rate
W = primal.states(8:7+Zn,:)*Wz ;% wheel rates
tau = primal.controls*Tauz ;% wheel torques

N = length(q4); %determine size and preallocate matrix sizes
qdot = zeros(4,N); q4dot = zeros(1,N);
wdot = zeros(3,N); Wdot = zeros(Zn,N);

% Equations of Motion:
for i = 1:N

    qdot(:,i) = 1/2*( q4(i)*w(:,i) - cross(w(:,i),q(:,i)) )*Tz/qz ;
    q4dot(:,i) = -1/2*w(:,i)'*q(:,i)*Tz/qz ;

    wdot(:,i) = Js\eye(3)*(-Z*tau(:,i) ...
        -cross(w(:,i),Js*w(:,i)+Z*Jw*W(:,i)) )*Tz/wz;
    Wdot(:,i) = Jw\eye(Zn)*tau(:,i) *Tz/Wz;

end

xdot = [qdot ; q4dot; wdot ; Wdot];

```

Figure 30. Dynamics Function Implemented as a DIDO Function

5. Main Function

With only a few dozen lines of code, the main m-file runs the four functions and DIDO. This is where the *CONSTANTS* are defined. Boundaries are set up for the states, controls, and endpoint conditions (see Figure 31).

```

tfMax = 40                ;[%[sec] upper bound for scaled problem

bounds.lower.time        = [0; 0];
bounds.upper.time        = [0; tfMax];

% Scaled initial conditions
q0 = q_0/qz              ;
w0 = [0;0;0]/wz          ;
W0 = zeros(Zn,1)/Wz      ;
h0 = Jw*W0               ;

% final conditions
qf = q_f/qz              ;
wf = [0;0;0]/qz          ;
Wf = zeros(Zn,1)/Wz      ;

% boundary conditions [ q1-q4      ; wx;wy;wz      ;      W1-Wn      ]
bounds.upper.states = [ones(4,1)/qz; ones(3,1) ; ones(Zn,1)*W_max/Wz];
bounds.lower.states = -bounds.upper.states;

bounds.upper.controls = ones(Zn,1)*tau_max/Tauz;
bounds.lower.controls = -bounds.upper.controls;

bounds.upper.events = [q0; w0; W0; qf; wf; Wf]; %(20x1)
bounds.lower.events = bounds.upper.events;

% Tell DIDO the bounds on the problem
MinTimeSlewRW.bounds = bounds;

```

Figure 31. DIDO Bounds Implemented within a DIDO script

DIDO is initially run with no guess and as little as 20 nodes to determine if a feasible solution will arise (see Figure 32).

```

%% RUN 1 - NO GUESS MADE
% Number of nodes for the spectral algorithm
algorithm.nodes = 20;

[cost, primal, dual] = dido(MinTimeSlewRW, algorithm);

```

Figure 32. DIDO No Guess (20 nodes) Implemented within a DIDO script

The results are then seeded back into DIDO as initial guesses along the entire dynamic range using the following code. This time a much more refined set of 120 nodes is used (see Figure 35)

```

%% RUN 2 - SEED RESULTS OF RUN 1 AS GUESS
algorithm.nodes = 120;
algorithm.guess = primal;

[cost, primal, dual] = dido(MinTimeSlewRW, algorithm);

```

Figure 33. DIDO Seeded Guess (120 nodes) Implemented within a DIDO script

This completes all steps required to run DIDO under both the “no-guess” and “seeded guess” scenarios. The results from run 1 can be looked at as an initial estimate to put DIDO on track.

E. OPTIMAL MANEUVER IMPLEMENTATION

The optimal control solution is fundamentally open loop and the control solution is applied directly to the individual wheels (see Figure 34). Additionally, the optimal quaternion path is presented as a shaped angular trajectory at the forefront of the loop. Since body rates are known, the EQF can follow the rate trajectory instead of being regulated to zero angular velocity. When plant uncertainties or external disturbances exist, the instantaneous quaternion error generates work for the EQF Controller, applying any additional wheel torque as required. With these changes, Figures 2 and 17 become Figures 34 and 35, respectively.

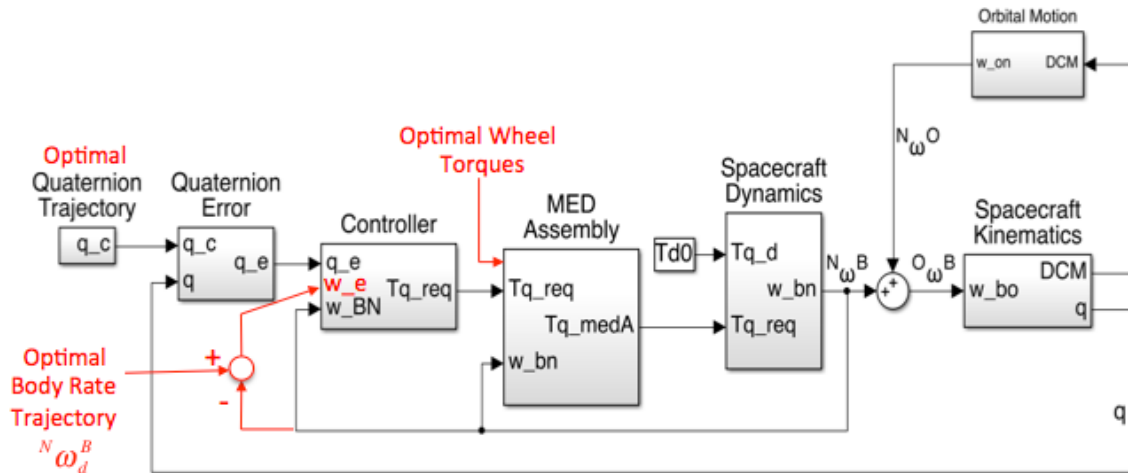


Figure 34. Architecture for Optimal Maneuver Implementation: Spacecraft Model

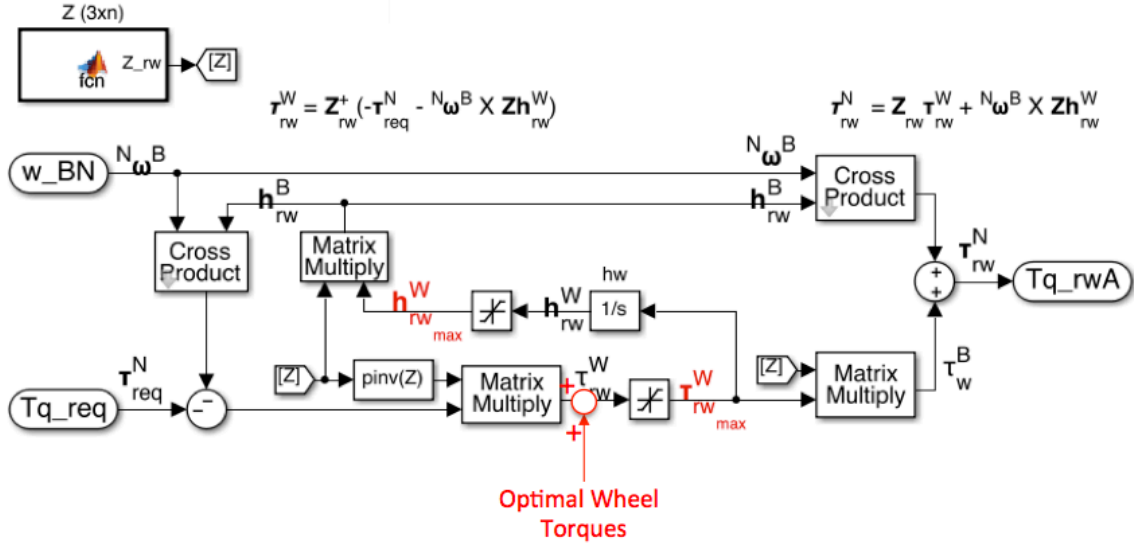


Figure 35. Architecture for Optimal Maneuver Implementation: Reaction Wheel Subsystem

Figure 36 shows the integration of the rate error into the eigenaxis quaternion feedback controller, a slight modification from Equation (28).

$$\tau_{req} = -k J_{s/c} q_{e_{123}} - c J_{s/c} {}^N\omega_e^B + {}^N\omega^B \times J_{s/c} {}^N\omega^B \quad (157)$$

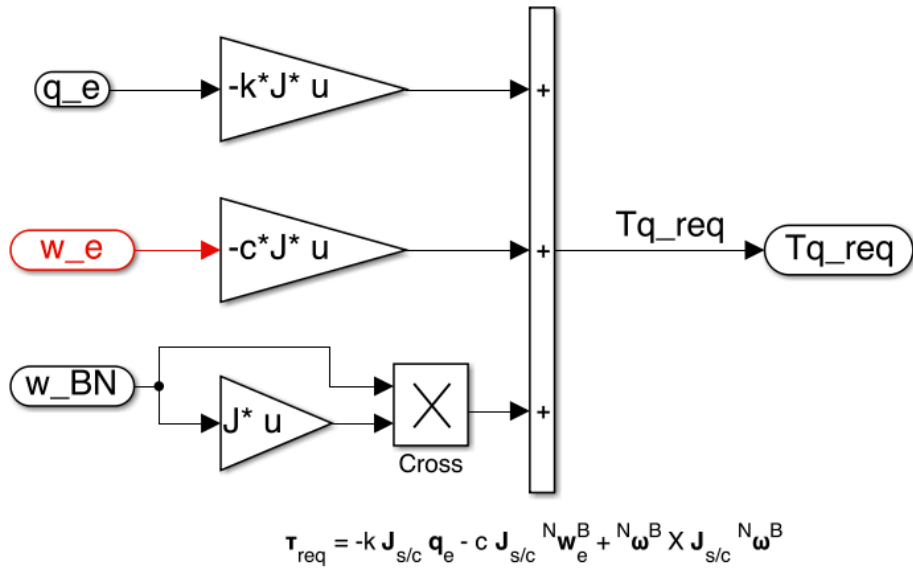


Figure 36. Architecture for Optimal Maneuver Implementation: Eigenaxis Quaternion Feedback Controller

By modifying the control architectures as per Figures 34 to 36, the full reaction wheel array torque and momentum is available for use. If the state quaternions \mathbf{q} feed back disturbances and/or uncertainty error, quaternion error is corrected by creating the quaternion error from the optimal quaternion trajectory. The EQF Controller then creates a torque requirement. Body rate error is propagated through both the EQF controller and wheel dynamics in the form of additional required torque. The total required torque τ_{req}^B is then passed through the pseudo-inverse to sum with the optimal torque $\tau_{w_{opt}}^W$.

$$\tau_w^W = \tau_{w_{opt}}^W + [{}^B Z_3^W]^+ \tau_{req}^B \quad (158)$$

The system will naturally require some correction torque τ_{req}^B , because the spacecraft inertia and external forces (if present) cannot be modeled perfectly. This leads to the requirement for the pseudo-inverse to perform the allocation of the feedback torques. Since the pseudo-inverse uses the minimum least-squares solution for converting body torque into n wheel torques, the feedback provided follows a minimum energy control allocation.

To accommodate the need for feedback, it is necessary to reduce the control authority of the optimal control solution. This is because if the optimal torque solution $\tau_{w_{opt}}^W$ is already utilizing the maximum system torque τ_{max}^W , the system will not have the authority needed to make the feedback corrections. The available control authority for optimal control should be reduced inversely proportional to the knowledge of the system. If the system knowledge is high, then the control authority should be reduced only slightly. For instance, if the system knowledge is high, an optimal control authority of 95% may be appropriate. If the system knowledge is low, an optimal control authority of 75% may be appropriate. Within the optimal control problem formulation presented here, the adjustments would resemble that in Equation (159).

$$-0.95 \tau_{max}^W \leq \tau_i^W \leq 0.95 \tau_{max}^W \quad (159)$$

F. EXAMPLE TIME-OPTIMAL MANEUVER

In this section, the feasibility and optimality of a representative time-optimal example will be documented. As a representative generic spacecraft, the following figures will be used.

$${}^B\mathbf{Z}_3^W = \frac{1}{\sqrt{3}} \begin{bmatrix} \sqrt{2} & 0 & -\sqrt{2} & 0 \\ 0 & \sqrt{2} & 0 & -\sqrt{2} \\ 1 & 1 & 1 & 1 \end{bmatrix}^W \quad (160)$$

$$\mathbf{J}_{s/c} = \begin{bmatrix} 2.54 & 0 & 0 \\ 0 & 2.54 & 0 \\ 0 & 0 & 2.54 \end{bmatrix}^B \text{ kg} \cdot \text{m}^2 \quad (161)$$

$$\tau_{w_i \max} = \pm 8.57 \text{ mN} \cdot \text{m} \quad (162)$$

$$\Omega_{w_i \max} = \pm 3000 \text{ rpm} = \pm 314.2 \text{ rad} / \text{s} \quad (163)$$

$$\mathbf{J}_w = \begin{bmatrix} j_{w_1 \ 33} & 0 & 0 & 0 \\ 0 & j_{w_2 \ 33} & 0 & 0 \\ 0 & 0 & j_{w_3 \ 33} & 0 \\ 0 & 0 & 0 & j_{w_4 \ 33} \end{bmatrix}^W \quad (164)$$

The designer units selected are:

Wheel torque: $\tau^* = \pm 8.57 \text{ mN} \cdot \text{m}$

Time: $T^* = 1 \text{ sec}$

Quaternion: $q^* = 1$ (no further scaling)

S/C Spin Rate: $\omega^* = 3 \text{ deg} / \text{s} = 0.0524 \text{ rad} / \text{s}$

Wheel Rate: $\Omega^* = 314.2 \text{ rad} / \text{s}$

A 120° rest-to-rest slew will be performed about the eigenaxis $\mathbf{e} = \begin{bmatrix} \sqrt{2/3} & 0 & \sqrt{1/3} \end{bmatrix}$, from $\mathbf{q}^0 = \begin{bmatrix} -\sqrt{1/2} & 0 & -1/2 & 1/2 \end{bmatrix}^T$ to the origin $\mathbf{q}^f = \begin{bmatrix} 0 & 0 & 0 & 1 \end{bmatrix}^T$. The boundary conditions are shown in Equation (165).

$$\begin{aligned} & \left(\bar{q}_{1_0}, \bar{q}_{2_0}, \bar{q}_{3_0}, \bar{q}_{4_0}, {}^N\bar{\omega}_{x_0}^B, {}^N\bar{\omega}_{y_0}^B, {}^N\bar{\omega}_{z_0}^B, \bar{\Omega}_{1_0}^W, \bar{\Omega}_{2_0}^W, \bar{\Omega}_{3_0}^W, \bar{\Omega}_{4_0}^W \right) \\ & = \left(-\sqrt{1/2}, 0, -1/2, 1/2, 0, 0, 0, 0, 0, 0, 0, 0 \right) \\ & \left(\bar{q}_{1_f}, \bar{q}_{2_f}, \bar{q}_{3_f}, \bar{q}_{4_f}, {}^N\bar{\omega}_{x_f}^B, {}^N\bar{\omega}_{y_f}^B, {}^N\bar{\omega}_{z_f}^B, \bar{\Omega}_{1_f}^W, \bar{\Omega}_{2_f}^W, \bar{\Omega}_{3_f}^W, \bar{\Omega}_{4_f}^W \right) \\ & = \left(0, 0, 0, 1, 0, 0, 0, 0, 0, 0, 0, 0 \right) \end{aligned} \quad (165)$$

1. Optimal Solution

The time history of the control allocation determined by DIDO is shown in Figure 37. For each of the 120 time nodes, DIDO determined the optimal control solution for each wheel. Linear interpolation was used to determine the feedforward control allocation that would be used for the simulation.

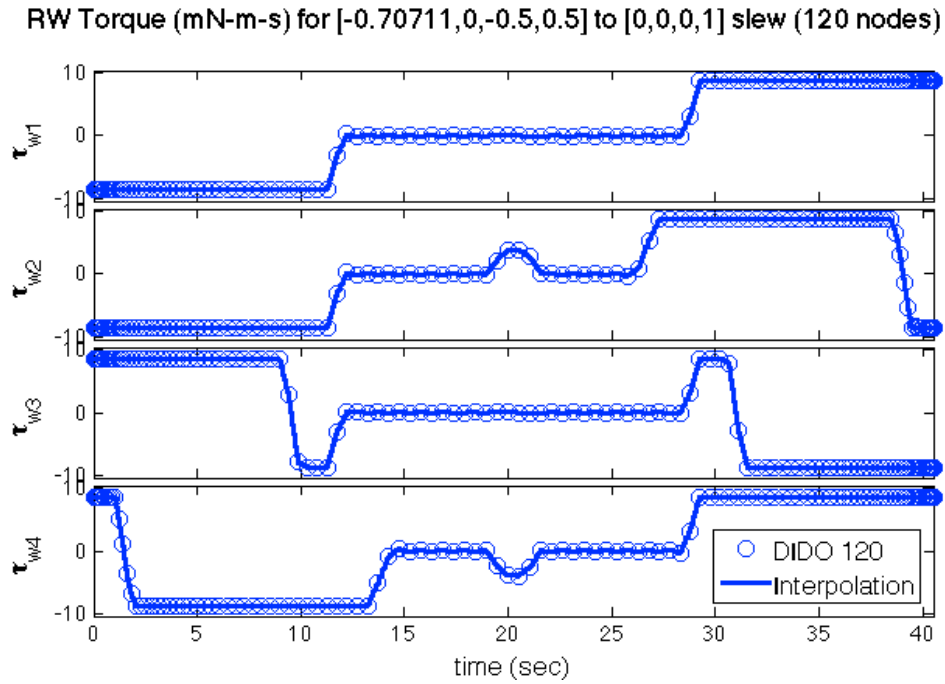


Figure 37. DIDO Control Solution (120 Nodes)

Figure 38 shows the time-optimal quaternion trajectory. The final node exists at $\mathbf{q}_f = \begin{bmatrix} 0 & 0 & 0 & 1 \end{bmatrix}^T$ as expected in the boundary conditions.

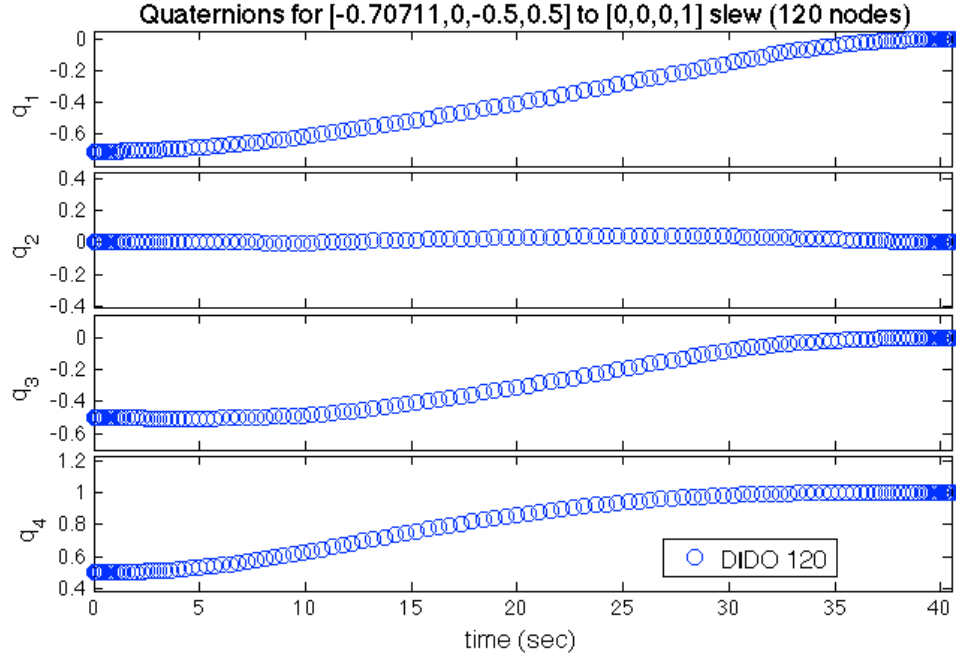


Figure 38. Optimal Quaternion Trajectory (120 Nodes)

Additionally, the final nodes for the angular rates all end at zero per the boundary conditions.

2. Feasibility

A feasible control solution is one that propagates through the system dynamics as expected and satisfies the boundary conditions. The feasibility of both solutions is checked by propagating DIDO's control solution through the system dynamics. First, the state values at each of the individual time nodes must align with the propagation of the dynamics at those specific times. Second, the dynamics must propagate to the appropriate final conditions. If both of these have been satisfied, then it is determined that enough nodes have been used and the solution is indeed feasible.

The interpolated control signal (Figure 37) is propagated through the spacecraft dynamics, modeled within Simulink per Figures 34 to 36. For DIDO propagation, EQF is turned off. The DIDO torque signal is fed into the reaction wheel dynamics for open-loop propagation. Since the knowledge of the spacecraft inertia is considered perfect, the feedback portion will only affect the conventional slew, later used for comparison.

States: Once propagation is complete for the full 120 nodes, the control and states for both runs and their respective control propagations can be plotted together. If the curves for each propagated state pass through its respective DIDO nodes, the DIDO-produced control solution can be deemed feasible.

Figures 39–41 show is a graphical comparison of the initial DIDO solution vs. the dynamically propagated solution from Simulink for all 11 states. By inspection, it appears that every single numerically calculated point is directly on top of its propagated trajectory. This shows that the DIDO solution is not only feasible, but also very accurate.

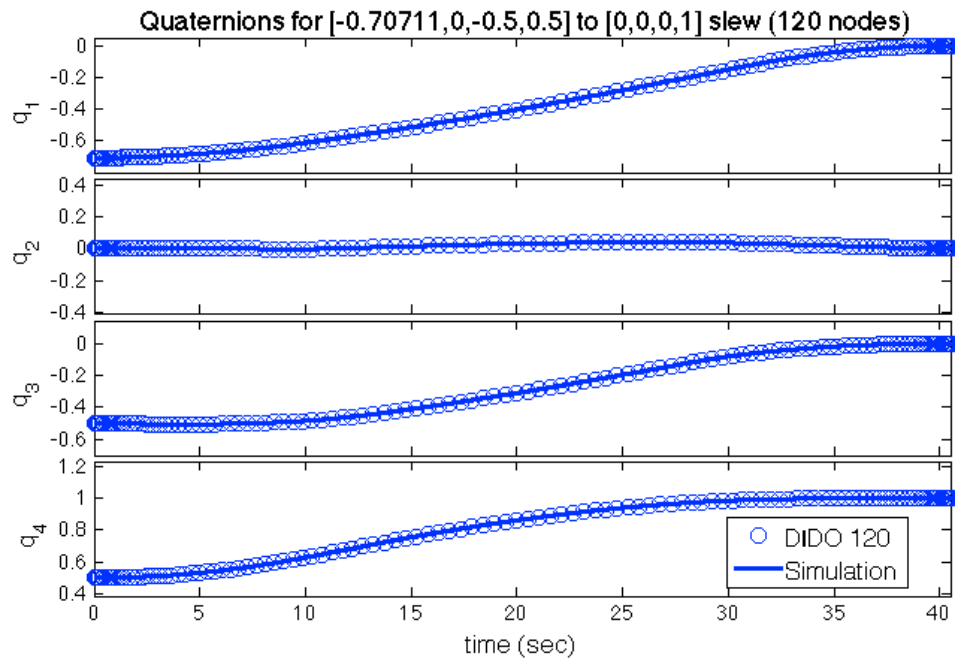


Figure 39. State Quaternion Propagation (120 Nodes)

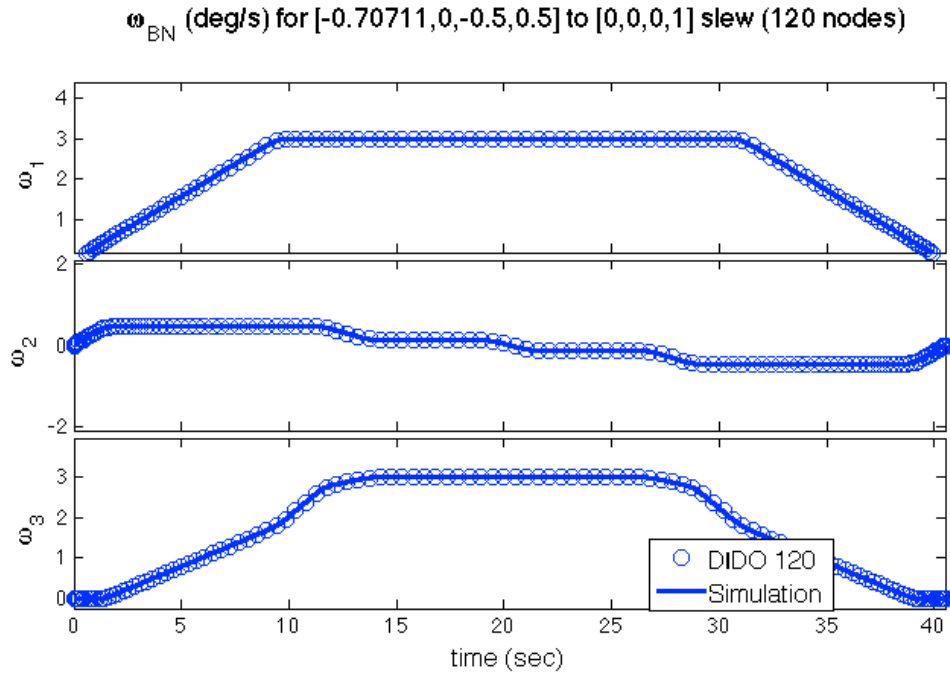


Figure 40. State Spacecraft Body Rate Propagation (120 Nodes)

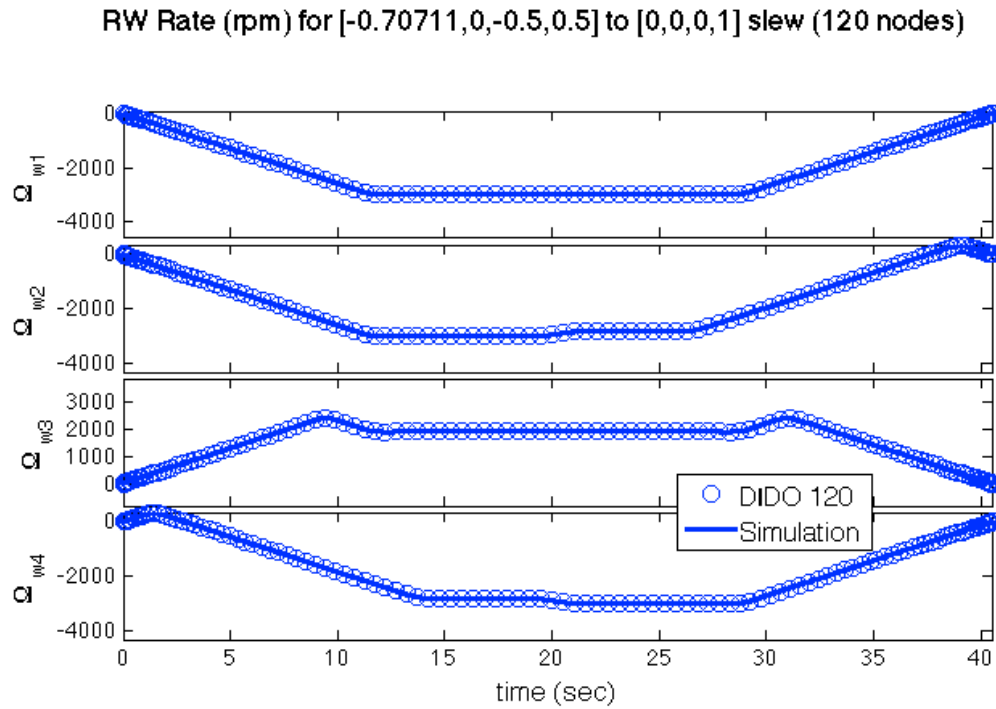


Figure 41. State Reaction Wheel Rate Propagation (120 Nodes)

Scaled States and Costates: Another important check to determine the efficiency of code is the relative magnitude of the scaled states and costates. In Figures 42 and 43, the scaled states and costates $(\bar{x}, \bar{\lambda})$ are represented in the selected designer units prior to their rescaling back into SI units. All states and controls are on the same order of magnitude, which demonstrates good scaling. Only a 1 order of magnitude difference shows up in the costates, which are very sensitive to scaling. The relative comparison shows that reasonable scaling was achieved during problem formulation. If the costates were to differ from each other by 1–2 orders of magnitude, scaling of the time constant T^* or turning the knobs on the state parameters could adjust this. Additionally, a key point to note is that the scaled states only differ from their costates by one to two orders of magnitude. A well-scaled problem will have them roughly the same order of magnitude [21, p. 33], therefore tweaking of the designer units could remedy this.

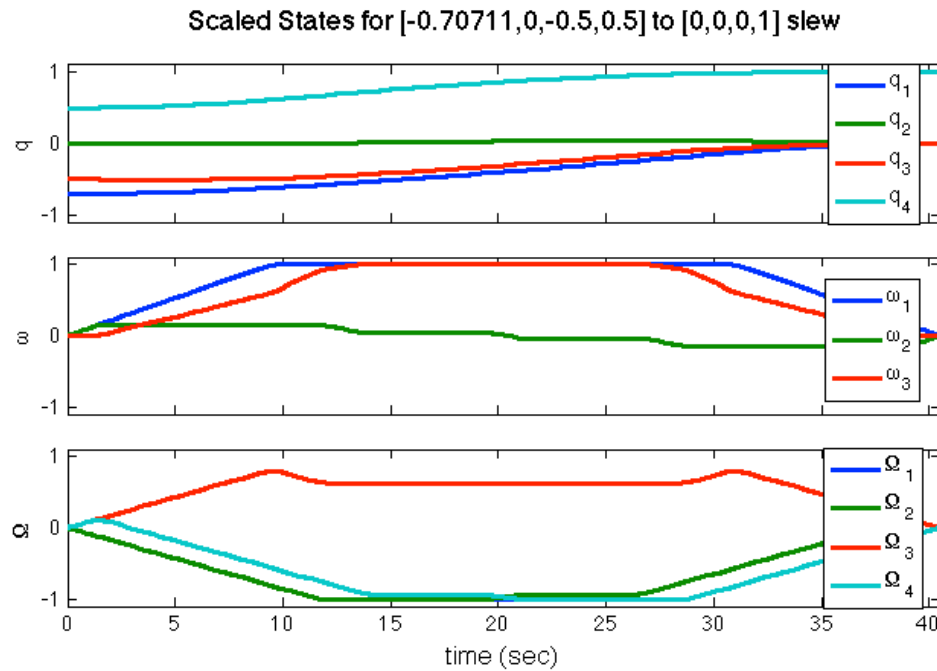


Figure 42. DIDO Scaled States

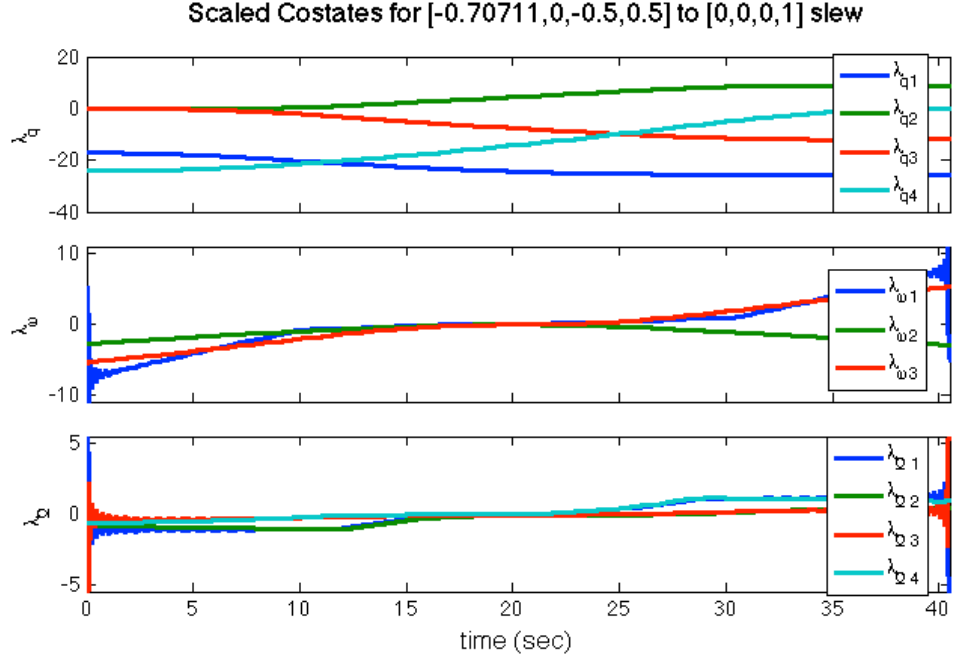


Figure 43. Scaled Costates

3. Optimality

The first place to check for optimality is the Hamiltonian. To ensure the optimal solution is found, the Hamiltonian must be held constant with respect to time. Additionally, the final time is free, so the Hamiltonian Value Condition is necessary, refer back to Equations (124) through (130) from Section A. Similarly, it can be shown that

$$H(t_f) = -\frac{\partial \bar{E}}{\partial t_f} = -1. \quad (166)$$

Equation (166) reveals a key point; for all time-optimal cases, the Hamiltonian is held constant at -1 . Figure 44 is a zoomed-in plot that shows that the time-history of the Hamiltonian on approximately $-1 \pm .007$, which is reasonable.

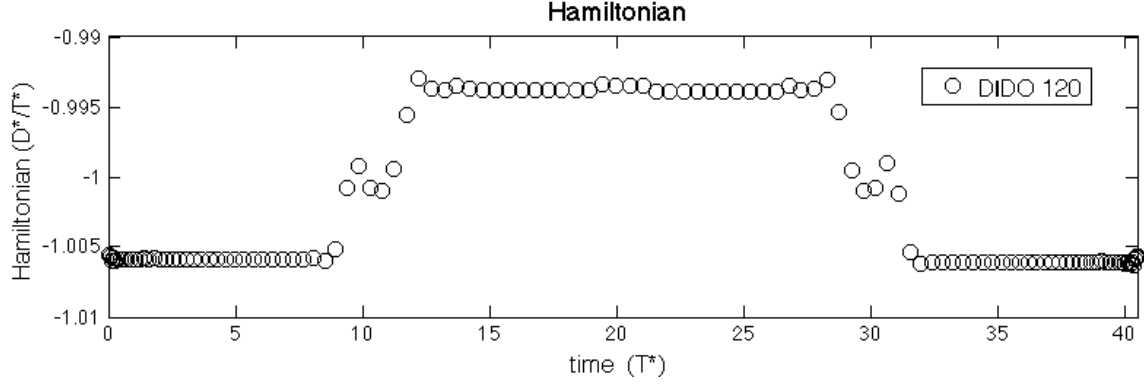


Figure 44. Hamiltonian

Although DIDO does not require inputs from the optimality analysis in Section A to run, this information can help further analyze the optimality of the solution. Pontryagin's switching functions are easily derived. For the four control torques, the switching functions are as follows.

$$\begin{aligned}
 S_1 &= \lambda_{\Omega 1} / j_w - \sqrt{1/3} \lambda_{\omega 3} / j_s - \sqrt{2/3} \lambda_{\omega 1} / j_s \\
 S_2 &= \lambda_{\Omega 2} / j_w - \sqrt{1/3} \lambda_{\omega 3} / j_s - \sqrt{2/3} \lambda_{\omega 2} / j_s \\
 S_3 &= \lambda_{\Omega 3} / j_w - \sqrt{1/3} \lambda_{\omega 3} / j_s - \sqrt{2/3} \lambda_{\omega 1} / j_s \\
 S_4 &= \lambda_{\Omega 4} / j_w - \sqrt{1/3} \lambda_{\omega 3} / j_s + \sqrt{2/3} \lambda_{\omega 2} / j_s
 \end{aligned} \tag{167}$$

where

$$S_i = \frac{\partial H}{\partial \tau_i^w} \tag{168}$$

Per Pontryagin's Principle (refer to Section A), these switching functions represent the slope of the Hamiltonian with respect to the control used. This defines the control space by further determining what control effort should be used at any instant in time. If the slope is negative, i.e., $S_i < 0$, the maximum torque should be used (minimum torque for positive slope). When the slope = 0, the value of the control does not really affect the Hamiltonian. The following switching logic represents the optimal use of the controls.

$$\text{If } S_i \begin{cases} < 0 \\ = 0 \\ > 0 \end{cases}, \text{ then use } \begin{cases} \tau_i = \tau_{max} \\ \tau_{min} < \tau_i < \tau_{max} \\ \tau_i = \tau_{min} \end{cases} \tag{169}$$

Figure 45 shows the dynamics of the reaction wheel assembly alongside the solution for the switching function at each of the 120 nodes. The torque responds very closely to the switching function logic in Equation (169), thereby further validating the optimality of the solution.

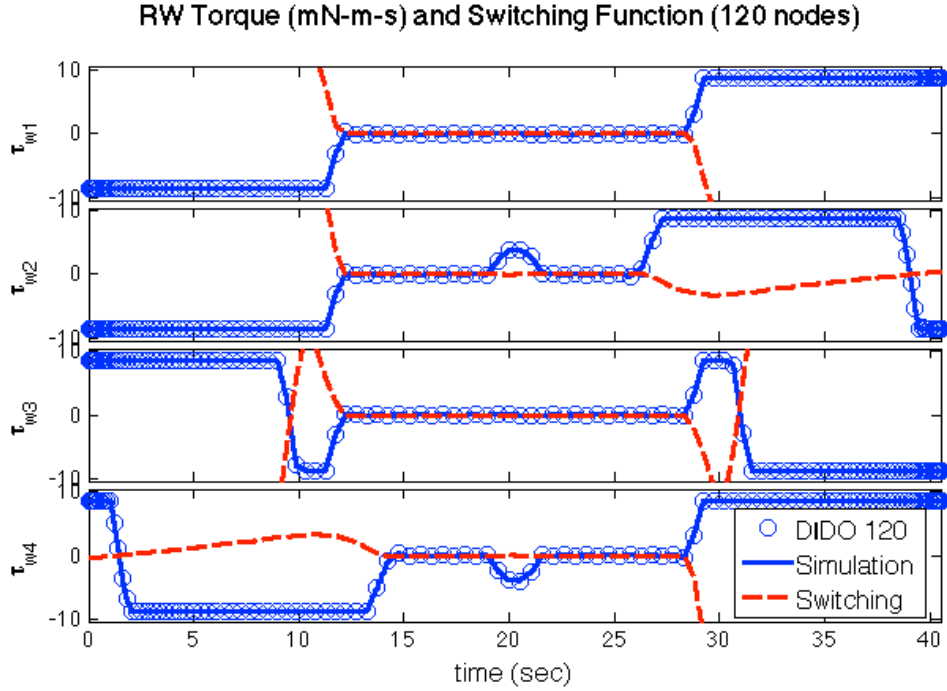


Figure 45. Torque and the Switching Functions

G. EIGENAXIS SLEW COMPARISON

For comparison purposes, the Eigenaxis Quaternion Feedback (EQF) Controller is used to perform a conventional eigenaxis slew maneuver via a shaped bang-coast-bang trajectory. EQF is governed by Equation (170), repeated from Chapter III, Equation (28).

$$\tau_{req} = -k J q_{e_{123}} - c J \omega + {}^N \omega^B \times J_{s/c} {}^N \omega^B \quad (170)$$

For this example, a 0.1 sec settling time was chosen. Recall, the step size is a function of the distance between discrete points used within the shaped quaternion trajectory. Therefore, a small settling time can now be used. The damping ratio was

chosen as 0.9 so that it does not allow for much overshoot. Using these criteria, the gains k and c can be found.

$$\begin{aligned}
 t_{\text{settle}} &= 0.1 \text{ sec} \\
 \zeta &= 0.9 \\
 \omega_n &= 4 / (t_{\text{settle}} \zeta) = 44.4 \\
 k &= \omega_n^2 = 1.97 E^3 \\
 c &= 2 \zeta \omega_n = 80
 \end{aligned} \tag{171}$$

A sanity check can be done by comparing the time-optimal slew against the classic EQF mentioned above. Figure 46 demonstrates the different paths taken by each slew. Notice that q_2 changed for the optimal slew only. Acceleration also occurred faster for the optimal slew. A detailed analysis of how acceleration and momentum are utilized differently occurs within Chapter VII.

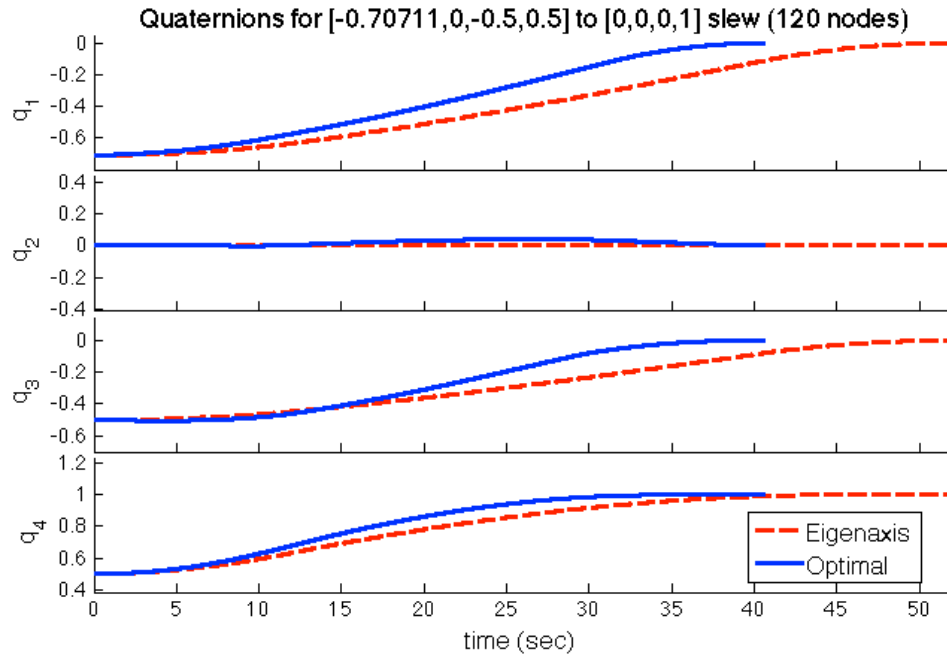


Figure 46. Optimal and Eigenaxis Comparison: Quaternions

Figure 47 represents this comparison with respect to the Euler angles. The DIDO run took only 40.5 seconds, 21.8% faster than the 51.8 second EQF slew. It does not

matter which axis is used, the time-optimal slew will always be just as fast or faster than the eigenaxis slew.

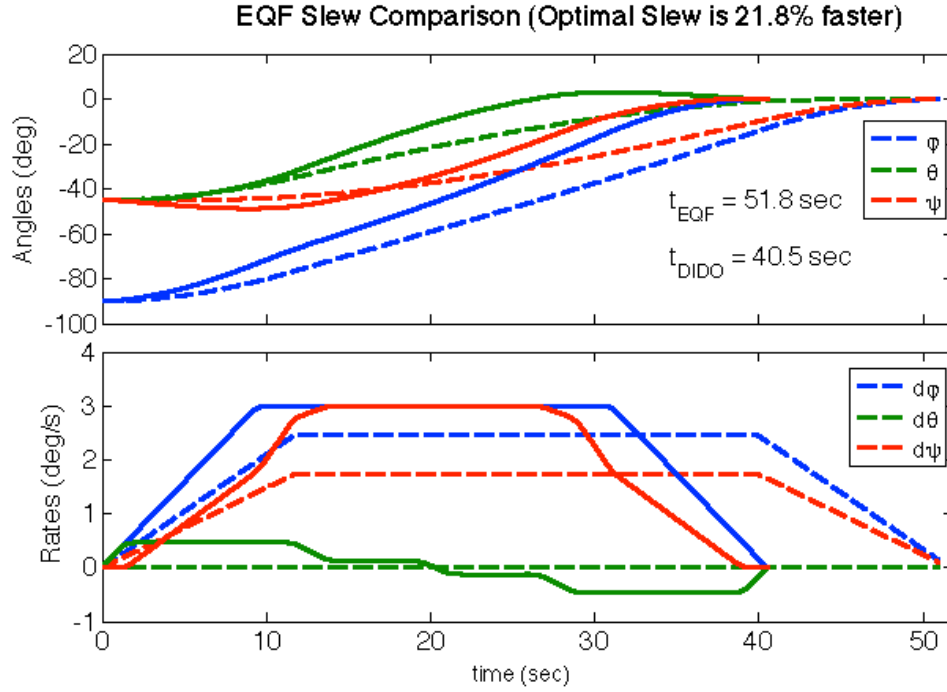


Figure 47. Optimal and Eigenaxis Comparison: Euler Angles and Rates

The optimal maneuver achieved the final boundary conditions much faster for two reasons. It was able to take advantage of off-eigenaxis motion, achieving much greater magnitudes in both torque and momentum. Figure 48 illustrates the additional torque (steeper slope) and momentum (maximum rate). The body rate of the eigenaxis slew confined by the pseudo-inverse was restricted to $3^\circ/\text{s}$. On the other hand, the optimal maneuver could reach momentum and torque outside the pseudo-inverse space, obtaining body rates of up to $4.24^\circ/\text{s}$, a 41.5% increase in maximum rate.

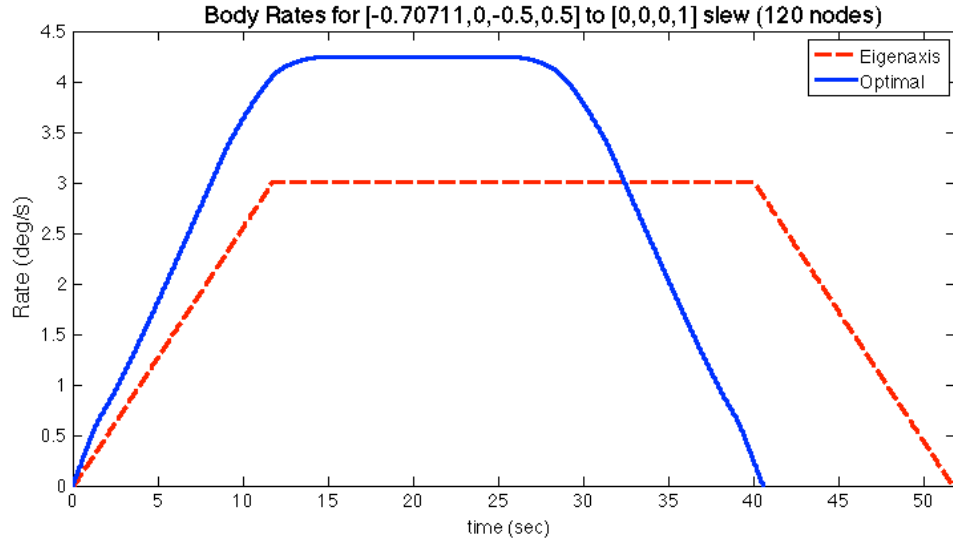


Figure 48. Optimal and Eigenaxis Comparison: Body Rates

Table 2 presents a maneuver-time comparison of a few more 120° slews. Each is moved from the initial quaternion back to the origin $[0,0,0,1]$. As the initial quaternion changed, eigenaxis slew rate increased. This is because the eigenaxis was limited only by the pseudo-inverse-limited octahedron, not the spherical surface (see Figure 24). As the eigenaxis approached a maximum vertex in run 2, the optimal slew only improved the time by 4.2%. Interestingly, the time-optimal maximum body rate was consistently between $4.0\text{--}4.3^\circ/\text{s}$, but this accounts for much off-eigenaxis movement.

q_0	Eigenaxis	Eigenaxis Slew		Optimal Slew		time improvement
		time (sec)	ω_{\max} ($^\circ/\text{s}$)	time (sec)	ω_{\max} ($^\circ/\text{s}$)	
$[-0.707, 0, -0.5, -0.5]$	$[0.8165, 0.0000, 0.5774]$	51.8	3.0	40.5	4.2	21.8%
$[-0.5, -0.5, -0.5, 0.5]$	$[0.5774, 0.5774, 0.5774]$	44.0	3.7	42.1	4.3	4.2%
$[-0.612, -0.433, -0.433, 0.5]$	$[0.7071, 0.5000, 0.5000]$	46.7	3.5	41.5	4.0	11.0%
$[0.612, 0, 0.612, 0.5]$	$[-0.7071, 0.0000, -0.7071]$	51.2	3.1	39.8	4.3	22.3%

Table 2. Optimal vs. Eigenaxis Comparison (120° slews)

H. EFFECTIVE EIGENAXIS OF TIME-OPTIMAL MANEUVER – ANALYTICAL APPROACH

It is important to introduce the concept of *effective eigenaxis*. Given any two quaternions, the optimal slew deviates off-eigenaxis, varying its rotation axis and rate

throughout the maneuver. The effective eigenaxis is defined as the axis of rotation for a minimum angle slew (original eigenaxis from \mathbf{q}_0 to \mathbf{q}_f), regardless of path actually traveled during the maneuver. For example: for Table 2, run 1, the effective eigenaxis of the optimal slew was $[0.8165, 0, 0.5774]$. The actual distance traveled by the time-optimal slew was 123° versus the minimum angle maneuver (120°) about the eigenaxis.

Using this concept, it is possible to determine the relationship between the effective eigenaxis and the effective eigenaxis torque and slew rate about that effective eigenaxis, the motivation for the next two sections. This is necessary to form a general comparison between the two very different maneuvers. The crucial advantage of the optimal maneuver is that it can access all of the dodecahedron momentum space, including that outside of the pseudo-inverse octahedron (Figure 49). This is because the optimal torque trajectories for each wheel are obtained as part of the solution to the optimal control problem. Hence the pseudo-inverse need not be employed (recall control law from Figure 34). This momentum envelope minimum begins at $1.633 h_{\max}$ at the center of the twelve flat faces, expanding to $2.309 h_{\max}$ at the maximum vertices ($1.633 \tau_{\max}$ to $2.309 \tau_{\max}$ in torque space).

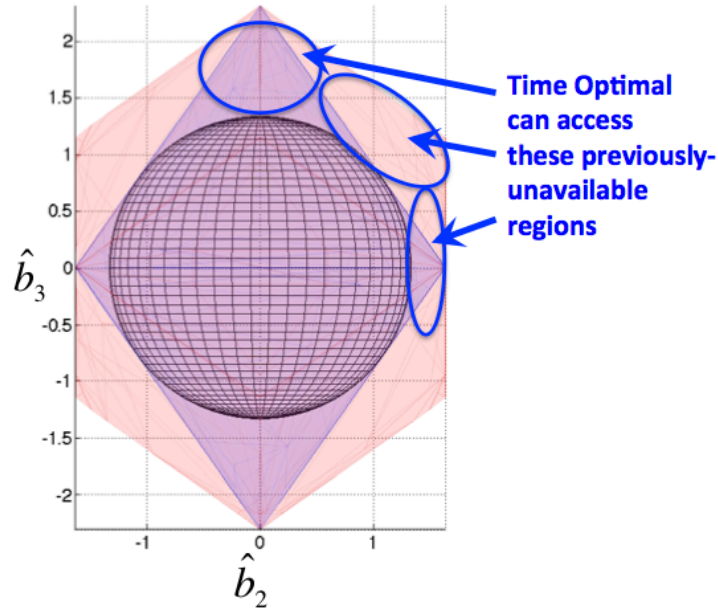


Figure 49. Time-Optimal Accessible Regions

It is difficult to compare a generic optimal maneuver against an eigenaxis slew, primarily because the precise shape of the optimal solution is not intuitive. The optimal maneuver is tailored to maximize performance of an individual maneuver. Thus, a 120° slew about one effective eigenaxis might be far different than a 120° slew about a different effective eigenaxis (see Table 2 for slew time comparison). Looking at Figure 50, the $\begin{bmatrix} 0 & 1 & 0 \end{bmatrix}$ (or \hat{b}_2) axis yields a limit at $1.633 h_{\max} (\tau_{\max})$, while the eigenaxis about $\begin{bmatrix} 0 & 0 & 1 \end{bmatrix}$ (or \hat{b}_3) yields $2.309 h_{\max} (\tau_{\max})$. This means that the rotation about the \hat{b}_3 axis can potentially accelerate and traverse 41% faster than a rotation about \hat{b}_2 .

Here, the effective eigenaxis momentum will be derived from the average eigenaxis momentum over 4π steradians. The first step will be to calculate the average amplitude of momentum or torque available about every possible eigenaxis. The average amplitude of a series of any set can be determined by the sum of the set divided by the number of entries in the set. Therefore, the average of magnitude of n (100, 1000, 1M) eigenaxis momentum vectors is the quotient of the sum and n .

$$h_{avg} = \frac{\sum_{i=1}^n h_i}{n} \quad (172)$$

If h_{avg} was placed back into 3D space along the same n eigenvectors, the shape would now be a sphere of radius h_{avg} . Consider each vector to have some volume associated with it. Since the total length of the sum is conserved, the sphere would have the same volume as the original dodecahedron.

This approach will be followed in reverse in order to attain h_{avg} , the radius of the sphere. Using MATLAB's *convhull* command, the volume of a shape is calculated as a subset of its three-dimensional points. Using this command, the volume of the dodecahedron is calculated as $\pi 4.632 h_{\max}^3$. A simple spherical relationship yields the radius of the sphere.

$$h_{avg} = \sqrt[3]{\frac{3}{4\pi} 24.632 h_{\max}^3} = 1.805 h_{\max} \quad (173)$$

Now, the equivalent spherical radius of the reaction wheel momentum (or torque) envelope is 1.805. The shape is shown in Figure 50.

$$\begin{aligned} h_{opt-sphere} &= 1.805 h_{\max} \\ \tau_{opt-sphere} &= 1.805 \tau_{\max} \end{aligned} \quad (174)$$

Since the sphere is not inscribed within the dodecahedron, it would appear that some torque/momentum described by the sphere is not available. This may not be the case though as the sphere simply represents the effective torque/momentum about the effective eigenaxis. Since the trajectory is allowed to deviate from the effective eigenaxis, the torque/momentum space at the vertices is exploited to raise the effective acceleration/rate limits outside the boundaries of the torque/momentum envelope.

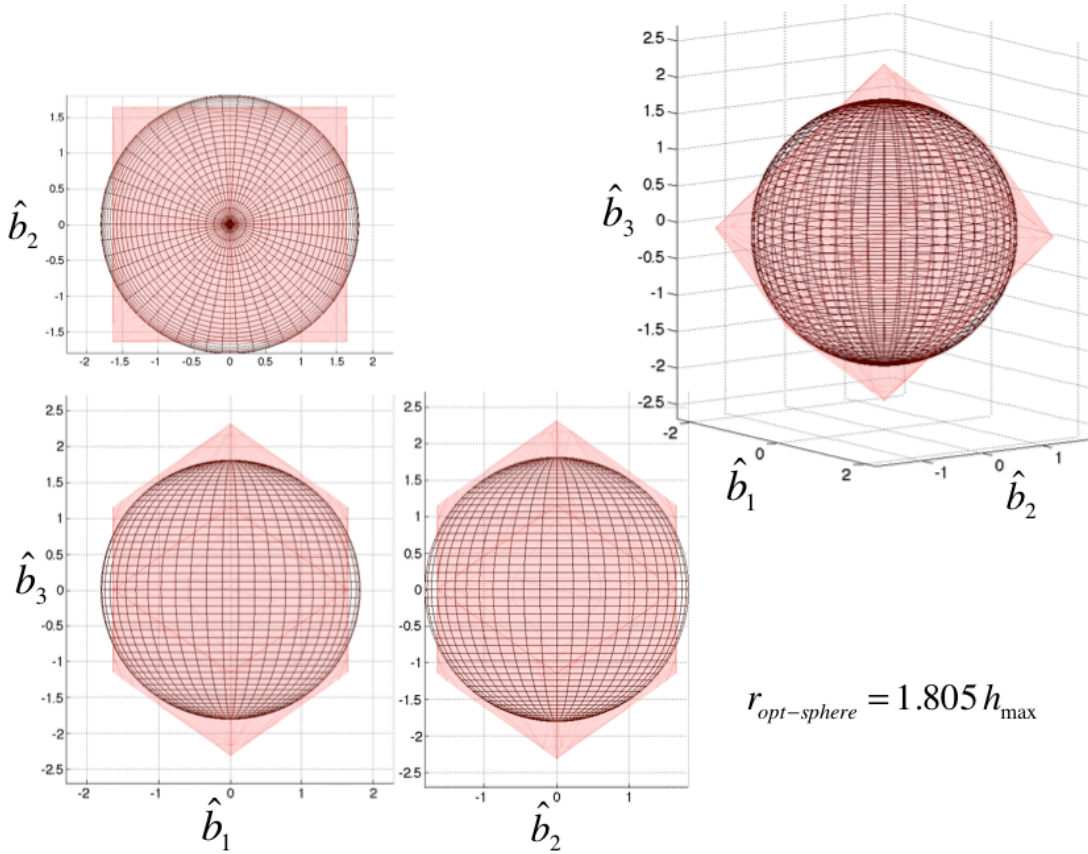


Figure 50. Reaction Wheel Effective Eigenaxis Sphere for Time-Optimal Maneuvers

Consider the optimal trajectory using only eigenaxis slews, but has access to the entire momentum space. The average slew rate (or acceleration) derives directly from the newly-created optimal momentum sphere with values per (174). Since both torque and momentum limitations are assumed, the average time for any given slew angle can be predicted using the simple trapezoidal trajectory: bang-bang (from Figure 26) or bang-coast-bang (from Figure 27), depending on whether the momentum limit is reached. The same spacecraft/wheel configuration from Section G will be used for comparison. Over the slew regime extending to 180° , the curve shown in Figure 51 is developed.

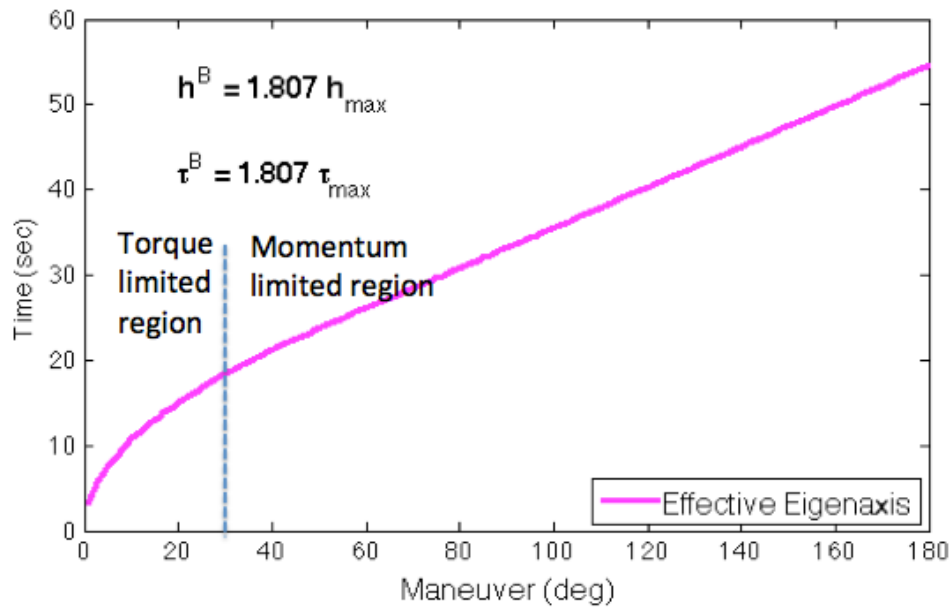


Figure 51. Reaction Wheel Effective Eigenaxis for Time-Optimal Maneuver – Analytical ($j_s=25.4 \text{ kg-m}^2$)

The curve at the beginning indicates a torque limited region. For slew angles of 30° or less, the reaction wheel array does not have the torque to reach its full momentum. Therefore, the maneuver is bang-bang. It will be in maximum torque mode (edge of the torque sphere, 0.1805 Nm), then reverse maximum torque to slow down without ever reaching the edge of the momentum envelope. For slews greater than 30° , the maximum momentum is reached and the system theoretically coasts at a constant rate (proportional to 1.805 Nms) for a portion of the maneuver.

In this section, the concept of effective eigenaxis was used as a baseline to compare the full spectrum of possible optimal maneuvers against the predictability of shaped eigenaxis slews. The relationship between effective eigenaxis torque/momentum for optimal maneuvers was developed. For the optimal maneuver, an effective momentum of $1.805 h_{\max}$ and torque of $1.805 \tau_{\max}$ can be used to represent the potential of the time-optimal maneuvers over 4π steradians. Additional comparisons will be carried out in Chapter VII.

I. EFFECTIVE EIGENAXIS OF TIME-OPTIMAL MANEUVER – NUMERICAL VERIFICATION OF ANALYTICAL APPROACH

The analytical approach from Section H must be validated. To gather sample data, 100 optimal simulations were completed using the spacecraft/wheel configuration from Section G. The only dependent variable used was the beginning attitude. A random quaternion was generated for each trial, and the system slewed to the origin.

$$\begin{aligned} \mathbf{q}_0 &= 2(\text{rand}(4,1) - 0.5) \\ \mathbf{q}_f &= \begin{bmatrix} 0 & 0 & 0 & 1 \end{bmatrix}^T \end{aligned} \tag{175}$$

This allows a random sampling of slew angles and eigenaxes. The sample data is plotted alongside the analytical curve, shown in Figure 52.

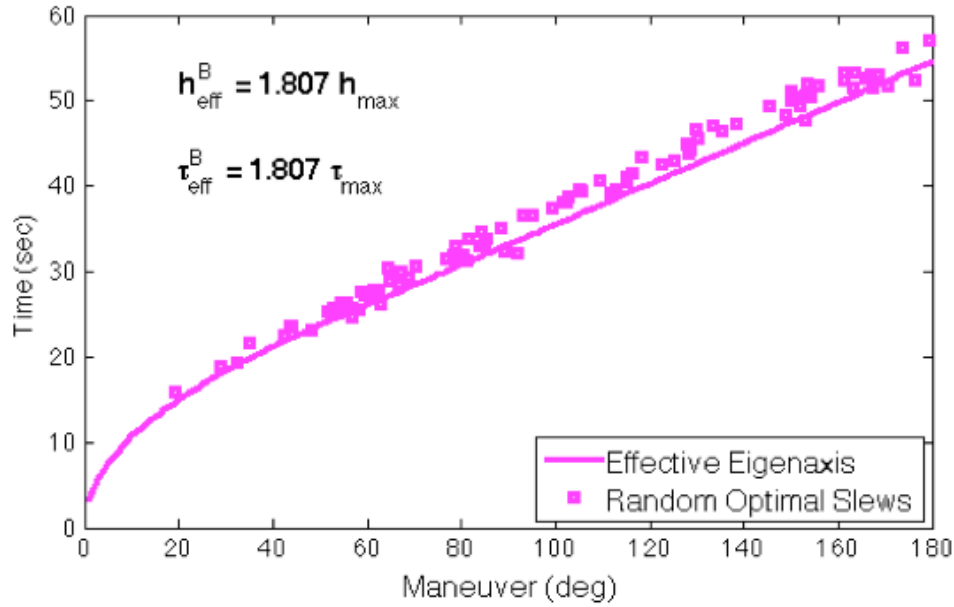


Figure 52. Reaction Wheel Effective Eigenaxis for Time-Optimal Maneuver – Numerical Approach with $1.807 \tau_{\text{max}}$ ($j_s=25.4 \text{ kg-m}^2$)

The majority of the sample data lies above the curve, demonstrating that the approach taken in Section H might be too aggressive. The slope of the momentum-limited region seems correct, but the intercept with the torque-limited region is too early. Therefore, the effective torque bound must be reduced. Several values for the effective torque are shown in Figure 53.

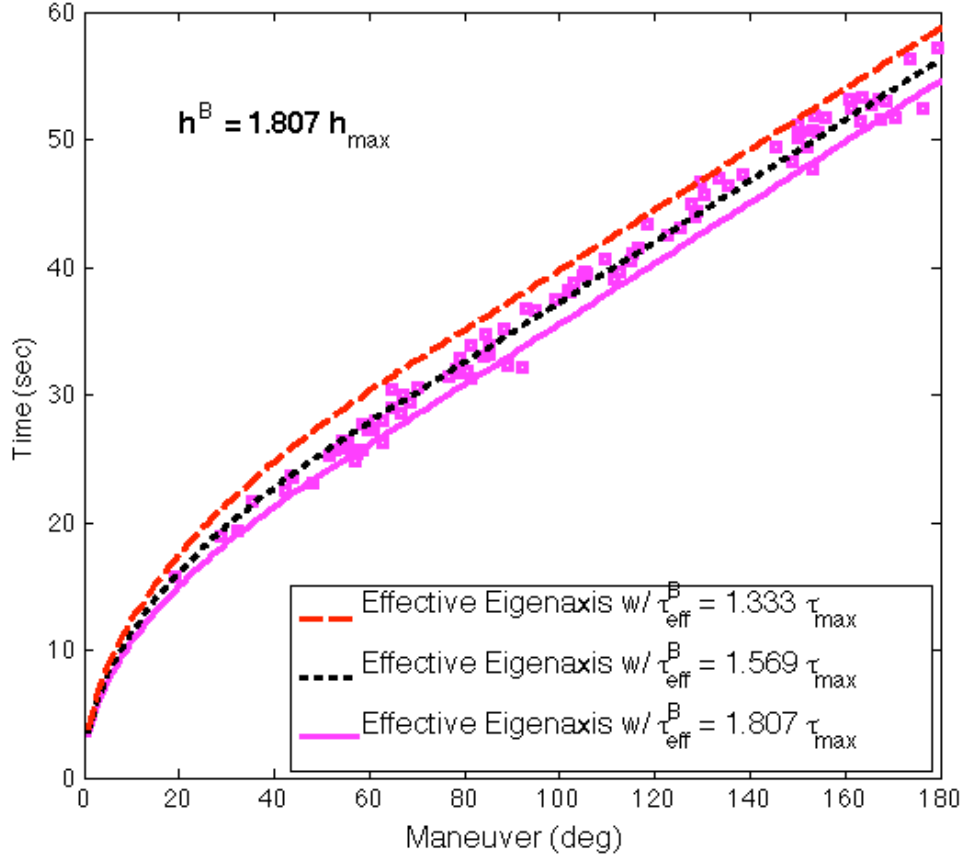


Figure 53. Reaction Wheel Effective Eigenaxis for Time-Optimal Maneuver – Numerical Approach with $[1.333, 1.569, 1.807] \tau_{\max}$ ($j_s = 25.4 \text{ kg-m}^2$)

The sample data points in Figure 53 are seen to lie below the $1.333\tau_{\max}$ curve, demonstrating that the spherical system devised during the analytical approach made an achievable configuration. Since the actual optimal runs were faster than the curve fit, it shows that the spherical approach using the reduced value of τ_{eff}^B tends to give a slightly conservative estimate of the true performance of time-optimal solutions. This demonstrates that the maneuver times obtained by assuming a trapezoidal input via an effective eigenaxis slew is achievable via optimal control all the time. This allows the spherical shape with momentum/torque radii equal to 1.805/1.333 of the individual wheel momentum/torque maximum to be used in later in this thesis to facilitate comparison. This 35% increase in momentum over 4π steradians is significant.

$$\frac{h_{opt_{avg}}^B}{h_{rw_{avg}}^B} = \frac{1.805 h_{max}}{1.333 h_{max}} = 1.354 \quad (176)$$

In Chapter VII, it will additionally be shown how the optimal maneuver maximizes the use of the momentum/torque envelope to achieve better-than-eigenaxis performance.

J. EFFECTIVE EIGENAXIS OF PSEUDO-INVERSE LIMITED TIME-OPTIMAL MANEUVER

If adding optimal torque signals directly to the individual wheels is out of the question, then the system can still be optimized for trajectory shaping by using a slight variation from the time-optimal logic used in Figures 34–36. The system must still employ the pseudo-inverse within the reaction wheel dynamics, but performance can be improved within this space. Figure 54 illustrates the pseudo-inverse limited optimal shaped trajectory being used in the spacecraft model.

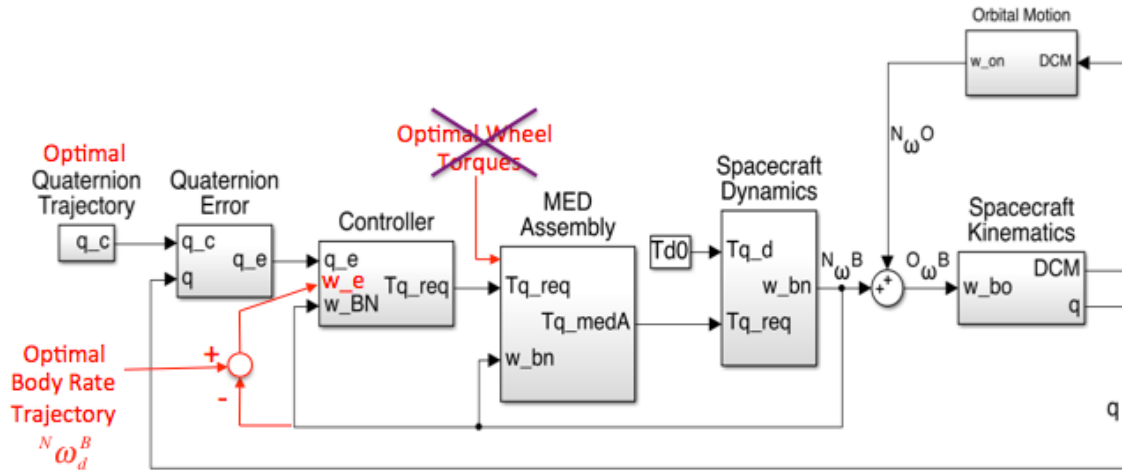


Figure 54. Pseudo-Inverse Limited Time-Optimal Spacecraft Model

The accessible gains are highlighted in Figure 55. Granted, the blue regions are accessible without the use of optimal control, but not about every eigenaxis. This section demonstrates how optimal control can be exploited for equal gain over 4π steradians.

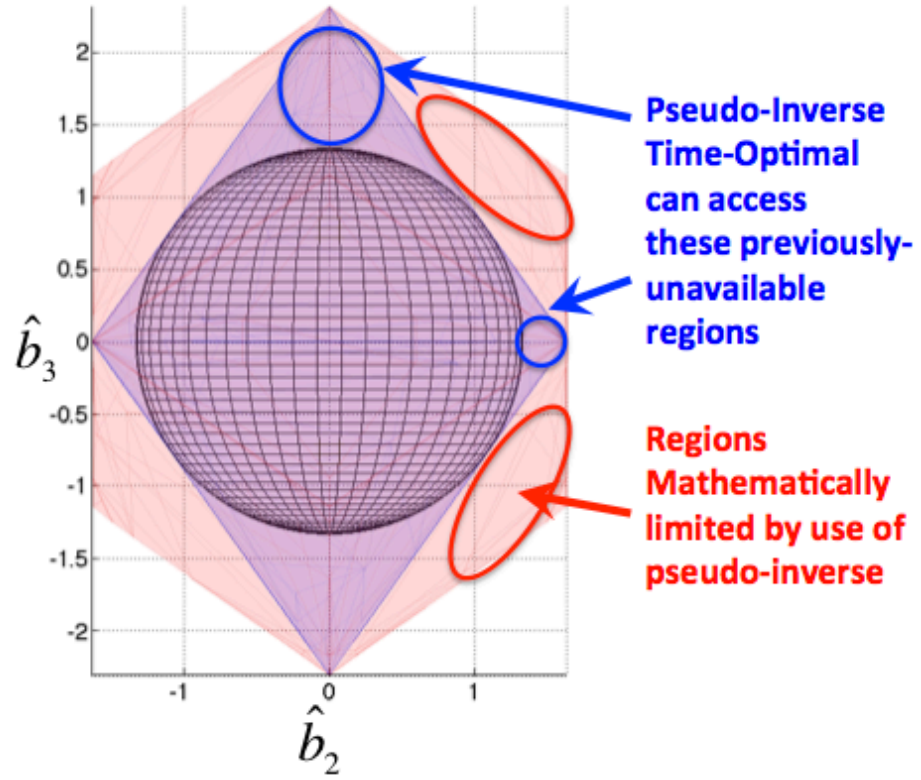


Figure 55. Pseudo-Inverse Limited Time-Optimal Accessible Regions

In the same fashion as analytically extracted for the time-optimal in Sections H and I, the analytical and numerical approach can be completed for the pseudo-inverse limited time-optimal maneuvers. It can be shown that the pseudo-inverse limited time-optimal space can be achieved by using maximum magnitudes of 1.577/1.333 of the individual wheel momentum/torque maximums.

$$\begin{aligned} h_{pseopt-sphere} &= 1.577 h_{\max} \\ \tau_{pseopt-sphere} &= 1.333 \tau_{\max} \end{aligned} \quad (177)$$

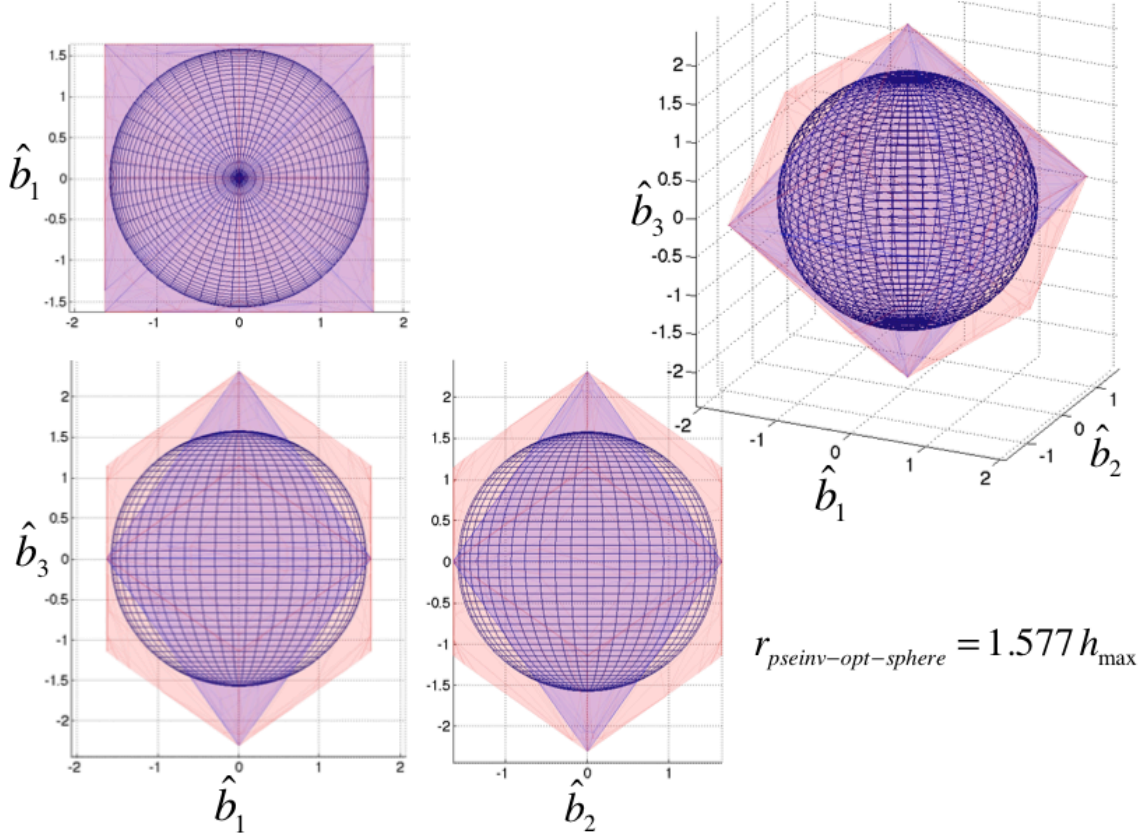


Figure 56. Pseudo-Inverse Limited Time-Optimal Momentum Sphere

By shaping the trajectory using pseudo-optimal inputs rather than the standard trapezoidal input, 18% increases in speed and acceleration can be achieved.

$$\frac{h_{pseopt_{avg}}^B}{h_{rw_{avg}}^B} = \frac{1.577 h_{\max}}{1.333 h_{\max}} = 1.183 \quad (178)$$

K. SUMMARY

This chapter was used to develop and analyze the time-optimal slews. First, the time-optimal slew for the eigenaxis-restricted case was demonstrated as a bang-bang, or as a bang-coast-bang maneuver when momentum-limited. Next, the eigenaxis was abandoned and the time-optimal reorientation was developed and implemented in DIDO. Slew time improved over the trapezoidal input by up to 22% for 120° slews. This optimal control approach allowed the limitations of the pseudo-inverse to be avoided, increasing

the available momentum and torque envelope. Next, the effective eigenaxis concept was introduced, which allowed a comparison between the eigenaxis reorientation and the time-optimal slew. The effective eigenaxis was further developed to show how, on average, the available momentum and torque for the time-optimal case are $1.805 h_{\max}$ and $1.333 \tau_{\max}$ about the effective eigenaxis. For the pseudo-inverse-limited time-optimal case, they are $1.577 h_{\max}$ and $1.333 \tau_{\max}$, respectively.

THIS PAGE INTENTIONALLY LEFT BLANK

VI. CONTROL MOMENT GYROSCOPES

Like reaction wheels, CMGs also have their physical limitations. They have maximum angular rates and accelerations that must be modeled. This ensures that only the maximum individual CMG torques can be applied, regardless of demanded torque. In order to appropriately apply limitations, a model of the CMGs must be created. This chapter is a focus on single gimbal control moment gyroscopes (SGCMGs). Dual gimbal and variable speed CMGs will not be discussed. The following introduction is simplistic regarding SGCMGs, but representative of the key interactions. The rest of this chapter will be used to derive these terms and show the interaction with the spacecraft body.

At the center of a CMG is a large momentum wheel, driven by its own wheel motor at a nominally constant speed. The basic concept of a CMG is for a wheel to spin freely within a secondary gimbal frame. The gimbal frame is rotated within the body frame by a gimbal motor. The change in the direction of the wheel angular momentum as a result of gimbal motion causes a large torque orthogonal to the gimbal and angular momentum axes, i.e. $\hat{\tau} = \hat{\delta} \times \hat{h}$. Since a relatively small gimbal torque input can become a much larger output torque, this concept is known as “torque multiplication” [27, p. 1] or “torque amplification” [28, p. 160].

A basic model of a CMG is shown in Figure 57. At the center of the CMG is a momentum wheel shown in the wheel frame \hat{W} . The \hat{w}_1 and \hat{w}_2 axes are fixed to the wheel and rotate in the gimbal frame as a function of the constant wheel rate Ω and time. It is important to note that the spin axis of the wheel frame is aligned with the gimbal frame, such that

$${}^G\boldsymbol{\omega}^W = \Omega\hat{w}_3 = \Omega\hat{g}_1. \quad (179)$$

The wheel motor is attached to the gimbal frame and drives rotation of the wheel. The wheel is spun at a constant rate; therefore, the simple rotation of the wheel alone does not cause a torque transfer between the wheel and gimbal frames.

$$\boldsymbol{\tau}_w^G = J_w\dot{\Omega}\hat{g}_3 = 0 \quad (180)$$

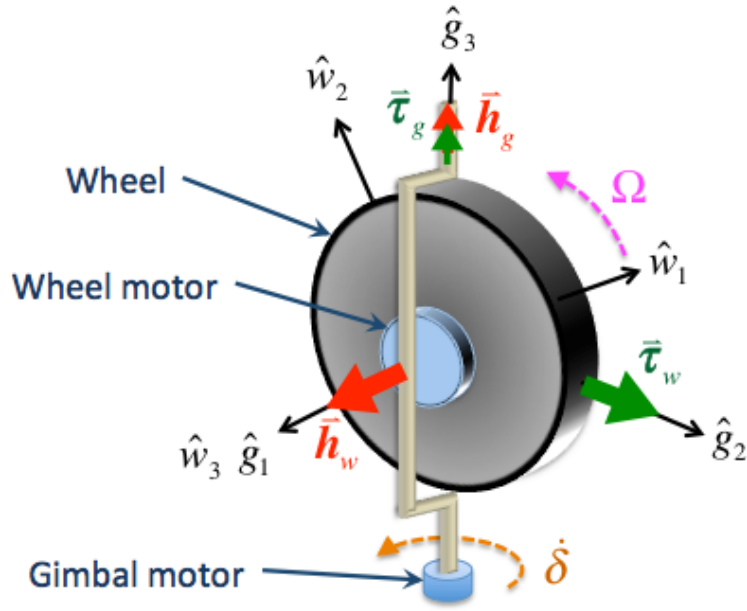


Figure 57. CMG Schematic

Figure 57 shows the small gimbal momentum and torques as small red and green arrows, respectively. The large wheel momentum and large resultant orthogonal torque are shown in with larger arrows. All of these momentums and torques can be labeled relative to the gimbal frame. For simplicity, gyroscopic coupling terms are not shown on the diagram.

$$\begin{aligned} \vec{h}_w &= h_w \hat{g}_1 \\ \vec{\tau}_w &= \tau_w \hat{g}_2 \end{aligned} \tag{181}$$

$$\begin{aligned} \vec{h}_g &= h_g \hat{g}_3 \\ \vec{\tau}_g &= \tau_g \hat{g}_3 \end{aligned} \tag{182}$$

Consider the spacecraft body frame aligned with the gimbal frame shown in Figure 57. Since the gimbal frame is allowed to rotate within the body frame, the following set of time derivatives with respect to the body frame are important to note. They will be used in the chapter's derivations.

$$\begin{aligned}
\frac{{}^B d}{dt}(\hat{g}_1) &= \dot{\delta} \hat{g}_2 \\
\frac{{}^B d}{dt}(\hat{g}_2) &= -\dot{\delta} \hat{g}_1 \\
\frac{{}^B d}{dt}(\hat{g}_3) &= 0
\end{aligned} \tag{183}$$

A. ORIENTATION

The description of the orientation of a CMG will be carried out much like that of the orientation of reaction wheels in Chapter IV. To avoid redundancy, some portions of the explanation will be condensed.

The fundamental formula for the angular momentum gimbal to body change of basis is given as

$$\mathbf{h}_i^B = [{}^B \mathbf{R}^{G_i}] \mathbf{h}_i^{G_i} \tag{184}$$

The dyadic form of this projection onto the body frame is

$$\mathbf{h}_i^B = [\hat{\mathbf{b}} \hat{\mathbf{g}}_i^T] \mathbf{h}_i^{G_i} = \begin{bmatrix} \hat{b}_1 \bullet \hat{g}_{i_1} & \hat{b}_1 \bullet \hat{g}_{i_2} & \hat{b}_1 \bullet \hat{g}_{i_3} \\ \hat{b}_2 \bullet \hat{g}_{i_1} & \hat{b}_2 \bullet \hat{g}_{i_2} & \hat{b}_2 \bullet \hat{g}_{i_3} \\ \hat{b}_3 \bullet \hat{g}_{i_1} & \hat{b}_3 \bullet \hat{g}_{i_2} & \hat{b}_3 \bullet \hat{g}_{i_3} \end{bmatrix}^{G_i} \mathbf{h}_i^{G_i} \tag{185}$$

The orientation will be placed in the \hat{B} frame, converting to the \hat{G}_i frame via ${}^{G_i} \mathbf{R}^B$, and then using the transpose ${}^B \mathbf{R}^{G_i}$ to convert back. In the example shown in Figure 58a, the MED is placed directly on the \hat{B} xyz origin, rotating about the \hat{b}_1 axis and gimbaling around the \hat{b}_3 axis per Figure 58b. This produces an angular momentum \mathbf{h}_w^B directly in the \hat{b}_1 direction for the wheel.

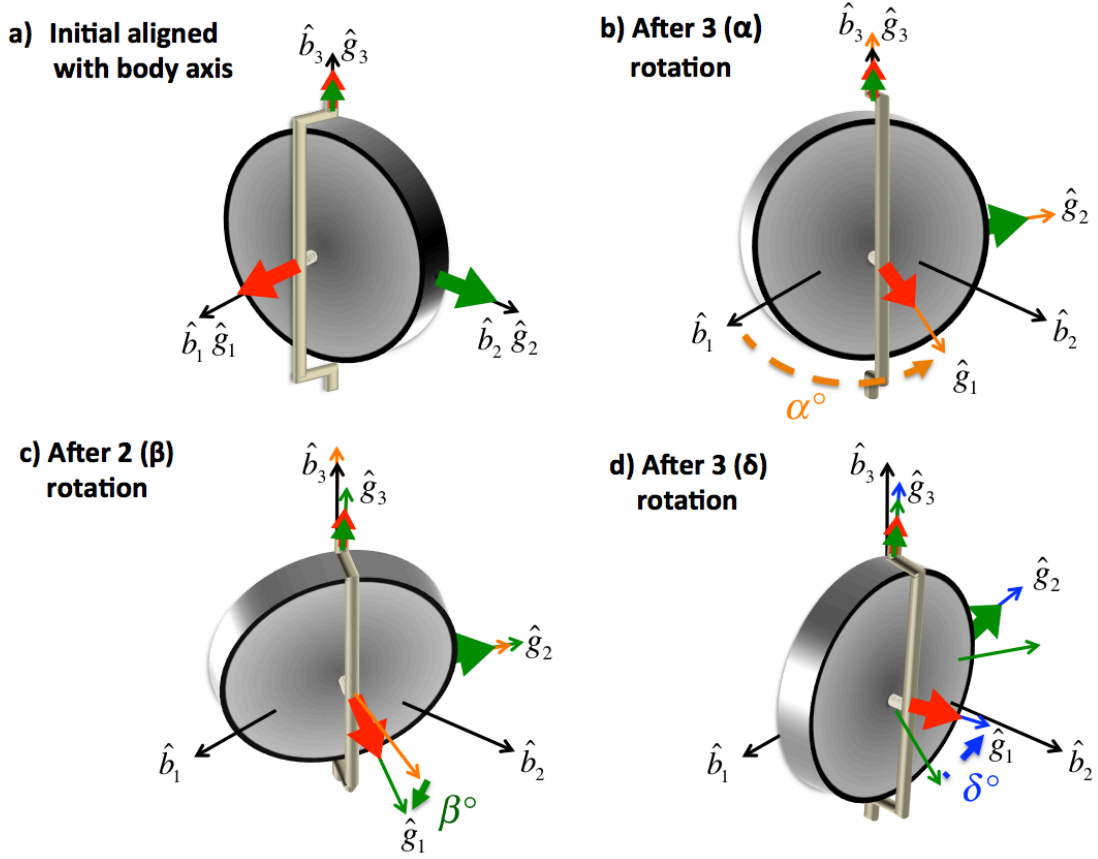


Figure 58. CMG Transformation

The first two orientation transformations are exactly like those for the reaction wheel. A fundamental 3 rotation about the share \hat{b}_3 / \hat{g}_3 axis is completed.

$$\mathbf{R}_3(\alpha_i) = \begin{pmatrix} \cos \alpha_i & \sin \alpha_i & 0 \\ -\sin \alpha_i & \cos \alpha_i & 0 \\ 0 & 0 & 1 \end{pmatrix} \quad (186)$$

A 2 rotation is now completed about the \hat{g}_2 axis (Figure 58c) to create the orientation skew angle β .

$$\mathbf{R}_2(\beta) = \begin{pmatrix} \cos \beta & 0 & -\sin \beta \\ 0 & 1 & 0 \\ \sin \beta & 0 & \cos \beta \end{pmatrix} \quad (187)$$

The distinct difference between reaction wheels and CMGs occurs in the third, gimbal rotation. This is where CMGs derive most of their advantage. The final rotation is a 3 rotation by angle δ about the new \hat{g}_3 axis (Figure 58d). For reaction wheels, it is assumed that $\delta = 0$.

$$\mathbf{R}_3(\delta_i) = \begin{pmatrix} \cos \delta_i & \sin \delta_i & 0 \\ -\sin \delta_i & \cos \delta_i & 0 \\ 0 & 0 & 1 \end{pmatrix} \quad (188)$$

The previous series of rotations can now be combined into a single transformation converting a vector from the body frame to the gimbal frame.

$$\begin{aligned} {}^{G_i}\mathbf{R}^B &= \mathbf{R}_3(\delta_i)\mathbf{R}_2(\beta)\mathbf{R}_3(\alpha_i) \\ &= \begin{bmatrix} c\delta_i & s\delta_i & 0 \\ -s\delta_i & c\delta_i & 0 \\ 0 & 0 & 1 \end{bmatrix}_3 \begin{bmatrix} c\beta & 0 & -s\beta \\ 0 & 1 & 0 \\ s\beta & 0 & c\beta \end{bmatrix}_2 \begin{bmatrix} c\alpha_i & s\alpha_i & 0 \\ -s\alpha_i & c\alpha_i & 0 \\ 0 & 0 & 1 \end{bmatrix}_3 \\ &= \begin{bmatrix} c\alpha_i c\beta c\delta_i - s\alpha_i s\delta_i & c\alpha_i s\delta_i + s\alpha_i c\beta c\delta_i & -s\beta c\delta_i \\ -s\alpha_i c\delta_i - c\alpha_i c\beta s\delta_i & c\alpha_i c\delta_i - s\alpha_i c\beta s\delta_i & s\beta s\delta_i \\ c\alpha_i s\beta & s\alpha_i s\beta & c\beta \end{bmatrix}^B \end{aligned} \quad (189)$$

It follows from Equation (45) that ${}^B\mathbf{R}^{G_i}$ is now the transpose of ${}^{G_i}\mathbf{R}^B$, which is equivalent to the reverse sequence via the negative angle of each rotation.

$$\begin{aligned} {}^B\mathbf{R}^{G_i} &= \mathbf{R}_3(-\alpha_i)\mathbf{R}_2(-\beta)\mathbf{R}_3(-\delta_i) = [{}^{G_i}\mathbf{R}^B]^T \\ &= \begin{bmatrix} c\alpha_i c\beta c\delta_i - s\alpha_i s\delta_i & -s\alpha_i c\delta_i - c\alpha_i c\beta s\delta_i & c\alpha_i s\beta \\ c\alpha_i s\delta_i + s\alpha_i c\beta c\delta_i & c\alpha_i c\delta_i - s\alpha_i c\beta s\delta_i & s\alpha_i s\beta \\ -s\beta c\delta_i & s\beta s\delta_i & c\beta \end{bmatrix}^{G_i} \end{aligned} \quad (190)$$

As an example, place the initial CMG at angle $\alpha = 0^\circ$. The resultant transformation from the \hat{G} frame to the \hat{B} frame is shown in Equation (191).

$${}^B\mathbf{R}_{cmg}^G = \mathbf{R}_3(-0^\circ)\mathbf{R}_2(-\beta)\mathbf{R}_3(-\delta) = \begin{bmatrix} c\beta c\delta & -c\beta s\delta & s\beta \\ s\delta & c\delta & 0 \\ -s\beta c\delta & s\beta s\delta & c\beta \end{bmatrix}^G \quad (191)$$

An array of four CMGs is typically arranged in a square pyramid (similar to reaction wheels) in which each of the CMGs are placed 90° apart. The arrangement used here will be: $\alpha_1 = 0^\circ, \alpha_2 = 90^\circ, \alpha_3 = 180^\circ, \alpha_4 = 270^\circ$. Figure 59 demonstrates this placement. This orientation matches that shown in [29, p. 3] given that the author's initial gimbal angles were each set at 90° rather than $\delta_i = 0^\circ$ as assumed in this thesis.

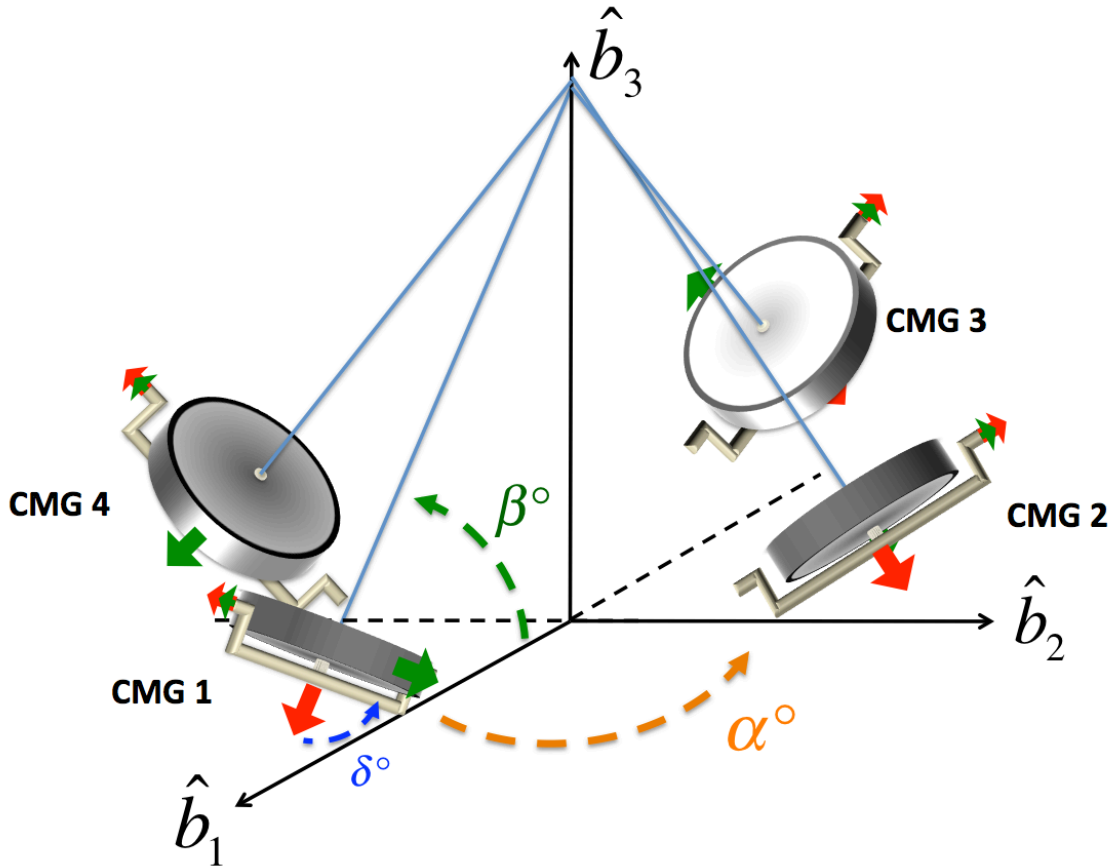


Figure 59. Body Frame to CMG Schematic

Based on the wheel axis description mentioned above, the gimbal and wheel angular momenta in the gimbal frames can be written as

$$\mathbf{h}_{g_i}^{G_i} = \begin{bmatrix} 0 \\ 0 \\ 1 \end{bmatrix}^{G_i} h_{g_i} \text{ and } \mathbf{h}_{w_i}^{G_i} = \begin{bmatrix} 1 \\ 0 \\ 0 \end{bmatrix}^{G_i} h_{w_i} \quad (192)$$

Transforming angular momentum from the \hat{G} frame to the \hat{B} frame using (184) and $\alpha = 0^\circ$ yields Equation (193). Note that the gimbal momentum in the body frame, Equation (193), is equal to the reaction wheel momentum in the body frame, Equation (53). This is because the orientation of the gimbal rotation axis is equal to that of the reaction wheel spin axis, and both were subject to the same two initial rotations.

$$\mathbf{h}_{g_i}^B = \begin{bmatrix} s\beta \\ 0 \\ c\beta \end{bmatrix}^B h_{g_i} \text{ and } \mathbf{h}_{w_i}^B = \begin{bmatrix} c\beta c\delta_i \\ s\delta_i \\ -s\beta c\delta_i \end{bmatrix}^B h_{w_i} \quad (193)$$

or in general form:

$$\mathbf{h}_{g_i}^B = \begin{bmatrix} \hat{b}_1 \cdot \hat{g}_{i_3} \\ \hat{b}_2 \cdot \hat{g}_{i_3} \\ \hat{b}_3 \cdot \hat{g}_{i_3} \end{bmatrix}^B h_{g_i} \text{ and } \mathbf{h}_{w_i}^B = \begin{bmatrix} \hat{b}_1 \cdot \hat{g}_{i_1} \\ \hat{b}_2 \cdot \hat{g}_{i_1} \\ \hat{b}_3 \cdot \hat{g}_{i_1} \end{bmatrix}^B h_{w_i} \quad (194)$$

Recall the total angular momentum of the system is the sum of each of the MEDs in the body frame. Unlike the single momentum set for reaction wheels in Equation (69), CMGs derive their momentum from two different transformation sets. This allows the gimbal momentum and gimbal torques to be translated separately to through each of the n CMGs to the body frame.

$$\sum_{i=1}^n \mathbf{h}_{g_i}^B = \begin{bmatrix} \hat{b}_1 \cdot \hat{g}_{1_3} & \hat{b}_1 \cdot \hat{g}_{2_3} & \dots & \hat{b}_1 \cdot \hat{g}_{n_3} \\ \hat{b}_2 \cdot \hat{g}_{1_3} & \hat{b}_2 \cdot \hat{g}_{2_3} & \dots & \hat{b}_2 \cdot \hat{g}_{n_3} \\ \hat{b}_3 \cdot \hat{g}_{1_3} & \hat{b}_3 \cdot \hat{g}_{2_3} & \dots & \hat{b}_3 \cdot \hat{g}_{n_3} \end{bmatrix}^B \begin{bmatrix} h_{g_1} \\ h_{g_2} \\ \vdots \\ h_{g_n} \end{bmatrix}^G \quad (195)$$

and
$$\sum_{i=1}^n \mathbf{h}_{w_i}^B = \begin{bmatrix} \hat{b}_1 \cdot \hat{g}_{1_1} & \hat{b}_1 \cdot \hat{g}_{2_1} & \dots & \hat{b}_1 \cdot \hat{g}_{n_1} \\ \hat{b}_2 \cdot \hat{g}_{1_1} & \hat{b}_2 \cdot \hat{g}_{2_1} & \dots & \hat{b}_2 \cdot \hat{g}_{n_1} \\ \hat{b}_3 \cdot \hat{g}_{1_1} & \hat{b}_3 \cdot \hat{g}_{2_1} & \dots & \hat{b}_3 \cdot \hat{g}_{n_1} \end{bmatrix}^B \begin{bmatrix} h_{w_1} \\ h_{w_2} \\ \vdots \\ h_{w_n} \end{bmatrix}^G \quad (196)$$

where
$${}^B \mathbf{Z}_3^G = \begin{bmatrix} \hat{b}_1 \cdot \hat{g}_{1_3} & \hat{b}_1 \cdot \hat{g}_{2_3} & \dots & \hat{b}_1 \cdot \hat{g}_{n_3} \\ \hat{b}_2 \cdot \hat{g}_{1_3} & \hat{b}_2 \cdot \hat{g}_{2_3} & \dots & \hat{b}_2 \cdot \hat{g}_{n_3} \\ \hat{b}_3 \cdot \hat{g}_{1_3} & \hat{b}_3 \cdot \hat{g}_{2_3} & \dots & \hat{b}_3 \cdot \hat{g}_{n_3} \end{bmatrix}^B \quad (197)$$

and
$${}^B \mathbf{Z}_1^G = \begin{bmatrix} \hat{b}_1 \cdot \hat{g}_{1_1} & \hat{b}_1 \cdot \hat{g}_{2_1} & \dots & \hat{b}_1 \cdot \hat{g}_{n_1} \\ \hat{b}_2 \cdot \hat{g}_{1_1} & \hat{b}_2 \cdot \hat{g}_{2_1} & \dots & \hat{b}_2 \cdot \hat{g}_{n_1} \\ \hat{b}_3 \cdot \hat{g}_{1_1} & \hat{b}_3 \cdot \hat{g}_{2_1} & \dots & \hat{b}_3 \cdot \hat{g}_{n_1} \end{bmatrix}^B . \quad (198)$$

Now, Equations (195) and (196) can be rewritten as

$$\mathbf{h}_g^B = \sum_{i=1}^n \mathbf{h}_{g_i}^B = {}^B \mathbf{Z}_3^G \mathbf{h}_g^G \quad (199)$$

$$\mathbf{h}_w^B = \sum_{i=1}^n \mathbf{h}_{w_i}^B = {}^B \mathbf{Z}_1^G \mathbf{h}_w^G \quad (200)$$

where
$$\mathbf{h}_g^G = \begin{bmatrix} h_{g_1} \\ h_{g_2} \\ \vdots \\ h_{g_n} \end{bmatrix}^G \quad \text{and} \quad \mathbf{h}_w^G = \begin{bmatrix} h_{w_1} \\ h_{w_2} \\ \vdots \\ h_{w_n} \end{bmatrix}^G . \quad (201)$$

For the square pyramid mentioned, the orientation matrices is shown in Equation (60) for CMGs.

$${}^B\mathbf{Z}_3^G = \begin{bmatrix} s\beta & 0 & -s\beta & 0 \\ 0 & s\beta & 0 & -s\beta \\ c\beta & c\beta & c\beta & c\beta \end{bmatrix}^G \quad (202)$$

$${}^B\mathbf{Z}_1^G = \begin{bmatrix} c\beta c\delta_i & -s\delta_i & -c\beta c\delta_i & s\delta_i \\ s\delta_i & c\beta c\delta_i & -s\delta_i & -c\beta c\delta_i \\ -s\beta c\delta_i & -s\beta c\delta_i & -s\beta c\delta_i & -s\beta c\delta_i \end{bmatrix}^G \quad (203)$$

B. MODELING CMG ORIENTATION MATRICES

These CMG orientation matrices can be created within Simulink. Figure 60 demonstrates how Equation (190) is implemented. Since α_i and β are fixed for the CMG, their respective rotation matrices will be held constant. The CMG transformation matrix ${}^B\mathbf{R}^{G_i}$ is only state dependent upon δ_i . The column selectors simply extract the first, second, and third columns individually.

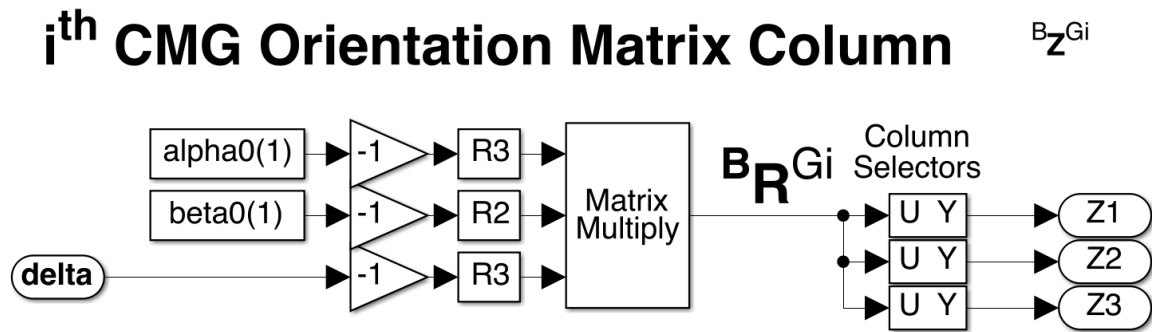


Figure 60. CMG i^{th} Orientation Matrix Column Model

Additionally, Figure 61 illustrates how the \mathbf{R}_3 and \mathbf{R}_2 matrices can be created for a generic angle.

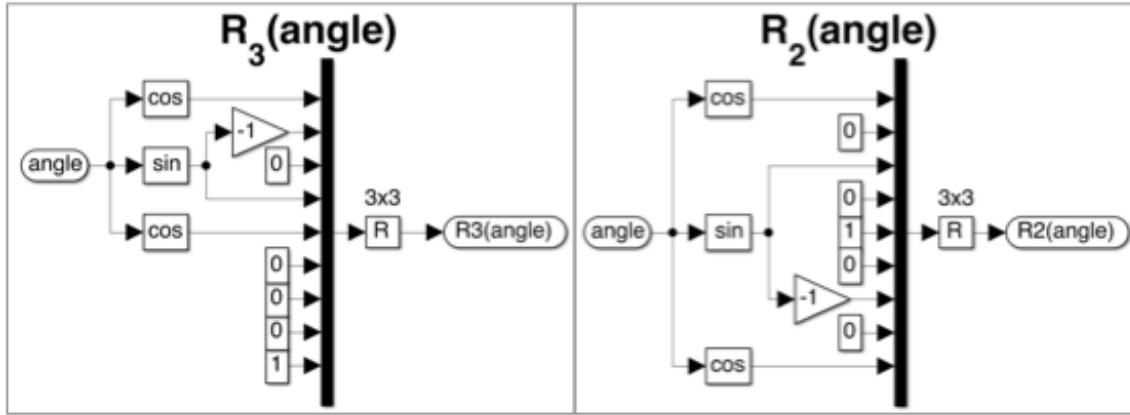


Figure 61. Rotation Matrix Model

Figure 62 fully creates all three orientation matrices. ${}^B\mathbf{Z}^{G_i}$ from Figure 60 is represented four times, once for each CMG. The individual columns are independently combined to create the appropriate 3x4 orientation matrices ${}^B\mathbf{Z}^G$.

Orientation Matrices

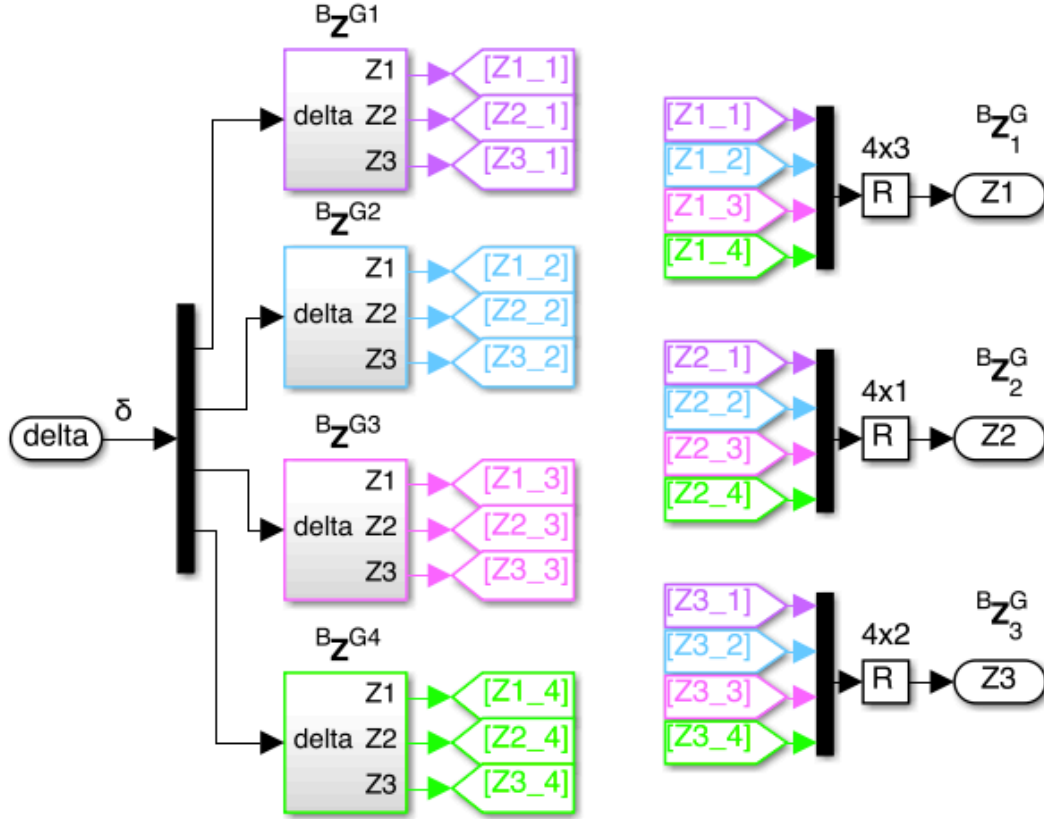


Figure 62. CMG Orientation Matrix Model

C. DIFFERENTIAL EQUATIONS OF MOTION

The momentum of a CMG can be defined as the sum of the wheel angular momentum and the gimbal angular acceleration.

$$\mathbf{H}_{CMG_i} = \mathbf{H}_{w_i}^N + \mathbf{H}_{g_i}^N \quad (204)$$

Each the wheel and gimbal can be independently modeled.

$$\begin{aligned} \mathbf{H}_{w_i} &= \mathbf{J}_{w_i}^N \boldsymbol{\omega}_i^{w_i} \\ &= \mathbf{J}_{w_i} \left({}^N \boldsymbol{\omega}_i^B + {}^B \boldsymbol{\omega}_i^{G_i} + {}^{G_i} \boldsymbol{\omega}_i^{w_i} \right) \\ &= \mathbf{J}_{w_i}^N \boldsymbol{\omega}_i^B + \mathbf{J}_{w_i}^B \boldsymbol{\omega}_i^{G_i} + \mathbf{J}_{w_i}^{G_i} \boldsymbol{\omega}_i^{w_i} \end{aligned} \quad (205)$$

$$\begin{aligned}
\mathbf{H}_{g_i} &= \mathbf{J}_{g_i}^N \boldsymbol{\omega}_i^{G_i} \\
&= \mathbf{J}_{g_i} \left({}^N\boldsymbol{\omega}_i^B + {}^B\boldsymbol{\omega}_i^{G_i} \right) \\
&= \mathbf{J}_{g_i}^N \boldsymbol{\omega}_i^B + \mathbf{J}_{g_i}^B \boldsymbol{\omega}_i^{G_i}
\end{aligned} \tag{206}$$

The wheel and gimbal inertias were combined into the spacecraft inertia within Equation (6). Likewise, when these body-rotating inertias are subtracted from (204), only the components rotating relative to the body remain.

$$\begin{aligned}
\mathbf{h}_{CMG_i} &= \mathbf{H}_{CMG_i} - \left(\mathbf{J}_{w_i} + \mathbf{J}_{g_i} \right)^N \boldsymbol{\omega}_i^B \\
&= \left(\mathbf{J}_{w_i}^B \boldsymbol{\omega}_i^{G_i} + \mathbf{J}_{w_i}^{G_i} \boldsymbol{\omega}_i^{W_i} \right) + \left(\mathbf{J}_{g_i}^B \boldsymbol{\omega}_i^{G_i} \right)
\end{aligned} \tag{207}$$

Next, the gimbal and wheel momenta will be analyzed separately.

1. Gimbal Momentum and Torque

a. CMG Gimbal Momentum – Single Gimbal

The gimbal momentum is shown first in matrix form.

$$\mathbf{h}_{g_i}^{G_i} = \mathbf{J}_{g_i}^B \boldsymbol{\omega}_i^{G_i} = \begin{bmatrix} j_{gi11} & 0 & 0 \\ 0 & j_{gi22} & 0 \\ 0 & 0 & j_{gi33} \end{bmatrix} \begin{bmatrix} 0 \\ 0 \\ \dot{\delta}_i \end{bmatrix}^{G_i} = \begin{bmatrix} 0 \\ 0 \\ J_{gi33} \dot{\delta}_i \end{bmatrix}^{G_i} \tag{208}$$

Shown in dyadic form:

$$\begin{aligned}
\mathbf{h}_{g_i}^{G_i} &= \left(j_{gi11} \hat{\mathbf{g}}_{i1} \hat{\mathbf{g}}_{i1} + j_{gi22} \hat{\mathbf{g}}_{i2} \hat{\mathbf{g}}_{i2} + j_{gi33} \hat{\mathbf{g}}_{i3} \hat{\mathbf{g}}_{i3} \right) \bullet \left(\dot{\delta}_i \hat{\mathbf{g}}_{i3} \right) \\
&= j_{gi33} \dot{\delta}_i \hat{\mathbf{g}}_{i3} \left(\hat{\mathbf{g}}_{i3} \bullet \hat{\mathbf{g}}_{i3} \right) \\
&= j_{gi33} \dot{\delta}_i \hat{\mathbf{g}}_{i3}
\end{aligned} \tag{209}$$

Change of basis to the body frame:

$$\begin{aligned}
\mathbf{h}_{g_i}^B &= j_{gi33} \dot{\delta}_i \hat{\mathbf{g}}_{i3} \bullet \left(\hat{\mathbf{b}}_1 \hat{\mathbf{b}}_1 + \hat{\mathbf{b}}_2 \hat{\mathbf{b}}_2 + \hat{\mathbf{b}}_3 \hat{\mathbf{b}}_3 \right) \\
&= j_{gi33} \dot{\delta}_i \left(\hat{\mathbf{g}}_{i3} \bullet \hat{\mathbf{b}}_1 \right) \hat{\mathbf{b}}_1 + j_{gi33} \dot{\delta}_i \left(\hat{\mathbf{g}}_{i3} \bullet \hat{\mathbf{b}}_2 \right) \hat{\mathbf{b}}_2 + j_{gi33} \dot{\delta}_i \left(\hat{\mathbf{g}}_{i3} \bullet \hat{\mathbf{b}}_3 \right) \hat{\mathbf{b}}_3
\end{aligned} \tag{210}$$

The resultant rotation matrix is shown as

$$\begin{aligned}
\mathbf{h}_{g_i}^B &= \begin{bmatrix} \hat{b}_1 \cdot \hat{g}_{i_1} & \hat{b}_1 \cdot \hat{g}_{i_2} & \hat{b}_1 \cdot \hat{g}_{i_3} \\ \hat{b}_2 \cdot \hat{g}_{i_1} & \hat{b}_2 \cdot \hat{g}_{i_2} & \hat{b}_2 \cdot \hat{g}_{i_3} \\ \hat{b}_3 \cdot \hat{g}_{i_1} & \hat{b}_3 \cdot \hat{g}_{i_2} & \hat{b}_3 \cdot \hat{g}_{i_3} \end{bmatrix}^{G_i} \begin{bmatrix} 0 \\ 0 \\ j_{gi_{33}} \dot{\delta}_i \end{bmatrix}^{G_i} \\
&= \begin{bmatrix} \hat{b}_1 \cdot \hat{g}_{i_3} \\ \hat{b}_2 \cdot \hat{g}_{i_3} \\ \hat{b}_3 \cdot \hat{g}_{i_3} \end{bmatrix}^B j_{gi_{33}} \dot{\delta}_i
\end{aligned} \tag{211}$$

b. CMG Gimbal Momentum – Gimbal Array

Similar to reaction wheels, the resultant orientation matrix can be created using the components from the 3rd column of the gimbal frame rotation matrix.

$$\begin{aligned}
\mathbf{h}_g^B &= \sum_{i=1}^n \begin{bmatrix} \hat{b}_1 \cdot \hat{g}_{i_3} \\ \hat{b}_2 \cdot \hat{g}_{i_3} \\ \hat{b}_3 \cdot \hat{g}_{i_3} \end{bmatrix}^B (j_{gi_{11}} \dot{\delta})^G \\
&= \begin{bmatrix} \hat{b}_1 \cdot \hat{g}_{1_3} & \hat{b}_1 \cdot \hat{g}_{2_3} & \dots & \hat{b}_1 \cdot \hat{g}_{n_3} \\ \hat{b}_2 \cdot \hat{g}_{1_3} & \hat{b}_2 \cdot \hat{g}_{2_3} & \dots & \hat{b}_2 \cdot \hat{g}_{n_3} \\ \hat{b}_3 \cdot \hat{g}_{1_3} & \hat{b}_3 \cdot \hat{g}_{2_3} & \dots & \hat{b}_3 \cdot \hat{g}_{n_3} \end{bmatrix}^B \begin{bmatrix} j_{g_{11}} \dot{\delta}_1 \\ j_{g_{21}} \dot{\delta}_2 \\ \vdots \\ j_{g_{n1}} \dot{\delta}_n \end{bmatrix}^G
\end{aligned} \tag{212}$$

$$\mathbf{h}_g^B = {}^B \mathbf{Z}_3^G \mathbf{h}_g^G = {}^B \mathbf{Z}_3^G \mathbf{J}_g \dot{\boldsymbol{\delta}}_g^G \tag{213}$$

where

$$\mathbf{h}_g^G = \mathbf{J}_g \dot{\boldsymbol{\delta}}_g^G = \begin{bmatrix} j_{g_{133}} & 0 & 0 & 0 \\ 0 & j_{g_{233}} & 0 & 0 \\ 0 & 0 & \ddots & 0 \\ 0 & 0 & 0 & j_{g_{n33}} \end{bmatrix}^G \begin{bmatrix} \dot{\delta}_1 \\ \dot{\delta}_2 \\ \vdots \\ \dot{\delta}_n \end{bmatrix}^G \tag{214}$$

c. CMG Gimbal Torque

The torque of the gimbal can now be determined with respect to the body frame. Since this is simply the gimbal axis, the orientation is fixed and $\dot{\mathbf{Z}} = 0$. The inertia is assumed not to change relative to the gimbal axis.

$$\boldsymbol{\tau}_g^B = \frac{d}{dt}(\mathbf{h}_g^B) = \frac{d}{dt}({}^B\mathbf{Z}_3^G \mathbf{J}_g \dot{\boldsymbol{\delta}}_g^G) \quad (215)$$

$$= \cancel{{}^B\dot{\mathbf{Z}}_3^G \mathbf{J}_g \dot{\boldsymbol{\delta}}_g^G} + \cancel{{}^B\mathbf{Z}_3^G \dot{\mathbf{J}}_g \dot{\boldsymbol{\delta}}_g^G} + {}^B\mathbf{Z}_3^G \mathbf{J}_g \ddot{\boldsymbol{\delta}}_g^G$$

$$\boldsymbol{\tau}_g^B = {}^B\mathbf{Z}_3^G \mathbf{J}_g \ddot{\boldsymbol{\delta}}_g^G \quad (216)$$

In dyadic form, a single CMG's gimbal torque can be found using the derivative of Equation (210).

$$\begin{aligned} \frac{d}{dt}(\mathbf{h}_{g_i}^G) = & j_{g_{i33}} \dot{\delta}_i (\hat{g}_{i_3} \cdot \hat{b}_1) \hat{b}_1 + j_{g_{i33}} \dot{\delta}_i (\hat{g}_{i_3} \cdot \hat{b}_2) \hat{b}_2 + j_{g_{i33}} \dot{\delta}_i (\hat{g}_{i_3} \cdot \hat{b}_3) \hat{b}_3 \\ & + j_{g_{i33}} \ddot{\delta}_i (\hat{g}_{i_3} \cdot \hat{b}_1) \hat{b}_1 + j_{g_{i33}} \ddot{\delta}_i (\hat{g}_{i_3} \cdot \hat{b}_2) \hat{b}_2 + j_{g_{i33}} \ddot{\delta}_i (\hat{g}_{i_3} \cdot \hat{b}_3) \hat{b}_3 \\ & + j_{g_{i33}} \dot{\delta}_i (\dot{\hat{g}}_{i_3} \cdot \hat{b}_1) \hat{b}_1 + j_{g_{i33}} \dot{\delta}_i (\dot{\hat{g}}_{i_3} \cdot \hat{b}_2) \hat{b}_2 + j_{g_{i33}} \dot{\delta}_i (\dot{\hat{g}}_{i_3} \cdot \hat{b}_3) \hat{b}_3 \end{aligned} \quad (217)$$

The inertia of the gimbal is not changing with respect to the gimbal frame. Also, the orientation of the 3 axis of gimbal frame is not moving with respect to the body frame as determined in Equation (183).

$$\dot{j}_{g_{i33}} = 0 \quad \text{and} \quad \dot{\hat{g}}_{i_3} = 0. \quad (218)$$

Equation (217) now becomes

$$\frac{d}{dt}(\mathbf{h}_{g_i}^G) = j_{g_{i33}} \ddot{\delta}_i (\hat{g}_{i_3} \cdot \hat{b}_1) \hat{b}_1 + j_{g_{i33}} \ddot{\delta}_i (\hat{g}_{i_3} \cdot \hat{b}_2) \hat{b}_2 + j_{g_{i33}} \ddot{\delta}_i (\hat{g}_{i_3} \cdot \hat{b}_3) \hat{b}_3. \quad (219)$$

$$\frac{d}{dt}(\mathbf{h}_g^B) = \begin{bmatrix} j_{g_{i33}} \ddot{\delta}_i (\hat{b}_1 \cdot \hat{g}_{i_3}) \\ j_{g_{i33}} \ddot{\delta}_i (\hat{b}_2 \cdot \hat{g}_{i_3}) \\ j_{g_{i33}} \ddot{\delta}_i (\hat{b}_3 \cdot \hat{g}_{i_3}) \end{bmatrix}^B = \begin{bmatrix} \hat{b}_1 \cdot \hat{g}_{i_3} \\ \hat{b}_2 \cdot \hat{g}_{i_3} \\ \hat{b}_3 \cdot \hat{g}_{i_3} \end{bmatrix}^B j_{g_{i33}} \ddot{\delta}_i \quad (220)$$

2. Wheel Momentum and Torque

a. CMG Wheel Momentum – Single Wheel

The CMG wheel momentum is shown first in matrix form.

$$\begin{aligned}
 \mathbf{h}_{w_i}^{G_i} &= \mathbf{J}_{w_i}^B \boldsymbol{\omega}_i^{G_i} + \mathbf{J}_{w_i}^{G_i} \boldsymbol{\omega}_i^{W_i} \\
 &= \begin{bmatrix} j_{w_i 11} & 0 & 0 \\ 0 & j_{w_i 22} & 0 \\ 0 & 0 & j_{w_i 33} \end{bmatrix} \begin{bmatrix} 0 \\ 0 \\ \dot{\delta}_i \end{bmatrix}^{G_i} + \begin{bmatrix} j_{w_i 11} & 0 & 0 \\ 0 & j_{w_i 22} & 0 \\ 0 & 0 & j_{w_i 33} \end{bmatrix} \begin{bmatrix} \boldsymbol{\Omega}_i \\ 0 \\ 0 \end{bmatrix}^{G_i} \\
 &= \begin{bmatrix} j_{w_i 11} \boldsymbol{\Omega}_i \\ 0 \\ j_{w_i 33} \dot{\delta}_i \end{bmatrix}^{G_i}
 \end{aligned} \tag{221}$$

An equivalent derivation is shown in dyadic form.

$$\begin{aligned}
 \mathbf{h}_{w_i}^{G_i} &= \left(j_{w_i 11} \hat{g}_{i_1} \hat{g}_{i_1} + j_{w_i 22} \hat{g}_{i_2} \hat{g}_{i_2} + j_{w_i 33} \hat{g}_{i_3} \hat{g}_{i_3} \right) \bullet \left(\boldsymbol{\Omega}_i \hat{g}_{i_1} + \dot{\delta}_i \hat{g}_{i_3} \right) \\
 &= j_{w_i 11} \boldsymbol{\Omega}_i \hat{g}_{i_1} \left(\hat{g}_{i_1} \bullet \hat{g}_{i_1} \right) + j_{w_i 33} \dot{\delta}_i \hat{g}_{i_3} \left(\hat{g}_{i_3} \bullet \hat{g}_{i_3} \right) \\
 &= j_{w_i 11} \boldsymbol{\Omega}_i \hat{g}_{i_1} + j_{w_i 33} \dot{\delta}_i \hat{g}_{i_3}
 \end{aligned} \tag{222}$$

Change of basis to the body frame:

$$\begin{aligned}
 \mathbf{h}_{w_i}^B &= \left(j_{w_i 11} \boldsymbol{\Omega}_i \hat{g}_{i_1} + j_{w_i 33} \dot{\delta}_i \hat{g}_{i_3} \right) \bullet \left(\hat{b}_1 \hat{b}_1 + \hat{b}_2 \hat{b}_2 + \hat{b}_3 \hat{b}_3 \right) \\
 &= j_{w_i 11} \boldsymbol{\Omega}_i \left(\hat{g}_{i_1} \bullet \hat{b}_1 \right) \hat{b}_1 + j_{w_i 11} \boldsymbol{\Omega}_i \left(\hat{g}_{i_1} \bullet \hat{b}_2 \right) \hat{b}_2 + j_{w_i 11} \boldsymbol{\Omega}_i \left(\hat{g}_{i_1} \bullet \hat{b}_3 \right) \hat{b}_3 \\
 &\quad + j_{w_i 33} \dot{\delta}_i \left(\hat{g}_{i_3} \bullet \hat{b}_1 \right) \hat{b}_1 + j_{w_i 33} \dot{\delta}_i \left(\hat{g}_{i_3} \bullet \hat{b}_2 \right) \hat{b}_2 + j_{w_i 33} \dot{\delta}_i \left(\hat{g}_{i_3} \bullet \hat{b}_3 \right) \hat{b}_3
 \end{aligned} \tag{223}$$

The resultant rotation matrix is shown as

$$\begin{aligned}
\mathbf{h}_{w_i}^B &= \begin{bmatrix} \hat{b}_1 \cdot \hat{g}_{i_1} & \hat{b}_1 \cdot \hat{g}_{i_2} & \hat{b}_1 \cdot \hat{g}_{i_3} \\ \hat{b}_2 \cdot \hat{g}_{i_1} & \hat{b}_2 \cdot \hat{g}_{i_2} & \hat{b}_2 \cdot \hat{g}_{i_3} \\ \hat{b}_3 \cdot \hat{g}_{i_1} & \hat{b}_3 \cdot \hat{g}_{i_2} & \hat{b}_3 \cdot \hat{g}_{i_3} \end{bmatrix}^{G_i} \begin{bmatrix} j_{w_{i11}} \Omega_i \\ 0 \\ j_{w_{i33}} \dot{\delta}_i \end{bmatrix}^{G_i} \\
&= \begin{bmatrix} (\hat{b}_1 \cdot \hat{g}_{i_1}) j_{w_{i11}} \Omega_i + (\hat{b}_1 \cdot \hat{g}_{i_3}) j_{w_{i33}} \dot{\delta}_i \\ (\hat{b}_2 \cdot \hat{g}_{i_1}) j_{w_{i11}} \Omega_i + (\hat{b}_2 \cdot \hat{g}_{i_3}) j_{w_{i33}} \dot{\delta}_i \\ (\hat{b}_3 \cdot \hat{g}_{i_1}) j_{w_{i11}} \Omega_i + (\hat{b}_3 \cdot \hat{g}_{i_3}) j_{w_{i33}} \dot{\delta}_i \end{bmatrix}^B
\end{aligned} \tag{224}$$

$$\mathbf{h}_{w_i}^B = \begin{bmatrix} \hat{b}_1 \cdot \hat{g}_{i_1} \\ \hat{b}_2 \cdot \hat{g}_{i_1} \\ \hat{b}_3 \cdot \hat{g}_{i_1} \end{bmatrix}^B j_{w_{i11}} \Omega_i + \begin{bmatrix} \hat{b}_1 \cdot \hat{g}_{i_3} \\ \hat{b}_2 \cdot \hat{g}_{i_3} \\ \hat{b}_3 \cdot \hat{g}_{i_3} \end{bmatrix}^B j_{w_{i33}} \dot{\delta}_i \tag{225}$$

b. CMG Wheel Momentum – Wheel Array

The resultant orientation matrix can be created using the components from the 1st and 3rd columns of the gimbal frame rotation matrix.

$$\begin{aligned}
\mathbf{h}_w^B &= \sum_{i=1}^n \left(\begin{bmatrix} \hat{b}_1 \cdot \hat{g}_{i_1} \\ \hat{b}_2 \cdot \hat{g}_{i_1} \\ \hat{b}_3 \cdot \hat{g}_{i_1} \end{bmatrix}^B j_{w_{i11}} \Omega_i + \begin{bmatrix} \hat{b}_1 \cdot \hat{g}_{i_3} \\ \hat{b}_2 \cdot \hat{g}_{i_3} \\ \hat{b}_3 \cdot \hat{g}_{i_3} \end{bmatrix}^B j_{w_{i33}} \dot{\delta}_i \right) \\
&= \begin{bmatrix} \hat{b}_1 \cdot \hat{g}_{1_1} & \hat{b}_1 \cdot \hat{g}_{2_1} & \dots & \hat{b}_1 \cdot \hat{g}_{n_1} \\ \hat{b}_2 \cdot \hat{g}_{1_1} & \hat{b}_2 \cdot \hat{g}_{2_1} & \dots & \hat{b}_2 \cdot \hat{g}_{n_1} \\ \hat{b}_3 \cdot \hat{g}_{1_1} & \hat{b}_3 \cdot \hat{g}_{2_1} & \dots & \hat{b}_3 \cdot \hat{g}_{n_1} \end{bmatrix}^B \begin{bmatrix} j_{w_{111}} \Omega_1 \\ j_{w_{211}} \Omega_2 \\ \vdots \\ j_{w_{n11}} \Omega_n \end{bmatrix}^G \\
&\quad + \begin{bmatrix} \hat{b}_1 \cdot \hat{g}_{1_3} & \hat{b}_1 \cdot \hat{g}_{2_3} & \dots & \hat{b}_1 \cdot \hat{g}_{n_3} \\ \hat{b}_2 \cdot \hat{g}_{1_3} & \hat{b}_2 \cdot \hat{g}_{2_3} & \dots & \hat{b}_2 \cdot \hat{g}_{n_3} \\ \hat{b}_3 \cdot \hat{g}_{1_3} & \hat{b}_3 \cdot \hat{g}_{2_3} & \dots & \hat{b}_3 \cdot \hat{g}_{n_3} \end{bmatrix}^B \begin{bmatrix} j_{w_{133}} \dot{\delta}_1 \\ j_{w_{233}} \dot{\delta}_2 \\ \vdots \\ j_{w_{n33}} \dot{\delta}_n \end{bmatrix}^G
\end{aligned} \tag{226}$$

$$\mathbf{h}_w^B = {}^B\mathbf{Z}_3^G \mathbf{J}_w \dot{\boldsymbol{\delta}}_g^G + {}^B\mathbf{Z}_1^G \mathbf{J}_w \boldsymbol{\Omega}_g^G \quad (227)$$

c. CMG Wheel Torque – Wheel Array

The torque of the gimbal can now be determined with respect to the body frame. Since this is simply the gimbal axis, the orientation is fixed and ${}^B\dot{\mathbf{Z}}_3^G = 0$. The inertia is assumed not to change relative to the gimbal axis. Also, the wheel is kept at a nominally constant speed.

$$\begin{aligned} \boldsymbol{\tau}_w^B &= \frac{d}{dt}(\mathbf{h}_w^B) = \frac{d}{dt}({}^B\mathbf{Z}_1^G \mathbf{J}_w \dot{\boldsymbol{\delta}}_g^G + {}^B\mathbf{Z}_3^G \mathbf{J}_w \boldsymbol{\Omega}_g^G) \\ &= \cancel{{}^B\dot{\mathbf{Z}}_3^G \mathbf{J}_w \dot{\boldsymbol{\delta}}_g^G} + \cancel{{}^B\mathbf{Z}_3^G \dot{\mathbf{J}}_w \dot{\boldsymbol{\delta}}_g^G} + {}^B\mathbf{Z}_3^G \mathbf{J}_w \ddot{\boldsymbol{\delta}}_g^G \\ &\quad + \cancel{{}^B\dot{\mathbf{Z}}_1^G \mathbf{J}_w \boldsymbol{\Omega}_g^G} + \cancel{{}^B\mathbf{Z}_1^G \dot{\mathbf{J}}_w \boldsymbol{\Omega}_g^G} + \cancel{{}^B\mathbf{Z}_1^G \mathbf{J}_w \dot{\boldsymbol{\Omega}}_g^G} \end{aligned} \quad (228)$$

$$\boldsymbol{\tau}_w^B = {}^B\mathbf{Z}_3^G \mathbf{J}_w \ddot{\boldsymbol{\delta}}_g^G + {}^B\dot{\mathbf{Z}}_1^G \mathbf{J}_w \boldsymbol{\Omega}_g^G \quad (229)$$

Using partial differentiation of the second term within Equation (229), the following is obtained.

$$\begin{aligned} {}^B\dot{\mathbf{Z}}_1^G \mathbf{J}_w \boldsymbol{\Omega}_g^G &= \frac{\partial \delta}{\partial \delta} \frac{d}{dt}({}^B\mathbf{Z}_1^G) \mathbf{J}_w \boldsymbol{\Omega}_g^G \\ &= \frac{d\delta}{dt} \frac{\partial}{\partial \delta}({}^B\mathbf{Z}_1^G) \mathbf{J}_w \boldsymbol{\Omega}_g^G \\ &= \frac{\partial}{\partial \delta}({}^B\mathbf{Z}_1^G) \dot{\delta} \mathbf{J}_w \boldsymbol{\Omega}_g^G \end{aligned} \quad (230)$$

$$\text{Therefore, } {}^B\dot{\mathbf{Z}}_1^G = \frac{\partial}{\partial \delta}({}^B\mathbf{Z}_1^G) \dot{\delta} \quad (231)$$

where $\frac{\partial}{\partial \delta}({}^B\mathbf{Z}_1^G)$ can be interpreted as a CMG Jacobian matrix.

$${}^B\dot{\mathbf{Z}}^{G_i} = \begin{bmatrix} c\alpha_i c\beta c\delta_i - s\alpha_i s\delta_i & -s\alpha_i c\delta_i - c\alpha_i c\beta s\delta_i & c\alpha_i s\beta \\ c\alpha_i s\delta_i + s\alpha_i c\beta c\delta_i & c\alpha_i c\delta_i - s\alpha_i c\beta s\delta_i & s\alpha_i s\beta \\ -s\beta c\delta_i & s\beta s\delta_i & c\beta_i \end{bmatrix}^{G_i} \quad (232)$$

By inspection of the transformation matrix, the partial derivative of the first column is equal to the second column.

$$\frac{\partial}{\partial \delta_i} ({}^B \mathbf{Z}_1^{G_i}) = {}^B \mathbf{Z}_2^{G_i} \quad (233)$$

Similarly, this is captured in the dynamic orientation matrix [6, pp. 464–467], where \mathbf{A} is introduced as a steering logic matrix.

$$\dot{h}_i^B = \mathbf{A} \dot{\delta} h_i^G \text{ where } \mathbf{A} = \frac{\partial h^B}{\partial \delta} \quad (234)$$

Upon close inspection, \mathbf{A} matrix is equivalent to the second column of the \mathbf{Z} matrix utilized within this thesis.

$$\mathbf{A} = {}^B \mathbf{Z}_2^G \quad (235)$$

An alternative proof follows using dyadics.

$${}^B \dot{\mathbf{Z}}_1^G \mathbf{J}_{w_i} \boldsymbol{\Omega}_{g_i}^{G_i} = \begin{bmatrix} \hat{b}_1 \cdot \dot{\hat{g}}_{i_1} \\ \hat{b}_2 \cdot \dot{\hat{g}}_{i_1} \\ \hat{b}_3 \cdot \dot{\hat{g}}_{i_1} \end{bmatrix}^B j_{w_{i11}} \boldsymbol{\Omega}_i \quad (236)$$

Using $\dot{\hat{g}}_1 = \dot{\delta} \hat{g}_2$ from Equation (183), Equation (236) becomes

$$\begin{aligned} {}^B \dot{\mathbf{Z}}_1^G \mathbf{J}_{w_i} \boldsymbol{\Omega}_{g_i}^{G_i} &= \begin{bmatrix} \hat{b}_1 \cdot \dot{\hat{g}}_{i_2} \\ \hat{b}_2 \cdot \dot{\hat{g}}_{i_2} \\ \hat{b}_3 \cdot \dot{\hat{g}}_{i_2} \end{bmatrix}^B j_{w_{i11}} \boldsymbol{\Omega}_i \dot{\delta}_i \\ &= {}^B \mathbf{Z}_{2_i}^G \mathbf{J}_{w_i} \boldsymbol{\Omega}_{g_i}^{G_i} \dot{\delta}_i \end{aligned} \quad (237)$$

In summary, all variations are equivalent

$$\begin{aligned} {}^B \dot{\mathbf{Z}}_1^G \mathbf{J}_w \boldsymbol{\Omega}_g^G &= {}^B \mathbf{Z}_2^G \mathbf{J}_w \boldsymbol{\Omega}_g^G \dot{\delta} = \mathbf{A} \mathbf{J}_w \boldsymbol{\Omega}_g^G \dot{\delta} = \frac{\partial}{\partial \delta} ({}^B \mathbf{Z}_1^G) \mathbf{J}_w \boldsymbol{\Omega}_g^G \dot{\delta} \\ {}^B \dot{\mathbf{Z}}_1^G &= {}^B \mathbf{Z}_2^G \dot{\delta} = \mathbf{A} \dot{\delta} = \frac{\partial}{\partial \delta} ({}^B \mathbf{Z}_1^G) \dot{\delta} \end{aligned} \quad (238)$$

The total wheel torque from Equation (229) now becomes

$$\boldsymbol{\tau}_w^B = {}^B\mathbf{Z}_3^G \mathbf{J}_w \ddot{\boldsymbol{\delta}}_g^G + {}^B\mathbf{Z}_2^G \mathbf{J}_w \boldsymbol{\Omega}_g^G \dot{\boldsymbol{\delta}} \quad (239)$$

Assuming like-sized wheels such that $h_w = j_{w_{11}} \boldsymbol{\Omega}_1 = j_{w_{21}} \boldsymbol{\Omega}_2 = j_{w_{n1}} \boldsymbol{\Omega}_n$ becomes a scalar term, the equation can be simplified into

$$\boldsymbol{\tau}_w^B = j_{w_{11}} {}^B\mathbf{Z}_3^G \ddot{\boldsymbol{\delta}}_g^G + j_{w_{11}} \boldsymbol{\Omega}_g^G {}^B\mathbf{Z}_2^G \dot{\boldsymbol{\delta}} \quad (240)$$

Equation (240) shows the final torque equation for the wheels of a CMG array. The equation is dominated by the second term [29]. The first term is dependent upon gimbal accelerations, which are generally slow [27]. The second term is dependent upon a slow gimbal angular velocity, but it is amplified significantly by the very high wheel rate. This is the “torque amplification” that the literature suggests [27, p. 1] [28, p. 160].

In dyadic form, a single CMG’s wheel torque can be found using the time derivative of Equation (223).

$$\begin{aligned} \frac{{}^B d}{dt}(\mathbf{h}_{w_i}^B) = & \dot{j}_{w_{i1}} \boldsymbol{\Omega}_i (\hat{\mathbf{g}}_{i1} \cdot \hat{\mathbf{b}}_1) \hat{\mathbf{b}}_1 + \dot{j}_{w_{i1}} \boldsymbol{\Omega}_i (\hat{\mathbf{g}}_{i1} \cdot \hat{\mathbf{b}}_1) \hat{\mathbf{b}}_1 + \dot{j}_{w_{i1}} \boldsymbol{\Omega}_i (\hat{\mathbf{g}}_{i1} \cdot \hat{\mathbf{b}}_1) \hat{\mathbf{b}}_1 \\ & + j_{w_{i1}} \dot{\boldsymbol{\Omega}}_i (\hat{\mathbf{g}}_{i1} \cdot \hat{\mathbf{b}}_2) \hat{\mathbf{b}}_2 + j_{w_{i1}} \dot{\boldsymbol{\Omega}}_i (\hat{\mathbf{g}}_{i1} \cdot \hat{\mathbf{b}}_2) \hat{\mathbf{b}}_2 + j_{w_{i1}} \dot{\boldsymbol{\Omega}}_i (\hat{\mathbf{g}}_{i1} \cdot \hat{\mathbf{b}}_2) \hat{\mathbf{b}}_2 \\ & + j_{w_{i1}} \boldsymbol{\Omega}_i (\dot{\hat{\mathbf{g}}}_{i1} \cdot \hat{\mathbf{b}}_3) \hat{\mathbf{b}}_3 + j_{w_{i1}} \boldsymbol{\Omega}_i (\dot{\hat{\mathbf{g}}}_{i1} \cdot \hat{\mathbf{b}}_3) \hat{\mathbf{b}}_3 + j_{w_{i1}} \boldsymbol{\Omega}_i (\dot{\hat{\mathbf{g}}}_{i1} \cdot \hat{\mathbf{b}}_3) \hat{\mathbf{b}}_3 \\ & + \dot{j}_{w_{i33}} \dot{\boldsymbol{\delta}}_i (\hat{\mathbf{g}}_{i3} \cdot \hat{\mathbf{b}}_1) \hat{\mathbf{b}}_1 + \dot{j}_{w_{i33}} \dot{\boldsymbol{\delta}}_i (\hat{\mathbf{g}}_{i3} \cdot \hat{\mathbf{b}}_1) \hat{\mathbf{b}}_1 + \dot{j}_{w_{i33}} \dot{\boldsymbol{\delta}}_i (\hat{\mathbf{g}}_{i3} \cdot \hat{\mathbf{b}}_1) \hat{\mathbf{b}}_1 \\ & + j_{w_{i33}} \ddot{\boldsymbol{\delta}}_i (\hat{\mathbf{g}}_{i3} \cdot \hat{\mathbf{b}}_2) \hat{\mathbf{b}}_2 + j_{w_{i33}} \ddot{\boldsymbol{\delta}}_i (\hat{\mathbf{g}}_{i3} \cdot \hat{\mathbf{b}}_2) \hat{\mathbf{b}}_2 + j_{w_{i33}} \ddot{\boldsymbol{\delta}}_i (\hat{\mathbf{g}}_{i3} \cdot \hat{\mathbf{b}}_2) \hat{\mathbf{b}}_2 \\ & + j_{w_{i33}} \dot{\boldsymbol{\delta}}_i (\dot{\hat{\mathbf{g}}}_{i3} \cdot \hat{\mathbf{b}}_3) \hat{\mathbf{b}}_3 + j_{w_{i33}} \dot{\boldsymbol{\delta}}_i (\dot{\hat{\mathbf{g}}}_{i3} \cdot \hat{\mathbf{b}}_3) \hat{\mathbf{b}}_3 + j_{w_{i33}} \dot{\boldsymbol{\delta}}_i (\dot{\hat{\mathbf{g}}}_{i3} \cdot \hat{\mathbf{b}}_3) \hat{\mathbf{b}}_3 \end{aligned} \quad (241)$$

The inertia of the wheel is not changing with respect to the gimbal frame. Also, the orientation of the 3 axis of gimbal frame is not moving with respect to the body frame as determined in Equation (183). The wheel speed is assumed constant.

$$\dot{j}_{w_{i1}} = 0, \dot{j}_{w_{i33}} = 0, \dot{\hat{\mathbf{g}}}_{i1} = \dot{\boldsymbol{\delta}}_i \hat{\mathbf{g}}_{i2}, \dot{\hat{\mathbf{g}}}_{i3} = 0, \dot{\boldsymbol{\Omega}}_i = 0 \quad (242)$$

Equation (241) now becomes

$$\begin{aligned} \frac{{}^B d}{dt}(\mathbf{h}_{w_i}^B) = & j_{wi_{11}} \Omega_i \dot{\delta}_i (\hat{g}_{i2} \cdot \hat{b}_3) \hat{b}_3 + j_{wi_{11}} \Omega_i \dot{\delta}_i (\hat{g}_{i2} \cdot \hat{b}_3) \hat{b}_3 + j_{wi_{11}} \Omega_i \dot{\delta}_i (\hat{g}_{i2} \cdot \hat{b}_3) \hat{b}_3 \\ & + j_{wi_{33}} \ddot{\delta}_i (\hat{g}_{i3} \cdot \hat{b}_2) \hat{b}_2 + j_{wi_{33}} \ddot{\delta}_i (\hat{g}_{i3} \cdot \hat{b}_2) \hat{b}_2 + j_{wi_{33}} \ddot{\delta}_i (\hat{g}_{i3} \cdot \hat{b}_2) \hat{b}_2 \end{aligned} \quad (243)$$

$$\frac{{}^B d}{dt}(\mathbf{h}_{w_i}^B) = \begin{bmatrix} \hat{b}_1 \cdot \hat{g}_{i_2} \\ \hat{b}_2 \cdot \hat{g}_{i_2} \\ \hat{b}_3 \cdot \hat{g}_{i_2} \end{bmatrix}^B j_{wi_{33}} \Omega_i \dot{\delta}_i + \begin{bmatrix} \hat{b}_1 \cdot \hat{g}_{i_3} \\ \hat{b}_2 \cdot \hat{g}_{i_3} \\ \hat{b}_3 \cdot \hat{g}_{i_3} \end{bmatrix}^B j_{gi_{33}} \ddot{\delta}_i . \quad (244)$$

The first term again validates the claim made in Equation (237).

3. Total Momentum and Torque

The combined CMG gimbal and wheel momentum and torque are now

$$\begin{aligned} \mathbf{h}_{CMG}^B &= \mathbf{h}_g^B + \mathbf{h}_w^B \\ &= ({}^B \mathbf{Z}_3^G \mathbf{J}_g \dot{\delta}_g^G) + ({}^B \mathbf{Z}_3^G \mathbf{J}_w \dot{\delta}_g^G + {}^B \mathbf{Z}_1^G \mathbf{J}_w \Omega_g^G) \\ &= {}^B \mathbf{Z}_3^G (j_{g33} + j_{w33}) \dot{\delta}_g^G + {}^B \mathbf{Z}_1^G j_{w11} \Omega_g^G \\ &= (j_{g33} + j_{w33}) {}^B \mathbf{Z}_3^G \dot{\delta}_g^G + j_{w11} {}^B \mathbf{Z}_1^G \Omega_g^G \end{aligned} \quad (245)$$

$$\begin{aligned} \boldsymbol{\tau}_{CMG}^B &= \boldsymbol{\tau}_g^B + \boldsymbol{\tau}_w^B \\ &= ({}^B \mathbf{Z}_3^G j_{g33} \ddot{\delta}_g^G) + ({}^B \mathbf{Z}_3^G j_{w33} \ddot{\delta}_g^G + {}^B \mathbf{Z}_2^G j_{w11} \Omega_g^G \dot{\delta}_g^G) \\ &= {}^B \mathbf{Z}_3^G (j_{g33} + j_{w33}) \ddot{\delta}_g^G + {}^B \mathbf{Z}_2^G (j_{w11} \Omega_g^G) \dot{\delta}_g^G \\ &= (j_{g33} + j_{w33}) {}^B \mathbf{Z}_3^G \ddot{\delta}_g^G + (j_{w11} \Omega_g^G) {}^B \mathbf{Z}_2^G \dot{\delta}_g^G \end{aligned} \quad (246)$$

By Euler's transport theorem, the inertial derivative is

$$\begin{aligned} \frac{{}^N d}{dt}(\mathbf{h}_{CMG}^N) &= \frac{{}^B d}{dt}(\mathbf{h}_{CMG}^B) + {}^N \boldsymbol{\omega}^B \times \mathbf{h}_{CMG}^B \\ \dot{\mathbf{h}}_{CMG}^N &= \dot{\mathbf{h}}_{CMG}^B + {}^N \boldsymbol{\omega}^B \times \mathbf{h}_{CMG}^B \end{aligned} \quad (247)$$

Equation (247) can be rewritten by substituting the angular momentum terms

$$\begin{aligned} \dot{\mathbf{h}}_g^N &= (j_{g33} + j_{w33}) {}^B \mathbf{Z}_3^G \ddot{\delta}_g^G + (j_{w11} \Omega_g^G) {}^B \mathbf{Z}_2^G \dot{\delta}_g^G \\ &\quad + {}^N \boldsymbol{\omega}^G \times ((j_{g33} + j_{w33}) {}^B \mathbf{Z}_3^G \dot{\delta}_g^G + j_{w11} {}^B \mathbf{Z}_3^G \dot{\delta}_g^G) \end{aligned} \quad (248)$$

Like reaction wheels, CMGs are subject to the same pseudo-inverse law. Much like the pseudo-inverse of the reaction wheel orientation matrix, ${}^B\mathbf{Z}_2^G$ (or \mathbf{A}) can be inverted using the same method. Here \mathbf{Z}^+ will be used to map the three body axes back to n CMGs.

$$\begin{aligned} -\boldsymbol{\tau}_{req}^N = & \left(j_{g_{33}} + j_{w_{33}}\right)^G \mathbf{Z}_3^G \dot{\boldsymbol{\delta}}_g^G + \left(j_{w_{11}} \Omega_g^G\right)^B \mathbf{Z}_2^G \dot{\boldsymbol{\delta}} \\ & + {}^N\boldsymbol{\omega}^G \times \left(\left(j_{g_{33}} + j_{w_{33}}\right)^G \mathbf{Z}_3^G \dot{\boldsymbol{\delta}}_g^G + j_{w_{11}} {}^B\mathbf{Z}_3^G \dot{\boldsymbol{\delta}}_g^G\right) \end{aligned} \quad (249)$$

Although Equation (249) shows the full dynamics, the gyroscopic coupling of the body motion with the gimbal rate can be assumed as very small [29]. Additionally the gimbal acceleration can be assumed small [29]. Therefore, Equation (249) can be reduced to Equation (250) and rearranged per Equation (251) using the pseudo-inverse.

$$\begin{aligned} -\boldsymbol{\tau}_{req}^N &= \left(j_{w_{11}} \Omega_g^G\right)^B \mathbf{Z}_2^G \dot{\boldsymbol{\delta}} \\ &= {}^B\mathbf{Z}_2^G h_w^G \dot{\boldsymbol{\delta}} \\ &= {}^B\mathbf{Z}_2^G \boldsymbol{\tau}_w^G \end{aligned} \quad (250)$$

$$\begin{aligned} \dot{\boldsymbol{\delta}}_g^G &= \left(j_{w_{11}} \Omega_g^G\right)^{-1} \left[{}^B\mathbf{Z}_2^G \right]^+ \left(-\boldsymbol{\tau}_{req}^N\right) \\ &= \left(h_w^G\right)^{-1} \left[{}^B\mathbf{Z}_2^G \right]^+ \left(-\boldsymbol{\tau}_{req}^N\right) \\ &= \left(h_w^G\right)^{-1} \left(\boldsymbol{\tau}_w^G\right) \end{aligned} \quad (251)$$

This is the same steering logic proposed in [6, Algorithm 7.147]. Therefore, the assumptions above were taken as well.

D. MODELING CMGS

In order to apply the physical actuator limitations of the CMG as part of the simulation model, the torque required of the assembly must be broken down, individual gimbal and wheel limit saturations applied, and then the torque of the CMG assembly rebuilt. Within Figure 63, (251) is used to break down the torque required and allocate it across the four wheels. The orientation matrix \mathbf{Z} block consists of Figures 60–62.

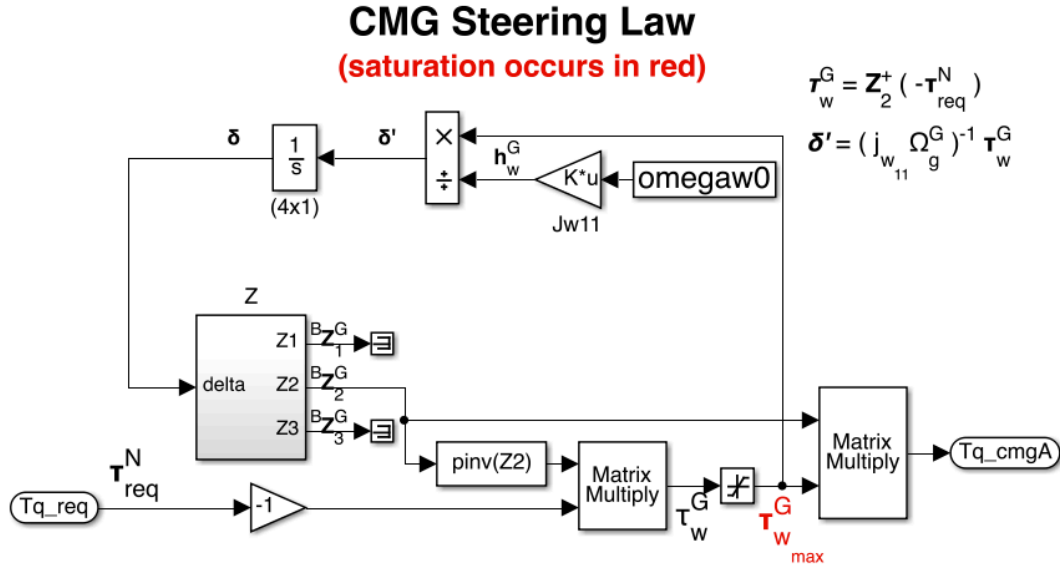


Figure 63. CMG Model

This CMG model can be further expanded to include null motion in the presence of near-singular ${}^B\mathbf{Z}_2^G$ conditions. Additionally, the components of Equation (249) can be modeled, but Equation (251) is modeled here for simplicity.

E. CMG MOMENTUM SPACE

The boundary created by the maximum momentum in any given direction for a particular CMG configuration is much more difficult to define than that of a reaction wheel configuration. The momentum space is no longer a three-dimensional geometric envelope with all interior points possible. The physical limitation is still the vector sum of the maximum capacities of the individual CMGs, where momentum saturation occurs. Unlike reaction wheels, the surface is not a polyhedron. Instead, the CMG momentum envelope is contains singular cavities that pass through the center from one edge of the momentum space to the other.

Like the reaction wheel case, maximum momentum space for an evenly spaced ($\Delta\alpha = 90^\circ$) four-CMG array is when $\beta = 54.73^\circ$ [30, p. 866]. The resulting surface is shown in Figure 64. Since the gimbal axis \hat{g}_{3_i} and the wheel angular momentum \hat{g}_{1_i} are always perpendicular, a reduced amount of wheel momentum is available on the surface

of the momentum envelope, which is set within the body frame ($\hat{g}_{i_3} \times \hat{h}_{cmgA}^B = 1$ or $\hat{g}_{i_1} \cdot \hat{h}_{cmgA}^B = \hat{g}_{i_2} \cdot \hat{h}_{cmgA}^B = 0$). These regions are identified by white cavities in Figure 64, in which 2^n cavities exist [28, p. 161]. The identification of singular surfaces will be discussed in Section E.

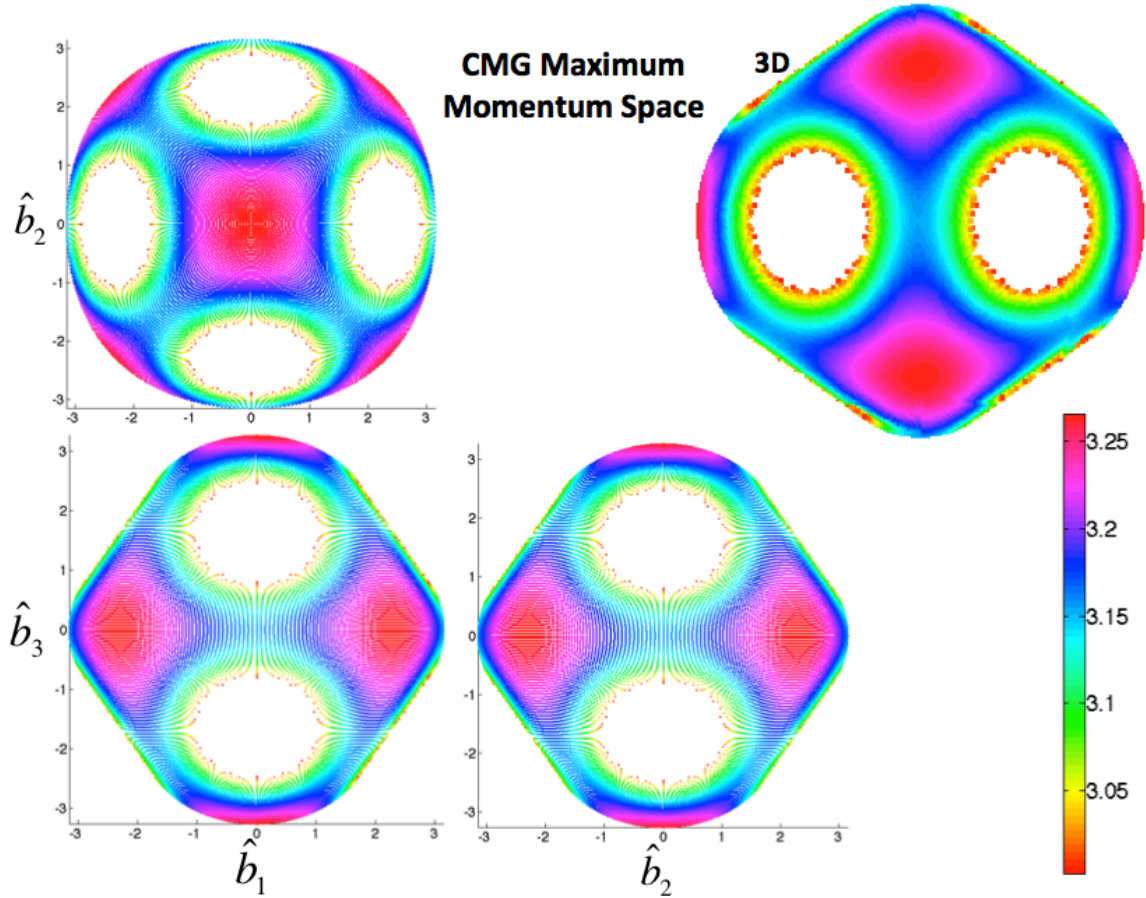


Figure 64. Momentum Space of a 4 CMG System Given $\beta=54.73^\circ$

The shape within Figure 64 is unique to this four-CMG system. The shape alone reveals configurations of maximum momentum. The momentum peaks help identify the best possible axes to rotate about. These maximums occur at $h_{\max}^B = 3.266h_{\max}$, revealing that when using CMGs in comparison with similarly sized reaction wheels, 40% more momentum is achievable about certain axes.

$$\frac{h_{cmg_{max}}^B}{h_{rw_{max}}^B} = \frac{3.266 h_{max}}{2.309 h_{max}} = 1.414 \quad (252)$$

The concept of placing a momentum sphere directly inside the minimum radius of this shape does not make sense because the shape is concave. This leads the discussion to CMG singularities.

F. CMG SINGULARITIES

Within a singular gimbal angle configuration, it is not possible to produce a torque in certain directions. Therefore, the required torque may or may not be produced. Singular states occur when the rank of ${}^B\mathbf{Z}_2^G$ is not full (less than n CMGs). This condition can occur because ${}^B\mathbf{Z}_2^G$ is state dependent.

$${}^B\mathbf{Z}_2^{G_i}(\delta_i) = \begin{bmatrix} -s\alpha_i c\delta_i - c\alpha_i c\beta s\delta_i \\ c\alpha_i c\delta_i - s\alpha_i c\beta s\delta_i \\ s\beta s\delta_i \end{bmatrix}^{G_i} \quad (253)$$

If a configuration of delta leads two CMGs to yield the same columns within their respective \mathbf{Z} matrix, then a singular state occurs. The entire array for the [0,90,180,270] arrangement is shown in Equation (254).

$${}^B\mathbf{Z}_2^G = \begin{bmatrix} -c\beta s\delta_1 & -c\delta_2 & c\beta s\delta_3 & -c\delta_4 \\ c\delta_1 & -c\beta s\delta_2 & -c\delta_3 & c\beta s\delta_4 \\ s\beta s\delta_1 & s\beta s\delta_2 & s\beta s\delta_3 & s\beta s\delta_4 \end{bmatrix}^G \quad (254)$$

For example, when $\delta_1 = 0^\circ$ and $\delta_3 = 180^\circ$, two columns are the same. Therefore, $rank({}^B\mathbf{Z}_2^G) = 2$, which is not full. Therefore, a singular condition results during the pseudo-inverse.

$${}^B\mathbf{Z}_2^G(0^\circ, \delta_2, 180^\circ, \delta_4) = \begin{bmatrix} 0 & -c\delta_2 & 0 & -c\delta_4 \\ 1 & -c\beta s\delta_2 & 1 & c\beta s\delta_4 \\ 0 & s\beta s\delta_2 & 0 & s\beta s\delta_4 \end{bmatrix}^G \quad (255)$$

This is just one of many different configurations can reduce the rank and cause a singular condition.

1. Solving Singularity Conditions

A detailed procedure and set of equations for determining the singularity conditions and associated singular momentum vectors is given in [6, pp. 676–678]. CMG singularity occurs when the magnitude of the dot product of the wheel momentum vector and the spacecraft rotation axis is one: $\hat{g}_{i_1} \cdot \hat{h}_{cmgA}^B = \hat{h}_i^B \cdot \hat{h}_{cmgA}^B = \pm 1$. In this thesis, only the results of the four CMG case will be analyzed. The singularity condition for each CMG can be written as

$$\mathbf{h}_i^B = \pm \frac{(\hat{g}_{i_3} \times \hat{h}_{cmgA}^B) \times \hat{g}_{i_3}}{\hat{h}_i^B \cdot \hat{h}_{cmgA}^B} = \pm \frac{(\hat{g}_{i_3} \times \hat{h}_{cmgA}^B) \times \hat{g}_{i_3}}{\hat{g}_{i_3} \times \hat{h}_{cmgA}^B} = \frac{(\hat{g}_{i_3} \times \hat{h}_{cmgA}^B) \times \hat{g}_{i_3}}{e_i}. \quad (256)$$

The vectors e_i contain the cross product of the individual CMG gimbal vectors and the total body momentum unit vector \hat{h}_{cmgA}^B . Both positive and negative variations are accounted for within Equation (257) by the sign function of Equation (258).

$$\begin{aligned} e_1 &= \pm \sqrt{1 - (s\beta \hat{h}_{cmgA_x}^B + c\beta \hat{h}_{cmgA_z}^B)^2} \\ e_2 &= \pm \sqrt{1 - (s\beta \hat{h}_{cmgA_y}^B + c\beta \hat{h}_{cmgA_z}^B)^2} \\ e_3 &= \pm \sqrt{1 - (-s\beta \hat{h}_{cmgA_x}^B + c\beta \hat{h}_{cmgA_z}^B)^2} \\ e_4 &= \pm \sqrt{1 - (-s\beta \hat{h}_{cmgA_y}^B + c\beta \hat{h}_{cmgA_z}^B)^2} \end{aligned} \quad (257)$$

$$\epsilon_i = \text{sign}(e_i) = \pm 1 \quad (258)$$

The total CMG array momentum in the body frame is created using Equation (259).

$$\mathbf{h}_{cmgA}^B = \sum_{n=1}^n \mathbf{h}_i^B = \sum_{n=1}^n \frac{(\hat{g}_{i_3} \times \hat{h}_{cmgA}^B) \times \hat{g}_{i_3}}{e_i} \quad (259)$$

Individually accounting for each body axis separately, Equation (259) can be written as Equation (260).

$$\begin{aligned}
h_x^B &= \frac{c\beta(c\beta\hat{\mathbf{h}}_{cmgA_x}^B - s\beta\hat{\mathbf{h}}_{cmgA_z}^B)}{e_1} + \frac{\hat{\mathbf{h}}_{cmgA_x}^B}{e_2} + \frac{c\beta(c\beta\hat{\mathbf{h}}_{cmgA_x}^B - s\beta\hat{\mathbf{h}}_{cmgA_z}^B)}{e_3} + \frac{\hat{\mathbf{h}}_{cmgA_x}^B}{e_4} \\
h_y^B &= \frac{\hat{\mathbf{h}}_{cmgA_y}^B}{e_1} + \frac{c\beta(s\beta\hat{\mathbf{h}}_{cmgA_z}^B - c\beta\hat{\mathbf{h}}_{cmgA_y}^B)}{e_2} + \frac{\hat{\mathbf{h}}_{cmgA_y}^B}{e_3} + \frac{c\beta(s\beta\hat{\mathbf{h}}_{cmgA_z}^B + c\beta\hat{\mathbf{h}}_{cmgA_y}^B)}{e_4} \\
h_z^B &= \frac{s\beta(s\beta\hat{\mathbf{h}}_{cmgA_z}^B - c\beta\hat{\mathbf{h}}_{cmgA_x}^B)}{e_1} + \frac{s\beta(s\beta\hat{\mathbf{h}}_{cmgA_z}^B - c\beta\hat{\mathbf{h}}_{cmgA_y}^B)}{e_2} \\
&\quad + \frac{s\beta(s\beta\hat{\mathbf{h}}_{cmgA_z}^B + c\beta\hat{\mathbf{h}}_{cmgA_x}^B)}{e_3} + \frac{s\beta(s\beta\hat{\mathbf{h}}_{cmgA_z}^B + c\beta\hat{\mathbf{h}}_{cmgA_y}^B)}{e_4}
\end{aligned} \tag{260}$$

Given four CMGs, there are 16 (2^n) combinations of ϵ_i that produce different singular conditions. When ϵ_i has the same sign for all CMGs ($\epsilon = \pm \begin{bmatrix} 1 & 1 & 1 & 1 \end{bmatrix}^T$), the outer singularity surface shown in Figure 64 is produced. Other combinations result in interior singularities: states that are contained within the volume of the CMG momentum envelope.

Interior singularities mean that at some non-maximum momentum (within the set defined by the geometry of Figure 64), the required torque magnitude or direction cannot be created exactly, creating an off-eigenaxis rotation. Two types of internal singularities exist: hyperbolic and elliptic singularities. The names derive from the shape of the gimbal angle motion in the neighborhood of a singular point. These are discussed in detail within [3, pp. 23–30].

2. Hyperbolic Singularities

Hyperbolic singularities are the milder of the two internal singularities, considered passible in [3, pp. 23–30]. This is the case when the CMG array cannot exactly produce the required torque. A specific gimbal signal can be added to the steering logic whenever a singular state is detected. This null motion produces no net torque on the system, but assists in passing through hyperbolic singularities. They occur when

exactly two of the ϵ_i have mismatched signs. The six combinations are shown in the following three cases.

$$\epsilon_i = \pm \begin{bmatrix} 1 \\ 1 \\ -1 \\ -1 \end{bmatrix}, \epsilon_i = \pm \begin{bmatrix} 1 \\ -1 \\ 1 \\ -1 \end{bmatrix}, \epsilon_i = \pm \begin{bmatrix} 1 \\ -1 \\ -1 \\ 1 \end{bmatrix} \quad (261)$$

The hyperbolic singularities make up the very center of the shape, extending from the origin (zero momentum) to a maximum momentum magnitude of 1.897 at its largest. A graphical depiction of case 2 ($\epsilon = \pm [1 \ -1 \ 1 \ -1]^T$) is shown in Figure 65. It is noteworthy that it is symmetric about all three body axes.

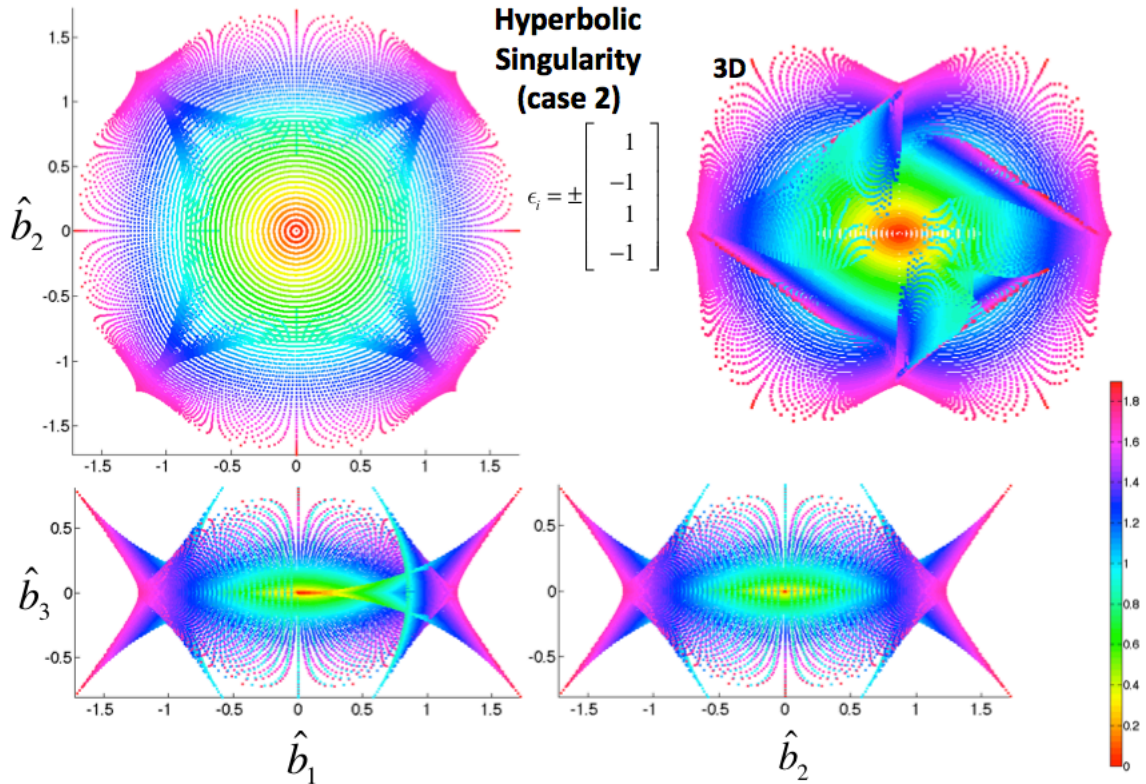


Figure 65. Hyperbolic Singularity Surface for $\epsilon_i = \pm [1 \ -1 \ 1 \ -1]^T$

Figure 66 demonstrates all three cases plotted together. Each of the cases extended from the origin to $1.897 h_{\max}$.

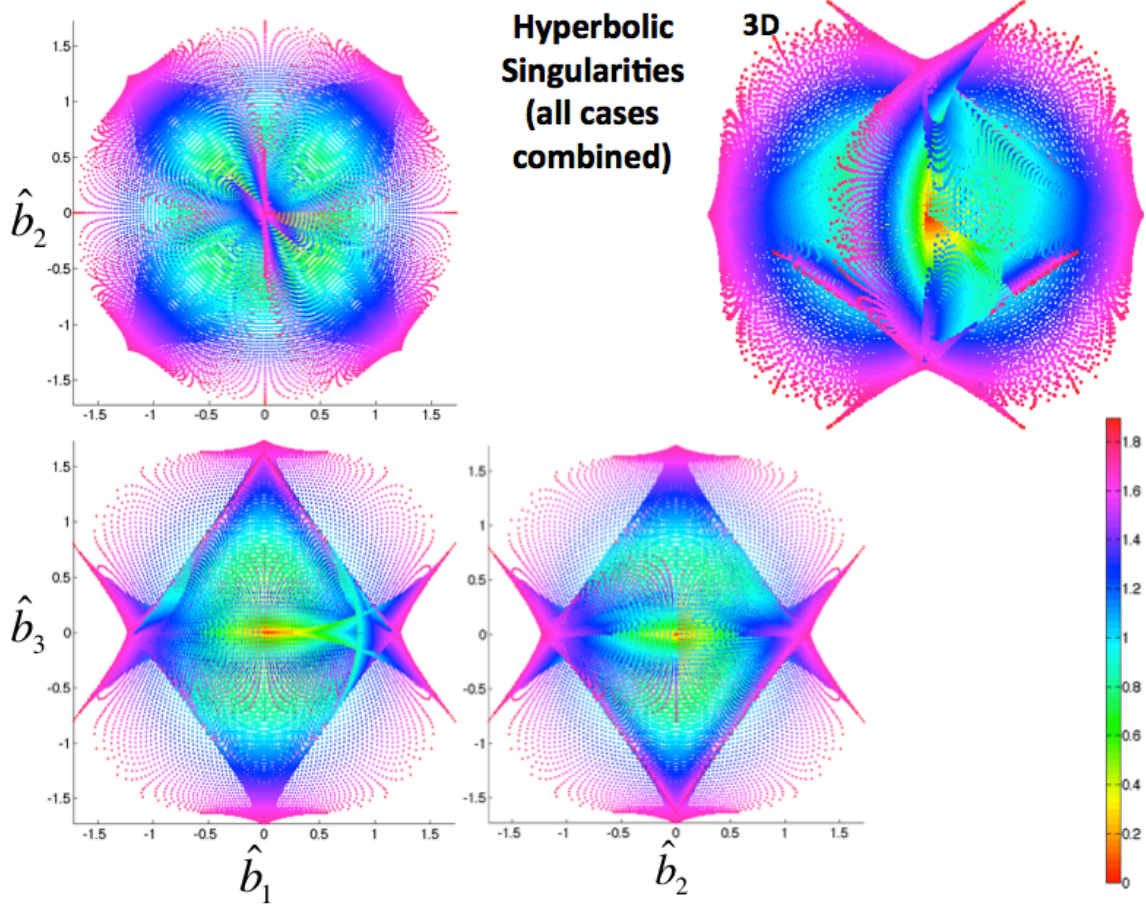


Figure 66. Hyperbolic Singularities

3. Elliptic Singularities

Elliptic Singularities occur when the torques allowable by the physical layout of the CMGs are perpendicular to the required torque [11, p. 179]. They are impassible [3]. Elliptic singularities occur when only one ϵ_i sign is mismatched. The eight possible combinations are shown.

$$\epsilon_i = \pm \begin{bmatrix} -1 \\ 1 \\ 1 \\ 1 \end{bmatrix}, \epsilon_i = \pm \begin{bmatrix} 1 \\ -1 \\ 1 \\ 1 \end{bmatrix}, \epsilon_i = \pm \begin{bmatrix} 1 \\ 1 \\ -1 \\ 1 \end{bmatrix}, \epsilon_i = \pm \begin{bmatrix} 1 \\ 1 \\ 1 \\ -1 \end{bmatrix} \quad (262)$$

The elliptic singularities extend across the width of the shape, extending from a minimum of 1.0069 to a maximum of $2.998 h_{\max}$ at its largest. A graphical depiction of case 1 $\left(\epsilon = \pm \begin{bmatrix} -1 & 1 & 1 & 1 \end{bmatrix}^T \right)$ is shown in Figure 67. It is noteworthy that the singular surface is oriented at the skew angle $(\beta = 54.73^\circ)$ due to the alignment of the CMG.

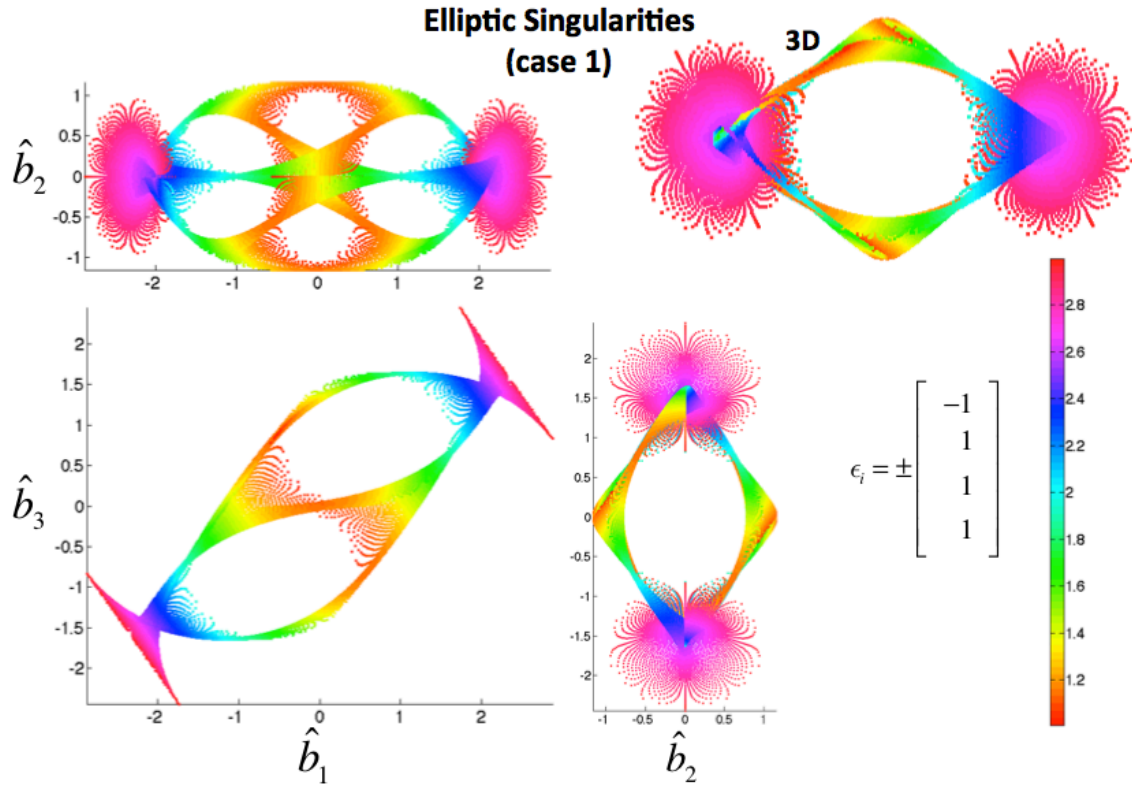


Figure 67. Elliptic Singularity Surface (case 1)

Given all cases at once, independent plots extend across the momentum space, shown in Figure 68.

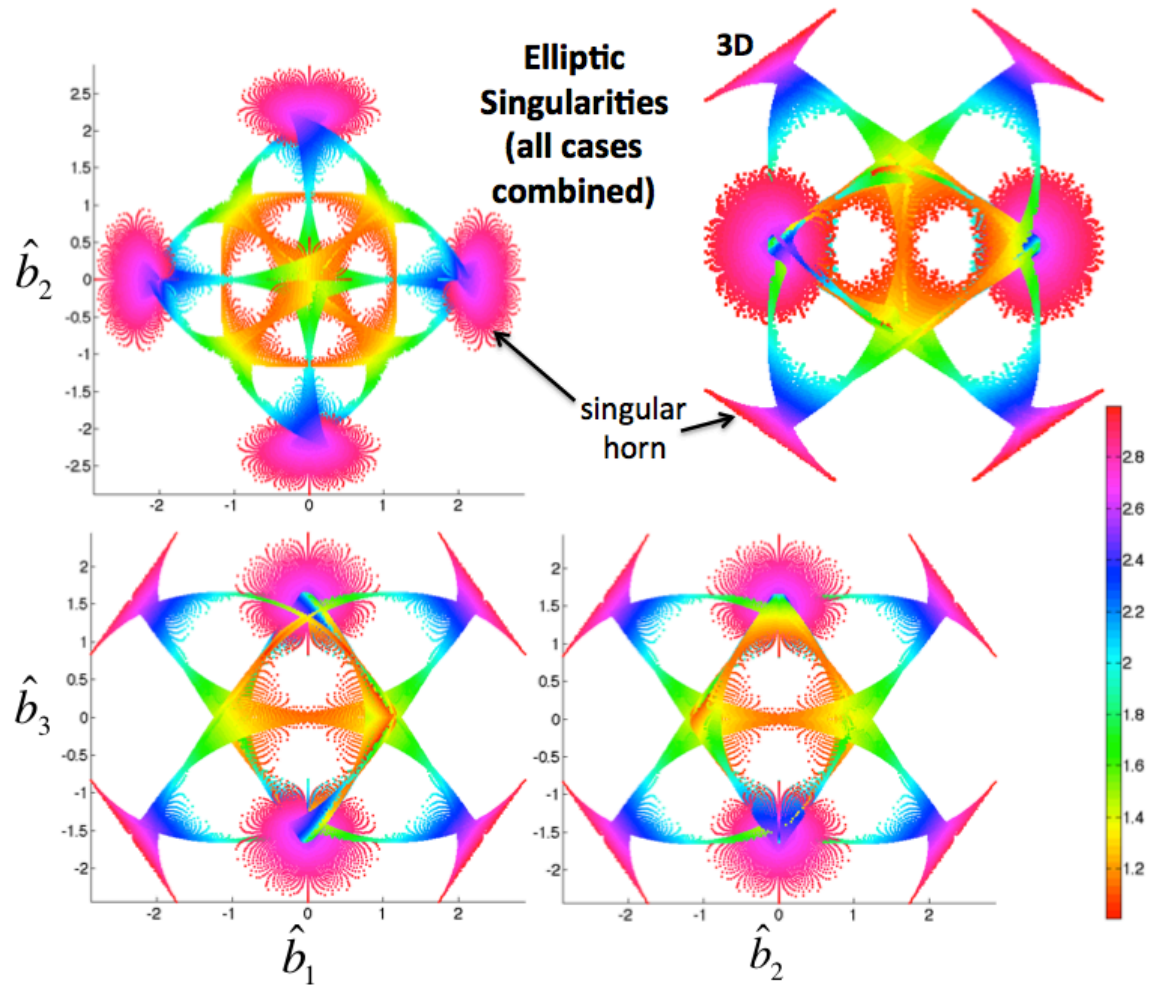


Figure 68. Elliptic Singularities

Most interestingly, the eight interior horns shown in Figure 68 align with the eight hollow circles shown in the perimeter volume in Figure 64. This union is shown in Figure 69.

Elliptic and Surface Singularities Combined

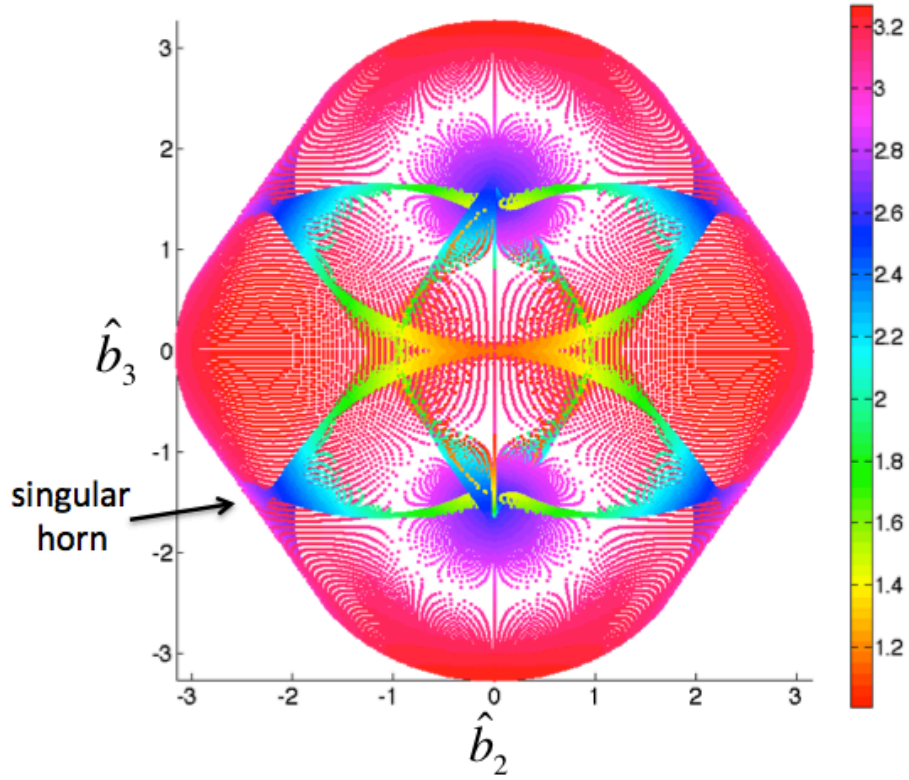


Figure 69. Elliptic and Surface Singularities

G. CMG LARGEST INSCRIBED SPHERE

This thesis will not focus on complicated CMG singularity avoidance algorithms, an ongoing and developing research area in its own regard. In CMG systems, it may be easiest to treat these singularities simply as impassible in order to avoid exotic controllers. To create a volume that is guaranteed reachable, the minimum momentum magnitude of the elliptic singularity region must be completely avoided. Since this minimum occurs at the calculated values of $1.0069h_{\max}$ ($1.0h_{\max}$ in [3]), this also creates the largest sphere of guaranteed momentum capability. Superimposing a sphere into the elliptic region creates the space of guaranteed mobility, shown in Figure 72.

Largest Guaranteed Passible Sphere

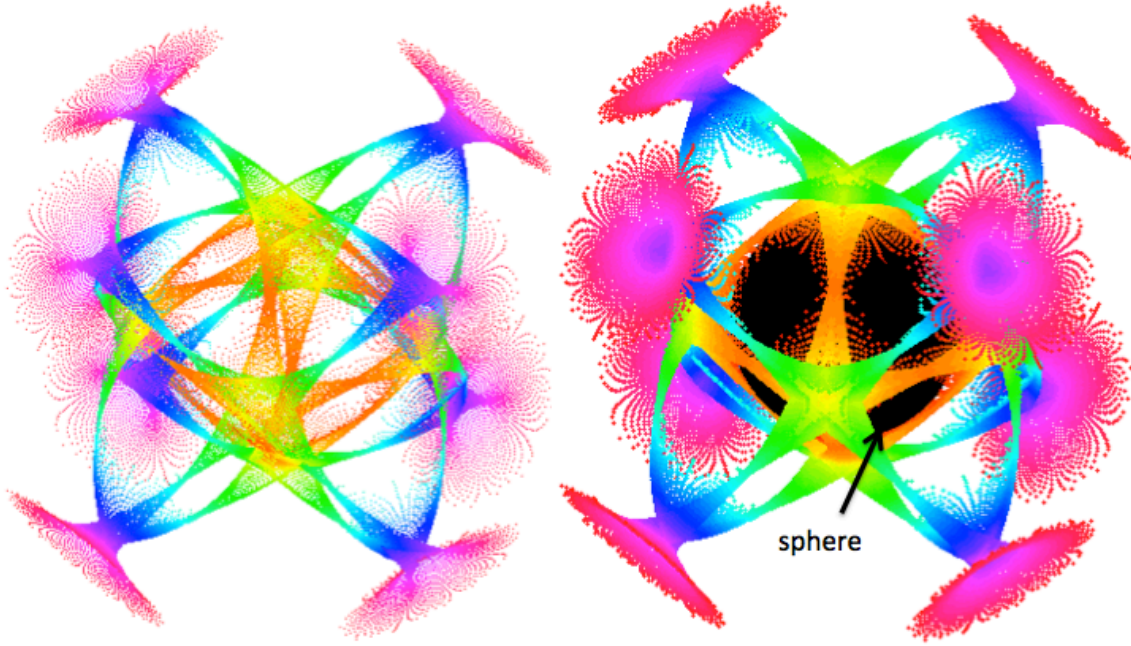


Figure 70. CMG Largest Sphere

This reveals that the maximum guaranteed momentum capacity is $1.0069 h_{\max}$, 69% smaller than originally estimated in Equation (252).

$$\frac{h_{cmg_{\max}}^B}{h_{rw_{\max}}^B} = \frac{1.0069 h_{\max}}{3.266 h_{\max}} = 0.3083 \quad (263)$$

This means the available momentum in the CMG case is actually less than that of the reaction wheel cases: recall $1.633 h_{\max}$ for the full reaction wheel and $1.333 h_{\max}$ for the pseudo-inverse limited reaction wheel.

H. SUMMARY

This chapter was used to develop the CMG equations of motion from the first principle of conservation of angular momentum. The additional moving frame causes CMG dynamics to be much more complex than reaction wheel dynamics. The orientation matrix was shown to be state-dependent, which leads to singularities. Certain CMG arrangements lead to different types of singularities that can cause controller failure. Elliptic singularities are non-passable and hyperbolic singularities are passable.

The singularities were individually mapped in three-dimensional momentum space to demonstrate where they occur. The momentum envelope was combined with both of the interior hyperbolic and elliptic singularities to demonstrate their intersection. Using the simplification that elliptic singularities must be avoided and hyperbolic singularities are passable, a sphere of accessible momentum was identified. The radius of this sphere guarantees the momentum of $1.0069h_{\max}$ about any axis of rotation. Therefore, this momentum value can be used to maneuver the CMG about any eigenaxis.

Despite the lost momentum capacity and required complex ACS architecture, torque amplification remains the primary driver for CMG desirability over reaction wheels. For CMGs, a small gimbal input results in a large torque output. This relationship is quantified in Chapter VII.

THIS PAGE INTENTIONALLY LEFT BLANK

VII. REACTION WHEEL AND CMG COMPARISON

The previous chapters were used to develop the necessary background and equations of motion to support a detailed discussion within this chapter. This chapter is used to help bridge the performance gap between reaction wheels and CMGs. Instead of insisting that CMGs must be used for highly agile spacecraft, this chapter will introduce some concepts for sizing reaction wheels to attain the required slew performance. In some cases CMGs will be more desirable, but this chapter will illustrate that for some satellite systems, reaction wheels can potentially outperform CMGs.

A. MOMENTUM SPACE AS A VISUALIZATION TOOL

In Chapter IV, the reaction wheel momentum space was discussed. Due to the use of the pseudo-inverse for control allocation, the entire momentum and torque space was not available for control. Also, there is no real reason to stay on the eigenaxis, despite the fact the eigenaxis maneuvers have been historically implemented on spacecraft. The input can be shaped in quaternion space to move around the momentum space, searching for the axes of maximum momentum and torque (vertices from Chapter IV). This allows the slew time to be reduced and/or optimized, regardless of the slew distance and path traveled. Recall from Chapter V that for a successful maneuver, it is the boundary conditions that must be satisfied, not the path itself.

Consider a 120° eigenaxis slew about $\mathbf{e} = \begin{bmatrix} \sqrt{2/3} & 0 & 2/\sqrt{3} \end{bmatrix}^T$. The same spacecraft/reaction wheel configuration from Chapter V, Sections F-G will be used. A trapezoidal input is fed into the system, accounting for the limitations of the pseudo-inverse. The dynamic response of the reaction wheel array is used to build Figures 71–72. The vectors in the body frame are normalized against the individual wheel maximum.

$$\begin{aligned} \mathbf{h}_{norm}^B &= \mathbf{h}^B / h_{\max} \\ \boldsymbol{\tau}_{norm}^B &= \boldsymbol{\tau}^B / \tau_{\max} \end{aligned} \tag{264}$$

For a reaction wheel system, the shapes of the momentum and torque envelopes are exactly the same. Thus, normalization via (264) allows both momentum and torque

signals to be compared on the same scale. Figure 73 shows the scaled system response to the shaped input. Only the relative magnitude is shown with no regard for direction. The system follows the signal exactly: bang-coast-bang. The only deviation is a discontinuity at Point 5. This occurred because the shaped trajectory implemented cut the velocity off when the angle reached 0.999 of the final angle, causing a split second of unpredictable acceleration, and is an artifact of the simulated model only.

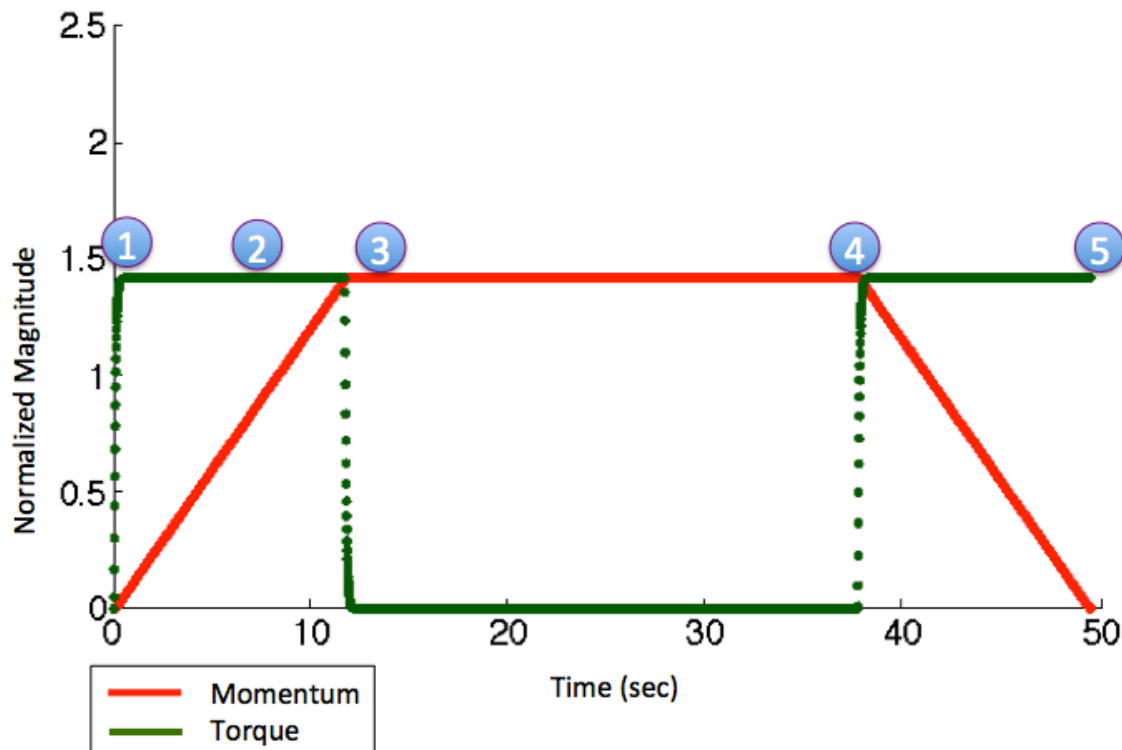


Figure 71. Normalized Momentum and Torque for a Trapezoidal Response

The same maneuver is next mapped onto the momentum and torque space in Figure 72. Since the maneuver is an eigenaxis maneuver, the momentum travels from zero to maximum momentum within the envelope defined by the pseudo-inverse control allocation, yet the axis of rotation remains fixed. The numbered points reflect those from Figure 71. On the right is the torque mapping. The locations of Points 1,2 are maximum torque in the direction of the eigenaxis. Point 5 demonstrates a strong torque reversal to decelerate the system.

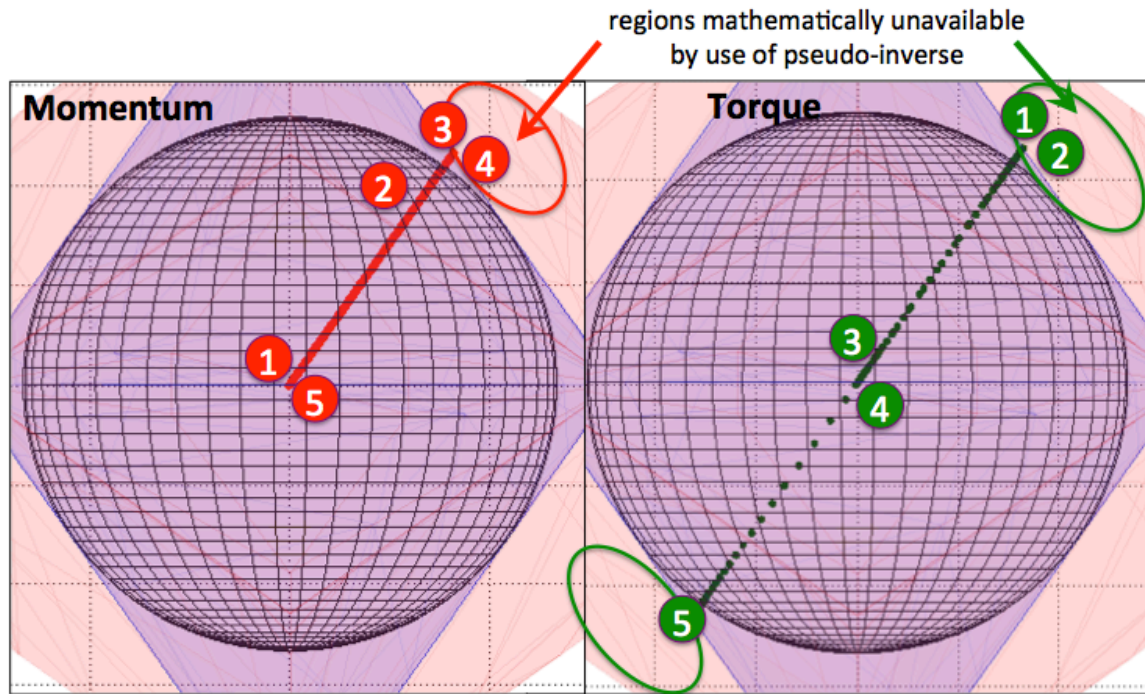


Figure 72. Momentum/Torque Space During Eigenaxis Slew

The results shown in Figure 72 are uninteresting, and it is not surprising that this envelope mapping is not used to help visualize conventional reorientations. The same maneuver will now be illustrated using the optimal control approach described in Chapter V, Figures 51–53.

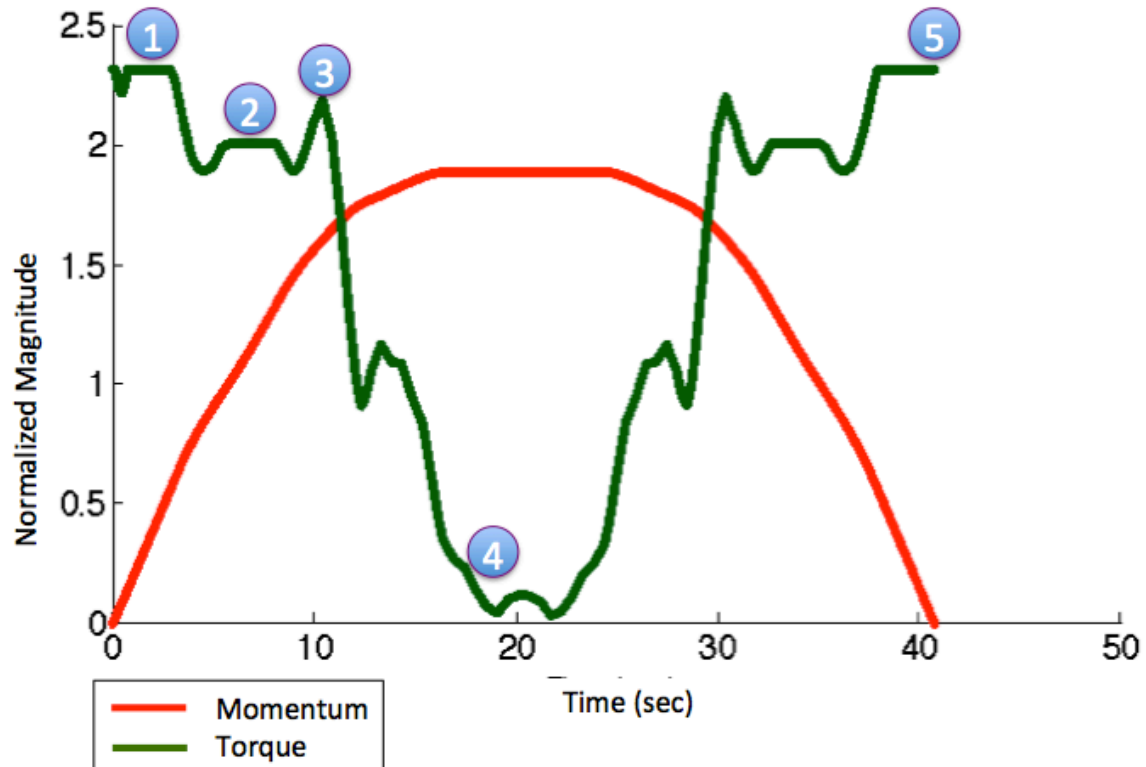


Figure 73. Normalized Momentum and Torque for an Optimal Maneuver

Now the temporal element of the identified points becomes important. The following is a description of the instantaneous rotation axis as it pertains to Points 1–5 given in Figures 73 and 74.

- Point 1. The array pulled far off eigenaxis at the point of maximum torque, a maximum vertex at $2.309 \tau_{\max}$. This allowed the system to gain momentum as quickly as possible.
- Point 2. The array quickly moved along the edge of the torque space to a minor vertex at $2.000 \tau_{\max}$.
- Point 3. The array rapidly changed directions again, this time to another maximum vertex at $2.309 \tau_{\max}$. Next, the torque decelerated the system as it pulled the rotation angle close to the eigenaxis.
- Point 4. The rotation angle wobbled around the eigenaxis, forming a lasso-like loop near maximum momentum. The torque remained close to zero, making a few adjustments necessary to keep the orientation direction on track.
- Point 5. Point 1 is reversed to decelerate the array.

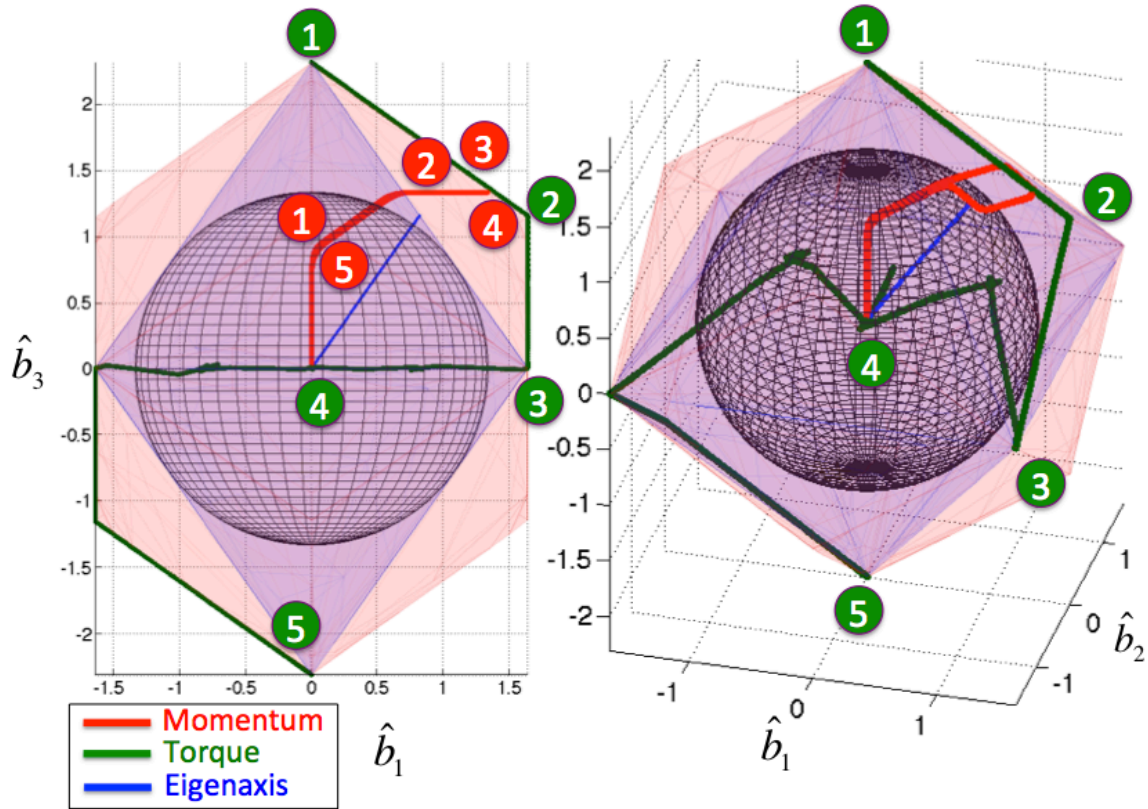


Figure 74. Momentum/Torque Space During Optimal Maneuver

The type of action shown in Figure 74 is common for most optimal maneuvers. The activity appears unintuitive, but trends develop. Torque seeks high ground to raise the momentum quickly. Torque and momentum follow the edges and vertices as they move around. Rarely does the maneuver stay very close to the actual eigenaxis. Figures 75 and 76 represent two more maneuvers to further illustrate some of the interesting behavior, obtained as a result of optimizing the slews. The same momentum limits are used, but the torque is doubled to 0.2 Nm to illustrate different maneuvers.

The optimal use of the full momentum and torque envelopes is extremely interesting. The momentum and torque move like water encased in a polyhedron, flowing to high surfaces. The system always seems to tend towards maximum torque in a particular direction to maximize the momentum in order to rapidly maneuver the spacecraft.

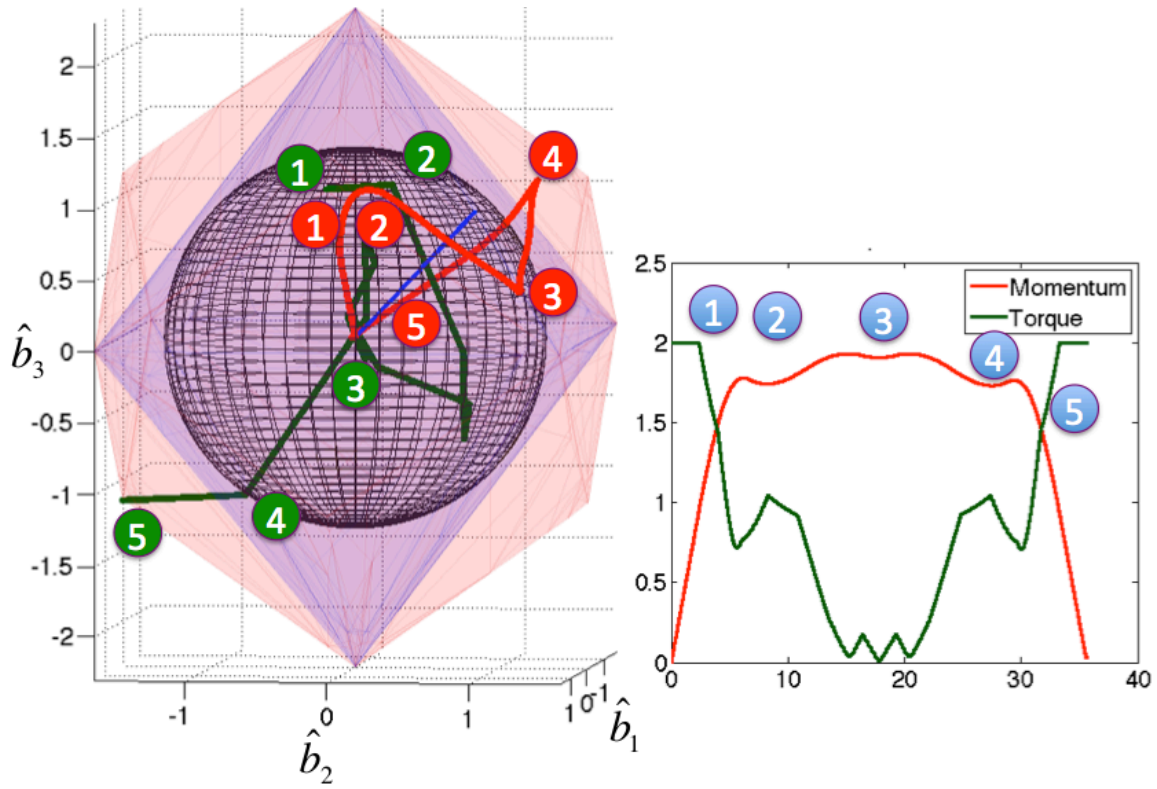


Figure 75. Optimal Slew Example 2, $q_0=[0.36 \ 0 \ 0.79 \ 0.5]$, $q_f=[0 \ 0 \ 0 \ 1]$

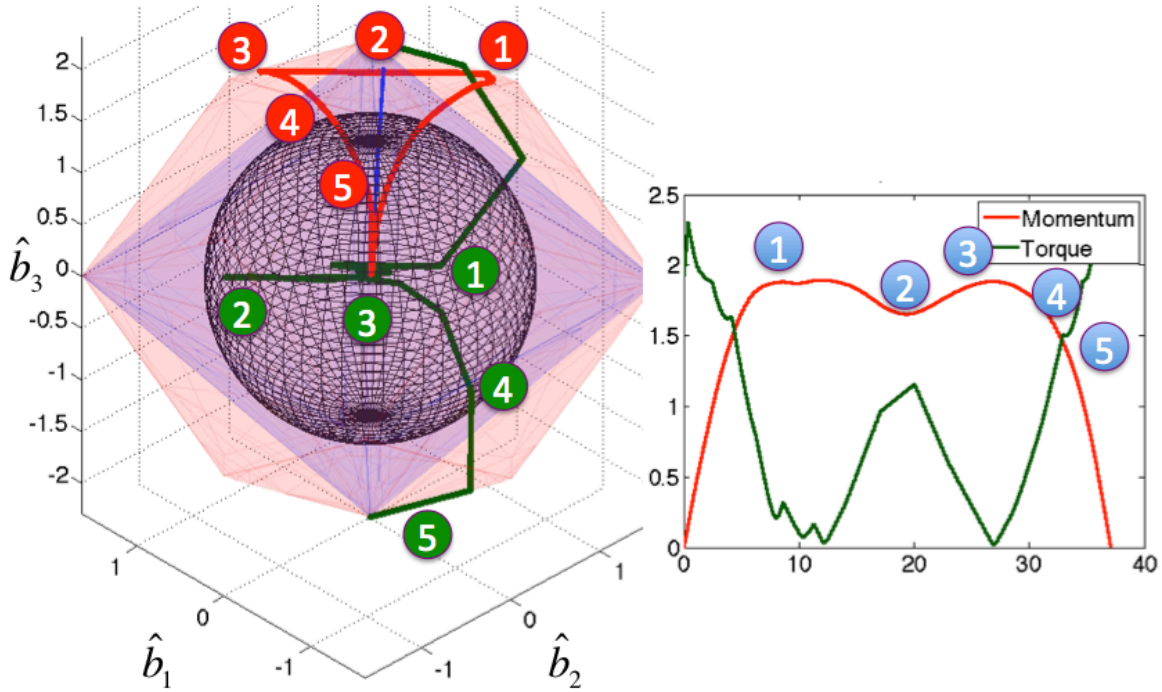


Figure 76. Optimal Slew Example 3, $q_0=[0.23 \ 0.17 \ 0.82 \ 0.5]$, $q_f=[0 \ 0 \ 0 \ 1]$

B. MOMENTUM AND TORQUE RELATIONSHIP

Many variables go into determining the torque output of reaction wheel and CMG systems. This section uses market data to develop a “rule of thumb” relationship that can be utilized in size comparisons between the two very different systems.

1. Simplified Dynamics

In order to size a MED array, a reasonable approach would be to use the largest inertia. In the same way that the minimum momentum limits angular rate, the largest inertia limits rate. A starting point for sizing wheels might begin without the complications of gyroscopic coupling per Equation (265).

$$\begin{aligned} \mathbf{h}_{medA}^N &\approx \mathbf{J}_{s/c}^N \boldsymbol{\omega}^B \\ \boldsymbol{\tau}_{medA}^N &\approx \mathbf{J}_{s/c}^N \dot{\boldsymbol{\omega}}^B \end{aligned} \quad (265)$$

In Chapter III, it was shown that the spacecraft can be modeled as a simple double integrator. This creates a linear relationship between spacecraft rate/acceleration and momentum/torque, as both use the same proportionality factor J . This allows a very basic relationship between the dynamics of the spacecraft and the momentum exchange device to be considered. As the engineer narrows down selection within a few reaction wheels, subsequent iterations should include gyroscopic coupling in the sizing analysis.

2. Market Research and Simplified Momentum and Torque Equations

Market data may be used to develop a relationship between momentum and torque for reaction wheel and CMG systems. Appendix B consists of a table of performance data collected from company specifications sheets and published papers across the Internet. Reaction wheels are more common and over fifty data points were readily available. CMGs are far less prevalent as less than twenty systems could be identified. Figure 77 offers a glimpse at this momentum and torque comparison for reaction wheels and CMGs. Reference [4, Figure 4] offers a similar chart and the six CMG data points presented in this paper are overlaid on the chart for comparison with the information presented in this thesis. The market data from Appendix B are marked with

“X’s.” The CMG data from [4] are marked with circles. Common points contain both marks, but are counted only once to facilitate curve-fitting of the data.

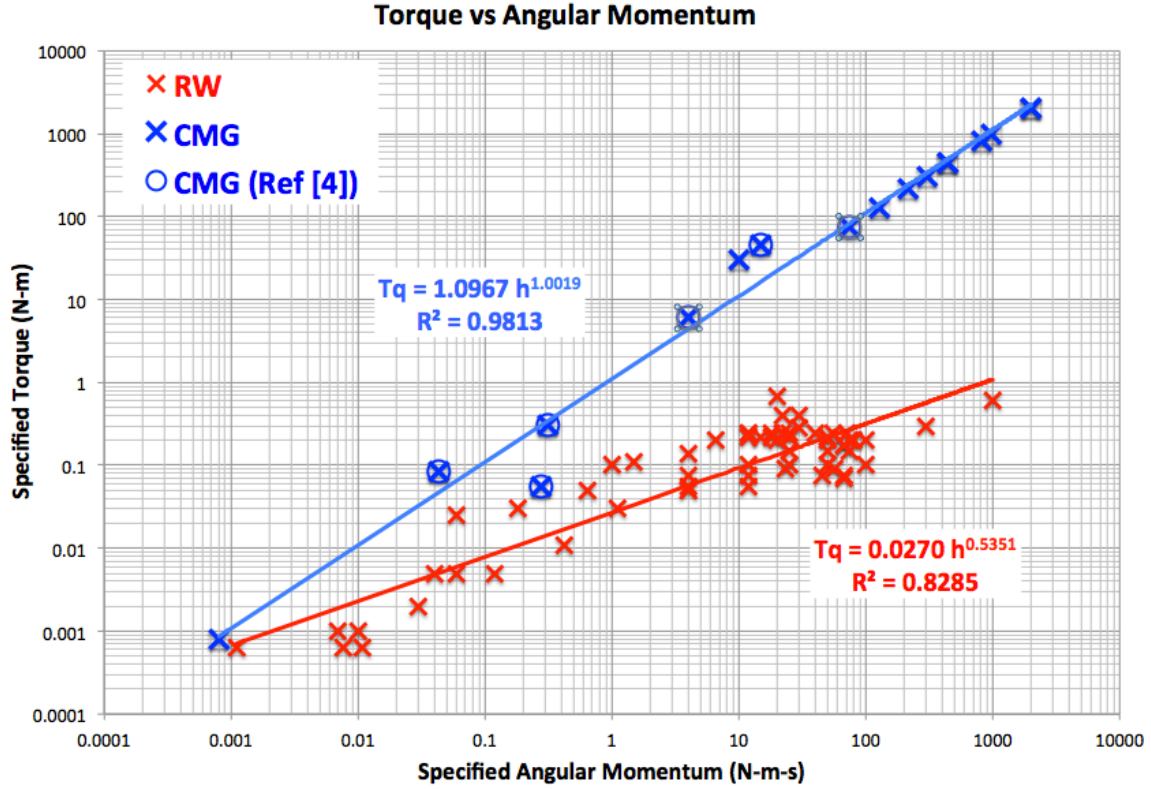


Figure 77. Market Research Torque vs. Angular Momentum for Reaction Wheel and CMG Systems

The data in Figure 77 is curve fit to obtain the trend for each type of system. A few things become clear. First, there is a near proportional balance between CMG momentum and torque, Equation (266). This is because the individual CMG torque is determined by the product of gimbal rate (commonly 1 rad/s [27, p. 8]) and momentum. On the other hand, reaction wheels seem to have an approximately square root relationship between momentum and torque with a proportionality constant of less than three percent, Equation (267). The market data confirms that reaction wheels have far less torque capability than CMGs.

$$\text{CMG: } \tau_{cmg}^w \approx h_{cmg}^w \text{ since } \dot{\delta} \approx 1 \text{ rad/s} \quad (266)$$

$$\text{Reaction Wheel: } \tau_{rw}^W \approx 0.027 \sqrt{h_{rw}^W} \quad (267)$$

where torque units are N-m and momentum units are N-m-s.

Figure 77 is created on a per-wheel/CMG basis. This means that MED arrays are not accounted for, so array calculations using orientation matrices are still necessary. Another notable figure is the large torque difference at high momentum levels. This reveals why so many CMGs are being developed in the 100+ Nms range. On the other hand, micro-CMGs are rare, seemingly for good reason. With the shape of the curves, there actually may be a torque advantage for reaction wheels around the 0.001 Nms momentum level. Regardless, these curves offer a basis for comparison. Therefore, given momentum storage of a reaction wheel or CMG, the torque available will be described as

$$\text{CMG: } \tau_{cmg}^G = 1.0967 (h_{cmg}^G)^{1.0019} \quad (268)$$

$$\text{Reaction Wheel: } \tau_{rw}^W = 0.0270 (h_{rw}^W)^{0.5351} \quad (269)$$

C. COMPARISON DEVELOPMENT

For comparison purposes, a propagation of effective eigenaxis trajectories for the optimal models will be completed, similar to Figures 51 to 53 from Chapter V. The optimal maneuvers will be propagated in a bang-bang or bang-coast-bang trajectory about its effective eigenaxis (Chapter V, Section H). Already derived previously in this thesis, the following spherically-available momenta will be used.

$$\begin{aligned} h_{rwA}^B &= 1.333 h_{rw_{\max}}^W \\ h_{rw-pseoptA}^B &= 1.577 h_{rw_{\max}}^W \\ h_{rw-optA}^B &= 1.805 h_{rw_{\max}}^W \\ h_{cmgA}^B &= 1.007 h_{rw_{\max}}^G \end{aligned} \quad (270)$$

The torque equations within Equations (268) and (269) will be used to compute reaction wheel and CMG output torques. Transformation of torque available to the body frame, given a 4 reaction wheel or 4 CMG array, is computed as follows.

$$\begin{aligned}
\tau_{rwA}^B &= 1.333 \tau_{rw_{\max}}^W \\
\tau_{rw-pseudo-optA}^B &= 1.333 \tau_{rw_{\max}}^W \\
\tau_{rw-optA}^B &= 1.333 \tau_{rw_{\max}}^W \\
\tau_{cmgA}^B &= 1.007 \tau_{rw_{\max}}^G
\end{aligned} \tag{271}$$

For 1 Nms wheels, the data in Table 3 can be determined using Equations (270) and (271).

	Wheel/Gimbal Frame		Body Frame	
	h_{\max} (Nms)	τ_{\max} (Nm)	h_{\max} (Nms)	τ_{\max} (Nm)
RW	1	0.027	1.333	0.036
RW_{pseudo-opt}	1	0.027	1.577	0.036
RW_{opt}	1	0.027	1.807	0.036
CMG	1	1.097	1.007	1.104

Table 3. Body Momentum/Torque Comparison Table – 1 Nms Momentum

Now a spacecraft size class must be established. Since the MED momentum storage is the starting point, either the spacecraft size or desired slew rate must be chosen. Spacecraft rate will be chosen next, because we are focusing on agile spacecraft. In the space industry, a $2-3^\circ/s$ slew is considered agile, even for CMGs. For example, Worldview 1 slews at $2.3^\circ/s$ [2]. Therefore, a rate of ${}^N\omega^B = 3^\circ/s$ will be the benchmark with which the spacecraft sizing will be determined. The base reaction wheel will be used for sizing, and all other systems will be required to slew the same spacecraft.

$$\begin{aligned}
|h_{rwA}^B| &= h_{req}^B = j_{s/c} {}^N\omega_{rwA}^B \\
\therefore j_{s/c} &= \frac{h_{rwA}^B}{{}^N\omega^B} = \frac{1.333 Nms}{3^\circ/s} = 25.5 kg \cdot m^2
\end{aligned} \tag{272}$$

Using these properties, the individual spacecraft rates for the various systems can be solved for.

$$\begin{aligned}
{}^N\omega_{rw-pseoptA}^B &= \frac{h_{rw-pseoptA}^B}{j_{s/c}} = \frac{1.577 \text{ Nms}}{25.5 \text{ kg} \cdot \text{m}^2} = 3.549^\circ / \text{s} \\
{}^N\omega_{rw-optA}^B &= \frac{h_{rw-optA}^B}{j_{s/c}} = \frac{1.807 \text{ Nms}}{25.5 \text{ kg} \cdot \text{m}^2} = 4.067^\circ / \text{s} \\
{}^N\omega_{cmgA}^B &= \frac{h_{cmgA}^B}{j_{s/c}} = \frac{1.007 \text{ Nms}}{25.5 \text{ kg} \cdot \text{m}^2} = 2.266^\circ / \text{s}
\end{aligned} \tag{273}$$

Likewise, the spacecraft accelerations can also be solved for.

$$\begin{aligned}
{}^N\alpha_{rwA}^B &= \frac{\tau_{rwA}^B}{j_{s/c}} = \frac{0.036 \text{ Nm}}{25.5 \text{ kg} \cdot \text{m}^2} = 0.081^\circ / \text{s}^2 \\
{}^N\alpha_{rw-pseoptA}^B &= \frac{\tau_{rw-pseoptA}^B}{j_{s/c}} = \frac{0.036 \text{ Nm}}{25.5 \text{ kg} \cdot \text{m}^2} = 0.081^\circ / \text{s}^2 \\
{}^N\alpha_{rw-optA}^B &= \frac{\tau_{rw-optA}^B}{j_{s/c}} = \frac{0.036 \text{ Nm}}{25.5 \text{ kg} \cdot \text{m}^2} = 0.081^\circ / \text{s}^2 \\
{}^N\alpha_{cmgA}^B &= \frac{\tau_{cmgA}^B}{j_{s/c}} = \frac{1.104 \text{ Nm}}{25.5 \text{ kg} \cdot \text{m}^2} = 2.485^\circ / \text{s}^2
\end{aligned} \tag{274}$$

The data from equations (268) through (274) are compiled in Table 4. Notice the higher momentum capacity for reaction wheels corresponds directly to the larger maximum spacecraft rotation rates. Note that this rotation rate only refers to the effective rotation rate about the eigenaxis. The actual rotation rate of the optimal case about the instantaneous axis of rotation can potentially be much faster so the values in Table 4 are conservative estimates. The body acceleration of the reaction wheels is more than an order of magnitude lower than the acceleration possible using the CMGs.

	Wheel/Gimbal Frame		S/C $j_{s/c}$ (kg-m ²)	Body Frame			
	h_{\max} (Nms)	τ_{\max} (mNm)		h_{\max} (Nms)	τ_{\max} (Nm)	ω (°/s)	α (°/s ²)
RW	1	0.027	25.458	1.333	0.036	3.000	0.081
RW_{pseudo-opt}	1	0.027	25.458	1.577	0.036	3.549 *	0.081 *
RW_{opt}	1	0.027	25.458	1.807	0.036	4.067 *	0.081 *
CMG	1	1.097	25.458	1.007	1.104	2.266	2.485
*effective rotation and acceleration rates given about an effective eigenaxis. Refer back to Section H of Chapter 6 for description of effective eigenaxis. The actual body rates and acceleration can be much higher throughout the maneuver.							

Table 4. Body Rate/Acceleration Comparison for a 25.5 kg-m² Class Spacecraft

Given the effective body rate and acceleration data from Table 4, the data can now be propagated through the “effective” or equivalent eigenaxis slews using trapezoidal input trajectories. This is the same as what was done for the optimal reaction wheel case from Chapter V. Recall the curve from Chapter V was built using a specific reaction wheel of 0.1 Nm torque, much higher than the one used here per the relationship in Equation (269). Therefore, the curves are built using different acceleration data, but the concept is the same.

The plot of the eigenaxis slew angle versus slew time for all four cases is shown in Figure 78. This figure demonstrates the shape of the curves. Since the reaction wheel arrays have higher momentum storage, the time/angle slope of the momentum-limited region is much smaller than the one for the CMG case. This causes the reaction wheel systems to eventually catch up with the CMG system. The time-optimal case would not catch up with the CMG until the maneuver exceeds 180°, which is an unrealistic slew. For a 25.5 kg-m² class spacecraft, the control system comparison shows CMGs to be more favorable for agile maneuvering.

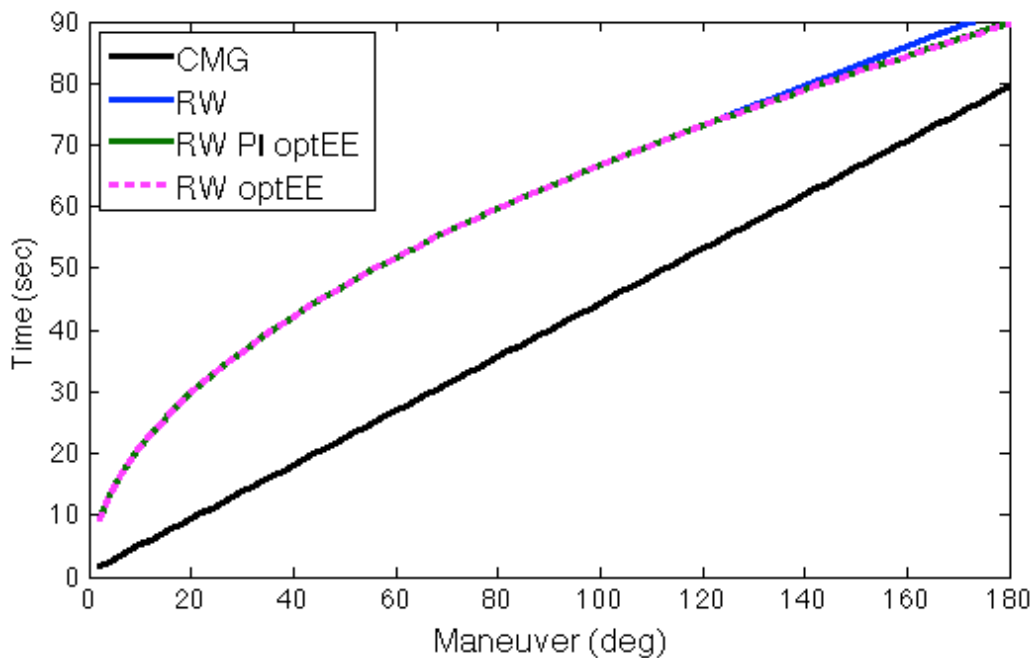


Figure 78. Slew Angle vs. Time Comparison for a 25.5 kg-m² Class Spacecraft

Now, suppose the wheel momentum is decreased by an order of magnitude ($h_{\max} = 0.1 \text{ Nms}$). Using the same ${}^N\omega^B = 3^\circ / s$ requirement, the corresponding spacecraft is now 2.55 kg-m^2 . The new comparison data is shown in Table 5.

	Wheel/Gimbal Frame		S/C	Body Frame			
	h_{\max} (Nms)	τ_{\max} (Nm)		h_{\max} (Nms)	τ_{\max} (Nm)	ω ($^\circ/s$)	α ($^\circ/s^2$)
RW	0.1	0.008	2.546	0.133	0.010	3.000	0.236
RW_{pseudo-opt}	0.1	0.008	2.546	0.158	0.010	3.549 *	0.236 *
RW_{opt}	0.1	0.008	2.546	0.181	0.010	4.067 *	0.236 *
CMG	0.1	0.109	2.546	0.101	0.110	2.266	2.474
*effective rotation and acceleration rates given about an effective eigenaxis. Refer back to Section H of Chapter 6 for description of effective eigenaxis. The actual body rates and acceleration can be much higher throughout the maneuver.							

Table 5. Body Rate/Acceleration Comparison for a 2.55 kg-m^2 Class Spacecraft

Notice the spacecraft rates did not change across the two models. Instead, the spacecraft acceleration is the important change. Due to the roughly 1:1 ratio CMG momentum to torque ratio ($\tau_{cmg}^W \approx h_{cmg}^W$) from Equation (268), the CMG trajectory did not change very much. On the other hand, the reaction wheel has a square root relationship, ($\tau_{rw}^W \approx 0.027\sqrt{h_{rw}^W}$) from (269). This causes the reaction wheel torque to momentum ratio to improve as the wheel size is decreased. The reaction wheel acceleration rates are now about three times higher than for the larger wheel (see Table 4). Generating the effective eigenaxis trajectories for each system gives Figure 79. Using these curves, it becomes evident that any slews greater than 77° will favor the time-optimal reaction wheel control system over the CMG.

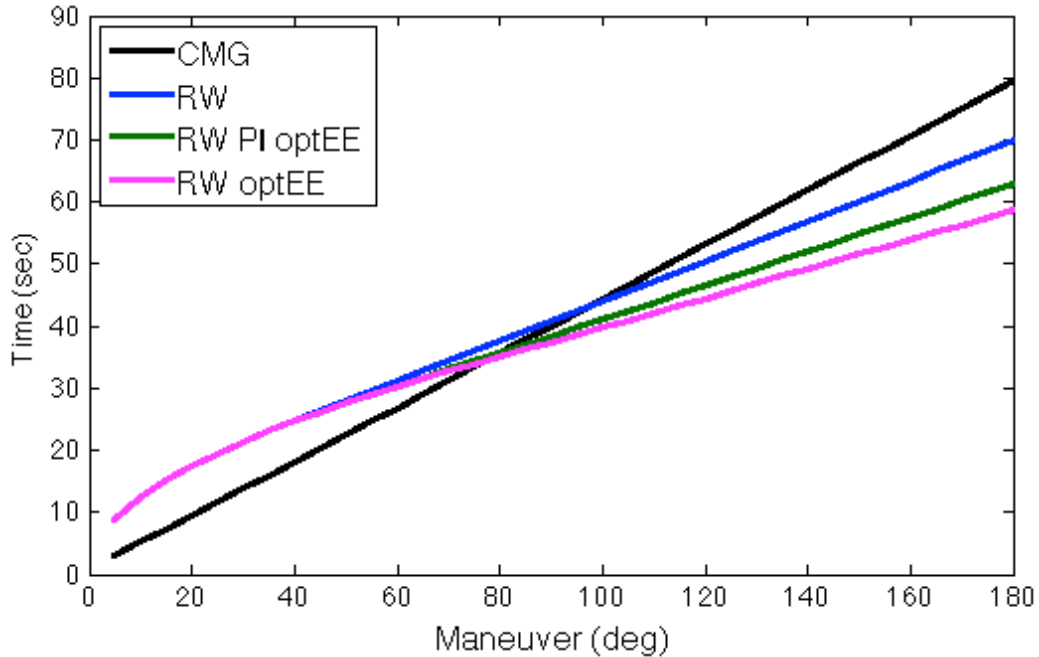


Figure 79. Slew Angle vs. Time Comparison for a 2.55 kg-m² Class Spacecraft

Notice the significant change in the reaction wheel curves. The spacecraft rates did not change across the two models, but the improved/larger spacecraft acceleration obtained from the reaction wheel system increased by about a factor of three. Because the angular rates are the same as before, the time/angle slope of the momentum-limited region did not change at all. Due to the higher available torque, the momentum-limited region starts at a lower angle for the reaction wheels. This causes an earlier intersection with the CMG curve. To better illustrate these transition points, the reaction wheel curves are looked at as a function of angle, after which the performance of the reaction wheel assembly exceeds that of the CMG assembly. This threshold will be referred to for the remainder of the thesis as the *reaction wheel advantage angle*, shown in Figure 80.

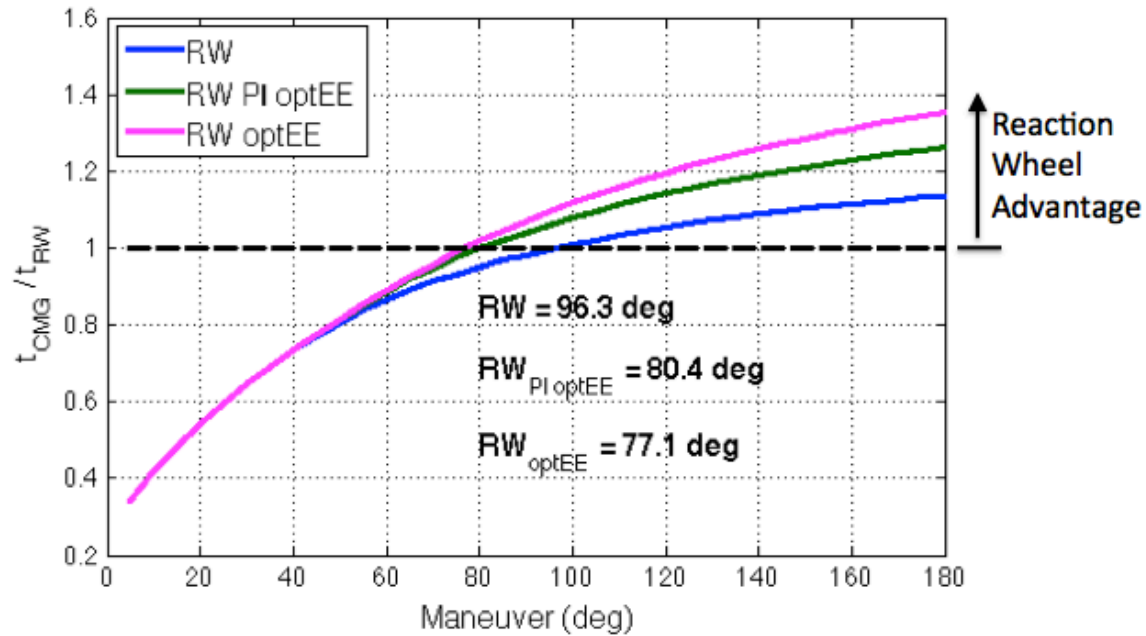


Figure 80. Maneuver Angles where Reaction Wheel Systems Outperform CMGs for a 2.55 kg-m² Class Spacecraft

The trend of rapidly increasing reaction wheel performance is continued when wheel momentum is decreased by another order of magnitude ($h_{\max} = 0.01 \text{ Nms}$). Using the same ${}^N\omega^B = 3^\circ/\text{s}$ requirement, the corresponding spacecraft size is now 0.255 kg-m². The comparison is shown in Table 6 and Figures 83–84, illustrating that the reaction wheel advantage angles decrease as body accelerations provided by the wheels increase.

	Wheel/Gimbal Frame		S/C $j_{s/c}$ (kg-m ²)	Body Frame			
	h_{\max} (Nms)	τ_{\max} (mNm)		h_{\max} (Nms)	τ_{\max} (Nm)	ω (°/s)	α (°/s ²)
RW	0.01	0.002	0.255	0.013	0.003	3.000	0.689
RW_{pseudo-opt}	0.01	0.002	0.255	0.016	0.003	3.549 *	0.689 *
RW_{opt}	0.01	0.002	0.255	0.018	0.003	4.067 *	0.689 *
CMG	0.01	0.011	0.255	0.010	0.011	2.266	2.464

*effective rotation and acceleration rates given about an effective eigenaxis. Refer back to Section H of Chapter 6 for description of effective eigenaxis. The actual body rates and acceleration can be much higher throughout the maneuver.

Table 6. Body Rate/Acceleration Comparison for a 0.255 kg-m² Class Spacecraft

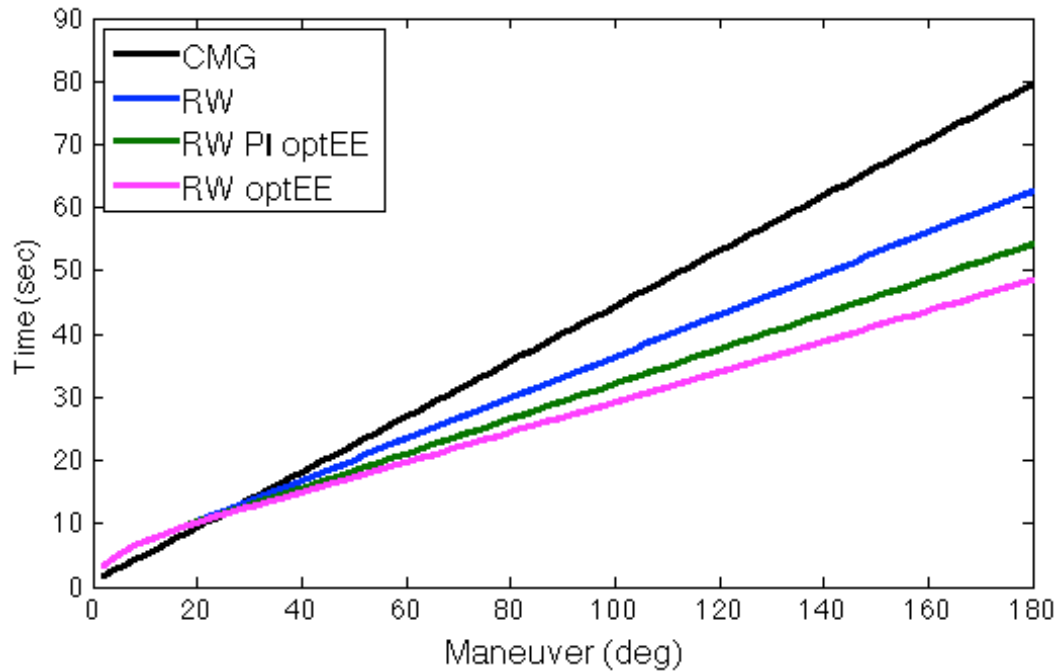


Figure 81. Slew Angle vs. Time Comparison for a 0.255 kg-m² Class Spacecraft

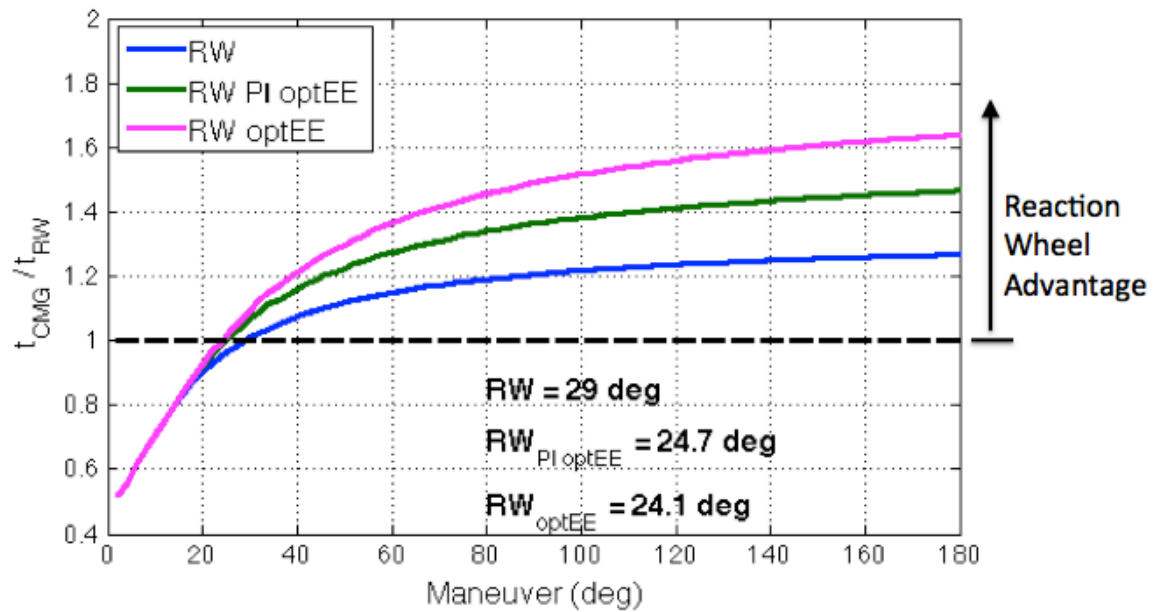


Figure 82. Maneuver Angles where Reaction Wheel Systems Outperform CMGs for a 0.255 kg-m² Class Spacecraft

Referring to Figures 78, 79, and 81, it is apparent that when using like-sized reaction wheels and CMGs, the larger momentum capacity of reaction wheels is much

more advantageous for small spacecraft than for larger spacecraft. In the case shown in Figure 83, the optimal reaction wheel control system becomes more agile than the CMG control system for all maneuvers greater than 24.1° . Standard operation of the reaction wheel array does not begin to outperform CMGs until the maneuver size exceeds 30.3° . If only the reaction wheel advantage angle is plotted against the wheel momenta, the curves in Figure 83 are obtained. The curves reveal that reaction wheels overcome CMGs at relatively small angles for small rotor momenta. As the spacecraft momentum increases, the reaction wheel advantage angle increases rapidly and reaction wheel control systems promptly lose their edge.

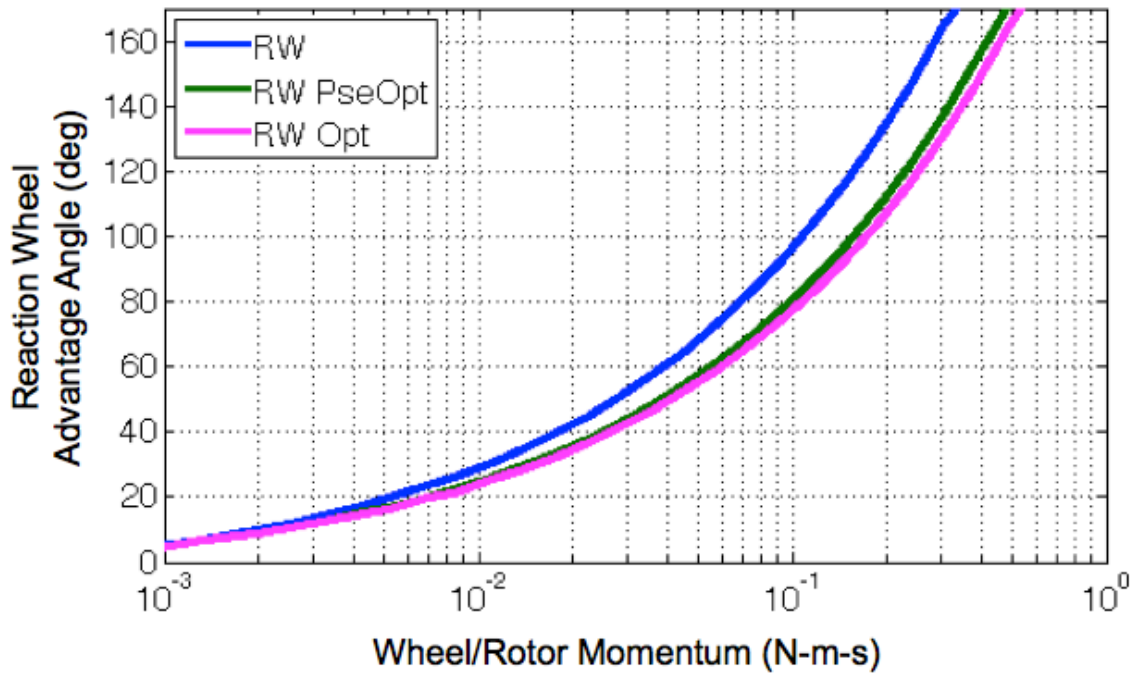


Figure 83. Reaction Wheel Advantage Angle vs. Wheel/Rotor Momentum: Where RWs Overcome CMGs ($\omega=3^\circ/\text{s}$)

Likewise, if the spacecraft inertia versus slew angle is plotted (assuming $\omega=3^\circ/\text{s}$), the trend is shown again (Figure 84). For small spacecraft, reaction wheels seem to outperform CMGs, especially for large angle maneuvers.

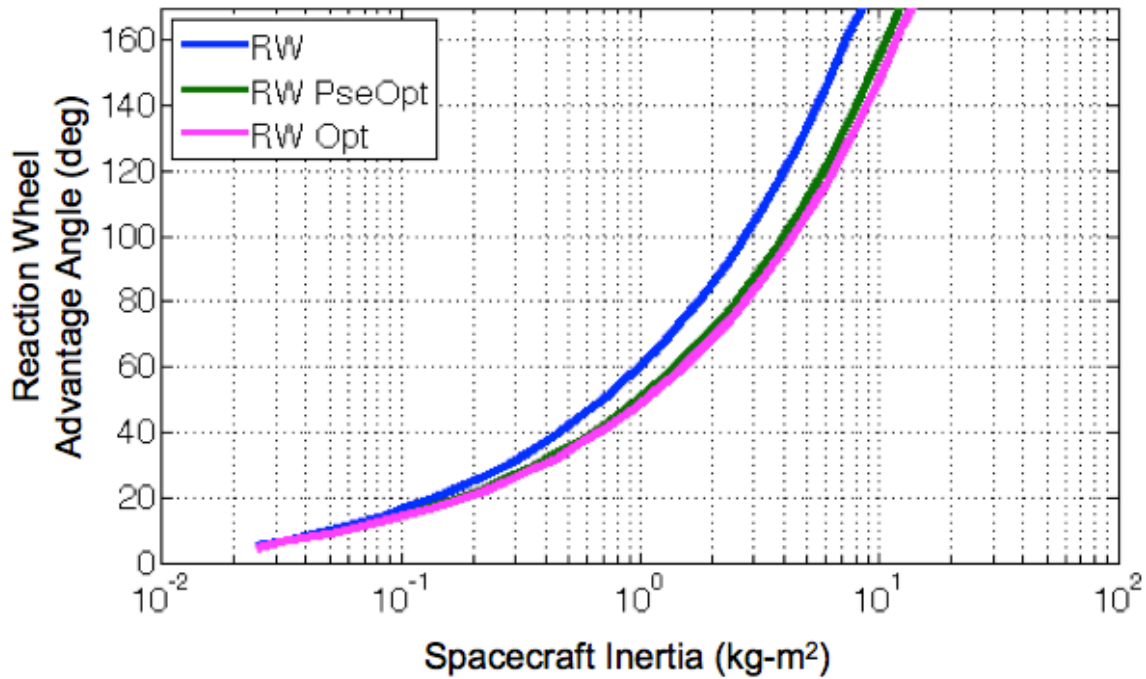


Figure 84. Reaction Wheel Advantage Angle vs. Spacecraft Inertia: Where RWs Overcome CMGs ($\omega=3^\circ/\text{s}$)

Thus far, the results of this chapter show that reaction wheels outperform CMGs for small spacecraft. In addition, the two optimal control approaches described significantly outperformed the heritage eigenaxis maneuver. For small spacecraft, the reaction wheel advantage angle was reduced by only a few degrees by using optimal reaction wheel methods (Figure 85). At larger slew angles, 40–60° improvement can be achieved by optimal systems over the heritage eigenaxis maneuver (Figure 85). This means for large angle slews, the optimal reaction wheel system outperforms the CMG system significantly more quickly than if heritage control logic were used.

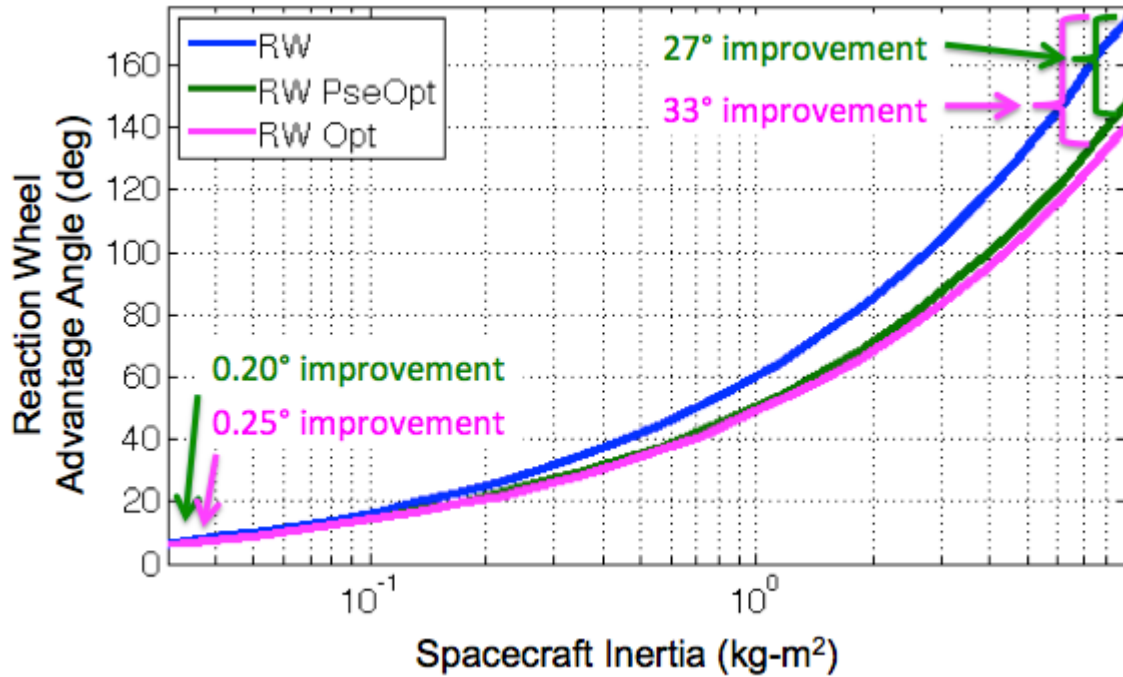


Figure 85. Zoom in: Reaction Wheel Advantage Angle vs. Spacecraft Inertia: Where RWs Overcome CMGs ($\omega=3^\circ/\text{s}$)

Figure 86 shows these reductions in reaction wheel advantage angles as a percentage improvement. The pseudo-inverse optimal method reduces the reaction wheel advantage angle by roughly 15% over the heritage eigenaxis shaped trajectory, while the full time-optimal solution reduces the reaction wheel advantage angle by 18% across the entire spacecraft inertia regime.

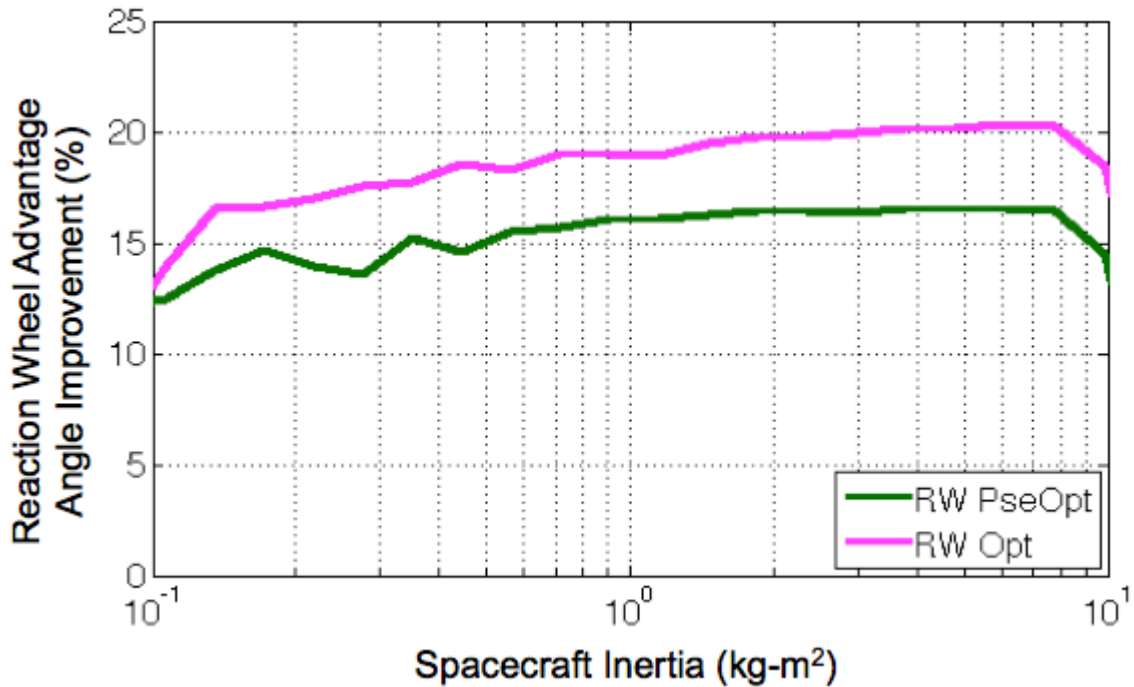


Figure 86. Optimal Improvement over normal Reaction Wheel Systems

D. MOMENTUM EXCHANGE DEVICE PERFORMANCE AS A FUNCTION OF MASS

In the analysis of Section C, equally sized reaction wheels and CMGs were used, i.e., both had the same momentum storage capacity. This does not have to be the case. Suppose the systems engineer gives a mass restriction for the entire MED array to the ADCS engineer. The ADCS engineer can quickly determine whether reaction wheels or CMGs would be better given this limitation. In this section, it will be shown how much more momentum can come of a reaction wheel array in comparison with CMGs given a mass constraint. Figure 87 shows the market research for individual MED mass and the output momentum the actuator can achieve. The data was curve fit to develop a general trend.

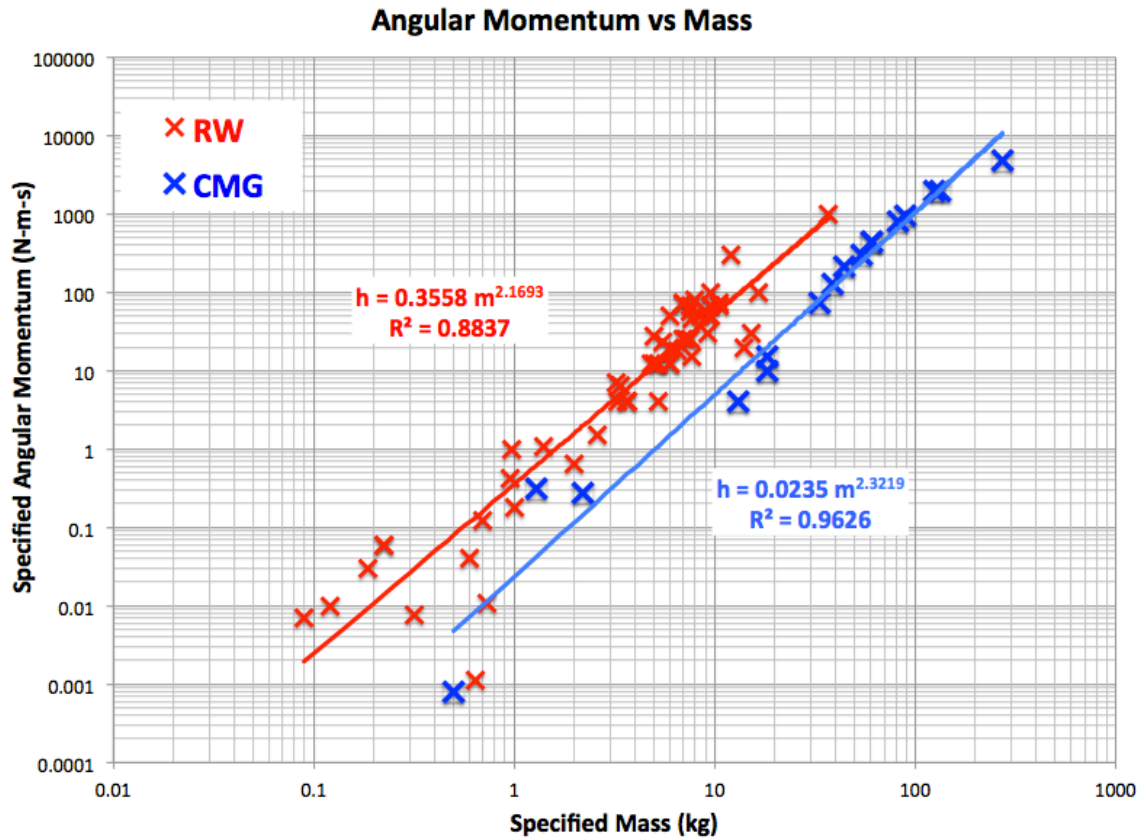


Figure 87. Market Research Angular Momentum vs. Mass

The mechanical complexity of CMGs requires additional mass and volume within the spacecraft. Using this knowledge and the relationships from Section C, the full array mass and body momentum can be created using the trend lines (Figure 88). This analysis shows that for the same array mass, an order of magnitude more momentum storage is typically available from reaction wheel arrays than from CMG arrays. This implies that if mass is a critical design constraint for the spacecraft, then engineers should take an even harder look at reaction wheels.

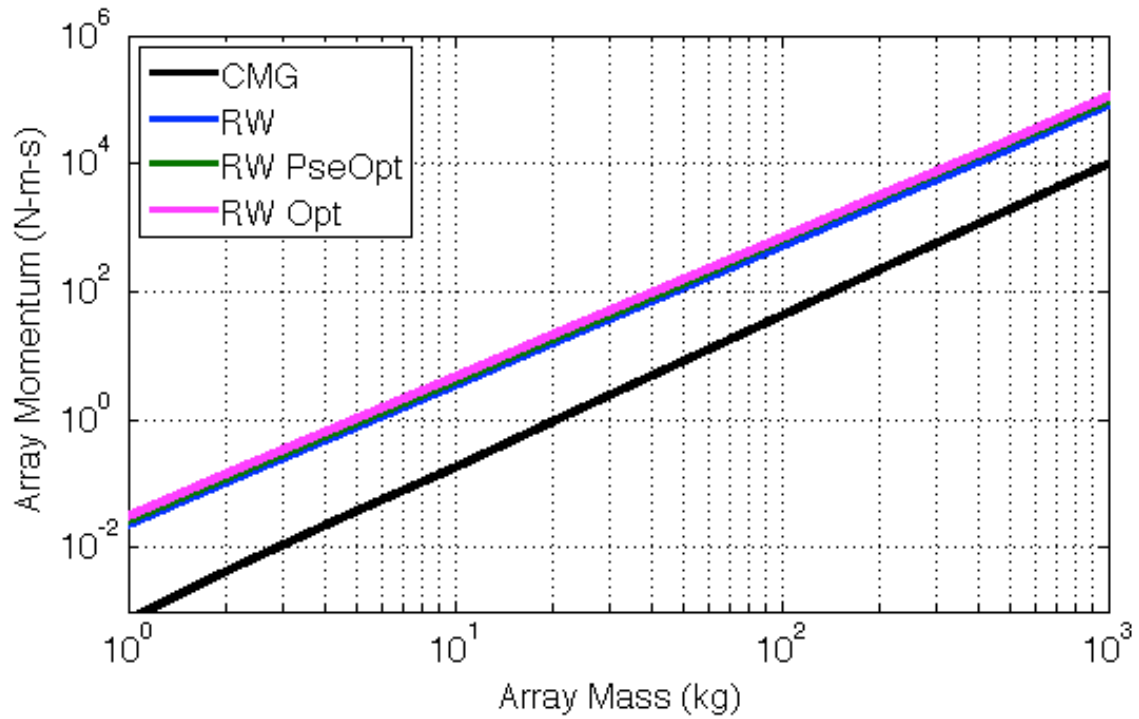


Figure 88. Array Momentum vs. Mass

Torque output, on the other hand, is better for large mass CMGs. Figure 89 demonstrates the transition where a CMG array will begin to create more torque than a reaction wheel array. This is an important point because it helps illustrate why few CMGs have been developed on the small scale. From the market research shown in Figure 87, only one CMG was actually smaller than 0.898 kg.

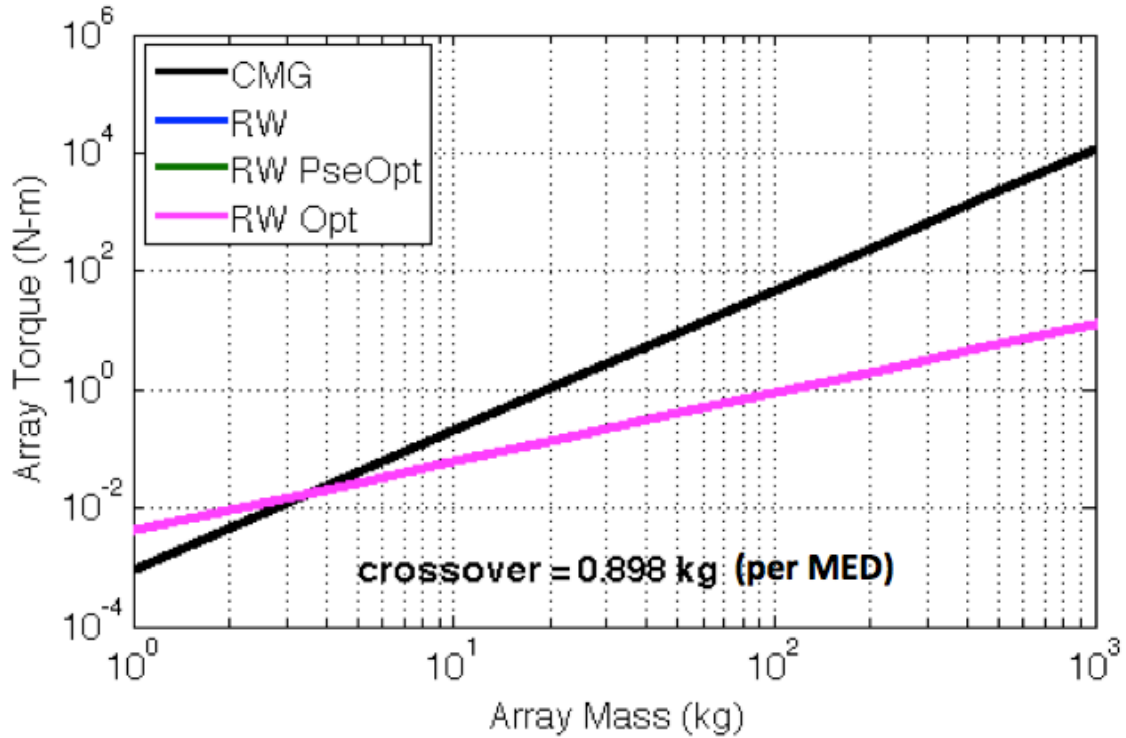


Figure 89. Array Torque vs. Mass

E. SUMMARY

In this chapter, it was shown that reaction wheels seem to perform better than CMGs for small spacecraft. As the spacecraft size decreases, the reaction wheel advantage increases. This increase can be further improved by the use of optimal control algorithms.

The CMG torque advantage is evident for large moments of inertia. On the other hand, the torque gap lessens as the spacecraft size (therefore the MED array momentum capacity) decreases. Although the gap does not completely close, the ratio of CMG torque to reaction wheel torque decreases significantly with spacecraft size.

Given arrangements of reaction wheels and CMGs with similar individual MED momentum, the reaction wheel array will have a larger momentum storage capacity. This causes reaction wheel systems to catch up with CMG systems over large angle slews. The reaction wheel advantage angle is the slew size in which a reaction wheels become a

better alternative than CMGs. For large spacecraft, the reaction wheel advantage angle is very high, possibly over 180 degrees.

Time-optimal shaped maneuvers of reaction wheel systems can be used to lower this reaction wheel advantage angle by 13 to 21%, depending upon algorithms used and spacecraft size. By shaping only the quaternion and body rate trajectories, the mathematical limitations of the pseudo-inverse control allocation must still be ascribed to. This allows a reduction of the time-optimal reaction wheel advantage angle by approximately 15% over the advantage angle of the shaped eigenaxis maneuver. The addition of shaped time-optimal wheel torques reduces the advantage angle by approximately 18%.

Considering the mass of the reaction wheels and CMGs, the reaction wheels produce a much higher momentum limit than CMGs for a given mass. Interestingly, the additional order of magnitude of momentum equates to additional torque in the similar-weight MEDs. For MEDs smaller than 0.898 kg, the reaction wheel array will actually produce more torque than a CMG array. This means that given a small spacecraft with weight restrictions, reaction wheels are the better alternative for both torque and momentum.

VIII. CONCLUSIONS AND FUTURE WORK

A. CONCLUSIONS

This thesis is an attempt to bridge the gap between reaction wheels and CMGs, particularly for small satellites. Using the software upgrades and relative sizing concepts proposed, reaction wheel arrays have the ability to outperform CMGs for some classes of spacecraft. The relatively low cost of reaction wheels can be attractive once again.

Reaction wheels are typically used inefficiently within the spacecraft industry. The standard maneuver, a shaped bang-coast-bang maneuver about the eigenaxis, should be reconsidered in the presence of new control algorithms. The results of this thesis show that the speed of this eigenaxis-restricted maneuver can be improved 18% in each of momentum and torque by applying the pseudo-inverse limited time-optimal shaped quaternion and rate trajectories. Furthermore, the speed of the standard eigenaxis maneuver can be improved by 36% by delivering the optimal torque inputs directly to the reaction wheels themselves. These two software solutions reduce the reaction wheel advantage angle by 15% and 18%, respectively. The CMG performance gap is closed and surpassed in many cases.

Due to their high torque capacity, CMGs dominate reaction wheels for small angle maneuvers. This is because a spacecraft using CMGs can accelerate to maximum angular velocity very quickly. Although CMGs have a lot more torque potential, they are exceedingly momentum-limited. A spacecraft using reaction wheels, on the other hand, is slower to accelerate, but has a much greater maximum velocity. Considering like-sized wheels, i.e., the same momentum capacity, this thesis shows that reaction wheels catch up and surpass CMGs due to their higher rate limits, provided the maneuver is large enough. The ramifications are particularly large for smallsats and cubesats as they require very small MEDs. For small satellites, this thesis has shown that reaction wheels have the ability to outperform like-sized CMGs at relatively small angle maneuvers. As wheel and spacecraft sizes decrease proportionally, reaction wheels catch up to CMGs even more quickly. Optimal control further improves this performance.

B. FUTURE WORK

This thesis did not include an exhaustive approach at validating the models of the analytical effective eigenaxis of each of the optimal control models. Only 100 random data points were used for a single combination of spacecraft/wheel sizing. The results of this work should be validated across the entire space of reaction wheel and spacecraft sizes. Gimbal momentum/torque and gyroscopic coupling relationships should be accounted for into this “rule of thumb.” For instance, as body rate increases, the gyroscopic coupling increases. Most likely, the optimal maneuvers will use this as an advantage to widen the performance gap over standard maneuvers.

The reaction wheel and CMG data should be analyzed further to account for variations in momentum size and torque output. To further understand the CMG momentum and torque relationship, research must be conducted to determine why a 1:1 relationship between momentum and output torque is so commonly used.

The different control approaches should also be explored from non-rest initial and final conditions. Given some calculable motion within a system, the optimal methods should be able to capitalize on this motion for further gains over the heritage maneuvers.

Optimal control of the CMG should be explored. The optimal maneuver, by its very nature, should be able to avoid the singularities altogether. This would allow the unused capacity of the CMG momentum space to be accessed without complicated singularity-avoidance algorithms. One consideration during this expansion would be the confidence level in the spacecraft inertia and states. If knowledge of these uncertainties is poor, then the optimal control approach would still have a pseudo-inverse limited and singularity-ridden feedback system to deal with. Therefore, methods such as those described in [31] could be tried.

Further analysis should be done on the momentum and torque envelope visualization method for optimal control maneuvers. Looking at these envelopes closely, it becomes obvious that the torque and momentum vectors tend toward the vertices and edges of the envelopes. If this space is studied in detail, it should be possible to predict the optimal slew times much more accurately. Just as the optimal eigenaxis-restricted

maneuver is a bang-coast-bang optimal path, certain characteristics of optimal maneuvers could be derived for maneuver size and eigenaxis orientation. This could allow quick on-board processing of semi-optimal maneuvers, without actually computing the exact computer-intensive optimal path. A controller much like the eigenaxis quaternion feedback could potentially be developed to drive the system toward the appropriate vertices and edges of the momentum and torque envelopes.

A comparison should be done with various reaction wheel and CMG arrangements. For example, if it is known that the pseudo-inverse limited time-optimal control logic is going to be used, then it may be possible to adjust the skew angle to maximize its envelope volume, thereby creating a larger momentum/torque radius (per Chapter V, Section G). Additionally, sizing wheels with different arrangements of wheel sizes could be considered. For example, a skew arrangement of five, six, or possibly ten smaller wheels may be more capable than four larger wheels, not to mention more redundancy. The shape would have more flat facets, but less loss. Like a cube and a regular octahedron of similar volumes, the octahedron allows a larger inscribed sphere. Mixed configurations of larger and smaller wheels could also be considered. Finally, hybrid reaction wheel and CMG configurations could be considered to maximize torque, yet maintain a high momentum envelope.

Explore the impact of external disturbances on optimal maneuvers. Integrate gravity gradient, solar pressure, and aerodynamic torques into the optimal control problem. Compare with the eigenaxis maneuvers. Most likely, the optimal maneuvers will be able to exploit the external disturbances to widen the performance gap between the shaped eigenaxis trajectory and the time-optimal trajectories.

THIS PAGE INTENTIONALLY LEFT BLANK

APPENDIX A. OPTIMAL CONTROL PROBLEM IN DESIGNER UNITS

$$\begin{aligned}
\text{Minimize: } \mathfrak{J}[x(\cdot), u(\cdot), t_f] &= t_f \text{ where } \mathfrak{J} = \bar{\mathfrak{J}}T^* \\
&\Rightarrow \bar{\mathfrak{J}}[\bar{x}(\cdot), \bar{u}(\cdot), \bar{t}_f]T^* = \bar{t}_fT^* \\
&\Rightarrow \bar{\mathfrak{J}}[\bar{x}(\cdot), \bar{u}(\cdot), \bar{t}_f] = \bar{t}_f
\end{aligned} \tag{275}$$

Subject to:

$$\begin{aligned}
\dot{q} &= \frac{1}{2}(q_4^N \omega^B - {}^N\omega^B \times q) \\
&\Rightarrow \dot{\bar{q}}\left(\frac{q^*}{T^*}\right) = \frac{1}{2}(\bar{q}_4^N \bar{\omega}^B(q^* \omega^*) - {}^N\bar{\omega}^B(\omega^*) \times \bar{q}(q^*)) \\
&\Rightarrow \dot{\bar{q}} = \frac{1}{2}(\bar{q}_4^N \bar{\omega}^B - {}^N\bar{\omega}^B \times \bar{q})(T^* \omega^*)
\end{aligned} \tag{276}$$

$$\begin{aligned}
\dot{q}_4 &= -\frac{1}{2}({}^N\omega^B)^T q \\
&\Rightarrow \dot{\bar{q}}_4\left(\frac{q^*}{T^*}\right) = -\frac{1}{2}({}^N\bar{\omega}^B)^T \bar{q}(\omega^* q^*) \\
&\Rightarrow \dot{\bar{q}}_4 = -\frac{1}{2}({}^N\bar{\omega}^B)^T \bar{q}(T^* \omega^*)
\end{aligned} \tag{277}$$

$$\begin{aligned}
{}^N\dot{\omega}^B &= J_{s/c}^{-1}(-{}^bZ_3^w \tau_w^W - {}^N\omega^B \times (J_{s/c}^N \omega^B + {}^bZ_3^w J_w \Omega^W)) \\
&\Rightarrow {}^N\dot{\bar{\omega}}^B\left(\frac{\omega^*}{T^*}\right) = J_{s/c}^{-1}\left(\begin{aligned} &-{}^bZ_3^w \bar{\tau}_w^W(\tau^*) - {}^N\bar{\omega}^B(\omega^*) \times \\ &(J_{s/c}^N \bar{\omega}^B(\omega^*) + {}^bZ_3^w J_w \bar{\Omega}^W(\Omega^*)) \end{aligned}\right) \\
&\Rightarrow {}^N\dot{\bar{\omega}}^B = J_{s/c}^{-1}\left(-{}^bZ_3^w \bar{\tau}_w^W\left(\frac{\tau^* T^*}{\omega^*}\right) - {}^N\bar{\omega}^B(T^*) \times (J_{s/c}^N \bar{\omega}^B(\omega^*) + {}^bZ_3^w J_w \bar{\Omega}^W(\Omega^*))\right)
\end{aligned} \tag{278}$$

$$\begin{aligned}
\dot{\Omega}^W &= J_w^{-1} \tau_w^W \\
&\Rightarrow \dot{\bar{\Omega}}^W\left(\frac{\Omega^*}{T^*}\right) = J_w^{-1} \bar{\tau}_w^W(\tau^*) \\
&\Rightarrow \dot{\bar{\Omega}}^W = J_w^{-1} \bar{\tau}_w^W\left(\frac{\tau^* T^*}{\Omega^*}\right)
\end{aligned} \tag{279}$$

$$\left(\bar{q}_{1_0}, \bar{q}_{2_0}, \bar{q}_{3_0}, \bar{q}_{4_0}, {}^N\bar{\omega}_{x_0}^B, {}^N\bar{\omega}_{y_0}^B, {}^N\bar{\omega}_{z_0}^B, \bar{\Omega}_{1_0}^W, \dots, \bar{\Omega}_{n_0}^W\right) = \left(\frac{q_1^0}{q^*}, \frac{q_2^0}{q^*}, \frac{q_3^0}{q^*}, \frac{q_4^0}{q^*}, 0, 0, 0, 0, \dots, 0\right) \quad (280)$$

$$\left(\bar{q}_{1_f}, \bar{q}_{2_f}, \bar{q}_{3_f}, \bar{q}_{4_f}, {}^N\bar{\omega}_{x_f}^B, {}^N\bar{\omega}_{y_f}^B, {}^N\bar{\omega}_{z_f}^B, \bar{\Omega}_{1_f}^W, \dots, \bar{\Omega}_{n_f}^W\right) = \left(\frac{q_1^f}{q^*}, \frac{q_2^f}{q^*}, \frac{q_3^f}{q^*}, \frac{q_4^f}{q^*}, 0, 0, 0, 0, \dots, 0\right) \quad (281)$$

$$\begin{aligned} -\tau_{\max}^W &\leq \tau_i^W \leq \tau_{\max}^W \\ \Rightarrow -\frac{\tau_{\max}^W}{\tau^*} &\leq \bar{\tau}_i^W \leq \frac{\tau_{\max}^W}{\tau^*} \\ \Rightarrow -1 &\leq \bar{\tau}_i^W \leq 1 \end{aligned} \quad (282)$$

$$\begin{aligned} -\Omega_{\max}^W &\leq \Omega_i^W \leq \Omega_{\max}^W \\ \Rightarrow -\frac{\Omega_{\max}^W}{\Omega^*} &\leq \bar{\Omega}_i^W \leq \frac{\Omega_{\max}^W}{\Omega^*} \\ \Rightarrow -1 &\leq \bar{\Omega}_i^W \leq 1 \end{aligned} \quad (283)$$

APPENDIX B. MARKET RESEARCH

A. REACTION WHEELS

Manufacturer	Model	Mass (kg)	h_{\max} (N-m-s)	τ_{\max} (N-m)	Reference
Bradford Engineering	W18	4.95	18	0.248	[32]
Bradford Engineering	W18E	5.5	22	0.248	[32]
Bradford Engineering	W18ES	5.85	25	0.248	[32]
Bradford Engineering	W45	6.45	40	0.248	[32]
Bradford Engineering	W45HT	6.5	22	0.403	[32]
Bradford Engineering	W45E	6.65	55	0.248	[32]
Bradford Engineering	W45ES	6.86	70	0.248	[32]
Dynacon MSCI	MicroWheel 4000	5.2	4	0.05	[33]
Dynacon MSCI	MicroWheel 1000	1.4	1.1	0.03	[34]
Dynacon MSCI	MicroWheel 200	1	0.18	0.03	[35]
Honeywell	HR0610	5	12	0.055	[36]
Honeywell	HR0610	3.6	4	0.055	[36]
Honeywell	HR12-12	6	12	0.1	[37]
Honeywell	HR12-25	7	25	0.15	[37]
Honeywell	HR12-50	9.5	50	0.2	[37]
Honeywell	HR14-25	7.5	25	0.1	[37]
Honeywell	HR14-50	8.5	50	0.15	[37]
Honeywell	HR14-75	10.6	75	0.2	[37]
Honeywell	HR16-50	6	50	0.1	[37]
Honeywell	HR16-75	7	75	0.15	[37]
Honeywell	HR16-100	9.5	100	0.2	[37]
L3	RWA-15	14	20	0.68	[38]
L3	MWA-50	10.5	67.8	0.07	[39]
Maryland Aerospace	MAI-101	0.64	0.0011	0.000635	[40]
Maryland Aerospace	MAI-201	0.73	0.0108	0.000625	[41]
Maryland Aerospace	MAI-300	0.317	0.0076	0.000625	[42]
NASA GSFC	SMEX RW	3.3	4	0.14	[43]

Table 7. Market Research Reaction Wheels

Manufacturer	Model	Mass (kg)	h_{\max} (N-m-s)	τ_{\max} (N-m)	Reference
Rockwell Collins	RSI 01-5/15	0.6	0.04	0.005	[44]
Rockwell Collins	RSI 01-5/28i	0.7	0.12	0.005	[44]
Rockwell Collins	RSI 12-75/60	4.85	12	0.075	[44]
Rockwell Collins	RSI 4-75/60	3.7	4	0.075	[44]
Rockwell Collins	RSI 15-215/20	7.7	15	0.215	[44]
Rockwell Collins	RSI 45-75/60	7.7	45	0.075	[44]
Rockwell Collins	RSI 12-220/45	6	12	0.22	[44]
Rockwell Collins	RSI 18-220/45	6.45	18	0.22	[44]
Rockwell Collins	RSI 25-220/45	7.15	25	0.22	[44]
Rockwell Collins	RSI 50-220/45	9.2	50	0.22	[44]
Rockwell Collins	RSI 30-280/30	9.2	30	0.28	[44]
Rockwell Collins	RSI 68-170/60	9.5	68	0.17	[44]
Rockwell Collins	RSI 68-170/60	9.5	68	0.17	[44]
Rockwell Collins	RDR 23-0	5.5	23	0.09	[44]
Rockwell Collins	RDR 57-0	7.6	57	0.09	[44]
Rockwell Collins	RDR 68-3	7.6	68	0.075	[44]
Rockwell Collins	MWI 100-100/100	16.5	100	0.1	[44]
Rockwell Collins	MWI 30-400/37	15.3	30	0.4	[44]
Sinclair	Picosatellite RW	0.09	0.007	0.001	[45]
Sinclair	Picosatellite RW	0.12	0.01	0.001	[45]
Sinclair	Nanosatellite RW	0.185	0.03	0.002	[45]
Sinclair	Microsatellite RW	0.225	0.06	0.005	[45]
Sinclair	Microsatellite RW	0.225	0.06	0.025	[45]
Sinclair	Microsatellite RW	0.97	1	0.1	[45]
SunSpace	SunStar	1.986	0.65	0.05	[46]
Surrey Space SSTL	MicroWheels 10SP-M	0.96	0.42	0.011	[47]
Surrey Space SSTL	MicroWheels 100SP-O	2.6	1.5	0.11	[47]
Surrey Space SSTL	Smallsat Wheels 200SP-M/O	5.2	12	0.24	[48]
Surrey Space SSTL	Smallsat Wheels 200SP-O	5.2	12	0.24	[48]
Teldix	20 cm	3.4	6.5	0.2	[5, p. 398]
Teldix	26 cm	6	20	0.2	[5, p. 398]
Teldix	35 cm	8	80	0.2	[5, p. 398]
Teldix	50 cm	12	300	0.3	[5, p. 398]
Teldix	60 cm	37	1000	0.6	[5, p. 398]

Table 8. Market Research Reaction Wheels (cont.)

B. CMGS

Manufacturer	Model	Mass (kg)	h_{\max} (N-m-s)	τ_{\max} (N-m)	$\dot{\delta}_{\max}$ (rad/s)	Reference
Astrium	CMG 4-6S	13	4	6	1.5	[49]
Astrium	CMG 15-45S	18.4	15	45	3	[50]
Astrium	CMG 10-30	18.4	10	30	3	[51]
Goodrich/Ithaco	Violet CMG	1.28	0.31	0.3100	1	[52]
Honeywell	M50	33.1	75	75	1	[53]
Honeywell	M95	38.6	129	129	1	[53]
Honeywell	M160	44	217	217	1	[53]
Honeywell	M225	54	305	305	1	[53]
Honeywell	M325	61.2	441	441	1	[53]
Honeywell	M325D	61.2	441	441	1	[53]
Honeywell	M715	89.8	969	969	1	[53]
Honeywell	M600	81.6	813	813	1	[53]
Honeywell	M1300	125	2000	2000	1	[53]
Honeywell	M1400	132	2000	2000	1	[53]
Surrey Space SSTL	BILSAT-1 CMG	2.2	0.28	0.0559	0.20	[54]
Swampsat	Swampsat	0.5	8.00E-04	8.00E-04	1	[55]

Table 9. Market Research Control Moment Gyroscopes

THIS PAGE INTENTIONALLY LEFT BLANK

LIST OF REFERENCES

- [1] J. R. Wertz, *et al.*, Eds., *Space Mission Engineering: The New SMAD*. Hawthorn, CA: Microcosm Press, 2011.
- [2] DigitalGlobe, “Worldview-1,” datasheet, [online] 2013, <http://www.digitalglobe.com/downloads/WorldView1-DS-WV1-Web.pdf> (Accessed 22 August 2013).
- [3] H. Kurokawa, “A geometric study of single gimbal control moment gyros – singularity problems and steering law,” Mechanical Engineering Lab. TR 175, Tsukuba, Japan, Jan. 1998.
- [4] R. Votel and D. Sinclair, “Comparison of control moment gyros and reaction wheels for small earth-observing satellites,” Doc. SSC12-X-1 in *Proceeding of 26th Annual AIAA/USU Conference on Small Satellites*, Logan, UT, 2012.
- [5] M. J. Sidi, *Spacecraft Dynamics and Control: A Practical Engineering Approach*. Cambridge: Cambridge University Press, 1997.
- [6] B. Wie, *Space Vehicle Dynamics and Control*, 2nd ed. Reston, VA: AIAA, 2008.
- [7] R. E. Mortensen, “A globally stable linear attitude regulator,” *Int. J. of Control*. Vol. 8, No. 3, pp. 297–302, 1968.
- [8] B. Wie and P. Barba, “Quaternion feedback for spacecraft large angle maneuvers,” *J. of Guidance, Control, and Dynamics*. Vol. 8, No. 3, pp. 360–365, 1985.
- [9] B. Wie, *et al.*, “Quaternion feedback regulator for spacecraft eigenaxis rotations,” *J. of Guidance, Control, and Dynamics*. Vol. 12, No. 3, pp. 375–380, 1985.
- [10] M. H. Kaplan, *Modern Spacecraft Dynamics and Control*. New York: Wiley, 1976.
- [11] H. Schaub and J. L. Junkins, *Analytical Mechanics of Space Systems*. AIAA, 2003.
- [12] G. Creamer, *et al.*, “Attitude determination and control of clementine during lunar mapping,” *J. of Guidance, Control, and Dynamics*. Vol. 19, No. 3, pp. 505–511, May-June 1996.
- [13] M. Karpenko, *et al.*, “Design and flight implementation of operationally relevant time-optimal spacecraft maneuvers.” *Advances in the Astronautical Sciences*, Vol. 142, 2011.

- [14] M. Frayman and R. Strunce, "Spacecraft slewing/guidance algorithm for hyperspectral imagers." AIAA Fifth Responsive Space Conference, 2007.
- [15] F. L. Markley, *et al.*, "Maximum torque and momentum envelopes for reaction-wheel arrays," *J. of Guidance, Control, and Dynamics*. Vol. 33, No. 5, pp. 1606–1614, Sep.-Oct. 2010.
- [16] R. Stengel, *Optimal Control and Estimation*. New York: Dover, 1986.
- [17] J. D. Turner and J. L. Junkins, "Optimal large angle single-axis rotational maneuvers of flexible spacecraft," *J. of Guidance, Control, and Dynamics*. Vol. 3, No. 6, pp. 578–585, 1980.
- [18] S. R. Vadali and J. L. Junkins, "Spacecraft large angle rotational maneuvers with optimal momentum transfer," *J. of the Astronautical Sciences*, Vol. 31, pp. 217–235, April-June 1983.
- [19] J. L. Junkins and J. D. Turner, *Optimal Spacecraft Rotational Maneuvers*. Amsterdam: Elsevier, 1986.
- [20] M. Karpenko, *et al.*, "First flight results on time-optimal spacecraft slews," *J. of Guidance, Control, and Dynamics*. Vol. 35, No. 2, pp. 367–376, Mar.-Apr. 2012.
- [21] I. Ross, "A Beginner's Guide to DIDO: A MATLAB Application Package for Solving Optimal Control Problems." V7.3, Doc. TR-711, Monterey, CA: Elissar, 2007.
- [22] N. S. Nise, *Control Systems Engineering*, 6th ed. Pomona, CA: Wiley, 2011.
- [23] P. W. Likins, *Elements of Engineering Mechanics*. New York: McGraw-Hill, 1973.
- [24] D. Verbin, *et al.*, "Time-efficient angular steering laws for rigid satellites," *J. of Guidance, Control, and Dynamics*. Vol. 34, No. 3, pp. 878–892, May-June 2011.
- [25] I. M. Ross, *A Primer on Pontryagin's Principle in Optimal Control*. San Francisco: Collegiate Publishers, 2009.
- [26] A. E. Bryson and Y. C. Ho, *Applied Optimal Control: Optimization, Estimation, and Control*. New York: Taylor & Francis, 1975.
- [27] C. J. Heiberg, "A practical approach to modeling single-gimbal control moment gyroscopes in agile spacecraft," in *AIAA Guidance, Navigation and Control Conference and Exhibit*, Denver, CO, 2000, pp. 1–11.

- [28] G. Margulies and J. N. Aubrun, "Geometric theory of single-gimbal control moment gyro systems," *The J. of the Astronautical Sciences*. Vol. 26, No. 2, pp. 159–191, Apr.-Jun. 1978.
- [29] C. D. McManus, "Development, verification and experimental analysis of high-fidelity mathematical models for control moment gyros," M.S. thesis, Mech. and Aero. Eng. Dept., NPS, Monterey, CA, 2011.
- [30] B. Wie, *et al.*, "Singularity robust steering logic for redundant single-gimbal control moment gyros," *J. of Guidance, Control, and Dynamics*. Vol. 24, No. 5, pp. 865–872, Sep.-Oct. 2001.
- [31] I. M. Ross and M. Karpenko, "A review of pseudospectral optimal control: from theory to flight," *Annual Reviews in Control*. Vol. 36, pp. 182–197, 2012.
- [32] E. J. van der Keide, *et al.*, "Reaction wheels at Bradford Engineering," in *8th International ESA Conf. on Guidance, Navigation, and Control Systems*, Karlovy Vary, Czech Republic, 5–10 Jun. 2011, pp. 1–10.
- [33] MSCI Microsat Systems Canada Inc., "MicroWheel 4000 (MW4000) reaction wheel," [online] 2013, <http://www.reactionwheel.com/products/mw-4000.html> (Accessed 28 July 2013).
- [34] MSCI Microsat Systems Canada Inc., "MSCI MicroWheel 1000," datasheet, [online] 2009, <http://www.reactionwheel.com/products/MicroWheel-1000.pdf> (Accessed 28 July 2013).
- [35] MSCI Microsat Systems Canada Inc., "MSCI MicroWheel 200," datasheet, [online] 2009, <http://www.msinc.ca/products/MicroWheel-200.pdf> (Accessed 28 July 2013).
- [36] Honeywell International Inc., "Honeywell Model HR 0610 reaction wheel," datasheet, [online] 2003, http://www51.honeywell.com/aero/common/documents/myaerospacecatalog-documents/HR_0610_Reaction_Wheel.pdf (Accessed 28 July 2013).
- [37] Honeywell International Inc., "Constellation series reaction wheels," datasheet, [online] 2003, ftp://apollo.ssl.berkeley.edu/pub/Pointing_Studies/Hardware/Honeywell%20Reaction%20Wheels.pdf (Accessed 28 July 2013).
- [38] L-3 Communications, "RWA-15 high torque reaction wheel," datasheet, [online] 2011, http://www2.l-3com.com/spacenav/space_and_nav/space_products/pdfs/SellSheet_RWA_15_Apr11.pdf (Accessed 28 July 2013).

- [39] L-3 Communications, “MWA-50 low cost momentum wheel assembly,” datasheet, [online] 2011, http://www2.l-3.com.com/spacnav/space_and_nav/space_products/pdfs/SellSheet_MWA_50_Apr11.pdf (Accessed 28 July 2013).
- [40] Maryland Aerospace, Inc., “MAI-101 miniature 3-axis reaction wheel product specification,” datasheet, [online] 2011, <http://www.miniadacs.com/linked/mai-101%20specification%203-18-11.pdf> (Accessed 28 July 2013).
- [41] Maryland Aerospace, Inc., “MAI-201 miniature 3-axis reaction wheel product specification,” datasheet, [online] 2011, <http://www.miniadacs.com/linked/mai-201%20specification%202-11-11.pdf> (Accessed 28 July 2013).
- [42] Maryland Aerospace, Inc., “MAI-300 single axis reaction wheel,” datasheet, [online] 2011, <http://www.miniadacs.com/linked/2012-04-27%20mai-300%20specification.pdf> (Accessed 28 July 2013).
- [43] NASA, “Innovative Partnerships Program Office: Featured technologies,” [online] 2011, http://ipp.gsfc.nasa.gov/ft_tech_reaction_moment_whl.shtm (Accessed 28 July 2013).
- [44] Rockwell Collins, “Satellite stabilization wheels,” [online] 2012, https://www.rockwellcollins.com/Products_and_Systems/Controls/Satellite_Stabilization_Wheels.aspx (Accessed 28 July 2013).
- [45] Sinclair Interplanetary, “Reaction wheels,” [online] 2013, <http://www.sinclairinterplanetary.com/reactionwheels> (Accessed 28 July 2013).
- [46] Sunspace, “Reaction wheel,” datasheet, [online] 2013, https://wiki.umn.edu/pub/FormationFlying/AttitudeDeterm/ReactionWheelsR03_092005.pdf (Accessed 28 July 2013).
- [47] Surrey Satellite Technology Ltd., “SSTL Microwheels,” datasheet, [online] 2013, <http://www.sstl.co.uk/getattachment/f31aaa67-3750-4a8a-9742-c1cd800c0a5b/Microwheels> (Accessed 28 July 2013).
- [48] Surrey Satellite Technology Ltd., “SSTL Microwheels,” datasheet, [online] 2013, <http://www.sstl.co.uk/getattachment/8ccf207d-1ada-4bfc-a21b-5c400a1f5d52/SmallWheel> (Accessed 28 July 2013).
- [49] EADS Astrium, “CMG 4–6S,” datasheet, [online] 2009, <http://www.astrium.eads.net/media/document/control-momentum-gyro-cmg-4-6s.pdf> (Accessed 28 July 2013).
- [50] EADS Astrium, “CMG 15–45S,” datasheet, [online] 2012, http://www.astrium.eads.net/media/document/astrium_gnc6_mdef.pdf (Accessed 28 July 2013).

- [51] EADS Astrium, “CMG 10–30,” datasheet, [online] 2012,
http://www.astrium.eads.net/media/document/astrium_gnc8_mdef.pdf (Accessed 28 July 2013).
- [52] J. Gersh and M. Peck, “Violet: A high-agility nanosatellite for demonstrating small control-moment gyroscope prototypes and steering laws.” *AIAA Guidance, Navigation and Control Conference*, 2009.
- [53] F. A. Leve, “Development of the spacecraft orientation buoyancy experimental kiosk,” M.S. thesis, College of Eng., University of Florida, Gainesville, FL, 2008.
- [54] V. Lappas, *et al.*, “Micro CMGs for agile small satellites: design and in-orbit tests.” *Guidance, Navigation and Control Systems*. Vol. 606, 2006.
- [55] EoPortal Directory, “Swampsat.” [online] 2012,
<https://directory.eoportal.org/web/eoportal/satellite-missions/s/swampsat>
(Accessed 28 July 2013).

THIS PAGE INTENTIONALLY LEFT BLANK

INITIAL DISTRIBUTION LIST

1. Defense Technical Information Center
Ft. Belvoir, Virginia
2. Dudley Knox Library
Naval Postgraduate School
Monterey, California